Boiling impact on acid water electrolysis process: fundamentals to application

李, 林軍

Boiling impact on acid water electrolysis process –fundamentals to application–

Examiner: Prof. Kohei Ito
Co-examiner: Prof. Yoko Yamanishi
Prof. Shoji Mori
Prof. Tatsumi Kitahara

LI LINJUN
Department of Hydrogen Energy Systems
Graduate School of Engineering
Kyushu University
Fukuoka, JAPAN
January, 2023

Contents

Contents ..... **I**

Acknowledgement ..... **IV**

List of figures ..... **V**

List of tables ..... **VIII**

1. Introduction **1**

1.1 Role of water electrolysis in next energy generation 1

1.2 Current status and problem to be solved 2

1.3 Previous studies to improve PEMWE 3

1.4 Boiling effect –an attempt to reduce electrolysis voltage 4

1.5 Methodology and strategy in this study 7

1.6 Outline of this study and originality 9

References 11

2. Experimental analysis of boiling effect on OER **16**

2.1 Introduction 16

2.2 Experiment and theoretical predictions 18

2.2.1 Working electrodes 18

2.2.2 Experiment system and conditions 21

2.2.3 Theoretical predictions 24

2.3 Results and discussion 28

2.3.1 Integrity verification of the three electrodes cell at 25°C 28

2.3.2 Boiling effect on the activation overvoltage 31

2.3.3 Boiling effect on Nernst loss 32

2.3.4 Highlighting boiling effect on OER 34

2.3.5 Corrected exchange current density 35

2.4 Conclusion 37

References 38

3. Theoretical analysis of boiling effect on OER **41**

3.1 Introduction 41

3.2 Model introduction of the OER superimposed with boiling 43

3.2.1 Overpotential and current density of the OER 50

3.2.2 Dissolved oxygen transfer in water 53

3.2.3 Liquid/gas flow in the PTL 55
3.3 Result and discussions 62
3.3.1 Comparison of theoretical and experimental results 63
3.3.2 Oxygen transfer and electrochemical performance during boiling 66
3.3.3 Mass transfer of the OER without boiling 74
3.4 Conclusions 79
References 80
4. Experimental and theoretical analysis of the boiling effect on the hydrogen evolution reaction 83
4.1 Introduction 84
4.2 Experiment 85
4.2.1 Experimental apparatus 86
4.2.2 Experimental method 89
4.3 Experimental results 91
4.3.1 Integrity verification of CL 91
4.3.2 Boiling effect on HER overpotential 94
4.4 Theoretical model of HER 96
4.4.1 Overpotential and current density 101
4.4.2 Dissolved hydrogen transfer 105
4.4.3 Liquid-gas transfer in the carbon paper 105
4.5 Theoretical results and discussions 109
4.5.1 HER model verification 109
4.5.2 Boiling effect on HER overpotential of the WE2 112
4.6. Conclusions 119
References 121
5. Theoretical analysis of boiling effect on electrolysis voltage of polymer electrolyte membrane water electrolyzer (PEMWE) 124
5.1 Introduction 125
5.2 PEMWE structure and experimental conditions 128
5.3 Mass transfer in the PEMWE 130
5.3.1 Molar fluxes of oxygen, hydrogen and water 131
5.3.2 Bubble detachment in the CH 134
5.3.3 Gas transfer in the PTL 138

5.3.4 Gas transfer in the dry PTL 140
5.3.5 Water vaporization 142
5.4 Electrolysis overvoltage 144
5.4.1 Nernst loss 145
5.4.2 Activation overvoltage 147
5.4.3 Ohmic overvoltage 149
5.4.4 Efficiency 149
5.5 Result and discussions 151
5.5.1 Model accuracy verification 151
5.5.2 Mass transfer in anodic PTL and CH 153
5.5.3 Boiling effect on overvoltage 155
5.5.4 Boiling effect at each current density and efficiency 159
5.6 Conclusion 160
References 162
6. Summary and prospect 165
6. 1 Summary 165
6.2 Prospect 167
References 170
Appendix A. Anodic and cathodic activation fraction 171
References 179

Acknowledgement

As Ph.D. graduation approaches, I decided to write acknowledgments to wrap up my dissertation. Over the past three and half years, many people have provided vital help and encouragement along the path of my doctoral research. Here, I will express my gratitude.

My supervisor, Professor Ito, provided me with the most help in both scientific research and life. The knowledgeable Mr. Ito strictly guided my research and paper writing with a rigorous scientific research attitude. Although we often have heated debates about certain scientific issues, Ito-sensei has always respected my views. While I feel academic freedom, I am constantly discovering the truth in the process of debate. Mr. Ito shows emphasis on cultivating the details of my writing by requiring me to consider every word and symbol carefully. These trainings have helped me a lot in dealing with the details of other things. Ito-sensei also actively helped me with the problems I encountered in my life. In particular, around the time my daughter was born, he didn't hesitate to hire me as a research assistant to help me through difficult financial times. Here, I would like to express my sincere gratitude to my supervisor, Prof. Ito, again. However, short words are still not enough to express my gratitude to him.

In addition, I would also like to thank Nakajima-sensei for his help with my research and thesis writing. Mr. Nakajima is always enthusiastic and patient to discuss with me the hard academic problems. He even helped me to review all the research papers and also provided key advice and assistance on my future career choices.

Next, I thank the Chinese Scholarship Council and the Chinese government, which sponsor my Ph.D. project. I would also like to thank my family. During my Ph.D., I never had the opportunity to return to my nation to reunite with my parents because the COVID-19 continues to this day. Thanks for their concern and encouragement. Fortunately, my wife, AN JIE, was always by my side. Thank her for following me to a foreign country without hesitation. During my Ph.D., she accompanies and supports my life and studies without any regrets. I would also like to thank my newly born daughter, LI ZHIYUE, who has brought so much joy to my life.

Finally, I would also like to thank my friends: Wang Peng, Yu Miao, Zhang Min, Ma Songsong, Chi Yintian, Wu Yifeng, Otaguro Koichi, Moriyama Junji, Ryuta Kohama, Muramatsu Ken and others. They provided timely help for my troubles in life and study.

List of figures

Fig. 1.1	Cell structure and component.	5
Fig. 1.2	Impact of boiling on electrolysis voltage at 0.1 MPa.	5
Fig. 1.3	Growth of vapor bubble from an oxygen bubble.	6
Fig. 1.4	SEM image of PTL	7
Fig. 1.5	Structures of three type WEs.	8
Fig. 2.1	Interior structures of three type WEs (WE: working electrode; CL: catalyst layer; PTL: Porous transfer layer; CH: channel).	19
Fig. 2.2	TEC with boiling function.	22
Fig. 2.3	Predicting Tafel plots of OER.	27
Fig. 2.4	Electrochemical performance of the custom-made CL at 25°C and 1 bar.	30
Fig. 2.5	Temperature influence on OER potentials (IR correction, vs. SSCE) for WE1.	31
Fig. 2.6	Temperature influence on WE1 potential.	32
Fig. 2.7	Temperature influence on OER potential for WE2 (IR correction, vs. SSCE).	33
Fig. 2.8	Temperature influence on WE2 potential.	34
Fig. 2.9	Temperature influence on the OER potential (IR correction, vs. SSCE) for the WE3.	34
Fig. 2.10	Temperature influence on WE3 potential.	35
Fig. 2.11	The dimensionless corrected exchange current density and oxygen activity on CL versus temperature for three WEs	36
Fig. 3.1	Calculation flow of theoretical model.	43
Fig. 3.2	Schematic drawings of OER process.	48
Fig. 3.3	Circuit diagram of three current density components (current density of the CL in bubbles, and in liquid water far from and surrounding the bubbles).	52
Fig. 3.4	Detachment of bubbles at the PUS.	59

Fig. 3.5	Schematic of evaporation area.	61
Fig.3.6	Theoretical and experimental comparison of overpotential.	64
Fig.3.7	Changes of basic mass transfer parameter.	67
Fig. 3.8	Boiling effect on the OER performance.	71
Fig. 3.9	Transfer characteristics of oxygen at 85 °C.	75
Fig. 3.10	Current density against the gas saturation at 85°C:	77
Fig. 3.11	The physical state of oxygen and water vapor at 85°C.	78
Fig.4.1	Apparatus introduction. a.three-electrode cell, b interior structures of WE1 and WE2, c potential correction.	87
Fig. 4.2	Basic property of the custom-made CL at 25 °C and 0.1013 MPa.	93
Fig. 4.3	Boiling effect on HER overpotentials (IR correction).	95
Fig. 4.4	Calculation flowchart of HER model.	96
Fig. 4.5	Theoretical model.	100
Fig. 4.6	Current density in water and bubbles.	102
Fig. 4.7	Comparison of HER overpotential in experiment and theory.	110
Fig. 4.8	Essential values of mass transfer at the CL.	113
Fig. 4.9	Gas and liquid velocity in the carbon paper of 0.11-mm thickness.	116
Fig. 4.10	Electrochemical performance of the WE2.	117
Fig. 4.11	HER current contribution ratio at the CL.	118
Fig. 5.1	Structure of a practical PEMWE.	126
Fig. 5.2	Structure (left) and mass flow rate (right) in a PEMWE.	132
Fig. 5.3	Growth and detachment for the gas bubbles on the PTL with time.	135
Fig. 5.4	Determining the relative evaporation area.	137
Fig. 5.5	Discretized PTL model.	139
Fig. 5.6	Transfer of gaseous oxygen and water vapor in the PTL.	141
Fig. 5.7	Calculating the relative evaporation area in the PTL.	143
Fig. 5.8	Schematic diagram of the water and oxygen activity at non-boiling (90 °C), boiling (105 °C), and dry condition (120 °C).	147
Fig. 5.9	Comparison between the theoretical and experimental voltages.	152
Fig. 5.10	Distribution of gas velocity, gas saturation, and capillary pressure in the anodic PTL	154

Fig. 5.11	Life cycle of bubbles from inception to detachment at the anode CH/PTL interface.	155
Fig. 5.12	Changes on the Nernst losses and activities of water, oxygen, and hydrogen with temperature.	156
Fig. 5.13	Changes on the activation overvoltage and activation fraction with temperature.	157
Fig. 5.14	Changes on the ohmic overvoltage, PEM resistivity, PEM water content, and RH in the anode with temperature.	158
Fig. 5.15	Voltage components.	159
Fig. 5.16	Variation of electrolysis voltage and PEMWE efficiency with temperature and current density.	160
Fig. 6.1	Structure of a PEMWE unit with boiling.	168
Fig. 6.2	Hydrogen production system	169
Fig. 6.3	Future energy society when the boiling effect is embedded in a water electrolyzer	169

List of tables

Table 1.1	Nomenclature.	2
Table 1.2	Comparison between SOWE, AWE, and PEMWE	3
Table 2.1	Nomenclature.	17
Table 2.2	Details of each component in the WEs	19
Table 2.3	Experiment conditions for each measurement	24
Table 3.1	Nomenclature.	44
Table 3.2	Calculation conditions	45
Table 3.3	Constants for the model	45
Table 3.4	The standard redox potential	65
Table 4.1	Parameters in the WEs	88
Table 4.2	Experiment conditions for each measurement	90
Table 4.3	Nomenclature	97
Table 4.4	Calculation condition	98
Table 4.5	Constants for the model	98
Table 5.1	Nomenclature	126
Table 5.2	PEMWE parameters	128
Table 5.3	Calculation conditions	129
Table 5.4	Model parameters	129

Chapter 1

Introduction

1.1 Role of water electrolysis in next energy generation

The carbon dioxide released by burning fossil fuels causes the greenhouse effect, continuously raising the global average temperature and seawater temperature for nearly a hundred years. The combustible ice in the seabed accelerates the release of methane gas with the increase in seawater temperature [1]. The greenhouse effect of methane gas in the atmosphere is more than 80 times that of carbon dioxide, which viciously exacerbates global warming [2]. The climate catastrophe caused by global warming may jeopardize mankind's survival in the future. In addition, the development of human society is inseparable from energy, but the continuous consumption of non-renewable fossil energy has gradually triggered a global energy crisis. Therefore, global countries are working hard to develop clean and renewable energy.

Today, the application of mature renewable energy power generation technologies includes nuclear power, wind power, solar power, ocean power generation, et al. [3]. However, the global renewable energy generation is still less than 30% of the total electricity generation [4]. One of the critical reasons is that renewable energy generation is unstable, and balancing power supply and demand is difficult. Therefore, leveling the power generated by renewable energy sources is a key to addressing renewable energy applications. Storing surplus electricity from renewable energy sources solves the shortage of renewable energy supply when energy demand is high. Candidates for storing the electricity are supercapacitors, batteries, electrolyzer, et al. [5-7]. Among them, electrolyzer convert electrical energy into chemical energy of substances, which can store a large amount of surplus power, and has a broader application prospect. Electrolytic energy storage methods have water electrolysis, carbon dioxide electrolysis, electrochemical nitrogen reduction, and steam-carbon dioxide reforming [8-10]. Among them, the hydrogen energy storage density is high, and the application cleanliness and renewability are satisfied. Hydrogen production by water electrolysis is an ideal energy storage method. As a convenience, the nomenclature in Table 1.1 lists some terms related to water electrolysis, which will be introduced as follows.

Table 1.1 Nomenclature.

Nomenclature	
AWE	Alkaline water electrolyzer
CH	Channel
CL	Catalyst layer
HER	Hydrogen evolution reaction
LSV	Linear sweep voltammetry
OER	Oxygen evolution reaction
PEM	Polymer electrolyte membrane
PEMWE	Polymer electrolyte membrane water electrolyzer
PTL	Porous transfer layer
SOWE	Solid oxide water electrolyzer
TEC	Three-electrode cell

1.2 Current status and problem to be solved

The water electrolysis for hydrogen production mainly comes from solid oxide water electrolyzer (SOWE), alkaline water electrolyzer (AWE), and polymer electrolyte membrane water electrolyzer (PEMWE) [11]. The technological parameters of these electrolyzers are compared in Table 1.2. The SOWE is highly efficient and uses non-precious metal catalysts. However, it has high operating temperatures (>900°C). The SOWE takes a long time to startup and is difficult to respond quickly to changing operating temperature. Additionally, the high operating temperatures can oxidize catalysts easily, reducing the durability of SOWE. Due to these disadvantages, SOWE is still in the experimental and research stage and has not yet achieved commercialization. The AWE of relatively low cost is more mature for commercialization, but hydrogen purity is insufficient. AWE has a low current density and requires additional space inside to store KOH aqueous, requiring a larger volume to meet the hydrogen yield. In addition, the electrolyte diaphragm between the AWE cathode and anode is weak and difficult to withstand the large pressure difference between the anode and cathode during dynamic response. The PEMWE has high power density, fast current response, and high hydrogen purity, which is more competitive in large-scale electrolytic hydrogen

production. However, the expensive cost of PEMWEs reduces the price of hydrogen production difficultly. There is an urgent need to solve the problem of its expensive initial cost.

Table 1.2 Comparison between SOWE, AWE, and PEMWE [12]

Specification	Unit	SOWE	AWE	PEMWE
Technology maturity	-	Research& development	Widespread commercialization	Commercialization
Cell temperature	°C	900-1000	60-80	50-80
Current density	$A \cdot cm^{-2}$	0.3-1.0	<0.45	1-5
Cell voltage	V	0.95-1.3	1.8-2.4	1.8-2.2
Voltage efficiency	%	81-86	62-82	67-82
Lifetime	kh	8-20	55-120	60-100
Hydrogen purity	%	-	>99.8	99.99
Start-up time	min	>60	15	<15
Investment costs	$€ \cdot kW^{-1}$	>2000	800-1500	1400-2100

1.3 Previous studies to improve PEMWE

To decrease the initial cost, many researchers have been attracted to cheaper catalysts and optimization of the porous structure of the catalyst layer (CL) used for the PEMWE [13–15]. Some researchers have focused on hybrid catalysts, such as $Ir/NiCoO_4$, which perform better than IrO_2 particles [16]. Co-based catalysts can function well in the oxygen evolution reaction (OER) and hydrogen evolution reaction (HER) [17,18]. In addition to the potentially excellent performance of Co-based catalysts, their nanowire structure can further lower the over-voltage [19,20].

In addition, reducing the reaction area can effectively lower the PEMWE investment cost. For a certain hydrogen production rate, increasing the current density can reduce the

reaction area of PEMWE. However, increasing the current density tends to increase the electrolysis voltage. The high voltage can reduce the durability of the PEMWE and will face cost problems due to the reduction of the PEMWE life. Many researchers have tried to reduce the electrolysis voltage by changing the component structure of PEMWE [21,22]. Grigoriev et al. [23] studied the porosity and pore size of the porous transfer layer (titanium meshes) to conclude that a dense pore structure increases the electrolysis overvoltage. Toghyani et al. found that the thin PEM reduces the ohmic overvoltage by CFD analysis [24]. However, more hydrogen penetrates through a thin polymer electrolyte membrane (PEM), especially at high pressure, increasing the risk of massive combustion and degrading hydrogen gas purity. [25]. Optimizing the operating conditions of PEMWE can simply and effectively reduce the voltage [26]. Equalizing assembly pressure and water distribution of a PEMWE stack are beneficial to reduce the voltage and improve the PEMWE durability [27]. Toghyani et al. found the high temperature, and low operation pressure lead to a low PEMWE voltage by the Taguchi method [28]. Grigoriev found that the electrolysis voltage is low when the PEMWE run at high temperature with a sufficient supply of liquid water [29]. However, a too-high operating temperature may dry the liquid water in the PEMWE, increasing the electrolysis overvoltage and decreasing the membrane durability [30, 31].

1.4 Boiling effect –an attempt to reduce electrolysis voltage

As such, Ito et. al proposed a novel method for improving the PEMWE performance by superimposing boiling on the PEMWE to reduce the electrolysis voltage [32]. This proposal was examined in experiments in which a lab-scale PEMWE is superimposed by boiling, as shown in Fig. 1,1. In Fig.1.2, the electrolysis voltage drops sharply after the boiling point at a small current density (0.002 $A \cdot cm^{-2}$) in the PEMWE.

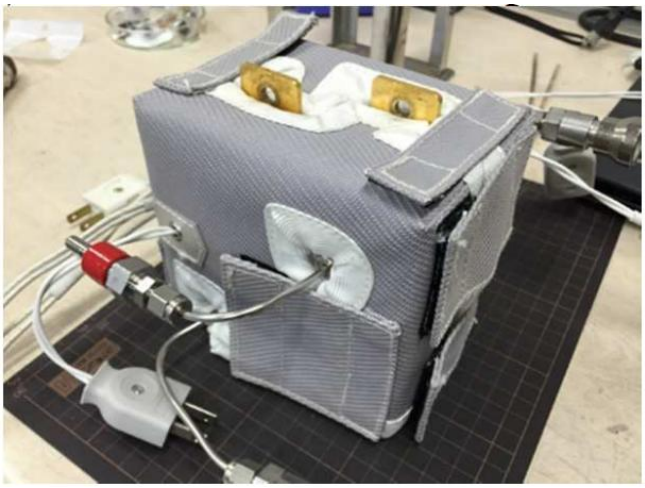

Fig. 1.1 Cell structure and component.

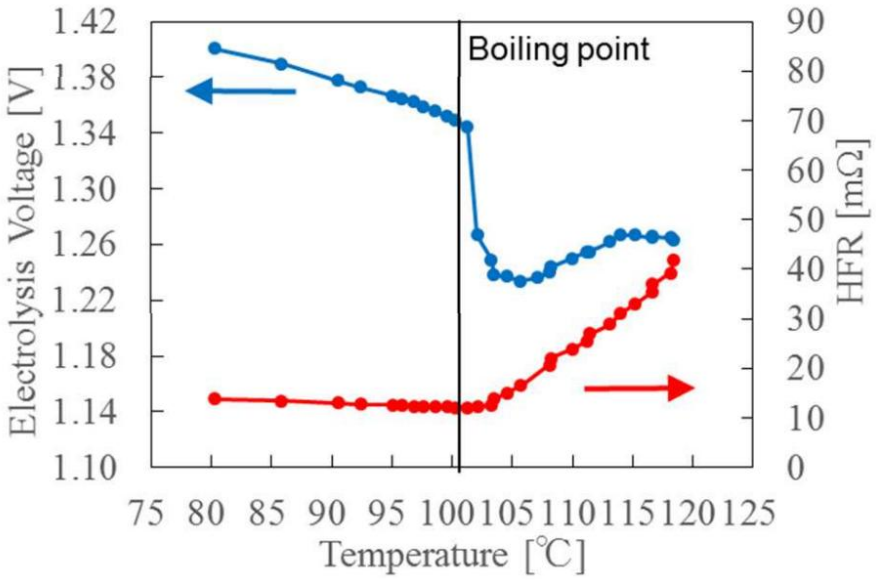

Fig. 1.2 Impact of boiling on electrolysis voltage at 0.1 MPa [32].

However, the mechanism by which boiling can reduce the voltage has not been clarified. Boiling itself possesses a couple of effects. A macroscopic modeling according to the De-Donder equation, which relies on non-equilibrium thermodynamics (entropy generation), suggests that boiling is a spontaneous process and that endothermic reactions of hydrogen generation followed by boiling can be accelerated [33]. In a more concrete manner, it is suggested that boiling may reduce the activation overvoltage by increasing the exchange current density of the anode OER. It is noted that massive vapor produced by boiling possibly reduces hydrogen and oxygen activities and results in a reduction of Nernst loss [34]. Theoretical analysis [32] following this macroscopic mechanism obtained a qualitative agreement in the voltage between theory and experiment.

Here are possible discussions of the mechanisms for the boiling effect. The water electrolysis voltage consists of the Nernst loss, the activation overvoltage of the oxygen evolution reaction (OER) and hydrogen evolution reaction (HER), and the ohmic overvoltage [35].

(1) The Nernst loss of water electrolysis depends on temperature. Increasing temperature can change the Gibbs free energy of water electrolysis [36]. Specially, the Gibbs free energy during the electrolysis reaction differs when the reactant is differed by water and vapor [37]. When boiling occurs, a large amount of vapor fills the oxygen bubbles, reducing the partial pressure of oxygen gas, as shown in Fig. 1.3. As a result, the low oxygen activity reduces the Nernst loss [38]. In terms of HER, boiling reduces hydrogen activity in the same manner as OER.

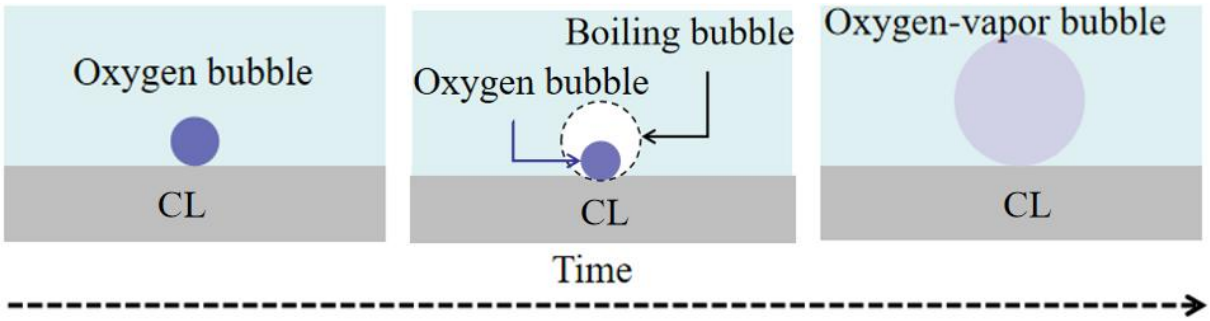

Fig. 1.3 Growth of vapor bubble from an oxygen bubble.

In PEMWE, the CL surface is covered by a PTL [39]. Fig. 1.4 shows the microstructure of PTL imaged by SEM [40]. The titanium fibers range in diameter from 10-30 μm. The hole diameter of the titanium mesh is about 100 μm. The pore structure in the PTL provides a dense vaporization core for boiling [41]. Boiling produces a large amount of water vapor, forming a high gas saturation in the PTL. The transfer resistance of oxygen gas in the gas phase is much lower than in the liquid phase [42]. Thus the gas-phase channels created by boiling can accelerate the removal of oxygen. Oxygen is quickly removed from the CL surface to reduce its concentration in the CL, reducing the Nernst loss of OER.

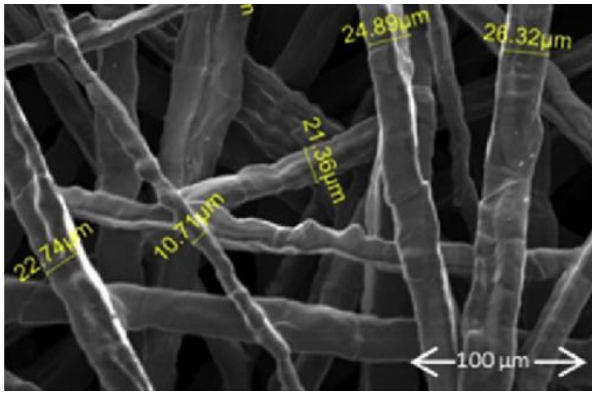

Fig. 1.4 SEM image of PTL [40].

(2) The sub-reaction activation energy of OER is affected by the dielectric constant between the catalyst and the adsorbate [43]. Catalysts and adsorbates in water have different dielectric constants than in vapor. Boiling may change the dielectric constants between water and vapor to reduce the activation overvoltage of OER. Similarly, in terms of HER occurring in water and vapor, the dielectric constants between the catalyst and the adsorbate are also different. Therefore, boiling may also change the activation overvoltage of HER.

(3) The proton transfer resistance in the PEM forms the main ohmic resistance, related to the water content of the PEM [44]. A large amount of vapor during boiling can reduce the water coverage on PEM, possibly reducing the water content and increasing ohmic resistance in the PEM [45]. Therefore, boiling may increase the ohmic overvoltage of water electrolysis.

1.5 Methodology and strategy in this study

Although candidates of the mechanism of boiling effect are suggested as just above, it is difficult to clarify which one is the mechanism. This is because a practical PEMWE obtains only the relationship between electrolysis voltage and current density and it cannot distinguish which voltage component the boiling impacts. Moreover, a practical PEMWE is opaque and cannot visualize how boiling bubbles influence electrolysis bubbles (oxygen and hydrogen bubbles).

To overcome the difficulty attributed to the conventional electrolyzer, this study introduces a three-electrode cell (TEC) instead of the practical PEMWE. TEC can examine the potential of OER and HER independently on a case-by-case basis by switching the role of

the working electrode between the OER and HER [46]. Besides, TEC with some electrochemical analysis can separate activation and concentration overvoltage [47]. TEC can visualize electrodes [48]. These advantages of TEC make it possible to examine the effect of boiling on activation and concentration overvoltages of the OER and HER, independently. Also, they allow observing the bubbles produced by boiling and electrolysis.

Different structured electrodes for the working electrode (WE) are carefully designed and embedded in TEC to clearly analyze which voltage component is reduced by boiling. As shown in Fig. 1.5 (for the case of OER), WE1 is a conventional WE with only a catalyst layer (CL). WE2 embeds a titanium mesh as the PTL on the CL. WE3 is similar to the anode side of a practical PEMWE, constituting a CL, a titanium mesh, and a serpentine channel (CH). WE3 comprises the highest oxygen transfer resistance, and WE2 is the second highest one. If the boiling causes activating electrochemical reaction and activation overvoltage reduction, they are highlighted in the case of WE1, and it is concluded that the mechanism of the boiling effect is activation overvoltage reduction caused by electrochemical reaction activation driven by boiling. If boiling causes mass transfer enhancement and concentration overvoltage reduction, they are highlighted in the cases of WE2 and WE3, and it is concluded that the mechanism of the boiling effect is concentration overvoltage reduction caused by mass transfer enhancement driven by boiling.

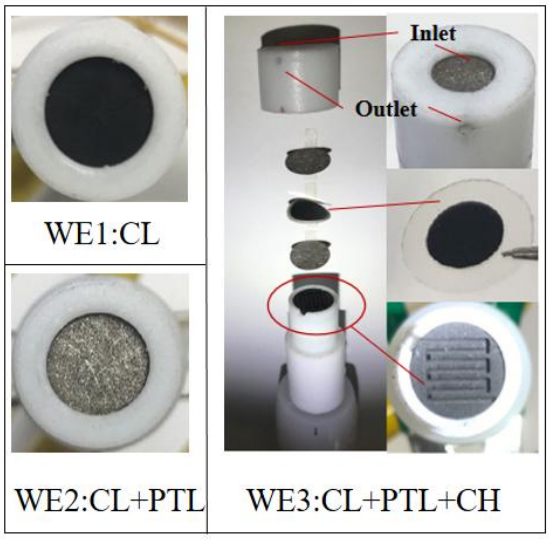

Fig. 1.5 Structures of three type WEs.

All three types of electrodes are electrochemically evaluated in two methods.

(1) The OER potential is examined by changing the temperature from 85°C to 115°C under a

galvanostatic conditions. If the boiling functions, the OER potential will abruptly decrease at the boiling temperature.

(2) These WEs are also tested using linear sweep voltammetry (LSV) [49,50] for each temperature sweep. The LSVs are converted to Tafel plots [51] to clarify which overvoltage component is reduced by boiling. It is noted that, although the discussion so far done in this sub-section is on OER, the boiling effect on HER is also examined and analyzed in a manner similar to the OER case.

Although TEC shows advantages in studying the effect of boiling on OER and HER, it cannot investigate the boiling mechanism quantitatively. How does boiling superimpose on OER improve oxygen transfer and decrease oxygen concentration? Is the boiling effect highlighted in the case of large oxygen transfer resistance and large oxygen concentration, such as when OER current and porous transfer layer (PTL) thickness are large? Do vapor bubbles accelerate the drainage of gaseous oxygen and dissolved oxygen somehow? Do these effects also act on HER? To respond to these questions, this study develops a new model to quantitatively clarify the mechanism of the boiling effect that improves electrolysis performance. After identifying the mechanism of boiling on the anodic OER and cathodic HER of PEMWE, the ohmic overvoltage of PEMWE during boiling needs to be further investigated. Because too high temperature may dry up the PEM, the ohmic overvoltage may rise sharply.

1.6 Outline of this study and originality

To solve the issues mentioned above, this thesis lists 6 chapters to introduce boiling impact on acid water electrolysis process.

Chapter 1 presents the background and introduction of this study, as so far shown.

The second chapter experimentally studies the OER performance without and with boiling.

The third chapter establishes a dimensionless numerical model to quantitatively study the mass transfer and electrochemical performance of the OER at boiling. The electrolysis reaction process in this model obeys the charge conservation. The mass transfer process obeys the conservation of molar flux and momentum. The gas saturation at the upper surface of the

PTL provides the boundary conditions for the liquid-gas flow model.

In chapter 4, the boiling mechanism on HER is investigated by experiments and theoretical models. The experimental and theoretical methods of studying HER are similar to that of OER.

Chapter 5 introduces how boiling theoretically changes the Nernst loss, activation overvoltage, and ohmic overvoltage based on a PEMWE model. In this model, the boiling is coupled with the PEMWE to quantify the voltage changes at unboiling, boiling, and drying conditions.

Finally, chapter 6 summarizes the conclusions of this study, and indicates possible future works.

In this thesis, by comparing experimental and theoretical electrolysis voltage, the boiling effect and mechanism on each voltage component of PEMWE are clarified. The originality of this paper is specifically introduced below:

(1) A sophisticated three-electrodes cell here developed enable to separate the boiling effect on OER and HER and to quantitavely evaluate their overpotential, independently.

(2) A comprehensive model here developed can reproduce and predict boiling effect on OER and HER overpotential. Moreover, theoretical calculation based on the model sheds light on the detail on the mechanism of boiling effect.

(3) A more practical model, that can be applied to a practical PEMWE, is developed, and can contribute to quantify how much boiling effect impact on each voltage component in the PEMWE. This model is ultimately dedicated to optimization of cell design and operation condition for real PEMWE.

References

[1] Graves CA, Steinle L, Rehder G, Niemann H, Connelly DP, Lowry D, Fisher RE, Stott AW, Sahling H, James RH. Fluxes and fate of dissolved methane released at the seafloor at the landward limit of the gas hydrate stability zone offshore western Svalbard. Journal of Geophysical Research: Oceans. 2015 ;120(9):6185-201.

[2] Ayodele BV, Alsaffar MA, Mustapa SI, Kanthasamy R, Wongsakulphasatch S, Cheng CK. Carbon dioxide reforming of methane over Ni-based catalysts: Modeling the effect of process parameters on greenhouse gasses conversion using supervised machine learning algorithms. Chemical Engineering and Processing-Process Intensification. 2021;166:108484.

[3] Acaroğlu H, Güllü M. Climate change caused by renewable and non-renewable energy consumption and economic growth: A time series ARDL analysis for Turkey. Renewable Energy. 2022.

[4] IEA (2021), Global Energy Review 2021, IEA, Paris https://www.iea.org/reports/global-energy-review-2021. Accessed on Jule 10 (2022)

[5] Changshi L. Reliable and precise evaluation energy-transfer and efficiency of super-capacitors. Renewable and Sustainable Energy Reviews. 2021;151:111566.

[6] Lipu MH, Ansari S, Miah MS, Hasan K, Meraj ST, Faisal M, Jamal T, Ali SH, Hussain A, Muttaqi KM, Hannan MA. A review of controllers and optimizations based scheduling operation for battery energy storage system towards decarbonization in microgrid: Challenges and future directions. Journal of Cleaner Production. 2022:132188.

[7] Zayat B, Mitra D, Irshad A, Rajan AS, Narayanan SR. Inexpensive and robust iron-based electrode substrates for water electrolysis and energy storage. Current Opinion in Electrochemistry. 2021;25:100628.

[8] Buttler A, Spliethoff H. Current status of water electrolysis for energy storage, grid balancing and sector coupling via power-to-gas and power-to-liquids: A review. Renewable and Sustainable Energy Reviews. 2018;82:2440-54.

[9] Liu Z, Yang H, Kutz R, Masel RI. CO2 electrolysis to CO and O2 at high selectivity, stability and efficiency using sustainion membranes. Journal of The Electrochemical Society. 2018;165(15):J3371.

[10] Bierschenk DM, Wilson JR, Miller E, Dutton E, Barnett SA. A proposed method for high

efficiency electrical energy storage using solid oxide cells. Ecs Transactions. 2011 ;35(1):2969.

[11] Naimi Y, Antar A. Hydrogen generation by water electrolysis. Advances In Hydrogen Generation Technologies. 2018 :1.

[12] David M, Ocampo-Martínez C, Sánchez-Peña R. Advances in alkaline water electrolyzers: A review. Journal of Energy Storage. 2019;23:392-403.

[13] Q. Deng, J. Zhao, T Wu, G. Chen, H.A. Hansen, T.Vegge, 2D transition metal–TCNQ sheets as bifunctional single-atom catalysts for oxygen reduction and evolution reaction (ORR/OER), J. Catal. 370 (2019) 378–384.

[14] L. Yaqoob, T. Noor, N. Iqbal, H. Nasir, M. Sohail, N. Zaman, M. Usmand, Nanocomposites of cobalt benzene tricarboxylic acid MOF with rGO: an efficient and robust electrocatalyst for oxygen evolution reaction (OER), Renew. Energ. 156 (2020) 1040–1054.

[15] J. Ding, S. Ji, H. Wang, H. Gai, F. Liu, V. Linkov, R. Wang, Mesoporous nickel-sulfide/nickel/N-doped carbon as HER and OER bifunctional electrocatalyst for water electrolysis, Int. J. Hydrogen Energ. 44(5) (2019) 2832–2840.

[16] W.Q. Zaman, W. Sun, M. Tariq, Z. Zhou, U. Farooq, Z. Abbas, L. Cao, J. Yang, Iridium substitution in nickel cobaltite renders high mass specific OER activity and durability in acidic media Appl. Catal. B-Environ. 244 (2019) 295–302.

[17] Y. Liu, Y. Bai, W. Yang, J. Ma, K. Sun, Self-supported electrode of NiCo-LDH/NiCo2S4/CC with enhanced performance for oxygen evolution reaction and hydrogen evolution reaction, Electrochim. Acta 367 (2021) 137534.

[18] X.Q. Xie, J. Liu, C. Gu, J. Li, Y. Zhao, C.-S. Liu, Hierarchical structured CoP nanosheets/carbon nanofibers bifunctional eletrocatalyst for high-efficient overall water splitting, J. Energy Chem. 64 (2022) 503–510.

[19] Y. Tang, K. Shen, J. Zheng, B. He, J. Chen, J. Lu, W. Ge, L. Shen, P. Yang, S. Deng, d-band Center Modulating of CoOx/Co9S8 by Oxygen Vacancies for Fast-Kinetics Pathway of Water Oxidation, Chem. Eng. J. 427 (2022) 130915.

[20] X. Zhou, X. Liu, J. Zhang, C. Zhang, S. J. Yoo, J.-G. Kim, X. Chu, C. Song, P. Wang, Z. Zhao, D. Li, W. Zhang, W. Zheng, Highly-dispersed cobalt clusters decorated onto nitrogen-doped carbon nanotubes as multifunctional electrocatalysts for OER, HER and ORR, Carbon 166 (2020) 284–290.

[21] Ito H, Maeda T, Nakano A, Hasegawa Y, Yokoi N, Hwang CM, Ishida M, Kato A,

Yoshida T. Effect of flow regime of circulating water on a proton exchange membrane electrolyzer. International journal of hydrogen energy. 2010;35(18):9550-60.

[22] Li H, Nakajima H, Inada A, Ito K. Effect of flow-field pattern and flow configuration on the performance of a polymer-electrolyte-membrane water electrolyzer at high temperature. International Journal of Hydrogen Energy. 2018;43(18):8600-10.

[23] Grigoriev SA, Millet P, Volobuev SA, Fateev VN. Optimization of porous current collectors for PEM water electrolysers. International journal of hydrogen energy. 2009;34(11):4968-73.

[24] Toghyani S, Afshari E, Baniasadi E, Atyabi SA, Naterer GF. Thermal and electrochemical performance assessment of a high temperature PEM electrolyzer. Energy. 2018;152:237-46.

[25] Sartory M, Wallnöfer-Ogris E, Salman P, Fellinger T, Justl M, Trattner A, Klell M. Theoretical and experimental analysis of an asymmetric high pressure PEM water electrolyser up to 155 bar. International Journal of Hydrogen Energy. 2017;42(52):30493-508.

[26] Majasan JO, Cho JI, Dedigama I, Tsaoulidis D, Shearing P, Brett DJ. Two-phase flow behaviour and performance of polymer electrolyte membrane electrolysers: Electrochemical and optical characterisation. international journal of hydrogen energy. 2018;43(33):15659-72.

[27] Millet P, Grigoriev SA. Electrochemical characterization and optimization of a PEM water electrolysis stack for hydrogen generation. Chemical Engineering Transactions. 2014;41:7-12.

[28] Toghyani S, Fakhradini S, Afshari E, Baniasadi E, Jamalabadi MY, Shadloo MS. Optimization of operating parameters of a polymer exchange membrane electrolyzer. International Journal of Hydrogen Energy. 2019;44(13):6403-14.

[29] Grigoriev SA, Kalinnikov AA, Millet P, Porembsky VI, Fateev VN. Mathematical modeling of high-pressure PEM water electrolysis. Journal of applied electrochemistry. 2010;40(5):921-32.

[30] Li H, Inada A, Fujigaya T, Nakajima H, Sasaki K, Ito K. Effects of operating conditions on performance of high-temperature polymer electrolyte water electrolyzer. Journal of Power Sources. 2016;318:192-9.

[31] Scheepers, Fabian, Markus Stähler, Andrea Stähler, Edward Rauls, Martin Müller, Marcelo Carmo, and Werner Lehnert.. Temperature optimization for improving polymer electrolyte membrane-water electrolysis system efficiency. Applied Energy, 2020: 116270.

[32] Ito K, Terabaru K, Li H, Inada A, Nakajima H. Challenging of Reducing Electrolysis Voltage by Superimposing Boiling on PEMWE–A Thermodynamic Coupling–. ECS Transactions. 2017;80(8):1117.

[33] Saito Y, Aramaki K, Hodoshima S, Saito M, Shono A, Kuwano J, Otake K. Efficient hydrogen generation from organic chemical hydrides by using catalytic reactor on the basis of superheated liquid-film concept. Chemical engineering science. 2008;63(20):4935-41.

[34] Sharma AK, Ahmed K, Birgersson E. Nernst voltage losses in planar fuel cells caused by changes in chemical composition: Effects of operating parameters. Ionics. 2018 Jul;24(7):2047-54.

[35] Shirvanian P, van Berkel F. Novel components in Proton Exchange Membrane (PEM) Water Electrolyzers (PEMWE): Status, challenges and future needs. A mini review. Electrochemistry Communications. 2020;114:106704.

[36] Panigrahy B, Narayan K, Rao BR. Green hydrogen production by water electrolysis: A renewable energy perspective. Materials Today: Proceedings. 2022;67:1310-4.

[37] Zhang Z, Xing X. Simulation and experiment of heat and mass transfer in a proton exchange membrane electrolysis cell. International Journal of Hydrogen Energy. 2020;45(39):20184-93.

[38] Scott SB, Sørensen JE, Rao RR, Moon C, Kibsgaard J, Shao-Horn Y, Chorkendorff I. The low overpotential regime of acidic water oxidation part II: trends in metal and oxygen stability numbers. Energy & Environmental Science. 2022;15(5):1988-2001.

[39] Majasan JO, Cho JI, Maier M, Shearing PR, Brett DJ. Optimisation of Mass Transport Parameters in a Polymer Electrolyte Membrane Electrolyser Using Factorial Design-of-Experiment. Frontiers in Energy Research. 2021;9:643587.

[40] Bromberger K, Ghinaiya J, Lickert T, Fallisch A, Smolinka T. Hydraulic ex situ through-plane characterization of porous transport layers in PEM water electrolysis cells. International Journal of Hydrogen Energy. 2018;43(5):2556-69.

[41] Xu P, Li Q, Xuan Y. Enhanced boiling heat transfer on composite porous surface. International Journal of Heat and Mass Transfer. 2015;80:107-14.

[42] FILIPPOU D, CHENG TC, DEMOPOULOS GP. Gas‐Liquid Oxygen Mass-transfer; from Fundamentals to Applications in Hydrometallurgical Systems.

[43] Fortunelli A, Goddard III WA, Sementa L, Barcaro G. Optimizing the oxygen evolution reaction for electrochemical water oxidation by tuning solvent properties. Nanoscale.

2015;7(10):4514-21.

[44] Santana J, Espinoza-Andaluz M, Li T, Andersson M. A Detailed Analysis of Internal Resistance of a PEFC Comparing High and Low Humidification of the Reactant Gases. Frontiers in Energy Research. 2020:217.

[45] Sierra JM, Pathiyamattom SJ, Gamboa S. Study of activation losses and ohmic resistance in a PEM fuel cell using computational fluid dynamics. ECS Transactions. 2009;20(1):395.

[46] Yu H, Quan T, Mei S, Kochovski Z, Huang W, Meng H, Lu Y. Prompt electrodeposition of Ni nanodots on Ni foam to construct a high-performance water-splitting electrode: efficient, scalable, and recyclable. Nano-micro letters. 2019;11(1):1-3.

[47] Kim JH, Park JE, Lee ES. Zinc Recovery through Electrolytic Refinement Using Insoluble Ir+ Sn+ Ta+ PdOx/Ti Cathode to Reduce Electrical Energy Use. Materials. 2019;12(17):2779.

[48] Ikeda H, Misumi R, Kojima Y, Haleem AA, Kuroda Y, Mitsushima S. Microscopic high-speed video observation of oxygen bubble generation behavior and effects of anode electrode shape on OER performance in alkaline water electrolysis. International Journal of Hydrogen Energy. 2022;47(21):11116-27.

[49] Li Y, Yang G, Yu S, Mo J, Li K, Xie Z, Ding L, Wang W, Zhang FY. High-speed characterization of two-phase flow and bubble dynamics in titanium felt porous media for hydrogen production. Electrochimica Acta. 2021;370:137751.

[50] Ito K, Terabaru K, Li H, Inada A, Nakajima H. Challenging of Reducing Electrolysis Voltage by Superimposing Boiling on PEMWE–A Thermodynamic Coupling–. ECS Transactions. 2017;80(8):1117.

[51] Liu Y, Wang B, Srinivas K, Wang M, Chen Z, Su Z, Liu D, Li Y, Wang S, Chen Y. CNT-interconnected iron-doped NiP2/Ni2P heterostructural nanoflowers as high-efficiency electrocatalyst for oxygen evolution reaction. International Journal of Hydrogen Energy. 2022;47(26):12903-13.

Chapter 2

Experimental analysis of boiling effect on OER

This chapter proposes a novel method in which boiling is superimposed on the oxygen evolution reaction (OER) to decrease electrolysis voltage. The vapor bubbles formed by boiling are expected to decrease the Nernst loss. The boiling effect was experimentally analyzed using a three-electrode cell. Although a general catalyst layer (CL) was formed on a working electrode (WE) bar, the structure of the working electrode (WE) bar was special, in which a 10-W heater was embedded and made boiling on the electrode under 1 bar condition. Increasing the electrode temperature under static OER current density slightly decreased the OER potential. However, an abrupt decrease in potential was observed when the temperature was scaled over the boiling temperature. Moreover, this abrupt decrease substantially intensified when, similar to a practical polymer electrolyte membrane water electrolyzer (PEMWE), a porous transfer layer (PTL) and flow channel were assembled on the CL.

2.1 Introduction

Reducing the OER overvoltage of the PEMWE anode increases the voltage efficiency of water electrolysis [1-3], and many efforts have been done according to this scenario. The CL filled with the nanowire structure in the through-plane direction increases the mass transfer and reduces the OER overvoltage compared with that filled with a granular structure [4]. An increasing number of researchers have improved the OER performance by developing nanowire catalysts that possess more active sites and lower mass transport resistance [5,6]. In addition, a loose and thin porous transfer layer (PTL) is preferable for smooth gas transfer [7,8].

A high concentration of oxygen near the catalyst increases the equilibrium potential of OER [9]. The dissolved oxygen in water oversaturates tenfold compared with the saturated value of oxygen gas [10]. A higher current density during the OER generates a higher concentration of dissolved oxygen [11]. Dissolved oversaturated oxygen precipitates considerable nano-oxygen bubbles [12]. Oxygen bubbles grow after merging with nanobubbles and detach from the CL [13]. From the CL to the flow channels, oxygen is

quickly transferred via oxygen bubbles rather than by diffusion in water [14]. Unfortunately, the titanium mesh as for a PTL in the anode of PEMWEs restricts the drainage of oxygen gas bubbles and increases their concentration in the CL, thereby worsening the OER performance [15].

This chapter challenges to clarity the boiling effect, where boiling superimposed on CL is expected to reduce the oxygen concentration near the CL and OER overvoltage. A three-electrode cell (TEC) is introduced to measure the galvanostatic potential and linear sweep voltammetry (LSV) of OER over a wide range of temperatures. Conclusion presents the effects of boiling on OER Nernst loss. For convenience, the nomenclature used in this chapter are summarized in Table 2.1.

Table 2.1 Nomenclature.

Nomenclature	
i	Current density, [A·cm^{-2}]
z	Electron transfer number, 4 [-]
a_t	Electron transfer coefficient, [-]
R	Universal gas constant, 8.314 [J·mol^{-1}·K^{-1}]
F	Faraday constant, 96 485 [C·mol^{-1}]
T	Temperature, [°C]
η	Overvoltage, [V]
E	Potential, [V]
C	Concentration, [mol·m^{-3}]
a	Activity, [-]
E_a	Activation energy, 76 000 [J·mol^{-1}]
j	Dimensionless current density, [-]
Superscripts and subscripts	
OER	Oxygen evolution reaction
SSCE	Silver-silver chloride electrode
B	Bulk
CL	Catalyst layer
0	Standard condition (25°C, 1 bar)

c	Corrected
eq	Equilibrium
act	Activation
e	Exchange
O_2	Oxygen
H_2O	Water
H^+	Hydrogen ion
k	Species type

2.2 Experiment and theoretical predictions

In this section, extensive details regarding tailor-made working electrodes (WEs) are presented. Temperature-controllable TEC and temperature control strategies are introduced below. The OER potential–current density characteristics at each temperature were measured using LSV and converted to Tafel plots with logarithmic transformation of the current density. Moreover, to understand the effect of boiling on the Tafel plot, a mathematical model qualitatively analyzes the boiling impact on OER overvoltage. This theoretical analysis contributes to proposing a mechanism on how boiling affects the overpotential of the OER.

2.2.1 Working electrodes

Fig. 2.1 illustrates WE1, WE2, and WE3. Table 2.2 lists the components embedded in each WE. The CL on all the WEs was fabricated using the sprayed and hot-pressed methods. Because the WEs function as OER electrodes, the CL loads IrO_2 particles of 1.5 $mg \cdot cm^{-2}$. The CL also contains an Aquivion ionomer as a binder and a proton conductor because the Aquivion ionomer withstands a higher temperature than Nafion ionomer.

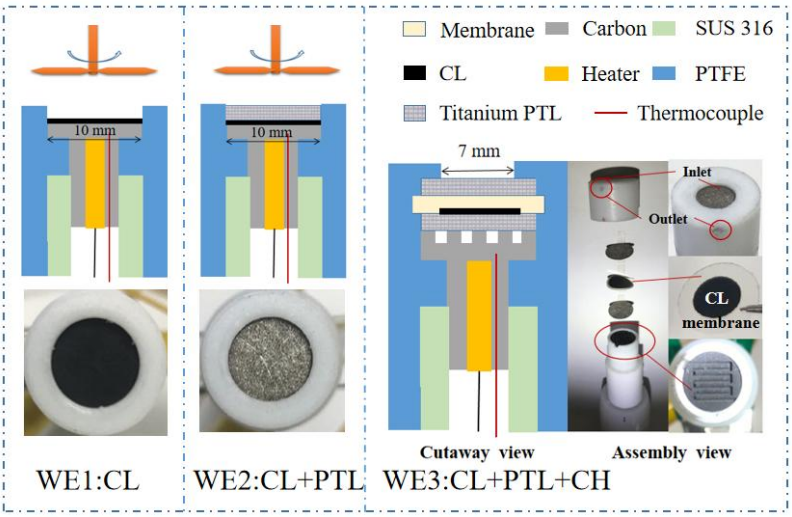

Fig. 2.1 Interior structures of three type WEs (WE: working electrode; CL: catalyst layer; PTL: Porous transfer layer; CH: channel)

Table 2.2 Details of each component in the WEs

Components	Specification
CL (Catalyst Layer)	Thickness: 10 μm Diameter: 10 mm for WE1 and WE2, 8 mm for WE3 Catalyst and its loading: IrO_2 (type IV, Tokuriki) and 1.5 mg·cm^{-2} Ionomer: Aquivion ionomer Material composition ratio: IrO_2 = 67 wt%, Ionomer = 33 wt%
PTL for the WE2 and WE3	Thickness: 200 μm Material: Titanium Coating platinum layer: 1-μm thickness (Surface of Ti fiber) Porosity: 72% Fiber diameter: 20 μm
Aquivion membrane for the WE3	Thickness: 183 μm Material: Aquivion 117
CH for the WE3	Pattern: Serpentine Channel depth: 0.3 mm

Channel width: 0.5 mm
Channel outlet: 0.785 mm^2

Each WE had a specific structure: WE1 only embedded a CL, WE2 was tightly covered with a PTL, and WE3 had a structure similar to that of a PEMWE anode. The cutaway and assembly view in Fig. 2.1 demonstrates that WE3 comprises an Aquivion membrane with a CL, PTLs, and serpentine channel. The upper surface of the membrane contained no CL and was immersed in the electrolyte because hydrogen ions produced by the OER drained into the electrolyte solution. The hydrogen ions produced in the CL can diffuse through the membrane and the upper Ti mesh and finally reach the bulk electrolyte solution. The oxygen gas produced flowed through the lower Ti mesh and channel. The water consumed in the OER can penetrate the upper Ti mesh and the membrane to reach the CL.

The heater and thermocouple embedded in the carbon module (gray-colored) in Fig. 2.1 control the WEs temperature to achieve boiling temperature in the CL. The temperature measured by thermocouples embedded in the WEs is slightly higher than that of the CL surface, with a temperature difference of less than 2 °C for the temperature range from 25 to 115 °C. This temperature difference was obtained in a preliminary experiment (replacing the electrolyte solution with pure water in TEC) by comparing the measurement temperature of the thermocouple (RKC ST-50) attached to the CL surface and the thermocouple embedded in WE. In WE1, both oxygen and vapor bubbles were released from the CL surface into the electrolyte solution. In the case of WE2, both the oxygen and vapor bubbles produced in the CL penetrated the PTL and were released from its surface. In the case of WE3, oxygen gas and vapor penetrated through the lower PTL, flowed along the serpentine channel, and finally drained into the electrolyte solution at the outlet (see Fig. 2.1). Thus, the WE3 has a similar structure to practical PEMWE cell.

Different specifications of the WEs cause different mass transport resistances during the OER. WE1 did not possess a PTL that disturbed the drainage of the oxygen bubbles. WE1 was located just under a stirrer, which rotated at 2,000 rpm to remove the oxygen bubbles that appeared on the CL surface. The stirrer faced the CL through the electrolyte solution and ensured the transfer of oxygen to the solution. Thus, in the case of WE1, the OER did not form a Nernst loss. In the case of WE1, if the overvoltage decreases substantially above the boiling temperature, we can conclude that the activation performance of the OER can be

enhanced by boiling. Conversely, if the overvoltage does not decrease substantially above the boiling temperature, we can conclude that the OER activation performance cannot be enhanced by boiling. Because WE2 possesses a PTL on the CL, the oxygen bubbles evolved from the CL must flow through the PTL to drain into the electrolyte solution. The capillary force in the PTL prevents oxygen bubbles from flowing and tends to accumulate in the PTL. Thus, WE2 had a higher oxygen transfer resistance than WE1. If the overvoltage decreases above the boiling temperature in WE2 but not in WE1, we can conclude that boiling can enhance the oxygen transfer and decrease the Nernst loss. Among the three WEs, WE3 had the largest oxygen transfer resistance because the oxygen bubbles produced in the CL must flow through the PTL and channel to drain into the electrolyte solution. If the experiments with WE1 and WE2 clarify in advance that boiling can accelerate oxygen transfer and reduce the Nernst loss, then this overvoltage reduction caused by boiling will be highlighted in WE3.

2.2.2 Experiment system and conditions

Fig. 2.2 illustrates the TEC, including the custom-made WE described in Fig. 2.1, temperature control strategy, and potential correction. The pressure in the TEC was 1 bar. The WE, counter electrode (CE), and reference electrode (RE) were immersed in an electrolyte solution. As for the electrolyte, this study used 0.1-M HClO4 solution to imitate the acid-type electrolyte in the PEMWE [16]. The WE functioned as the OER electrode, and the CE made with a platinum wire functioned as the HER electrode. During operation, oxygen and hydrogen bubbles formed on the WE and CE, respectively. Boiling bubbles also formed when the WE temperature exceeded the boiling temperature. For the RE, Ag/AgCl (sat.), called the standard silver chloride electrode (SSCE), was used to provide the WE potential [17]. An IR correction was applied to the OER potential. Hereafter, the IR-corrected OER potential will be referred to as the OER potential.

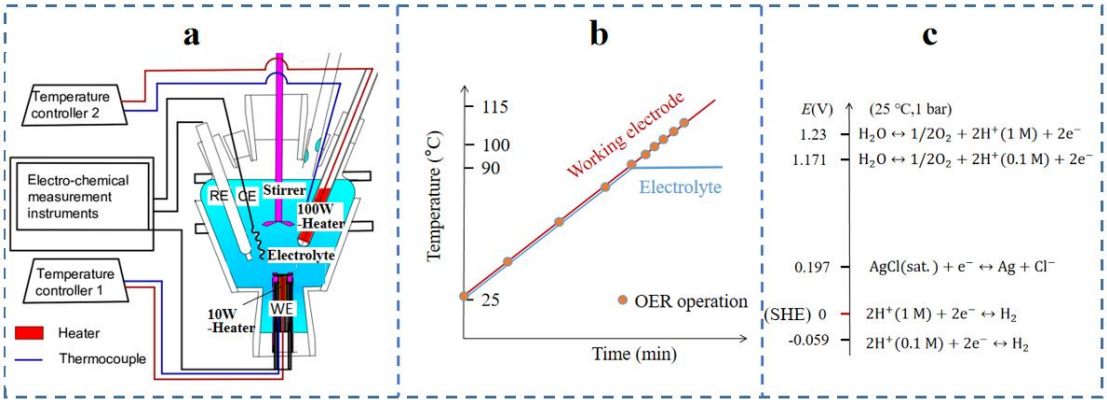

Fig. 2.2 TEC with boiling function. a. its structure, b. temperature control strategy, and c. potential correction (TEC: Three-electrode cell; WE: working electrode; CE: counter electrode; RE: reference electrode)

As shown in Fig. 2.2a, two heaters were embedded in TEC. The 10 W-heater in the WE controlled the WE temperature, whereas that in the electrolyte bath adjusted the electrolyte temperature. The temperature control strategy is illustrated in Fig. 2.2b. First, to examine the effect of boiling on OER, the WE temperature was swept from 25 to 115°C. The Aquivion ionomer can withstand higher temperatures than the Nafion ionomer because the Aquivion membrane and ionomer have high-temperature tolerances [18]. Thus, the CL containing the Aquivion ionomer did not undergo high-temperature degradation at 115°C during the short-testing duration in this study. Subsequently, the temperature of the electrolyte solution was controlled such that it synchronized with the WE temperature. However, the maximum temperature of the solution was 90°C, which is limited by its boiling point, as shown in Fig. 2.2b.

Fig. 2.2c shows the OER potential measured in this TEC system under standard conditions (25 °C, 1 bar). As mentioned above, the RE used in this study was SSCE and not the standard hydrogen electrode (SHE). The electrolyte was a 0.1-M $HClO_4$ solution. As shown in Fig. 2.2c, compared with the SHE, the acid electrolyte shifted OER standard electrode potential from $E_0^{\mathrm{OER}} = 1.23\ \mathrm{V}$ to $E_{0,\mathrm{Shifted}}^{\mathrm{OER}} = 1.171\ \mathrm{V}$. In contrast to SHE, SSCE was $E_0^{\mathrm{SSCE}} = 0.197\ \mathrm{V}$. Thus, the measured OER standard electrode potentials per Eq. (2.1) is,

$$E_{0,\mathrm{Measured}}^{\mathrm{OER}} = E_{0,\mathrm{Shifted}}^{\mathrm{OER}} - E_0^{\mathrm{SSCE}} = 1.171 - 0.197 = 0.974\ [\mathrm{V}]\ \mathrm{vs.\ SSCE} \quad (2.1)$$

Temperature correction for the SSCE and OER is indispensable for providing precise RE and WE potentials at a given temperature, resulting in precise measurement of the OER

over-voltage. The temperature dependence of the equilibrium potential of SSCE is expressed by Eq. (2.2) [19],

$$E_{\mathrm{eq}}^{\mathrm{SSCE}}(T) = E_{0}^{\mathrm{SSCE}} - \frac{1.01(T-25)}{1000} = 0.197 - \frac{1.01(T-25)}{1000}\ [\mathrm{V}]\ \mathrm{vs.\ SHE} \quad (2.2)$$

The temperature dependence of the equilibrium electrode potential of the OER in the 0.1-M acid electrolyte is given by Eq. (2.3).

$$\mathrm{E}_{\mathrm{eq,Shifted}}^{\mathrm{OER}}(\mathrm{T}) = \mathrm{E}_{\mathrm{0,Shifted}}^{\mathrm{OER}} - \frac{0.85(\mathrm{T}-25)}{1000} = 1.171 - \frac{0.85(\mathrm{T}-25)}{1000}\ [\mathrm{V}]\ \mathrm{vs.\ SHE} \quad (2.3)$$

Before using the custom-made WE for boiling coupled OER experiments, we need to verify the integrity of the basic electrochemical performance. Cyclic voltammetry (CV) can measure the electrochemically active surface area (ECSA) of CL. Eq. (2.4) gives the method to get ECSA [20].

$$\mathrm{ECSA} = \frac{C_{\mathrm{dl}}^{\mathrm{E}}}{C_{\mathrm{dl}}} \quad (2.4)$$

IrO_2 usually has a specific capacitance density, C_{dl}, of 0.059 mF·cm^{-2} [20]. $C_{\mathrm{dl}}^{\mathrm{E}}$ is the capacitance value of the catalyst sample, which can be determined from the slope of the double layer charging current versus the potential scanning rate. CV measurement in the non-Faraday potential range can determine the capacitance of the catalyst. At 25 °C, the number of the CV was set at 20 cycles to obtain an accurate charge-discharge current. The operating conditions of the CV are listed in Table 2.3. Finally, the 20th cycle CV is selected as the experimental data. Measurement result for ECSA will be shown at the chapter 2.3.1.

Linear sweep voltammetry can obtain the OER exchange current density of this CL. At 25 °C, the OER potential of the CL was scanned at 5 mV·s^{-1} from 0.9 V to 1.8 V to get a voltammetric curve. Then, the voltammetry curves were transformed into Tafel plots to determine the OER exchange current density for CL. Finally, the exchange current density of this CL was obtained for subsequently calculating the oxygen activity in the CL.

Two electrochemical methods were introduced to examine the effect of boiling on reducing OER overvoltage. The first was to measure the OER potential for a static electrolysis current density by sweeping the WE temperature from 85 to 115 °C. The potential was measured for 300 s at a specific temperature to obtain a stable value. The average value of all the potential samples picked up at this temperature was selected as the experimental result. The second was a linear sweep voltammetry (LSV) performed at each corresponding temperature. To eliminate the charging current and obtain the OER current precisely, the sweeping speed of the LSV was slow at 5 mV·s^{-1}. Finally, to quantitatively clarify which

component of the OER overvoltage was reduced by boiling, the LSV data were converted into a Tafel plot of the OER. The detailed experimental conditions for the two electrochemical methods are summarized in Table 2.3.

Table 2.3 Experiment conditions for each measurement

Measurement Method	Specification	
IR correction	Potential	1.4 V vs. SSCE
	Disturbance frequency	1000 Hz
	Testing time for a value	100 s
	AC amplitude	10 mV
Galvanostatic conditions	Testing time for a value	300 s
	OER current	2, 5, 10, 15, 25 mA
LSV condition	Potential range	0.9–1.8 V vs. SSCE
	Sweeping speed	5 $mV \cdot s^{-1}$
CV condition	Potential range	0.7–0.8 V vs. SSCE
	Sweeping speed	1-50 $mV \cdot s^{-1}$

2.2.3 Theoretical predictions

It is worth theoretically predicting how superimposing boiling changes the Tafel plot. This theoretical prediction will help us understand the experimental results in advance. Although the theoretical prediction is qualitatively discussed here, it contributes toward considering the mechanisms of how boiling concretely reduces overvoltage.

Even when the OER superimposes boiling, the activity of each species is considerable in expressing overvoltage. The reaction equation for the OER is given by Eq. (2.5).

$$H_2O \leftrightarrow 2e^- + 2H^+ + \frac{1}{2}O_2 \quad (2.5)$$

The activity of each species given by Eq. (2.5) should consider the concentration at CL, as follows:

$$a_{\mathrm{k}}^{\mathrm{CL}} = \frac{C_{\mathrm{k}}^{\mathrm{CL}}}{C_{\mathrm{k}}^{0}} \quad (2.6)$$

The specific expression for the activity of each species was as follows: both the electron and water activities at the CL ($a_{\mathrm{e}^-}^{\mathrm{CL}}$, $a_{\mathrm{H_2O}}^{\mathrm{CL}}$) were 1. The proton activity at the CL ($a_{\mathrm{H}^+}^{\mathrm{CL}}$) was considered to be 0.1, because this study used 0.1 M $HClO_4$ aq [21]. Generally, oxygen gas in bubbles has the same activity as dissolved oxygen: $a_{\mathrm{O_2}}^{\mathrm{CL}} = \frac{P_{\mathrm{O_2}}^{\mathrm{CL}}}{P_{\mathrm{O_2}}^{0}} = \frac{C_{\mathrm{O_2}}^{\mathrm{CL}}}{C_{\mathrm{O_2}}^{0}}$. However, when boiling is superimposed, it may change the local equilibrium state of the concentration and activity of oxygen in the CL. This is because dissolved oxygen may diffuse into vapor bubbles caused by boiling, resulting in a lower concentration of dissolved oxygen. Another possible reason is that the vapor produced by boiling mixes in the oxygen gas bubbles lowers the partial pressure of oxygen gas. Both these factors reduce the oxygen gas activity and OER potential. This interesting phenomenon is the key to the boiling effect and is addressed in the following theoretical discussion.

The OER potential (E^{OER}) with and without boiling should have the same expression, as shown in Eq. (2.7) [22]:

$$E^{\mathrm{OER}} = E_{\mathrm{Nernst}}^{\mathrm{OER}} + \eta_{\mathrm{act}}^{\mathrm{OER}} \quad (2.7)$$

It should be noted that the OER potential in Eq. (2.7) excludes the ohmic overvoltage because the OER potential is treated after the IR correction.

As mentioned in section 2.2.1, boiling is expected to reduce the concentration and/or activation overvoltage of OER. This study attributed the Nernst loss to the Nernst potential ($E_{\mathrm{Nernst}}^{\mathrm{OER}}$). The activation overvoltage ($\eta_{\mathrm{act}}^{\mathrm{OER}}$) was assumed to follow the general Tafel equation [19], as shown in Eq. (2.8), where the exchange current density depends on the temperature.

$$\eta_{\mathrm{act}}^{\mathrm{OER}} = \frac{RT}{a_{\mathrm{t}} z F} \ln\left[\frac{i}{i_{\mathrm{e}}(T)}\right] \quad (2.8)$$

Where, the a_{t} is electron transfer coefficient, and the z is electron transfer number of OER.

Substituting these components into Eq. (2.7) yields a concrete expression for the OER potential, as expressed in Eq. (2.9). The first and second terms on the RHS of the first line constitute the Nernst potentials. The third term on the first line of Eq. (2.9) represents the activation overvoltage: The second term is responsible for the activity of each species in the CL and reflects the Nernst loss. The second term for this study was obtained by substituting the known activities of water ($a_{\mathrm{H_2O}}^{\mathrm{CL}} = 1$), electrons ($a_{\mathrm{e}^-}^{\mathrm{CL}} = 1$), and protons ($a_{\mathrm{H}^+}^{\mathrm{CL}} = 0.1$) into Eq. (2.9). It should be noted that the equilibrium potential $E_{\mathrm{eq}}^{\mathrm{OER}}(T)$ is shifted to $E_{\mathrm{eq,Shifted}}^{\mathrm{OER}}(T)$

owing to the proton activity of 0.1. The last line in Eq. (2.9) yields a concrete expression for the OER potential:

$$E^{\mathrm{OER}} = E_{\mathrm{eq}}^{\mathrm{OER}}(T) + \frac{RT}{zF}\ln\left[\frac{\left(a_{\mathrm{H^+}}^{\mathrm{CL}}\right)^2\left(a_{\mathrm{e^-}}^{\mathrm{CL}}\right)^2\left(a_{\mathrm{O_2}}^{\mathrm{CL}}\right)^{1/2}}{a_{\mathrm{H_2O}}^{\mathrm{CL}}}\right] + \frac{RT}{a_t zF}\ln\left[\frac{i}{i_{\mathrm{e}}(T)}\right]$$

$$= E_{\mathrm{eq}}^{\mathrm{OER}}(T) + \frac{RT}{zF}\ln[(0.1)^2] + \frac{RT}{zF}\ln\left[\left(a_{\mathrm{O_2}}^{\mathrm{CL}}\right)^{1/2}\right] + \frac{RT}{a_t zF}\ln\left[\frac{i}{i_{\mathrm{e}}(T)}\right]$$

$$= E_{\mathrm{eq,Shifted}}^{\mathrm{OER}}(T) + \frac{RT}{zF}\ln\left[\left(\frac{C_{\mathrm{O_2}}^{\mathrm{CL}}}{C_{\mathrm{O_2}}^{0}}\right)^{1/2}\right] + \frac{RT}{a_t zF}\ln\left[\frac{i}{i_{\mathrm{e}}(T)}\right] \quad (2.9)$$

The overvoltage η^{OER} can be defined by subtracting $E_{\mathrm{eq,Shifted}}^{\mathrm{OER}}(T)$ from the OER potential in Eq. (2.9).

$$\eta^{\mathrm{OER}} = \mathrm{E}^{\mathrm{OER}} - \mathrm{E}_{\mathrm{eq,Shifted}}^{\mathrm{OER}}(\mathrm{T}) = \frac{2.3RT}{zF}\log\left[\left(\frac{C_{\mathrm{O_2}}^{\mathrm{CL}}}{C_{\mathrm{O_2}}^{0}}\right)^{1/2}\right] + \frac{2.3RT}{a_t zF}\log(i) - \frac{2.3RT}{a_t zF}\log[i_{\mathrm{e}}(T)]$$

(2.10)

The first term on the right-hand side can be treated as the Nernst loss. Eq. (2.10) suggests that the OER overvoltage can be reduced by decreasing oxygen concentration.

Some assessments of the boiling effect on the overvoltage are discussed below according to Eq. (2.10). Here, the boiling effect was examined in the case of WE1, which is located immediately below the stirrer in Fig. 2.1. The stirrer continuously supplied the electrolyte solution and disturbed any dissolved or gas-phase oxygen accumulation near the CL, resulting in $P_{\mathrm{O_2}}^{\mathrm{CL}} = P_{\mathrm{O_2}}^{0}$, $C_{\mathrm{O_2}}^{\mathrm{CL}} = C_{\mathrm{O_2}}^{0}$, and $a_{\mathrm{O_2}}^{\mathrm{CL}} = \frac{P_{\mathrm{O_2}}^{\mathrm{CL}}}{P_{\mathrm{O_2}}^{0}} = \frac{C_{\mathrm{O_2}}^{\mathrm{CL}}}{C_{\mathrm{O_2}}^{0}}$=1. Therefore, boiling has no chance to further decrease the oxygen activity and OER overvoltage η^{OER}. This scenario is schematically illustrated in Fig. 2.3a, where increasing the temperature improves the exchange current density according to $i_{\mathrm{e}}(T)$ in Eq. (2.10) and thus monotonically lowers the η^{OER} on the Tafel plot. Therefore, even when the temperature rises over the boiling temperature of 100 °C, increasing temperature monotonously lowers the η^{OER}.

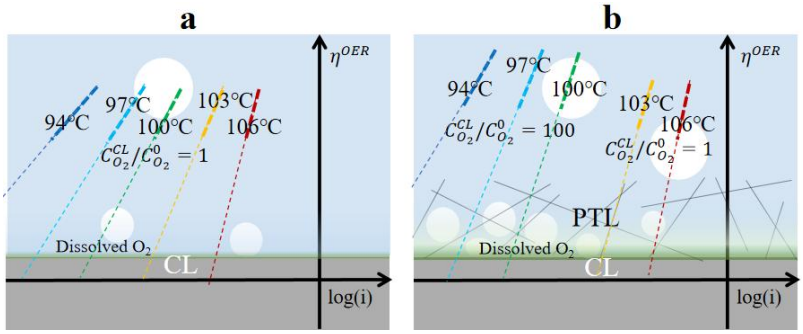

Fig. 2.3 Predicting Tafel plots of OER. Where the case “a” and “b” indicate WE1 and WE2, respectively. The plot and values are schematic and virtual for explaining.

Similar to WE1, the boiling effect was examined for WE2. The PTL embedded on the CL causes mass transport resistance and accumulates oxygen bubbles, increasing the oxygen activity on the CL to a high level, such as $a_{O_2}^{CL} = \frac{P_{O_2}^{CL}}{P_{O_2}^{0}} = \frac{C_{O_2}^{CL}}{C_{O_2}^{0}} = 100$. According to the first term in Eq. (2.10), the higher oxygen activity causes a higher η^{OER} activity than that in the case of WE1. In this circumstance, when the temperature exceeds the boiling point, vapor bubbles caused by boiling may abruptly decrease the oxygen activity $a_{O_2}^{CL}$ from 100 to 1 because the vapor bubble dilutes the oxygen concentration on the CL considerably. This abrupt decrease in oxygen activity owing to boiling can lower the Nernst loss of the OER. Fig. 2.3b describes this scenario, where the Tafel plot jumps when the temperature crosses the boiling point. Because of the larger oxygen transfer resistance in the case of WE3, which possesses a structure similar to that of the anode of a practical PEMWE, the Tafel plot jump is expected to enlarge.

Eq. (2.10) can be used to derive the corrected exchange current density, which provides direct evidence of the boiling effect. The corrected exchange current density i_e^c is the current density i when the OER overvoltage η^{OER} is 0 V. A simple mathematical manipulation can be employed to yield the corrected exchange current density i_e^c.

$$i_e^c = i_e(T)\left(\frac{C_{O_2}^{0}}{C_{O_2}^{CL}}\right)^{a_t/2} \quad (2.11)$$

The corrected exchange current density depends on the temperature and oxygen concentration near the CL. In Fig. 2.3, the corrected exchange current densities at each temperature are marked at the intersection of the log(i) axis and extension lines of the Tafel plots. The term i_e (T) in Eq. (2.11) is simply the exchange current density, which generally possesses an Arrhenius type of temperature dependence with some specific activation energy E_a as follows:

$$i_e(T) = i_e^0 \exp\left[-\frac{E_a}{R}\left(\frac{1}{T} - \frac{1}{T_{ref}}\right)\right] \quad (2.12)$$

Assuming IrO_2 as the OER catalyst, the activation energy E_a was 76 000 J·mol^{-1} [23], and the exchange current density i_e^0 was experimentally measured by LSV [24]. Substituting Eq. (2.12) into Eq. (2.11) yields the complete form of the corrected exchange current density:

$$i_e^c = i_e^0 \exp\left[-\frac{E_a}{R}\left(\frac{1}{T}-\frac{1}{T_{ref}}\right)\right]\left(\frac{C_{O_2}^0}{C_{O_2}^{CL}}\right)^{a_t/2} \quad (2.13)$$

For the convenience of discussion in the following section, a dimensionless exchange current density is defined as $j_e^c = \frac{i_e^c}{i_e^0}$.

The corrected exchange current density in Eq. (2.13) is worth further discussion. When the oxygen concentration near the CL, $C_{O_2}^{CL}$, decreased rapidly during boiling, the corrected exchange current density i_e^c showed a substantial increase. This interesting feature was examined in the Results and Discussion sections. Conversely, once the corrected exchange current density i_e^c is obtained from the Tafel plot in the electrochemical measurements, the oxygen activity near the CL, $a_{O_2}^{CL}$, can be estimated as

$$a_{O_2}^{CL} = \frac{C_{O_2}^{CL}}{C_{O_2}^0} = \left\{\frac{i_e^0}{i_e^c}\exp\left[-\frac{E_a}{R}\left(\frac{1}{T}-\frac{1}{T_{ref}}\right)\right]\right\}^{2/a_t} \quad (2.14)$$

2.3 Results and discussion

As indicated by the results, the potentials and overvoltages of the OER measured over a wide temperature range confirmed the boiling effect predicted in section 2.2.3. In particular, the oxygen activity on the CL, which was derived using the Tafel plot, successfully indicates the boiling effect mechanism for reducing the OER potential.

2.3.1 Integrity verification of the three electrodes cell at 25°C

Verifying the integrity of the experimental apparatus and the working electrode material is crucial for OER research. The ECSA of CL formed by spraying catalyst ink and hot pressing was measured by CV. The CL loaded IrO_2 catalyst of 1.5 mg·cm^{-2} has a circular area of 0.785cm^2. Fig. 2.4 shows the current variation with the potential scanning rate in the non-Faraday potential region of the OER. Fig. 2.4a shows the raw CV data. The higher the scanning rate of the potential, the greater the charge and discharge current. This result well fits with the characteristics of the capacitors.

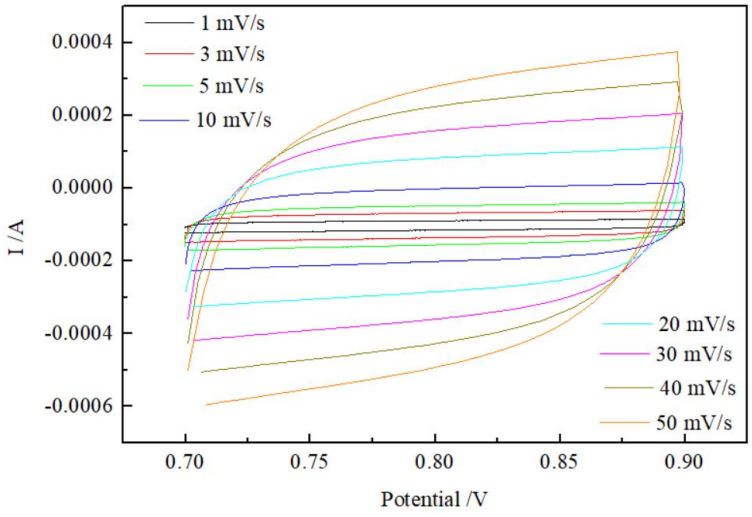

a. Non-faraday current with potential (potential vs. SSCE)

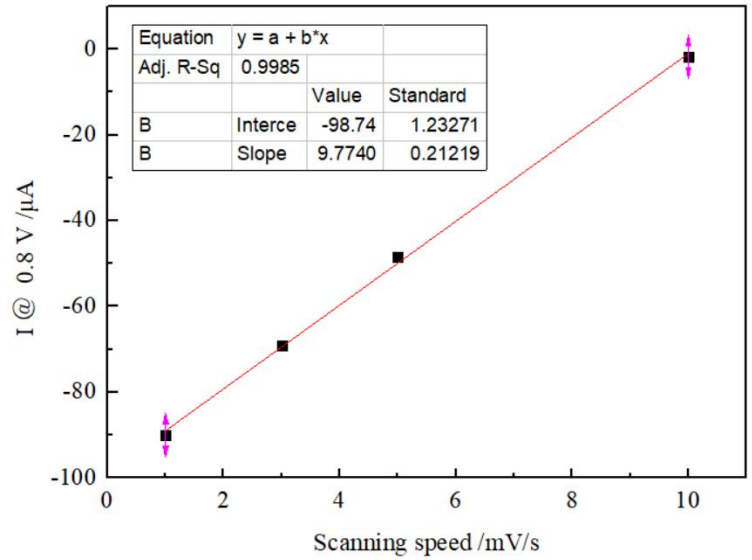

b. Non-faraday current with scanning speed of potential

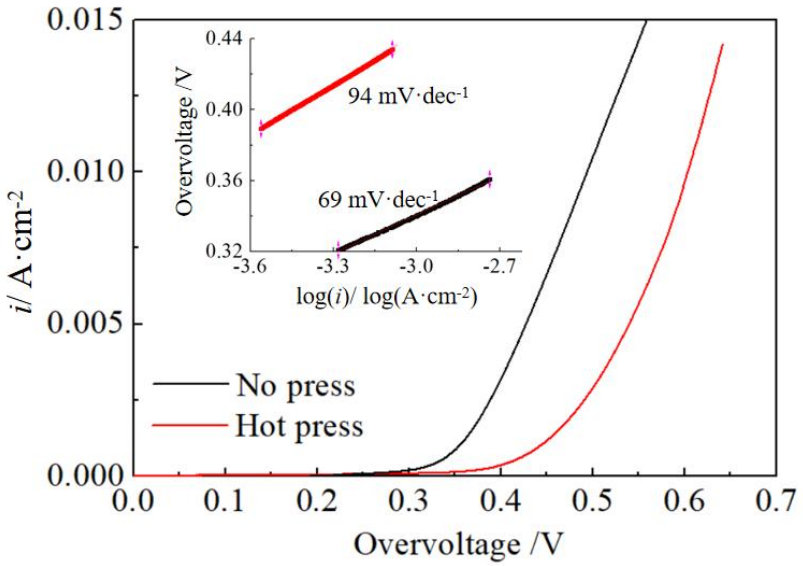

c. OER voltammetry curve

Fig. 2.4 Electrochemical performance of the custom-made CL at 25°C and 1 bar.

The current at 0.8V in Fig. 2.4a is approximately equal to the average current in 0.7-0.9V and is selected as the charging current in Fig. 2.4b. The potential scanning rate and charging current are approximately linear. The slope of the straight line is the capacitance of the CL sample, which is 9.77mF. The catalyst, IrO_2, has a load of 1.5 $mg \cdot cm^{-2}$ in the CL and a specific capacitance density of 0.059 $mF \cdot cm^{-2}$. Therefore, the ECSA of a CL with a diameter of 10mm is $(9.77mF)/(0.059mF \cdot cm^{-2})=165.7\ cm^2$ according to Eq. (2.4). The ratio of ECSA and geometric area of CL is $(165.7cm^2)/(0.785cm^2)=211$, which is well close to the reference value, 200, in Ref. [24].

Exchange current density for the CL formed by spraying an ink composed of the IrO_2-Aquivion ionomer on a carbon tablet with or without hot pressing was evaluated through LSVs, as shown in Fig. 2.4c. When the potential was above 0.3 V, the CL without hot pressing demonstrated a higher current density than that with it. The CL without hot pressing presented a Tafel slope of 69 $mV \cdot dec^{-1}$, which was close to that of IrO_2-NNL (57 $mV \cdot dec^{-1}$ [25]), IrO_2/Au (57.8 $mV \cdot dec^{-1}$ [26]), and IrO_2/Ti (61 $mV \cdot dec^{-1}$ [27]) reported by other researchers. The agreement between the Tafel slopes of the custom-made IrO_2/Aquivion and the reference IrO_2 catalysts confirms that the experimental apparatus and catalyst of the IrO_2-Aquivion ionomer are acceptable. Conversely, the hot-pressed CL exhibited a Tafel slope of 94 $mV \cdot dec^{-1}$ because hot pressing resulted in fewer reactive sites and greater mass transfer resistance in the CL. This is different from the OER of a rotating WE, in which the attached catalysts hardly suffer from a Nernst loss. It should be noted that WE1, WE2, and WE3 used hot-pressed CL because it possessed a higher mechanical strength. The Tafel plot for the hot-press CL in Fig. 2.4 demonstrates that the geometric current density, i_e, and the electron transfer coefficient, a_t, are 5.56×10^{-7} $A \cdot cm^{-2}$ and 0.15, respectively. These electrochemical properties were subsequently employed to calculate the oxygen activity in the CL. Note that, although the CL itself did not show outstanding electrochemical performance, we can still evaluate the boiling effect regardless of the performance of CL.

2.3.2 Boiling effect on the activation overvoltage

Fig. 2.5 demonstrates the influence of temperature on the OER potentials (IR correction vs. SSCE) for WE1. The WE1 does not embed PTL and flow channel, and any mass transfer resistance attributed to WE1 is negligible. The three colored lines represent the OER potentials for 6.4, 12.7, and 31.8 $mA \cdot cm^{-2}$. If the boiling effect exists, the OER potential abruptly decreases through an abrupt reduction of activation overvoltage when the temperature exceeds the boiling point. Although the boiling effect is thus expected, the OER potentials for any current density case only monotonically decrease with increasing temperature, with slight scattering, as shown in Fig. 2.5. No abrupt potential drop was observed when the temperature exceeded 100 °C. Thus, it was concluded that the boiling effect does not influence the activation overvoltage.

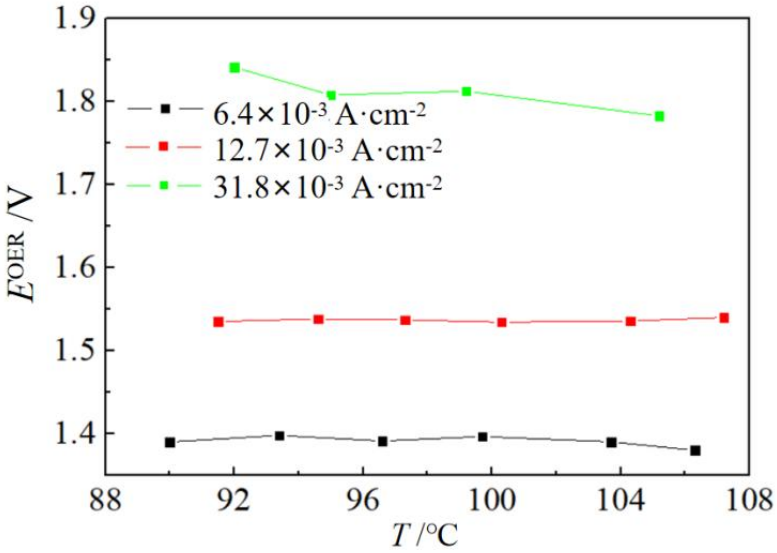

Fig. 2.5 Temperature influence on OER potentials (IR correction, vs. SSCE) for WE1.

Fig. 2.6 also shows an evidence that boiling does not reduce the OER potential through the activation overvoltage. Figs. 2.6a and 2.6b illustrate the OER overvoltage–current density (η^{OER}–i) and Tafel plot, respectively, in the case of WE1, where no PTL and flow channel were embedded and where activation overvoltage was the only possible component of overvoltage after IR correction. The plots in Fig. 2.6a are scattered and it is difficult to obtain certain characteristics. However, the Tafel plot in Fig. 2.6b shows a rather monotonous temperature dependence, where increasing the temperature monotonously shifts the Tafel plot. This result agrees with that depicted in Fig. 2.3a, which is a schematic illustration showing the

lack of boiling effect of WE1. Thus, it is concluded that boiling does not decrease the activation overvoltage, that is, boiling does not influence the OER potential when the OER progresses without Nernst loss.

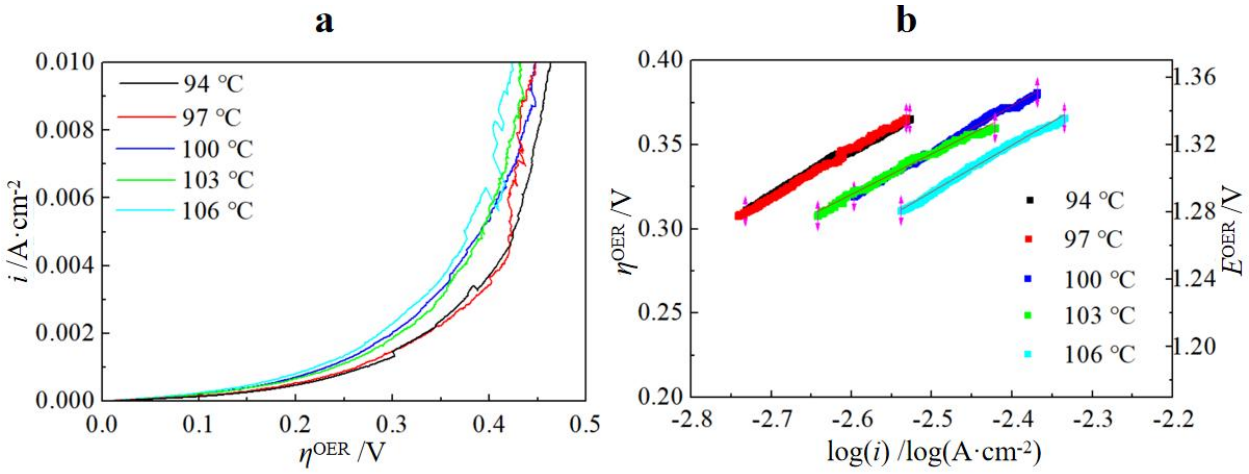

Fig. 2.6 Temperature influence on WE1 potential. a. the η^{OER}–i characteristics and b. Tafel plots with IR correction for WE1

2.3.3 Boiling effect on Nernst loss

Unlike that in WE1, we expected to observe a boiling effect in WE2, which embeds the PTL and causes oxygen transfer resistance to form Nernst loss in addition to activation overvoltage. Fig. 2.7 illustrates the OER potentials at three current densities similar to the case of WE1. A closer look at Fig. 2.7 indicates that the OER potentials for any current density decreased more rapidly when the temperature exceeded 100 °C. The trends in Fig. 2.7 differ from those shown in Fig. 2.5. Evidently, the unique potential decreases just above 100 °C, suggesting that boiling can reduce the oxygen concentration on the CL and the Nernst loss, according to Eq. (2.9).

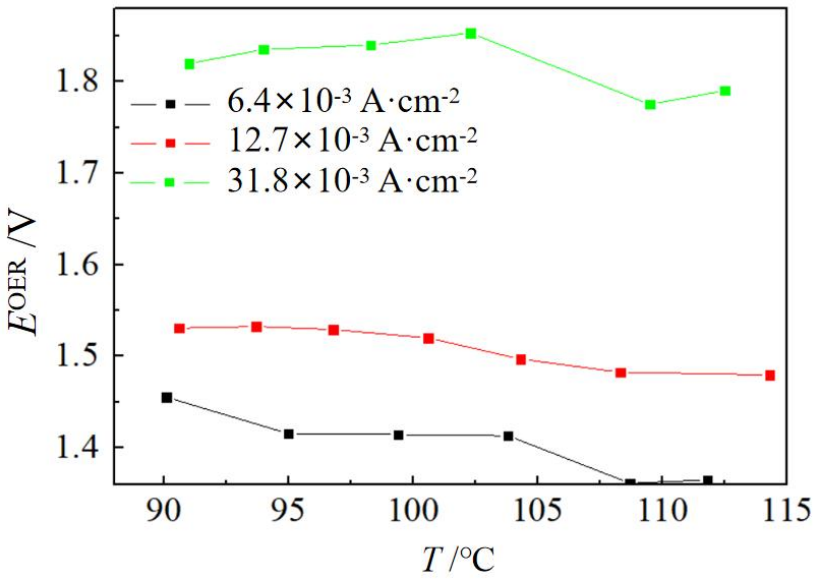

Fig. 2.7 Temperature influence on OER potential for WE2 (IR correction, vs. SSCE)

Fig. 2.8a and 2.8b show the η^{OER}–i performance and Tafel plot for WE2, respectively. The η^{OER}–i curves of Fig. 2.8a follow a general tendency, such that higher temperatures increase the current. However, a notable change appeared near the boiling point from 100 to 103 °C, where the current abruptly increased at a given overvoltage such at 0.3 V. Tafel plots (Fig. 2.8b) also suggested the abrupt current rise, where Tafel plots were discretely shifted when the temperature changed from 100 to 103°C. This discrete shift was highlighted by an orange circle, consistent with that shown in Fig. 2.3b. Thus, it is concluded that boiling can decrease the oxygen concentration in the CL and the Nernst loss, resulting in abrupt reduction of the OER potential at boiling temperature. In summary, the electrochemical evaluations performed for WE1 and WE2 suggest that boiling can lower the OER potential by reducing the Nernst loss and not by reducing the activation overvoltage.

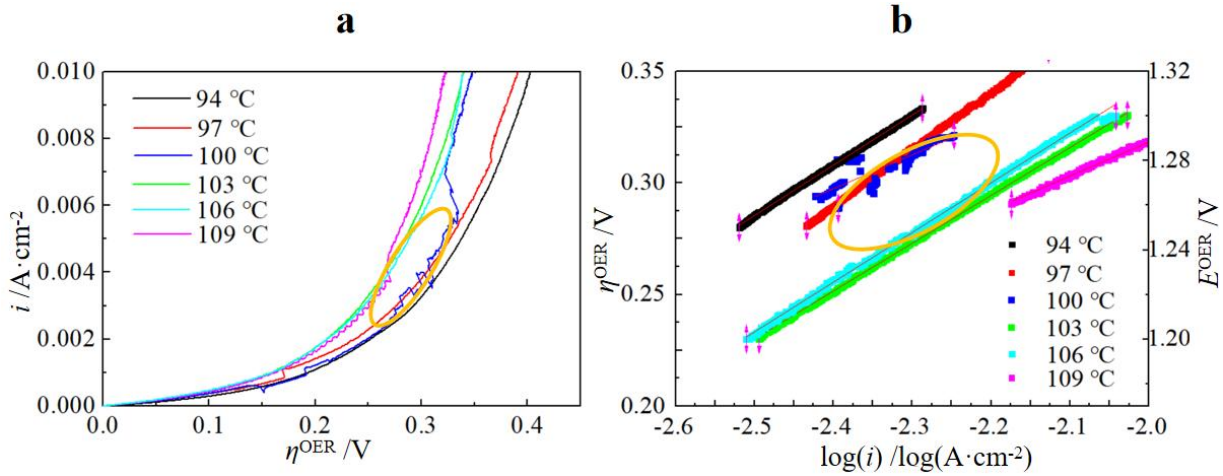

Fig. 2.8 Temperature influence on WE2 potential. a. the η^{OER}–i characteristics and b. Tafel plots for WE2 with IR correction

2.3.4 Highlighting boiling effect on OER

The OER potential of WE3 is shown in Fig. 2.9. WE3 has a structure similar to that of a real PEMWE and thus can examine the boiling effect in a more realistic manner. WE3 possesses a channel and a PTL, which causes a large oxygen transfer resistance. In contrast to that of WE2, WE3 case in Fig. 2.9 show a clearer evidence, where the OER potentials around the boiling temperature decreased substantially. It was also noted that the smaller the current, the lower the temperature at which the potential started to decrease, such as 97 °C at 4 mA·cm^{-2}, 100 °C at 10 mA·cm^{-2}, and 103 °C at 30 mA·cm^{-2}. This result suggests that a more intense boiling with a larger overheating temperature is necessary to effectively decrease the OER potential at a higher current density.

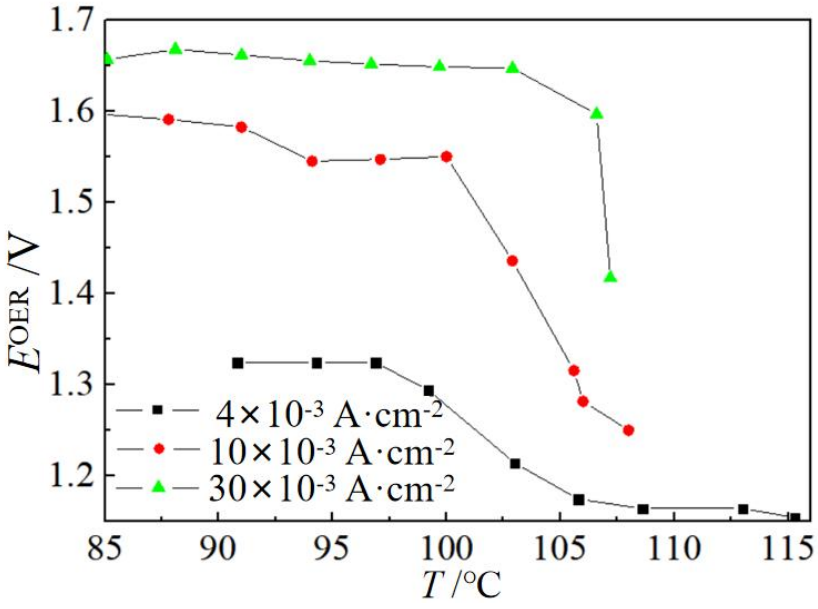

Fig. 2.9 Temperature influence on the OER potential (IR correction, vs. SSCE) for the WE3.

A more apparent boiling effect is observed in the η^{OER}–i characteristic curves and Tafel plots, as shown in Fig. 2.10. The η^{OER}–i curves below 97 °C indicate a gradual improvement in the performance as the temperature increases. This gradual improvement is attributed to the general activation overvoltage characteristic, where increasing the temperature increases the

exchange current density, as shown in Fig. 2.3a. However, the η^{OER}–i curves above 97 °C shifted considerably for every 3 °C increase in temperature, as shown in Fig. 2.10a. This large shift between the plots for each temperature case suggests a boiling effect. As mentioned above, WE3 has similar structure to PEMWE cell and has a large mass transfer resistance, which cause a high oxygen concentration on the CL. Once boiling superimposes on OER, boiling bubble can intensely dilutes the oxygen concentration. Thus, as shown in Fig. 2.10, boiling remarkably improved the OER performance.

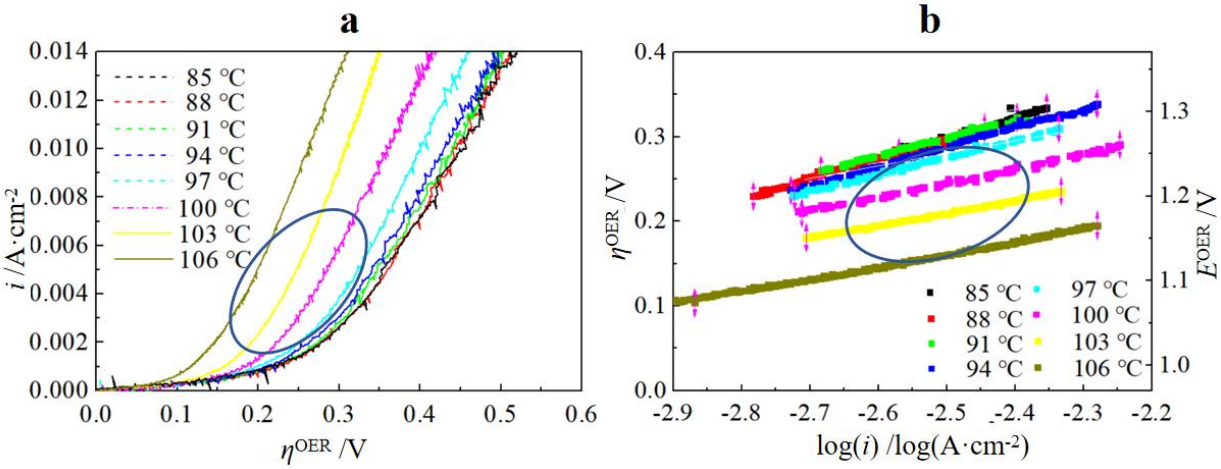

Fig. 2.10 Temperature influence on WE3 potential. a. η^{OER}–i characteristics and b.Tafel plots for WE3 with IR correction.

The same trend was observed in the Tafel plots of WE3 (Fig. 2.10b). Two adjacent Tafel plots at temperatures above 100 °C showed a significant shift. Above 100 °C, increasing the temperature continuously and substantially decreased the overvoltage, and more intense boiling as the temperature increased provided a more substantial reduction in the oxygen concentration on the CL. This large potential of the boiling effect for decreasing the OER concentration is attributed to the similar structure of WE3 to that of a PEMWE anode, where a larger oxygen transfer resistance exists.

2.3.5 Corrected exchange current density

As mentioned in section 2.2.3, another crucial piece of evidence that boiling reduces the oxygen concentration in the CL can be observed from the corrected exchange current

density. As described in Eq. (2.12), the corrected exchange current density i_e^c is related to the temperature and oxygen concentration in the CL. The dimensionless corrected current density j_e^c expresses the relative value versus exchange current density under standard conditions. Fig.s 2.11a–c show the dimensionless corrected current densities for WE1, WE2, and WE3, respectively, whose numerical ranges are marked on the left-side y-axis of the three figures and were obtained using the Tafel plots and Eq. (2.12). The j_e^c in the three WEs all exponentially increased with temperature. Moreover, the degree of increase was different between the three WEs. The case of WE3 was the highest, followed by that of WE2. This tendency agrees with the results of the electrochemical analysis. With a similar structure to real PEMWE, WE3 has the highest oxygen mass transport resistance; consequently, the boiling effect on WE3 works significantly and raises the dimensionless corrected current density j_e^c considerably. It was noticed that the j_e^c of WE2 and WE3 was almost double that of WE1. This is because the platinum-coated PTL is embedded in the WEs, and because the PTL also functions as an OER catalyst. Thus, it is worth qualitatively comparing the increase of j_e^c with increasing temperature between the three electrodes.

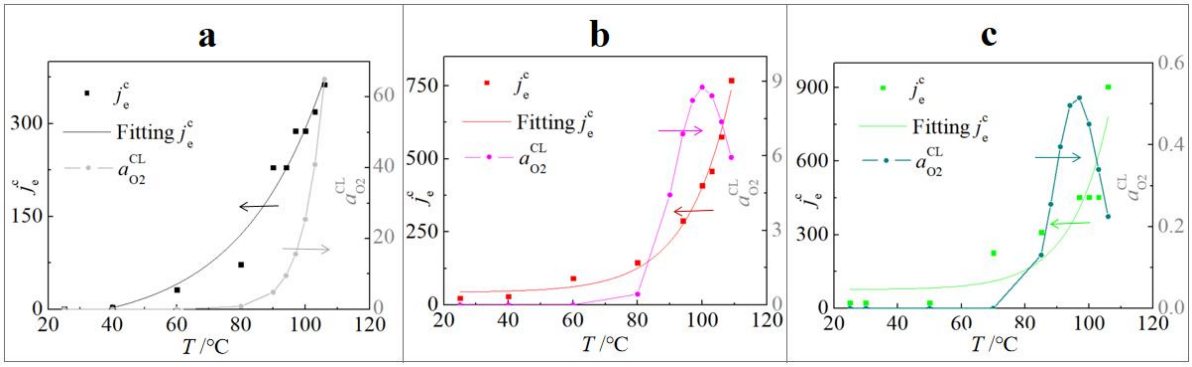

Fig. 2.11 The dimensionless corrected exchange current density and oxygen activity on CL versus temperature. for three WEs: a. WE1, b.WE2, and c.WE3

The oxygen activities on the CL, which were determined using Eq. (2.13), and the fitting line for j_e^c plotted points are shown as a dotted line in Fig. 2.11, and the range of values is marked on the right-side y-axis of the three figures. The temperature dependence of $a_{O_2}^{CL}$ provides a qualitative understanding of the boiling effect. Does boiling reduce the oxygen concentration in the CL? As predicted, the oxygen activities of WE2 and WE3 decreased at temperatures above 100 °C. Unlike the other two WEs, WE1 did not exhibit this tendency.

Thus, we conclude that boiling can mitigate the dense oxygen concentration caused by the large oxygen mass transfer resistance of the embedded PTL.

2.4 Conclusion

To clarify which overvoltage component in the OER was reduced by the boiling effect, this study conducted unique electrochemical measurements with three custom-made working electrodes: WE1 comprising only a CL and a directly faced electrolyte, WE2 embedded with a PTL on the CL, and WE3 with a similar structure to that of the anode of the PEMWE. The step-by-step electrochemical analysis with specific working electrodes yielded the following results:

1) Boiling decreased the OER overvoltage by lowering the Nernst loss. A considerable amount of vapor generated by boiling diluted the oxygen gas and dissolved oxygen gas in the catalyst layer.

2) Thus, the boiling effect is highlighted when the oxygen mass transfer resistance is high, as in a real PEMWE with embedded PTL and flow channel.

3) A low OER overvoltage caused by superimposed boiling can be converted to a higher current density operation and reduce the electrode area, resulting in a cost reduction of the PEMWE.

References

[1] E. Petkucheva, G. Borisov, E. Lefterova, J. Heiss, U. Schnakenberg, E. Slavcheva, Gold-supported magnetron sputtered Ir thin films as OER catalysts for cost-efficient water electrolysis, Int. J. Hydrogen Energ. 43(35) (2018) 16905–16912.

[2] P.T. Babar, A.C. Lokhande, M.G. Gang, B.S. Pawar, S.M. Pawar, J.H. Kim, Thermally oxidized porous NiO as an efficient oxygen evolution reaction (OER) electrocatalyst for electrochemical water splitting application, J. Ind. Eng. Chem. 60 (2018) 493–497.

[3] M. Wei, Y. Han, Y. Liu, B. Su, H.Yang, Z. Lei, Green preparation of Fe3O4 coral-like nanomaterials with outstanding magnetic and OER properties, J. Alloy Compd. 831 (2020) 154702.

[4] J. Cheng, B. Shen, Y. Song, J. Liu, Q. Ye, M. Mao, Y. Cheng, FeOOH decorated CoP porous nanofiber for enhanced oxygen evolution activity, Chem. Eng. J. 428 (2022) 131130.

[5] X. Li, Z. Kou, S. Xi, W. Zang, T. Yang, L. Zhang, J. Wang, Porous NiCo2S4/FeOOH nanowire arrays with rich sulfide/hydroxide interfaces enable high OER activity, Nano Energy 78 (2020) 105230.

[6] A. Yang, K. Su, S.Wang, Y. Wang, X. Qiu, W. Lei, Y. Tang, Self-stabilization of zero-dimensional PdIr nanoalloys at two-dimensional manner for boosting their OER and HER performance, Appl. Surf. Sci. 510 (2020) 145408.

[7] F. Xue, S. Kang, Y. Dai, T. Li, P.K. Shen, J. Zhu, S. Lu, X. Fu, L. Wang, S. Feng, H. Sun, Z. Xue, W. Lu, M. Nie, Hierarchical lead grid for highly stable oxygen evolution in acidic water at high temperature, J. Power Sources 493 (2021) 229635.

[8] E. López-Fernández, J. Gil-Rostra, C. Escudero, I.J. Villar-Garcíac, F. Yubero, A. de Lucas Consuegra, A.R. González-Elipe, Active sites and optimization of mixed copper-cobalt oxide anodes for anion exchange membrane water electrolysis, J. Power Sources 485 (2020) 229217.

[9] Anwar S, Khan F, Zhang Y, Djire A. (2021). Recent development in electrocatalysts for hydrogen production through water electrolysis, Int. J. Hydrogen Energ. 46(63) (2021) 32284-32317.

[10] T. Ma, Y. Kimura, H. Yamamoto, X. Feng, A. Hirano-Iwata, M. Niwano, Characterization of bulk nanobubbles formed by using a porous alumina film with ordered nanopores, J Phys.

Chem B 124(24) (2020) 5067–5072.

[11] I.S. Filimonenkov, S.Y. Istomin, E.V. Antipov, G.A.Tsirlina, E.R. Savinova, Rotating ring-disk electrode as a quantitative tool for the investigation of the oxygen evolution reaction, Electrochim. Acta 286 (2018) 304–312.

[12] F.Y. Ushikubo, T. Furukawa, R. Nakagawa, M. Enari, Y. Makino, Y. Kawagoe, T. Shiina, S. Oshita, Evidence of the existence and the stability of nano-bubbles in water, Colloid Surface A 361(1-3) (2010) 31–37.

[13] Yaparatne S, Doherty ZE, Magdaleno AL, Matula EE, MacRae JD, Garcia-Segura S, Apul OG. Effect of air nanobubbles on oxygen transfer, oxygen uptake, and diversity of aerobic microbial consortium in activated sludge reactors, Bioresource Technology, 351 (2022) 127090.

[14] A. Angulo, P. van der Linde, H. Gardeniers, M. Modestino, D.F. Rivas, Influence of bubbles on the energy conversion efficiency of electrochemical reactors, Joule 4(3) (2020) 555–579.

[15] Y. Li, G. Yang, S. Yu, J. Mo, K. Li, Z. Xie, L. Ding, W. Wang, F.-Y. Zhang, High-speed characterization of two-phase flow and bubble dynamics in titanium felt porous media for hydrogen production, Electrochim. Acta, 370 (2021) 137751.

[16] Martínez-Séptimo A, Valenzuela MA, Del Angel P, González-Huerta RD. IrRuOx/TiO2 a stable electrocatalyst for the oxygen evolution reaction in acidic media, Int. J. Hydrogen Energ. 46(51) (2021) 25918-28.

[17] G. Yang, H. Xiang, M. Rauf, H. Mi, X. Ren, P. Zhang, Y. Li, Plasma enhanced atomic-layer-deposited nickel oxide on Co3O4 arrays as highly active electrocatalyst for oxygen evolution reaction, J. Power Sources 481 (2021) 228925.

[18] K. Ito, K. Terabaru, H. Li, A. Inada, H. Nakajima, Challenging of Reducing Electrolysis Voltage by Superimposing Boiling on PEMWE–A Thermodynamic Coupling, ECS Transactions 80(8) (2017) 1117.

[19] E. Afshari, S. Khodabakhsh, N. Jahantigh, S. Toghyani, Performance assessment of gas crossover phenomenon and water transport mechanism in high pressure PEM electrolyzer, Int. J. Hydrogen Energ. 46(19) (2021) 11029–11040.

[20] Vos JG, Liu Z, Speck FD, Perini N, Fu W, Cherevko S, Koper MT. Selectivity trends between oxygen evolution and chlorine evolution on iridium-based double perovskites in acidic media. ACS catalysis. 2019 ;9(9):8561-74.

[21] Antoniou A, Berastain A, Hernandez D, Celis C. Mathematical modelling of coupled and decoupled water electrolysis systems based on existing theoretical and experimental studies, Int. J. Hydrogen Energ. 47(40) (2022) 17526-17543.

[22] A.S. Tijani, N.A.B. Kamarudin, F.A.B. Mazlan, Investigation of the effect of charge transfer coefficient (CTC) on the operating voltage of polymer electrolyte membrane (PEM) electrolyzer, Int. J. Hydrogen Energ. 43(19) (2018) 9119–9132.

[23] M. Sartory, E. Wallnöfer-Ogris, P. Salman, T. Fellinger, M. Justl, A. Trattner, M. Klell, Theoretical and experimental analysis of an asymmetric high pressure PEM water electrolyzer up to 155 bar, Int. J. Hydrogen Energ. 42(52) (2017) 30493–30508.

[24] Sartory M, Wallnöfer-Ogris E, Salman P, Fellinger T, Justl M, Trattner A, Klell M. Theoretical and experimental analysis of an asymmetric high pressure PEM water electrolyser up to 155 bar. International Journal of Hydrogen Energy. 2017;42(52):30493-508.

[25] Z. Kang, S.M. Alia, M. Carmo, G. Bender, In-situ and in-operando analysis of voltage losses using sense wires for proton exchange membrane water electrolyzers, J. Power Sources 481 (2021) 229012.

[26] F. Aubras, M. Rhandi, J. Deseure, A. J.-J. Kadjo, M. Bessafi, J. Majasan, B. Grondin-Perez, F. Druart, J.-P. Chabriat, Dimensionless approach of a polymer electrolyte membrane water electrolysis: Advanced analytical modelling, J. Power Sources 481 (2021) 228858.

[27] J.K. Lee, C.H. Lee, A. Bazylak, Pore network modelling to enhance liquid water transport through porous transfer layers for polymer electrolyte membrane electrolyzers, J. Power Sources 437 (2019) 226910.

Chapter 3

Theoretical analysis of boiling effect on OER

This chapter constructs a theoretical model to quantitatively explore the mechanism of how boiling reduces the oxygen evolution reaction (OER) overpotential. As chapter 2 suggested, boiling can reduce Nernst loss by accelerating oxygen transfer by vaporizing large amounts of water vapor. The model considers dissolved oxygen, liquid water, gaseous oxygen and water vapor flowing through the porous transfer layer (PTL) on a catalyst layer (CL). The model determines two oxygen fluxes as gas phase and dissolved case, and also can estimate the concentration of dissolved oxygen at the CL. The model clarified boiling has a role in increasing the molar flux of gaseous oxygen and reducing the dissolved oxygen concentration. Then, the reduction of the dissolved oxygen concentration is responded to OER electrochemical equation, which shows the relationship with OER overvoltage. The PTL embedded on the CL enlarges the mass transfer resistance of the dissolved oxygen and raises the dissolved oxygen concentration at the CL. Even in this case, once the boiling is superimposed on OER, the boiling attracts more dissolved oxygen into water vapor bubbles and significantly decreases the dissolved oxygen concentration at the CL, reducing the Nernst loss of the OER. That's the scenario of how boiling reduces OER overpotential.

3.1 Introduction

Oxygen bubbles in the PEMWE anode tend to increase the anode overvoltage [1]. Oxygen bubbles cover some active areas of the catalyst layer (CL) [2], decreasing apparent electrochemical surface area and increasing activation overvoltage. In particular, the rough contact between the CL and porous transfer layer (PTL) leaves more space for storing bubbles, reducing the active area [3, 4]. In addition, the oxygen bubbles prevent water from flowing into the CL, reducing the OER current density at the CL covered by the oxygen bubbles [5,6]. Therefore, other regions of CL covered by water need to increase the current density to share more current load [7]. Once current density rises locally, water starvation may occur there and raises concentration overvoltage [8].

To reduce the OER overvoltage, in addition to material development, some efforts

utilizing physical effects are proposed. Applying ultrasound and magnetic fields succeeded in rapidly draining oxygen bubbles [9,10]. But implementing these operations will increase equipment investment. Lickert et al. thought a PTL with large-pore and high-porosity decreases oxygen transfer resistance, which is beneficial to draining oxygen bubbles [1,3]. However, increasing the pore size and porosity increases the contact resistance of PTL and CL, increasing the ohmic overvoltage [11]. Todd et al. considered applying a high-pressure operation to shrink the volume of the gas bubbles to decrease gas saturation in a PTL [12]. High-pressure operation is easily achieved in OER without changing the PTL structure. Among the efforts thus introduced, the high-pressure operation is thought to be worth doing regarding the reduction of OER overvoltage.

However, the high-pressure operation to suppress water starvation by decreasing the gas saturation in OER causes a trade-off issue. The oxygen produced in OER is drained as oxygen bubbles and as dissolved oxygen in the water. The gaseous oxygen pressure decides the dissolved oxygen concentration [13, 14]. Although the high operating pressure can shrink the oxygen bubbles at the CL, it also increases the dissolved oxygen concentration in the water surrounded by high-pressure oxygen bubbles. The high dissolved oxygen concentration forms a high concentration overvoltage in OER [15]. Increasing the operating temperature is suggested as a countermeasure, which can lower dissolved oxygen concentration [16]. However, the way to increase the temperature is generally limited so that it is lower than the boiling point to ensure the water supply for OER in the liquid phase. Thus, superimposing boiling, the target in this thesis, is the only way to reduce OER potential among the physical effect.

However, the mechanism of how boiling reduces the OER potential has yet to be verified. To respond to this question, this chapter develops a model to quantitatively clarify the mechanism that the boiling reduces the OER potential. Domain for the model here developed supposes the three WEs (WE1, WE2 and WE3) in chapter 2. Thus, the numerically calculated results based on the model are compared with the OER experimental results in chapter 2. The following sub-chapter carefully explains the model, whose main idea is conservation law for the charge, molar flux, and momentum in the through PTL direction with boundary conditions. In the model, liquid water replaces the name bulk electrolyte for ease of understanding. Then, chapter 3.3.1 makes a comparison between the experiment and prediction by a model in terms of OER overpotential. Good consistency will be shown,

suggesting that the model can precisely reproduce key phenomena in the boiling effect.

3.2 Model introduction of the OER superimposed with boiling

To help understand the model's computational logic, the model's flowchart is shown in Fig. 3.1, where the meaning of the symbols is listed in the nomenclature (Table 3.1). In Fig. 3.1, the momentum equations in the PTL serve as the core formulations of the transfer equation. In addition, the capillary pressure (P_c) equation and the molar flux equations for dissolved oxygen ($Q_{O,dis}$) and water vapor ($Q_{w,g}$) are supplemented to help solve the molar flux and momentum equations. The boundary conditions at the upper surface of the PTL, at which the location is simply named PUS (porous transport layer upper surface), are the pressure of liquid water ($P_{w,l}$), the pressure and saturation of the gas bubbles (P_g and S_g). The boundary conditions at the CL/PTL interface are oxygen molar flux (Q_O) and water vapor molar flux by boiling ($Q_{w,g}^b$). The concentrations of dissolved oxygen, gaseous oxygen, water vapor, etc., output from the transfer equation are transferred to the electrochemical equations of the OER. Ultimately, the electrochemical equation outputs the potential (E) of the OER, etc. The numerical calculation was executed in Python with a convergence accuracy of 1%. Table 3.2 is the calculation condition, so the impact of OER temperature and PTL thickness is examined. Table 3.3 shows the constants used in the calculation.

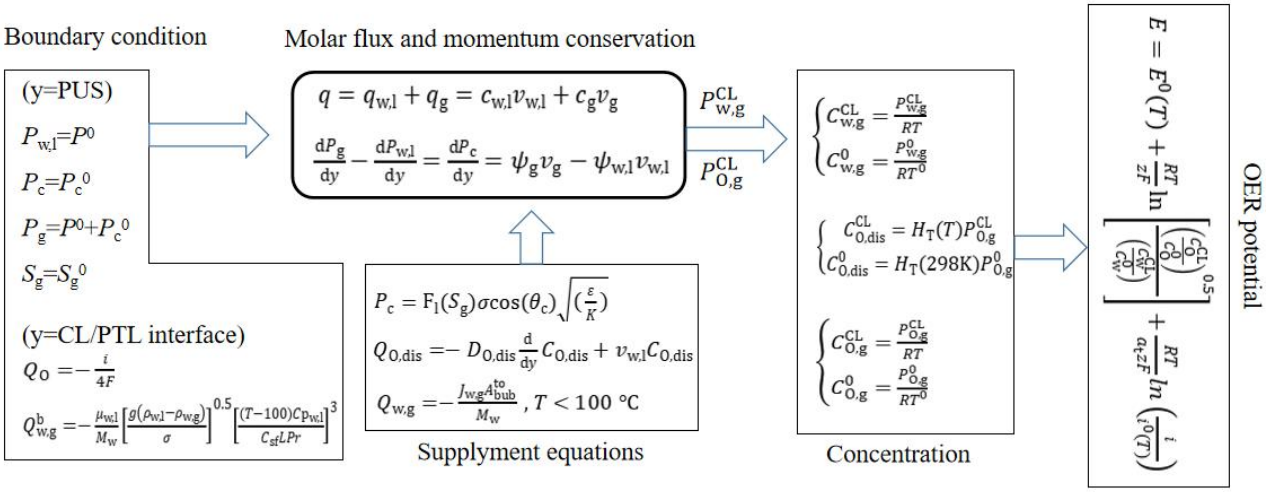

Fig. 3.1 Calculation flow of theoretical model.

Table 3.1 Nomenclature.

Nomenclature

A	Bubble side-wall area for a unit geometric area, [-]	L	Latent heat, [$J \cdot kg^{-1}$]
C	Concentration, [$mol \cdot m^{-3}$]	N	Bubble number for a unit geometric area, [-]
$\bar{c}$	Relative concentration, [$s \cdot m^{-1}$]	P	Pressure, [Pa]
cr	Current contribution ratio, [-]	Pr	Prandtl number, [-]
D	Diffusion coefficient, [$m^2 \cdot s^{-1}$]	Q	Molar flux, [$mol \cdot m^{-2} \cdot s^{-1}$]
E	Potential, [V]	q	Relative molar flux, [-]
H_T	Henry coefficient, [$mol \cdot m^{-3} \cdot Pa^{-1}$]	R	Diffusion resistance, [$s \cdot m^{-1}$]
i	Current density, [$A \cdot m^{-2}$]	r	Radius, [m]
J	Evaporation rate, [$kg \cdot m^{-2} \cdot s^{-1}$]	S	Saturation, [-]
j	Relative current density, [-]	T	Temperature, [K]
K	Permeability, [m^2]	v	Velocity, [$m \cdot s^{-1}$]

Greek symbols

α	Activity, [-]	λ	Dimensionless concentration, [-]
γ	Relative molar flow rate, [-]	μ	Dynamic viscosity, [Pa·s]
δ	Thickness, [m]	ρ	Density, [$kg \cdot m^{-3}$]
ε	Porosity, [-]	σ	Water surface tension, [Pa·m]
ς	Dimensionless transfer resistance, [-]	τ	Relative pressure of water vapor, [-]
θc	Contact angel of PTL, [°]		

Superscripts and subscripts

b	Boiling	ls	Liquid water surrounding gas bubbles
bub	Bubble	O	Oxygen
CL	Catalyst layer	PUS	Upper surface of the PTL
dis	Dissolved	to	Total

det	Detachment	w	Water
g	Gas	0	Standard
l	Liquid		

Table 3.2 Calculation conditions.

Case	Current density ($A \cdot cm^{-2}$)	PTL thickness (mm)	Temperature (°C)	Pressure (MPa)
1	0.001-1.024	0.01	85	0.1013
2	0.001-1.024	0.02	85	0.1013
3	0.001-1.024	0.05	85	0.1013
4	0.001-1.024	0.2	85	0.1013
5	0.001-1.024	1	85	0.1013
6	0.001-1.024	0.2	94	0.1013
7	0.001-1.024	0.2	97	0.1013
8	0.001-1.024	0.2	100	0.1013
9	0.001-1.024	0.2	103	0.1013
10	0.001-1.024	0.2	106	0.1013

Table 3.3 Constants for the model.

C_{sf}	0.013	-	Surface fluid combination coefficient [28]
$Cp_{w,l}$	4184	$J \cdot kg^{-1} \cdot K^{-1}$	Specific heat of water
d	20	μm	Average pore diameter of the Ti mesh
d_{IrO_2}	8.35×10^{-7}	m	Particle diameter of IrO_2 [29]
En^{an}	76 000	$J \cdot mol^{-1}$	Anodic reference activation energy [29]
F	96 485	$C \cdot mol^{-1}$	Faraday constant
g	9.81	$m \cdot s^{-2}$	Gravity acceleration

H_{298K}	1.2×10^{-5}	$mol\cdot Pa^{-1}\cdot m^{-3}$	Henry coefficient [21]
ΔH	1.4×10^{4}	$J\cdot mol^{-1}$	Dissolution enthalpy [21]
i_{ref}^{0}	2.64×10^{-9}	$A\cdot cm^{-2}$	OER exchange current density
L	2.27×10^{6}	$J\cdot kg^{-1}$	Latent hear of water vaporization
L^{s}	6×10^{-9}	$kg\cdot K\cdot s\cdot m^{-4}$	Evaporation coefficient [27]
M_{w}	18	$g\cdot mol^{-1}$	Molar mass of water
m_{IrO_2}	1.5	$mg\cdot cm^{-2}$	IrO_2 load
P^{0}	101 325	Pa	Base pressure
R	8.314	$J\cdot mol^{-1}\cdot k^{-1}$	Universal gas constant
T^{0}	298.15	K	Reference temperature
z	2	-	Number of electron transfer
a_{t}	0.5	-	Charge transfer coefficient
ε	0.4	-	Porosity of the Ti mesh
θ_{c}	30	°	Contact angle of the Ti mesh [29]
$\mu_{w,g}$	1.2×10^{-5}	Pa·s	Dynamic viscosity of water vapor
μ_{O}	1.04×10^{-5}	Pa·s	Dynamic viscosity of oxygen [30]
$\mu_{w,l}$	2.822×10^{-4}	Pa·s	Dynamic viscosity of liquid water
ρ_{IrO_2}	11.66	$g\cdot cm^{-3}$	IrO_2 mass density
φ_{I}	0.75	-	Contact fraction of ionomer and catalyst [29]

This section details the OER process and how boiling enhances oxygen transfer. Boiling is expected to reduce the partial pressure of gaseous oxygen in bubbles to reduce the dissolved oxygen concentration in the water surrounding bubbles. Thus, boiling is expected to exhibit special effects on OER, such as lowering its overpotential. To quantitatively clarify the exceptional OER performance under boiling, the theoretical models are developed, consisting of

(1) the electrochemical reaction at the CL,

(2) the mass transfer through the PTL,

(3) and the water vaporization in the PTL.

These processes are introduced in the next sub-sections.

The OER process includes water electrolysis and the transfer of water, oxygen, and protons, as shown in Fig. 3.2. Fig. 3.2a is the calculation domain for the OER process, which

consists of a CL and a hydrophilic PTL. This structure is supposed to be the WE2 of the three-electrodes cell (see Fig. 2.1) in chapter 2. This structure applies to WE1 and WE3 models, whose experimental structures are described in chapter 2. The difference between the WE1, WE2, and WE3 models is the thickness of the mass transfer layer. The transfer layer over the WE1 CL surface is only a 10- μ m thickness [17]. The PTL thickness of WE3 is set to 1 mm, a virtual thickness formed by a 0.2-mm-thickness PTL and 0.5-mm-width ribs. OER occurs at the CL to generate oxygen and forms different current densities in liquid water and bubbles, such as i_l and i_g, since the oxygen activity differs between in liquid water and bubbles. The oxygen and water transfer through the PTL. The saturation of gas bubbles, which mainly consists of gaseous oxygen with a small amount of water vapor at room temperature, decreases continuously from the CL to the PUS owing to the capillary pressure between gas and liquid phases. Thus, bubbles flow from the CL to the PUS. Then, the flowing water above the PTL continuously removes these bubbles from the PUS to the bulk water. The velocity of the flowing water was 1.05 $m \cdot s^{-1}$, equal to the linear speed determined by the experimental rotator with a 2000 $r \cdot min^{-1}$ and a 10 mm diameter. Contrary to the gas saturation, the water saturation decreases continuously from the PUS to PTL/CL interface, driving the flow of liquid water from the PUS to the CL [18].

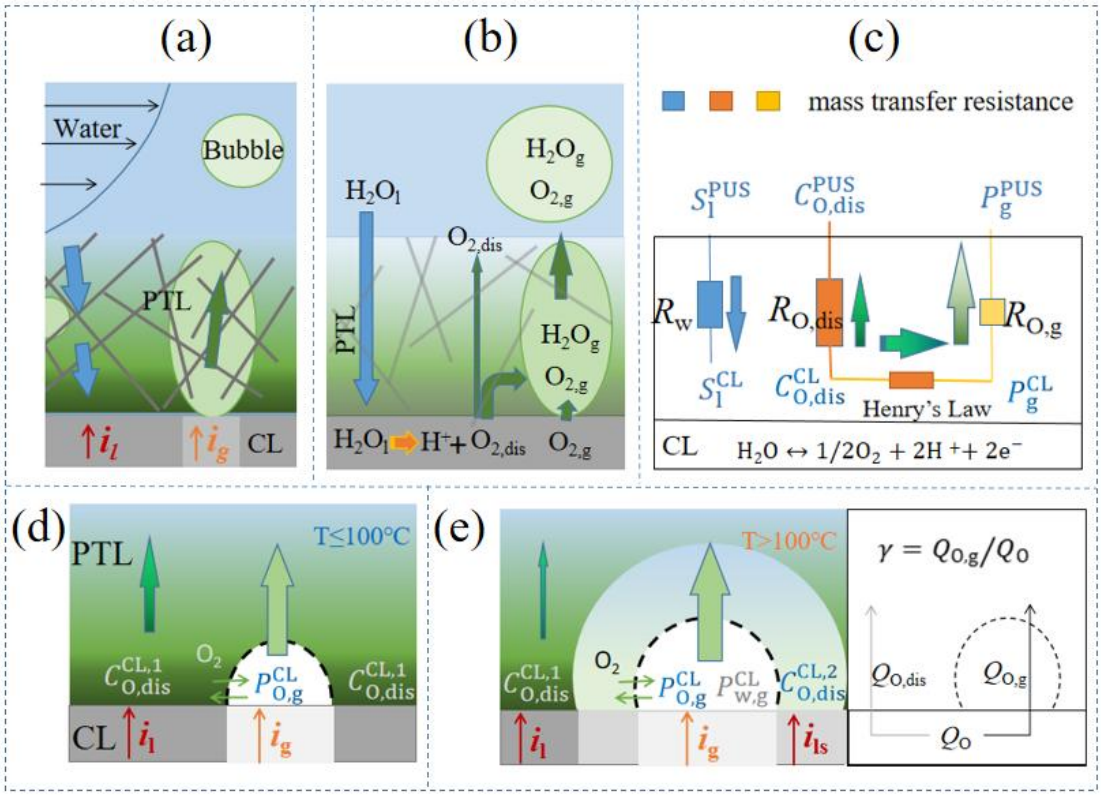

Fig.3.2 Schematic drawings of OER process. a. structure of the CL and PTL, b. introduction of the OER process, c. oxygen transfer resistance, d. oxygen transfer at unboiling, e. oxygen transfer at boiling

Fig. 3.2b depicts water electrolysis in detail. The water flows from the PUS to the CL and is electrolyzed into proton and oxygen at the CL. The oxygen molecules produced at the CL dissolve into the water first and then form oxygen bubbles when the dissolved oxygen concentration exceeds its saturation concentration [13]. The oxygen bubbles are mixed with water vapor and cover the partial areas of the CL. In the following text, the bubbles mixed with gaseous oxygen and water vapor are called just “bubbles”.

Fig. 3.2c presents the flow and transfer resistance of oxygen bubbles, dissolved oxygen, and liquid water. Gaseous oxygen and water vapor mix in the bubbles and have respective pressure as $P_{O,g}$ and $P_{w,g}$. The bubble has total pressure, $P_g = P_{O,g} + P_{w,g}$. The high bubble pressure at the CL, P_g^{CL}, drives the bubble to flow to the low gas pressure, P_g^{PUS}, in the bulk water region. In terms of the dissolved oxygen in water, diffusion and convection transfer it from the CL toward the PUS. In general, oxygen transfer through bubbles has lower resistance than that in a dissolved manner through liquid water. Thus, oxygen is drained mostly through the bubble (gas phase).

Fig. 3.2d is a picture magnifying the CL/PTL interface of Fig. 3.2a. It is noted that the gaseous oxygen in the bubble equilibrates the dissolved oxygen, whose concentration in water obeys Henry's law with the partial pressure of gaseous oxygen . The situation of Fig. 3.2d supposes the case without boiling (in the case of less than 100 °C). The bubble shown in this figure is occupied mostly by gaseous oxygen and secondary by water vapor. Fig. 3.2d also indicates the existence of two OER current components at the CL. One is i_l, where liquid water and dissolved oxygen are the reactant and product, respectively. The other one is i_g, where water vapor and gaseous oxygen are the reactant and product, respectively.

Eqs. (3.1) and (3.2) define the relative current density, which is the ratio of local current density to the average current density and can reflect the multiple of the local current density relative to the average current density. If this relative current density exceeds 1, the local current density exceeds the average current density and vice versa. The average current density is the applied current density, the ratio of the applied current to the geometric area of CL. The relationship between the average current density and the local current density will be

given in Eq. (3.4). For the CL in the liquid water, the relative current density is

$$j_{\mathrm{l}} = \frac{i_{\mathrm{l}}}{i} \quad (3.1)$$

For the CL under bubbles:

$$j_{\mathrm{g}} = \frac{i_{\mathrm{g}}}{i} \quad (3.2)$$

Fig. 3.2e is the case when the temperature rises to over 100 °C, and boiling begins to be superimposed on the OER. Unlike Fig. 3.2d, the bubble marked with a dashed line is occupied mainly by water vapor and secondary by gaseous oxygen. This is because boiling tends to take the oxygen bubbles as the vaporization nucleus, and the water vapor produced by boiling fills in the oxygen bubbles to form the mixed bubble. According to Henry's law, the low oxygen partial pressure thus formed in the bubble will attract dissolved oxygen into the bubble. As a result, a lower concentration region of dissolved oxygen forms next to the bubble. This new region can be characterized as a different OER current density, i_{ls}, as shown in Fig. 3.2e. This current density also can be replaced with a relative value as follows.

$$j_{\mathrm{ls}} = \frac{i_{\mathrm{ls}}}{i} \quad (3.3)$$

Gas saturation at the CL, $S_{\mathrm{g}}^{\mathrm{CL}}$, decides the applied current. Eq. (3.4) gives the relation between the partial current density and the average current density, where the $S_{\mathrm{g}}^{\mathrm{CL}}$ is the gas saturation at the CL and approximates the fractional coverage of bubbles at the CL [18], which is dimensionless. As shown in Fig. 3.2e, the oxygen produced by the CL is expelled in dissolved and gaseous states, forming respective molar fluxes. Among them, boiling cannot decrease the concentration of dissolved oxygen discharged through the liquid water. The γ in Eq. (3.4) is the ratio of gaseous oxygen molar flux, $Q_{\mathrm{O,g}}$, to the sum of Q_{O}, as plotted in Fig. 3.2e. The dissolved oxygen molar flux, $Q_{\mathrm{O,dis}}$, is also shown in this figure. The relative molar flux of dissolved oxygen discharged through liquid water, 1-γ, is the fraction of dissolved oxygen whose concentration is not changed by boiling. Accordingly, the relative molar flux of dissolved oxygen flowing into the bubbles and expelling through bubbles approaches the relative molar flux of gaseous oxygen, γ, which is the fraction of dissolved oxygen whose concentration is lowered by boiling.

$$i = S_{\mathrm{g}}^{\mathrm{CL}} i_{\mathrm{g}} + \gamma(1 - S_{\mathrm{g}}^{\mathrm{CL}}) i_{\mathrm{ls}} + (1 - \gamma)(1 - S_{\mathrm{g}}^{\mathrm{CL}}) i_{\mathrm{l}} \quad (3.4)$$

The current contribution ratio, cr_{x} (subscript x represents g, ls, or l), is the contribution of the three OER current components in Fig. 3.2e. This cr_{x} has a role in understanding which

OER current component is the highest and how to optimize the boiling effect to reduce OER overpotential. Eq.s (3.5-3.7) list the contribution ratio of the three OER current components. Each current contribution ratio is less than 1, and the sum of the three components equals 1.

$$cr_{\mathrm{g}} = \frac{i_{\mathrm{g}}}{i} S_{\mathrm{g}}^{\mathrm{CL}} = j_{\mathrm{g}} S_{\mathrm{g}}^{\mathrm{CL}} \quad (3.5)$$

$$cr_{\mathrm{ls}} = \left(1 - S_{\mathrm{g}}^{\mathrm{CL}}\right)\gamma \frac{i_{\mathrm{ls}}}{i} = \left(1 - S_{\mathrm{g}}^{\mathrm{CL}}\right)\gamma j_{\mathrm{ls}} \quad (3.6)$$

$$cr_{\mathrm{l}} = \left(1 - S_{\mathrm{g}}^{\mathrm{CL}}\right)(1-\gamma) \frac{i_{\mathrm{l}}}{i} = \left(1 - S_{\mathrm{g}}^{\mathrm{CL}}\right)(1-\gamma) j_{\mathrm{l}} \quad (3.7)$$

γ can be used to approximate the fractional coverage of the boiling effect on the dissolved oxygen since the dissolved oxygen near the boiling bubbles eventually flows into the bubbles.

3.2.1 Overpotential and current density of the OER

In an acidic environment, the reaction equation for OER is $\mathrm{H_2O} \rightarrow 2\mathrm{H^+} + \frac{1}{2}\mathrm{O_2} + 2\mathrm{e^-}$. OER potential consists of Nernst potential and overvoltages. The Nernst potential of the OER is,

$$E^{\mathrm{Nernst}} = E^0(T) + \frac{RT}{zF} \ln\left(\frac{\alpha_{\mathrm{O}}^{0.5}}{\alpha_{\mathrm{w}}}\right) \quad (3.8)$$

The first term on the right-hand side (RHS) of Eq. (3.8) is the standard redox potential. It is noted that this equation assumes that the activity of proton is 1 because of abundant proton in ionomer forming in the CL. Activity in the second term comes from the concentration ratio of the oxygen and water at the CL with reference to a standard state, then $\alpha = C_{\mathrm{x}}^{\mathrm{CL}} / C_{\mathrm{x}}^{0}$. Substituting the activities of oxygen and water to Eq. (3.8) in terms of concentration,

$$E^{\mathrm{Nernst}} = E^0(T) + E^{\mathrm{NL}} = E^0(T) + \frac{RT}{zF} \ln\left[\frac{\left(\frac{C_{\mathrm{O}}^{\mathrm{CL}}}{C_{\mathrm{O}}^{0}}\right)^{0.5}}{\left(\frac{C_{\mathrm{w}}^{\mathrm{CL}}}{C_{\mathrm{w}}^{0}}\right)}\right] \quad (3.9)$$

where the subscript of "O" and "w" is oxygen and water, respectively. In this work, a concept of Nernst loss, E^{NL}, is defined, which corresponds to the second term on the RHS of Eq. (3.9) and is denoted as E^{NL}. If the oxygen activity is rather less than 1, the Nernst loss can be negative, contributing to a lower OER potential.

Adding activation overvoltage on the Eq. (3.9) yields OER potential [7], where a_{t} is the charge transfer coefficient, and z is the number of electron transfer.

$$E = E^0(T) + \frac{RT}{zF}\ln\left[\frac{\left(\frac{C_O^{CL}}{C_O^0}\right)^{0.5}}{\left(\frac{C_w^{CL}}{C_w^0}\right)}\right] + \frac{RT}{a_t zF} ln\left(\frac{i}{i^0(T)}\right) \quad (3.10)$$

The third term is the activation overvoltage, where the exchange current density $i^0(T)$ is defined at standard oxygen concentration, $C_O{}^0$, and standard water concentration, $C_w{}^0$ [19]. In Eq. (3.10), the ohmic overvoltage is not included because the ohmic overvoltage of chapter 2 conducted IR correction. Additionally, ohmic overvoltage, as usually considered, is not intentionally involved in the OER potential. This is because boiling is thought not to influence electron conduction through the porous electrode.

The sum of the Nernst loss (second term) and activation overvoltage (third term) in Eq. (3.10) is the OER overpotential, ΔE, which is,

$$\Delta E = E - E^0(T) = \frac{RT}{zF}\ln\left[\frac{\left(\frac{C_O^{CL}}{C_O^0}\right)^{0.5}}{\left(\frac{C_w^{CL}}{C_w^0}\right)}\right] + \frac{RT}{a_t zF} ln\left(\frac{i}{i^0(T)}\right) \quad (3.11)$$

Precisely speaking, it is recognized as an OER overpotential with reference to the standard redox potential. The overpotential functions with OER current density and the concentration of oxygen and water at the CL. A simple mathematical manipulation from Eq. (3.11) yields and explicitly shows the OER current density [20]. Around the exchange current density, the reverse current density of OER will become significant. The current expression of Eq. (3.12) is only applicable when the current density should be much higher than the exchange current density.

$$i = i^0(T)\frac{\left(\frac{C_w^{CL}}{C_w^0}\right)^{a_t}}{\left(\frac{C_O^{CL}}{C_O^0}\right)^{0.5a_t}}\exp\left(\frac{za_tF\Delta E}{RT}\right) \quad (3.12)$$

The OER current density, i, is divided into three components, i_g, i_l, i_{ls}, as shown in Fig. 3.2e. Each component of the current density is affected by oxygen and water states (gaseous oxygen, dissolved oxygen, liquid water, and water vapor). Oxygen may have different activities in a dissolved manner in water and in a gaseous manner in bubbles. Water may also form different activities in a liquid and gas phase. Thus, the bubbles and liquid water part on the CL yield different current densities of OER.

The redox potential in the liquid water and gas bubbles ($E_l^0(T)$ and $E_g^0(T)$) is unequal due to different formations of Gibbs free energy between liquid water and water vapor

($\Delta G^0_{f,l}(T)$ and $\Delta G^0_{f,g}(T)$), except at boiling point. The OER overpotential in liquid water, $\Delta E_l = E - E^0_l(T)$, is naturally different from that in bubbles, $\Delta E_g = E - E^0_g(T)$, as shown in Fig. 3.3.

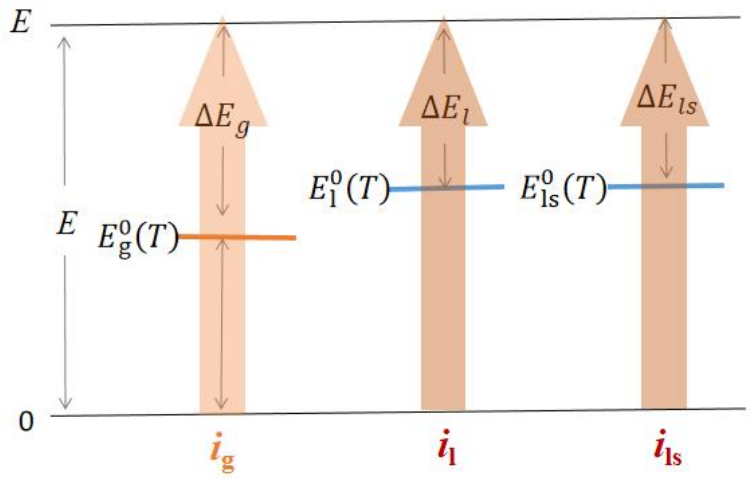

Fig. 3.3 Circuit diagram of three current density components (current density of the CL in bubbles, and in liquid water far from and surrounding the bubbles).

Eq. (3.13) provide the equations for OER current density in gas bubbles. Specially, current density at the CL covered with the bubbles:

$$i_g = i^0(T)\frac{\left(\frac{C^{CL}_{w,g}}{C^0_{w,g}}\right)^{a_t}}{\left(\frac{C^{CL}_{O,g}}{C^0_{O,g}}\right)^{0.5a_t}}\exp\left(\frac{za_tF\Delta E_g}{RT}\right) \quad (3.13)$$

The gaseous oxygen and water vapor are regarded as ideal gases in the bubbles. Their concentrations in Eq. (3.13) are expressed in Eq.s (3.14) and (3.15). Superscript "0" means under standard conditions of 25°C and 0.1013MPa.

$$\begin{cases} C^{CL}_{O,g} = \frac{P^{CL}_{O,g}}{RT} \\ C^0_{O,g} = \frac{P^0_{O,g}}{RT^0} \end{cases} \quad (3.14)$$

$$\begin{cases} C^{CL}_{w,g} = \frac{P^{CL}_{w,g}}{RT} \\ C^0_{w,g} = \frac{P^0_{w,g}}{RT^0} \end{cases} \quad (3.15)$$

Current density at the CL immersed in liquid water far from bubbles:

$$i_l = i^0(T)\frac{\left(\frac{C_{\mathrm{w,l}}^{\mathrm{CL}}}{C_{\mathrm{w,l}}^0}\right)^{a_t}}{\left(\frac{C_{\mathrm{O,dis}}^{\mathrm{CL},1}}{C_{\mathrm{O,dis}}^0}\right)^{0.5a_t}}\exp\left(\frac{za_tF\Delta E_l}{RT}\right) \quad (3.16)$$

In Eq. (3.16), the concentrations of liquid water and dissolved oxygen at the CL are critical parameters for determining the OER current density in the water. According to Henry's law, the partial pressure of the gaseous oxygen determines the concentration of dissolved oxygen in the water.

$$\begin{cases} C_{\mathrm{O,dis}}^{\mathrm{CL},1} = H_{\mathrm{T}}(T)P_{\mathrm{O,g}}^{\mathrm{CL}} \\ C_{\mathrm{O,dis}}^{0} = H_{\mathrm{T}}(T^0)P_{\mathrm{O,g}}^{0} \end{cases} \quad (3.17)$$

where the Henry coefficient refers to Eq. (3.18) [21]. In Eq. (3.18), ΔH is the dissolution enthalpy of oxygen.

$$H_{\mathrm{T}}(T) = H_{\mathrm{T}}(T^0)\exp\left[\frac{-\Delta H}{\mathrm{R}}\left(\frac{1}{T}-\frac{1}{T^0}\right)\right] \quad (3.18)$$

The concentration of liquid water is related to water density. Although Eq. (3.19) introduces a precise water concentration to determine water activity, the water activity of $\frac{C_{\mathrm{w,l}}^{\mathrm{CL}}}{C_{\mathrm{w,l}}^0}$ becomes approximately 1 because of the incompressibility of water.

$$\begin{cases} C_{\mathrm{w,l}}^{\mathrm{CL}} = \frac{\rho_{\mathrm{w,l}}^{\mathrm{CL}}}{M_{\mathrm{w}}} \\ C_{\mathrm{w,l}}^{0} = \frac{\rho_{\mathrm{w,l}}^{0}}{M_{\mathrm{w}}} \end{cases} \quad (3.19)$$

Current density at the CL in liquid water surrounding bubbles:

$$i_{ls} = i^0(T)\frac{\left(\frac{C_{\mathrm{w,l}}^{\mathrm{CL}}}{C_{\mathrm{w,l}}^0}\right)^{a_t}}{\left(\frac{C_{\mathrm{O,dis}}^{\mathrm{CL},2}}{C_{\mathrm{O,dis}}^0}\right)^{0.5a_t}}\exp\left(\frac{za_tF\Delta E_l}{RT}\right) \quad (3.20)$$

Both $C_{\mathrm{O,dis}}^{\mathrm{CL},1}$ and $C_{\mathrm{O,dis}}^{\mathrm{CL},2}$ refer to the dissolved oxygen concentration in water. Still, the $C_{\mathrm{O,dis}}^{\mathrm{CL},1}$ refers specifically to the high dissolved oxygen concentration not affected by boiling, and the $C_{\mathrm{O,dis}}^{\mathrm{CL},2}$ refers to the low dissolved oxygen concentration under the boiling effect. Under the boiling condition, the dissolved oxygen concentration around the bubble plummeted from $C_{\mathrm{O,dis}}^{\mathrm{CL},1}$ to $C_{\mathrm{O,dis}}^{\mathrm{CL},2}$, as shown in Fig. 3.2e.

3.2.2 Dissolved oxygen transfer in water

The dissolved oxygen concentration in the water facing the CL is important, which

significantly impacts the OER current density component, i_{ls} and i_{l}, as shown in Fig. 3.2e. The dissolved oxygen transfer through the PTL with a molar flux, $Q_{O,dis}$, is driven by diffusion and convection [17, 22]. The transfer equation can be simplified to the one-dimensional model along the direction of the PTL thickness, y.

$$Q_{O,dis} = -D_{O,dis}\frac{d}{dy}C_{O,dis} + v_{w,l}C_{O,dis} \quad (3.21)$$

where $D_{O,dis}$ and $C_{O,dis}$ is the diffusion coefficient and concentration of dissolved oxygen in water, respectively, and $v_{w,l}$ is the liquid water velocity.

Integrating Eq. (3.21) with the dissolved oxygen concentration at the PUS, $C_{O,dis}^{PUS}$, yields the dissolved oxygen concentration at the CL.

$$C_{O,dis}^{CL} = C_{O,dis}^{PUS}\exp\left(\frac{\delta v_{w,l}}{D_{O,dis}}\right) + \frac{Q_{O,dis}}{v_{w,l}}\left[1 - \exp\left(\frac{\delta v_{w,l}}{D_{O,dis}}\right)\right] \quad (3.22)$$

It is noted that the dissolved oxygen concentration at the CL, $C_{O,dis}^{CL}$, in the LHS of Eq. (3.22) represents $C_{O,dis}^{CL,1}$ and $C_{O,dis}^{CL,2}$ in Eq. (3.16) and (3.20), respectively. Eq. (3.22) can determine both $C_{O,dis}^{CL,1}$ and $C_{O,dis}^{CL,2}$. Because the liquid water flowing on PTL removes the dissolved oxygen timely, the dissolved oxygen concentration at the PUS is close to zero. If assuming $C_{O,dis}^{PUS}$ zero, the dissolved oxygen concentration at the CL is determined in Eq. (3.23).

$$C_{O,dis}^{CL} = \frac{Q_{O,dis}}{v_{w,l}}\left[1 - \exp\left(\frac{\delta v_{w,l}}{D_{O,dis}}\right)\right] \quad (3.23)$$

, and the molar flux of the dissolved oxygen, $Q_{O,dis}$, is,

$$Q_{O,dis} = \frac{C_{O,dis}^{CL} v_{w,l}}{1-\exp\left(\frac{\delta v_{w,l}}{D_{O,dis}}\right)} \quad (3.24)$$

Adding the molar flux of gaseous oxygen, $Q_{O,g}$, to $Q_{O,dis}$ yields the total molar flux of the produced oxygen, Q_{O}.

$$Q_{O} = Q_{O,g} + Q_{O,dis} \quad (3.25)$$

Subsequently, several relative values are introduced to effectively judge the molar flux variation. The relative molar flux of the gaseous oxygen is defined to measure the proportion of gaseous oxygen to the total oxygen molar flux,

$$\gamma = \frac{Q_{O,g}}{Q_{O}} \quad (3.26)$$

Treated in this way, the dimensionless flux is not affected by the changable current density, and the boiling-enhanced oxygen transfer can be highlighted.

Moreover, the dissolved oxygen concentration at a standard condition (25 °C,

0.1013MPa) as a reference defines the dimensionless concentration of dissolved oxygen at the CL.

$$\lambda = \frac{C_{\mathrm{O,dis}}^{\mathrm{CL}}}{C_{\mathrm{O,dis}}^{0}} \quad (3.27)$$

The transfer resistance of the dissolved oxygen through PTL is worthwhile when PTL thickness is discussed. It can be derived just from dividing the concentration difference of the dissolved oxygen through the PTL by the molar flux of the dissolved oxygen.

$$R_{\mathrm{O,dis}} = \frac{C_{\mathrm{O,dis}}^{\mathrm{CL}} - C_{\mathrm{O,dis}}^{\mathrm{PUS}}}{Q_{\mathrm{O,dis}}} = \frac{C_{\mathrm{O,dis}}^{\mathrm{CL}}}{Q_{\mathrm{O,dis}}} \quad (3.28)$$

It is noted that the concentration of the dissolved oxygen at PUS is assumed to be zero. Finally, the relative flux and dimensionless concentration of dissolved oxygen just above defined yield a dimensionless transfer resistance of the dissolved oxygen after substituting Eq.(3.26) and (3.27) into Eq.(3.28).

$$\varsigma = \frac{R_{\mathrm{O,dis}}}{R_{\mathrm{O,dis}}^{0}} = \frac{\frac{C_{\mathrm{O,dis}}^{\mathrm{CL}}}{Q_{\mathrm{O,dis}}}}{\frac{C_{\mathrm{O,dis}}^{0}}{Q_{\mathrm{O}}}} = \frac{\lambda}{1-\gamma} \quad (3.29)$$

3.2.3 Liquid/gas flow in the PTL

As introduced in chapter 3.2.2, dissolved oxygen transfers in liquid water by convection and diffusion, while the gaseous oxygen and water vapor are drained through bubbles, as schematically plotted in Fig. 3.2b. The bubble pressure consists of the partial pressures of the gaseous oxygen and water vapor. In PTL, liquid water and the bubbles flow in opposite directions. The following formulates the balance equations of molar flux and momentum in liquid and gas phases to analyze the liquid/gas transfer. In addition, the boundary conditions imposed on the balance equations and the water vaporization rate are also introduced below.

Molar flux

A dimensionless molar flux for supplied water and produced oxygen is specified here. The advantage of dimensionless treatment of molar flux is to exclude the interference of current density on molar flux variation. The positive flow direction of water in the PTL is specified from the PUS facing bulk water to the CL/PTL interface. Because water needs to be

supplied to the CL for water electrolysis, the net molar flux of the supplied water is simply estimated with Faraday's law, as to be $Q_{\mathrm{w}} = \frac{i}{2F}$. The net molar flux of the supplied water includes liquid water and water vapor. According to the definition of the dimensionless flux above indicated as $q = \frac{Q}{i/F}$, the net molar flux of the supplied water has a dimensionless value of $\frac{1}{2}$, as follows.

$$q_{\mathrm{w}} = q_{\mathrm{w,l}} + q_{\mathrm{w,g}} = \frac{1}{2} \quad (3.30)$$

where $q_{\mathrm{w,l}}$ and $q_{\mathrm{w,g}}$ are the dimensionless fluxes of the supplied liquid water and water vapor, respectively. It is noted that, in practice, electrolyzed water from PUS to CL can be supplied in the liquid phase, and thus the liquid water flux $q_{\mathrm{w,l}}$ tends to take a positive value. Whereas the water vapor in the oxygen bubble is produced at the CL by evaporation or by boiling, the water vapor produced drains from CL to PUS, resulting in the water vapor molar flux, $q_{\mathrm{w,g}}$, becomes a negative value.

The dimensionless flux of produced oxygen can be expressed similarly. Faraday's law suggests the molar flux of produced oxygen to be $Q_{\mathrm{O}} = -\frac{i}{4F}$. Thus, the sum of the dimensionless fluxes of the produced gaseous and dissolved oxygen becomes $-\frac{1}{4}$, as follows.

$$q_{\mathrm{O}} = q_{\mathrm{O,g}} + q_{\mathrm{O,dis}} = -\frac{1}{4} \quad (3.31)$$

The dimensionless fluxes of oxygen are defined as $q_{\mathrm{O,dis}} = \frac{Q_{\mathrm{O,dis}}}{i/F}$, $q_{\mathrm{O,g}} = \frac{Q_{\mathrm{O,g}}}{i/F}$, and $q_{\mathrm{O}} = \frac{Q_{\mathrm{O}}}{i/F}$, where $q_{\mathrm{O,dis}}$, $q_{\mathrm{O,g}}$, q_{O} is the dimensionless flux of dissolved, gaseous and total oxygen, respectively.

The partial pressure of gaseous oxygen in the bubbles is related to the water vapor molar flux. Here, the conservation relationship between the molar flux of liquid water and water vapor is introduced. Because the water vapor flows out of the PTL continuously with oxygen, the partial pressure of the water vapor in the bubble is in a non-equilibrium state. The partial pressure of water vapor is determined by its molar flux. The τ in Eq. (3.32) is the ratio of water vapor molar flux to the total molar flux of the mixed gas in the bubbles [20]. It is also the relative pressure of water vapor, which is the ratio of water vapor partial pressure to the bubble pressure.

$$\tau = \frac{q_{\mathrm{w,g}}}{q_{\mathrm{w,g}} + q_{\mathrm{O,g}}} = \frac{P_{\mathrm{w,g}}}{P_{\mathrm{g}}} \quad (3.32)$$

Thus, the dimensionless flux between water vapor and gaseous oxygen are related in Eq.

(3.33), derived from Eq. (3.32).

$$q_{\mathrm{w,g}} = \frac{\tau q_{\mathrm{O,g}}}{1-\tau} \quad (3.33)$$

Eq. (3.34) gives the dimensionless flux of the mixed gas composed of gaseous oxygen and water vapor.

$$q_{\mathrm{g}} = q_{\mathrm{O,g}} + q_{\mathrm{w,g}} = \frac{q_{\mathrm{O,g}}}{1-\tau} \quad (3.34)$$

Eq. (3.35) expresses the dimensionless flux of the liquid water.

$$q_{\mathrm{w,l}} = \frac{1}{2} - q_{\mathrm{w,g}} \quad (3.35)$$

The dimensionless flux of the liquid water, and mixed gas holds the total dimensionless flux, q, in Eq. (3.36), [23]. The q will be a critical intermediate parameter when substituting the flux equation into momentum equation.

$$q = q_{\mathrm{w,l}} + q_{\mathrm{g}} = \bar{c}_{\mathrm{w,l}} v_{\mathrm{w,l}} + \bar{c}_{\mathrm{g}} v_{\mathrm{g}} \quad (3.36)$$

where $\bar{c}_{\mathrm{w,l}}$ represents the intermediate parameter of liquid water concentration, which is $\bar{c}_{\mathrm{w,l}} = \frac{C_{\mathrm{w,l}}}{i/F}$, and $\bar{c}_{\mathrm{g}}$ is the intermediate parameter of gas concentration, which is $\bar{c}_{\mathrm{g}} = \frac{C_{\mathrm{g}}}{i/F}$.

Momentum balance

In order to determine the dimensionless fluxes of liquid water, water vapor, dissolved oxygen and gaseous oxygen, additional momentum equations need to be supplemented, such as Eq.s (3.37) and (3.38) [24]. In Eq. (3.37), the pressure gradient of liquid water in the PTL creates the water velocity, $v_{\mathrm{w,l}}$. Likewise, the gas velocity, v_{g}, in the PTL is formed by the gas pressure gradient.

$$\frac{\mathrm{d}P_{\mathrm{w,l}}}{\mathrm{d}y} = -\frac{\mu_{\mathrm{w,l}}}{K_{\mathrm{w,l}}} v_{\mathrm{w,l}} = \psi_{\mathrm{w,l}} v_{\mathrm{w,l}} \quad (3.37)$$

$$\frac{\mathrm{d}P_{\mathrm{g}}}{\mathrm{d}y} = -\frac{\mu_{\mathrm{g}}}{K_{\mathrm{g}}} v_{\mathrm{g}} = \psi_{\mathrm{g}} v_{\mathrm{g}} \quad (3.38)$$

where $\mu_{\mathrm{w,l}}$ and μ_{g} are the dynamic viscosity of liquid water and mixed gas. In Eq. (3.37), the expression for $-\frac{\mu_{\mathrm{w,l}}}{K_{\mathrm{w,l}}}$ is replaced by $\psi_{\mathrm{w,l}}$ as a simplified expression for the subsequent derivation of molar flux. Eq. (3.38) also performs the same simplification processing as Eq. (3.37), such as ψ_{g}. In Eq.s (3.37) and (3.38), K_{wl} and K_{g} are the permeabilities of the liquid water and mixed gas in the PTL, respectively. The two permeabilities are related to gas saturation, S_{g}, as shown in Eqs. (3.39) and (3.40), [25]. The cubic index of the permeability coefficient is a usual value for liquid and gas phases [24,25].

$$K_{w,l} = KK_{rl} = K(1 - S_g)^3 \quad (3.39)$$

$$K_g = KK_{rg} = KS_g^{\,3} \quad (3.40)$$

Capillary pressure, P_c, between the liquid water pressure and bubbles gas pressure can be obtained in Eq. (3.41) after Eq. (3.38) subtracting Eq. (3.37).

$$\frac{dP_g}{dy} - \frac{dP_{w,l}}{dy} = \frac{dP_c}{dy} = \psi_g v_g - \psi_{w,l} v_{w,l} \quad (3.41)$$

Combine dimensionless mass flux and momentum equation

After combining Eq.s (3.36) and (3.41), the dimensionless mass fluxes of the mixed gas and liquid water are obtained in Eq.s (3.42) and (3.43).

$$q_g = \frac{c_g \psi_{w,l}}{c_{w,l}\psi_g + c_g \psi_{w,l}} q + \frac{c_{w,l} c_g}{c_{w,l}\psi_g + c_g \psi_{w,l}} \frac{dP_c}{dx} \quad (3.42)$$

$$q_{w,l} = \frac{c_{w,l} \psi_g}{c_{w,l}\psi_g + c_g \psi_{w,l}} q - \frac{c_{w,l} c_g}{c_{w,l}\psi_g + c_g \psi_{w,l}} \frac{dP_c}{dx} \quad (3.43)$$

Additional capillary pressure expressions must be supplemented to solve Eq.s (3.42) and (3.43). The capillary pressure is expressed in Eq. (3.44) [25] with the Leverett function, $F_l(S_g)$, in Eq. (3.45). In Eq. (3.44), the σ is the surface tension of liquid water, and the θ_c is the contact angel of PTL, and ε is the PTL porosity.

$$P_c = F_l(S_g)\sigma\cos(\theta_c)\sqrt{(\frac{\varepsilon}{K})} \quad (3.44)$$

$$F_l(S_g) = 1.417S_g - 2.12S_g^{\,2} + 1.263S_g^{\,3} \quad (3.45)$$

where the PTL permeability, *K*, is expressed in Eq. (3.46) [24].

$$K = \frac{d^2\varepsilon^3}{180(1-\varepsilon)^2} \quad (3.46)$$

In Eq. (3.46), *d* is the average pore diameter of the PTL..

Finally, the gas saturation can be determined after combining the dimensionless mass flux and momentum equations. Denoting $\frac{c_g}{c_l} = \beta_c$ and $\frac{\mu_g}{\mu_l} = \beta_\mu$, the equation $\frac{\psi_g}{\psi_l} = \frac{\mu_g}{K_g}\frac{K_l}{\mu_l} = \beta_\mu \frac{(1-S_g)^3}{S_g^{\,3}}$ is derived. Substituting Eq. (3.44) into Eq. (3.42), the dimensionless flux of the mixed gas is given in Eq. (3.47). So far, the relationship between dimensionless flux and gas saturation is obtained in Eq. (3.47), which is the core gas-liquid transfer equation in the model.

$$q_g = \frac{\beta_c S_g^3}{\beta_\mu(1-S_g)^3 + \beta_c S_g^3} q - \frac{c_g S_g^3 (1-S_g)^3}{\beta_\mu(1-S_g)^3 + \beta_c S_g^3} \frac{\sigma\cos(\theta_c)\sqrt{\varepsilon K}}{\mu_l}(1.417 - 4.24S_g + 3.789S_g^2)\frac{dS_g}{dx}$$

(3.47)

Gas saturation at the PUS

The saturation at the PUS provides the boundary condition for solving the gas-liquid transfer equation. If the bubble capillary pressure at the PUS is known, the gas saturation at the PUS can be determined according to Eq.s (3.44) and (3.45). The bubbles keep growing before detaching from the PUS. As Fig. 3.4, if the drag force, F_u, by flowing water exceeds the self-adhesion force, F_σ, that functions on the bubbles, the bubbles detach periodically [26].

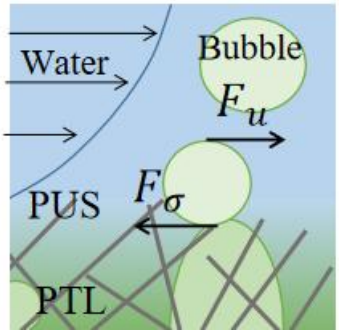

Fig. 3.4 Detachment of bubbles at the PUS.

Eq. (3.48) provides the detachment radius, r_{det}. This equation comes from force balance, $F_\sigma = F_u$, on the bubble between attachment force pulled by PTL surface, and drag force pushed by convection flow [26].

$$r_{\mathrm{det}} = \sqrt{\frac{l_s d\,\sigma \sin\theta_c}{36\mu_l v_0}} \quad (3.48)$$

where l_s is the characteristic length of water flowing through PUS, which is the diameter of PUS taken from the experimental WE, 10 mm. The μ_l and v_0 are the dynamic viscosity of liquid water and its average velocity flowing above the PUS (1.05 $m \cdot s^{-1}$).

The detachment radius of the bubble in Eq. (3.48) can determine its detachment time. The relation between detachment radius and time is derived from the gaseous oxygen molar flux and gas state equations. The gas state equation in the bubble is $P_g V_g = m_g RT$. The bubble gas pressure is related to liquid water pressure, as $\frac{2\sigma}{r_{\mathrm{det}}} = P_g - P_{w,l}$. The bubbles attached to the PTL are approximately spherical and have a volume of $V_g = \frac{4\pi r_{\mathrm{det}}^3}{3}$. In order to obtain the bubble volume, it is necessary to know the gas molar number in the bubble, $m_g = m_0 \frac{P_g}{P_{0,g}}$, at the detachment time, where the molar number of gaseous oxygen is $m_0 = \frac{i}{4F}\frac{\bar{A}_0 t_{\mathrm{det}}}{N_{\mathrm{bub}}}$.

The $\overline{A}_0$ is the unit geometric area on the PUS, while N_{bub} is the bubble number over a unit geometric area. After combining these equations, the bubble detachment time has a relation with the detachment radius as

$$t_{det} = \frac{16\pi F N_{bub} P_{0,g}\left(P_{w,l} {r_{det}}^3 + 2\sigma {r_{det}}^2\right)}{3RTiP_g\overline{A}_0} \quad (3.49)$$

The gas pressure changes in a growing bubble since the increasing bubble radius reduces gas pressure according to Young–Laplace equation, $\frac{2\sigma}{r_{bub}} = P_g - P_{w,l}$. The average pressure of the bubble within one growth period is expressed in Eq. (3.50),

$$P_g^{ave} = \frac{\sum_{k=1}^{k=100} P_g\left(\frac{kt_{det}}{100}\right)}{100} \quad (3.50)$$

In order to obtain the average gas pressure of the bubbles attached to the PTL surface during the growth process, the lifetime, t_{det}, of the bubble on the PTL is divided into 100 equal parts. The k increases from 1 to 100 in turn, and $\frac{kt_{det}}{100}$ represents the incremental moments in turn. Substitute time, $\frac{kt_{det}}{100}$, into Eq. (3.49) to replace t_{det}, then the bubble radius, r_{bub}, at this moment will be determined. Then, substituting r_{bub} into Young–Laplace equation, the bubble pressure, $P_g(\frac{kt_{det}}{100})$, at $\frac{kt_{det}}{100}$ will be obtained. The average pressure, P_g^{ave}, can be obtained by averaging the bubble pressures at these 100 moments. Next, the capillary pressure at PUS, P_c^{PUS}, can be obtained by equation $P_c^{PUS} = P_g^{ave} - P_{w,l}$. Finally, the gas saturation at the PUS can be determined by substituting P_c^{PUS} into Eq. (3.44).

Vaporization rate of evaporation and boiling

The water vapor molar flux described below plays an important role in the Nernst loss of the OER. The Nernst loss is related to the partial pressure of gaseous oxygen in the bubbles. According to Eq. (3.32), the increased molar flux of water vapor, $q_{w,g}$, in the PTL increases the partial pressure of the water vapor, $P_{w,g}$, decreasing the partial pressure of the gaseous oxygen in the bubbles. The different water vaporization rates below and above the boiling-point temperature is a critical issues because the water vapor under boiling reduces the overpotential of the OER, as shown in chapter 2.3.4. Below the boiling temperature, liquid water is rather slowly evaporated to water vapor. The molar flux at evaporation with a unit of $mol \cdot m^{-2} \cdot s^{-1}$ is expressed in Eq. (3.51),

$$Q_{w,g} = -\frac{J_{w,g} A_{bub}^{to}}{M_w}, T \leq 100\ ^\circ C \quad (3.51).$$

$A_{\text{bub}}^{\text{to}}$ is a relative area, which is explained below. M_{w} is the molar mass of water, which is 0.018 kg·mol^{-1}. $J_{\text{w,g}}$ is the water evaporation rate with a unit of kg·m^{-2}·s^{-1}, as shown in Eq. (3.52) [27].

$$J_{\text{w,g}} = -L^{\text{s}} \frac{R}{M_{\text{w}}} \ln\left(\frac{P_{\text{w,g}}}{P_{\text{sat}}}\right) \quad (3.52)$$

In Eq. (3.52), L^{s} is the vaporization rate, which is listed in Table 3.3, and P_{sat} is the saturated vapor pressure with a unit of Pa given by Eq. (3.53) [27]. The temperature, T, in Eq. (3.53) has a unit of K.

$$P_{\text{sat}} = 10^{10.08354 - \frac{1663.125}{T - 45.622}} \quad (3.53)$$

The $A_{\text{bub}}^{\text{to}}$ in Eq. (3.51) is the relative evaporation area over a unit geometric area ($\overline{A}_0$), which is a crucial parameter in determining the molar flux of evaporation. The $A_{\text{bub}}^{\text{to}}$ is the relative area, where the cylindrical bubbles' side wall, as shown in Fig. 3.5, is divided by a unit geometric area ($\overline{A}_0$). The $A_{\text{bub}}^{\text{to}}$ is a dimensionless value derived with the following procedure.

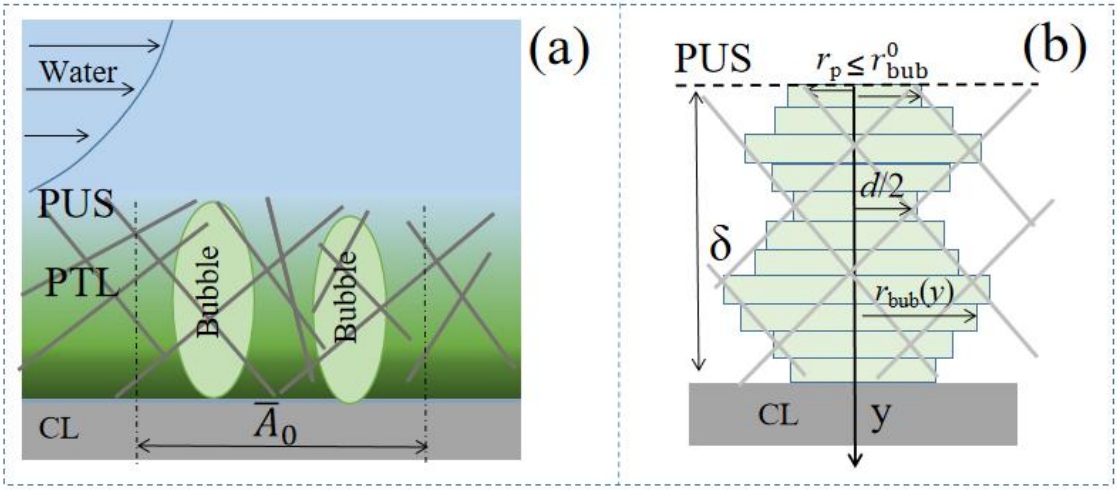

Fig. 3.5 Schematic of evaporation area. a. the relative evaporation area, $A_{\text{bub}}^{\text{to}}$, which corresponds to the side-wall area of bubbles through PTL (light green colored) on a unit area, b. the discretized side-wall area of a bubble.

The gas phase occupies an area of $\overline{A}_0 S_{\text{g}}^0$, where S_{g}^0 is the gas saturation at the PUS. Assuming that the bubble radius at the PUS is r_{bub}^0 as Fig. 3.5b, then the number of bubbles, N_{bub}, attached to the PUS over the unit geometric area is

$$N_{\text{bub}} = \frac{\overline{A}_0 S_{\text{g}}^0}{\pi r_{\text{bub}}^{0\ 2}} \quad (3.54)$$

The cross-section of the bubbles at each discrete layer of the PTL is assumed to be circular with a radius, $r_{bub}(y)$, as Fig. 3.5b. Eq. (3.55) introduces the bubble radius at any discrete location.

$$r_{\mathrm{bub}}(y) = \sqrt{\frac{\overline{A}_0 S_{\mathrm{g}}(y)}{\pi N_{\mathrm{bub}}}} \quad (3.55)$$

Eq. (3.56) gives the side-wall area of a cylindrical bubble, $\overline{A}_{\mathrm{bub}}$, by the area integral of each discrete layer as Fig. 3.5b. The $\overline{A}_{\mathrm{bub}}$ has a unit of cm^2.

$$\overline{A}_{\mathrm{bub}} = \int_0^{\delta} 2\pi r_{\mathrm{bub}}(y)\mathrm{d}y \quad (3.56)$$

As shown in Fig. 3.5a, the cylindrical bubble exists in a plurality. Thus, the relative evaporation area, $A_{\mathrm{bub}}^{\mathrm{to}}$, is the ratio of the total side-wall surface area for all bubbles in the PTL to a unit geometric area, $\overline{A}_0$.

$$A_{\mathrm{bub}}^{\mathrm{to}} = \frac{N_{\mathrm{bub}}\overline{A}_{\mathrm{bub}}}{\overline{A}_0} \quad (3.57)$$

Finally, Eq. (3.58) shows the total area by substituting Eqs. (3.54) and (3.56) into (3.57).

$$A_{\mathrm{bub}}^{\mathrm{to}} = \frac{2\sqrt{S_{\mathrm{g}}^0}}{r_{\mathrm{bub}}^0}\int_0^{\delta}\sqrt{S_{\mathrm{g}}(y)}\mathrm{d}y \quad (3.58)$$

Because the bubble radius at the PUS, r_{bub}^0, is equal to or greater than the average pore radius, $d/2$, of the PTL, the inequality, $A_{\mathrm{bub}}^{\mathrm{to}} \le \frac{2\sqrt{S_{\mathrm{g}}^0}}{d/2}\int_0^{\delta}\sqrt{S_{\mathrm{g}}(y)}\mathrm{d}y$, is established.

Under boiling, Eq. (3.59) expresses the molar flux of water vapor through the bubbles. Based on the maximum molar flux of water vapor produced by evaporation at the boiling temperature, boiling above the boiling temperature further increases the water vapor molar flux.

$$Q_{\mathrm{w,g}} = -\frac{J_{\mathrm{w,g}}A_{\mathrm{bub}}^{\mathrm{to}}}{M_{\mathrm{w}}} + Q_{\mathrm{w,g}}^{\mathrm{b}}, T > 100\ ^{\circ}\mathrm{C} \quad (3.59)$$

, where $Q_{\mathrm{w,g}}^{\mathrm{b}}$ is the water vapor molar flux by boiling, as shown in Eq. (3.60) [29].

$$Q_{\mathrm{w,g}}^{\mathrm{b}} = -\frac{\mu_{\mathrm{w,l}}}{M_{\mathrm{w}}}\left[\frac{g(\rho_{\mathrm{w,l}}-\rho_{\mathrm{w,g}})}{\sigma}\right]^{0.5}\left[\frac{(T-100)C_{\mathrm{pw,l}}}{C_{\mathrm{sf}}LPr}\right]^3 \quad (3.60)$$

where $Cp_{\mathrm{w,l}}$ is the heat capacity of liquid water, C_{sf} is the surface fluid combination coefficient, L is the latent heat of water vaporization, and Pr is the Prandtl number.

3.3 Result and discussions

Chapter 3.3 makes the following three discussions. The first one is dedicated to

comparing theoretical and experimental voltages on the OER. The comparison is carried out especially under boiling conditions, leading to verification for the model above developed. The second one is dedicated to exploring how boiling affects the dissolved oxygen concentration in the liquid phase surrounding bubbles and how boiling reduces the OER overpotential. Thirdly, it is indicated that the dissolved oxygen is almost drained from the bubbles, providing conditions for boiling to enhance OER performance.

3.3.1 Comparison of theoretical and experimental results

Validating the correctness of the model is crucial for theoretical analysis to clarify the effect of boiling on OER. The IrO_2 load in the model is 1.5 mg·cm^{-2}, as shown in Table 3.3. The electrochemical exchange current density in the model is 2.64×10^{-9} A·cm^{-2}, taken from the experimental results in chapter 2.3.1 to match the same condition between the model and experiment. Fig. 3.6 compares the theoretical and experimental overpotential of the OER formed at three WEs. The three WEs correspond to the specific structure in Fig. 2.1 of chapter 2. The WE1 has an exposed CL, and a 0.2-mm-thickness PTL covers the CL in WE2, while the WE3 has a CL, PTL, and CH. The overpotential, ΔE_l, is the difference between the OER potential, E, and the redox potential, $E_1^0(T)$, in the liquid water. It is noted that the redox potential, $E_1^0(T)$, in the liquid water is used for both experimental and theoretical OER even beyond boiling temperature.

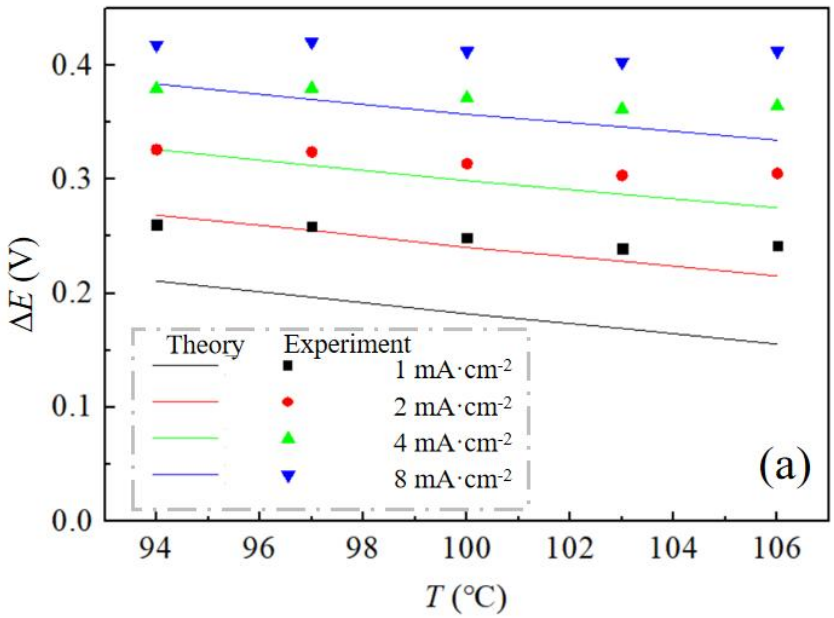

a. WE1(CL)

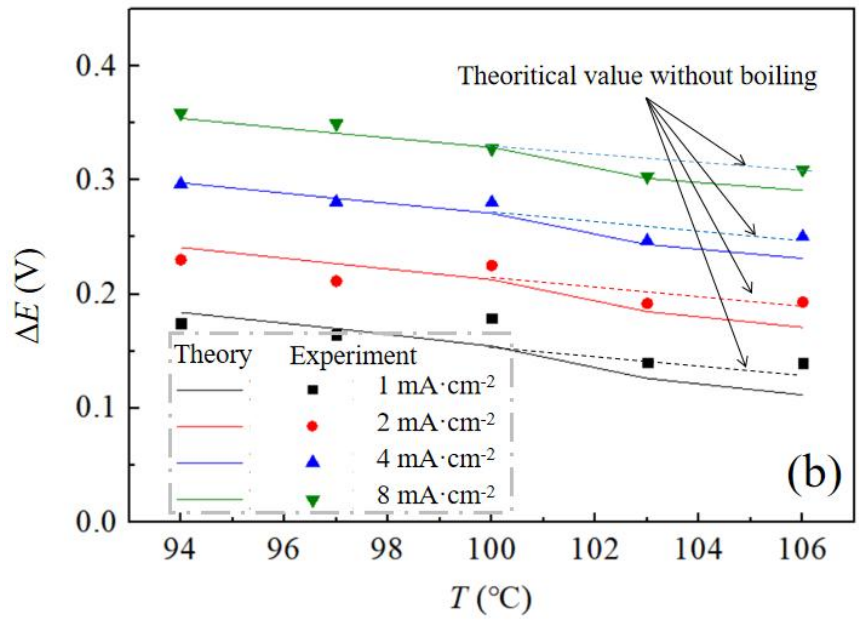

b. WE2(CL+PTL)

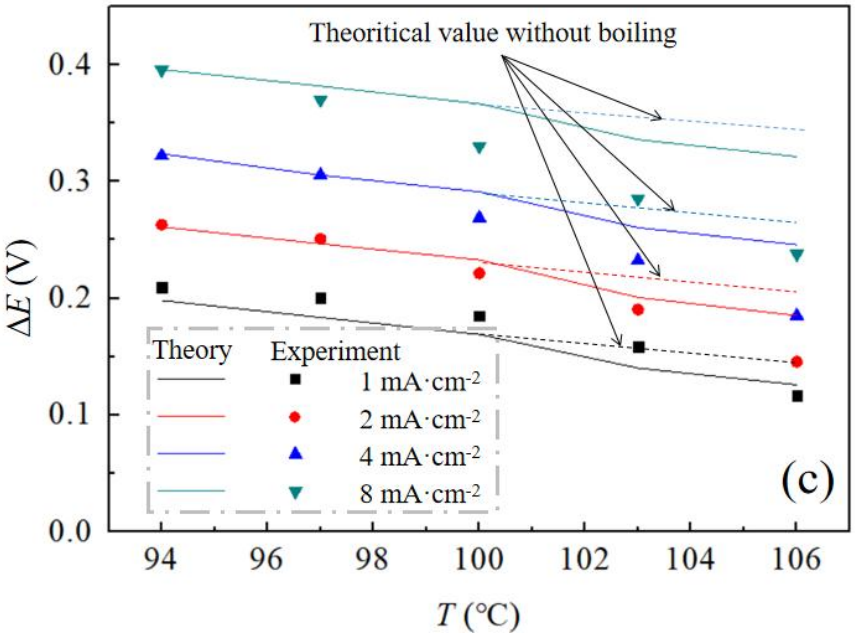

c. WE3(CL+PTL+CH)

Fig.3.6 Theoretical and experimental comparison of overpotential.

Fig. 3.6a compares the theoretical and experimental overpotentials of the WE1. Both theoretical and experimental overpotentials decrease linearly with temperature. Temperatures above 100 °C do not specifically reduce the theoretical and experimental overpotentials. The PTL did not cover the CL surface of WE1 in the experiment, and some dissolved oxygen can be discharged through a thin liquid water layer over the CL surface. The thickness of the

liquid water layer is about 10 μm [17], a thickness where the dissolved oxygen concentration changes drastically. Because the water layer is thin, some dissolved oxygen is more likely to be drained directly through the liquid water besides oxygen gas bubbles. Boiling cannot reduce the concentration of dissolved oxygen expelled directly through the liquid water. The experimental OER overpotentials are higher than the theoretical values at the four current densities (1, 2, 4, and 8 $mA \cdot cm^{-2}$). In the experiment, the flowing water might not timely remove the oxygen bubbles attached to the CL, resulting in a partial loss of active area. Although the theoretical overpotential cannot perfectly fit the experimental results, the model can reproduce the tendency that the overpotential of the WE1 is not significantly decreased by boiling.

For the WE2 in Fig. 3.6b, the experimental OER overpotential at every current density (1, 2, 4, and 8 $mA \cdot cm^{-2}$) shows its abrupt decrease at the boiling temperature. The theoretical overpotentials also agree with this tendency shown in the experiment. This agreement suggests acceptable reliability of the theoretical model. Both the experimental and theoretical overpotential show the same abrupt decrease of OER potential at boiling temperature. The abrupt decrease is approximately 25 mV between 100 °C and 103 °C for any current density condition (1, 2, 4, and 8 $mA \cdot cm^{-2}$). The question is whether this OER overpotential decrease at boiling temperature attributes to redox potential change or some overvoltage component change. The standard redox potentials in liquid water, $E_l^0(T)$, and water vapor, $E_g^0(T)$, are listed in Table 3.4. $E_g^0(T)$ is higher than $E_l^0(T)$ above boiling temperature. The redox potential difference between liquid water and water vapor, E_l^0- E_g^0, is only 2 mV at 103 °C, as shown in Table 3.4. Therefore, the standard redox potential change at boiling point decreases the OER overpotential to only 2 mV. This differs from the experimental result in that the OER potential decrease was 25 mV. Thus, the redox potential difference between the liquid and gas phases cannot explain the large OER potential decrease at the boiling point.

Table 3.4 The standard redox potential

T (°C)	E_l^0 (V)	E_g^0 (V)	E_l^0-E_g^0 (mV)
85	1.179	1.170	9
94	1.172	1.168	4

97	1.169	1.167	2
100	1.167	1.167	0
103	1.164	1.166	-2
106	1.162	1.165	-3

Among the three WEs, WE3 produced the largest oxygen transfer resistance because its CL is covered with a Ti mesh (thickness: 0.2 mm) and ribs (width: 0.5 mm). The PTL of WE3 is thickened to 1 mm in the model to approximate the oxygen transfer resistance formed by Ti mesh and ribs. In addition, the water in the channel of WE3 is slowly drained by self-propelled bubbles, and its velocity is related to the gas flow rate in the channel. In Fig. 3.6c, the experimental overpotential over 100 °C has a larger drop, which is close to 70 mV. In contrast, the theoretical results show a drop of 30 mV over 100 °C. Besides WE2, the theoretical model for the WE3 can also qualitatively reproduce the boiling effect to reduce the OER overpotential. However, the theoretical results cannot quantitatively reproduce and explain the overpotentials significantly reduced over 100 °C in the experiment, which will be a future research work.

In summary, for WE2 and WE3, the large OER overpotential decrease at the boiling point is possibly explained by a decrease of Nernst loss at the point. The following chapter clarifies how the Nernst loss significantly decreases at boiling point.

3.3.2 Oxygen transfer and electrochemical performance during boiling

This sub-section discusses how boiling changes the oxygen transfer, OER voltage, and current density based on the model shown in chapter 3.2. The OER temperature gradually increases from 94 to 106 °C, covering the unboiled and boiled temperature range. The current density increases from 0.001 to 1.024 $A \cdot cm^{-2}$ to analyze whether boiling reduces the OER overpotential at any current density. Additionally, the broad current density range predicts the tendency of how much boiling decreases the OER overpotential with current density. Fig. 3.7 shows the temperature and current density influence on important values at the PTL/CL interface:

–the dimensionless concentration of dissolved oxygen, λ

–the relative pressure of gaseous oxygen, 1-τ

–the relative molar flux of gaseous oxygen, γ

–gas saturation at CL, S_g^{CL}.

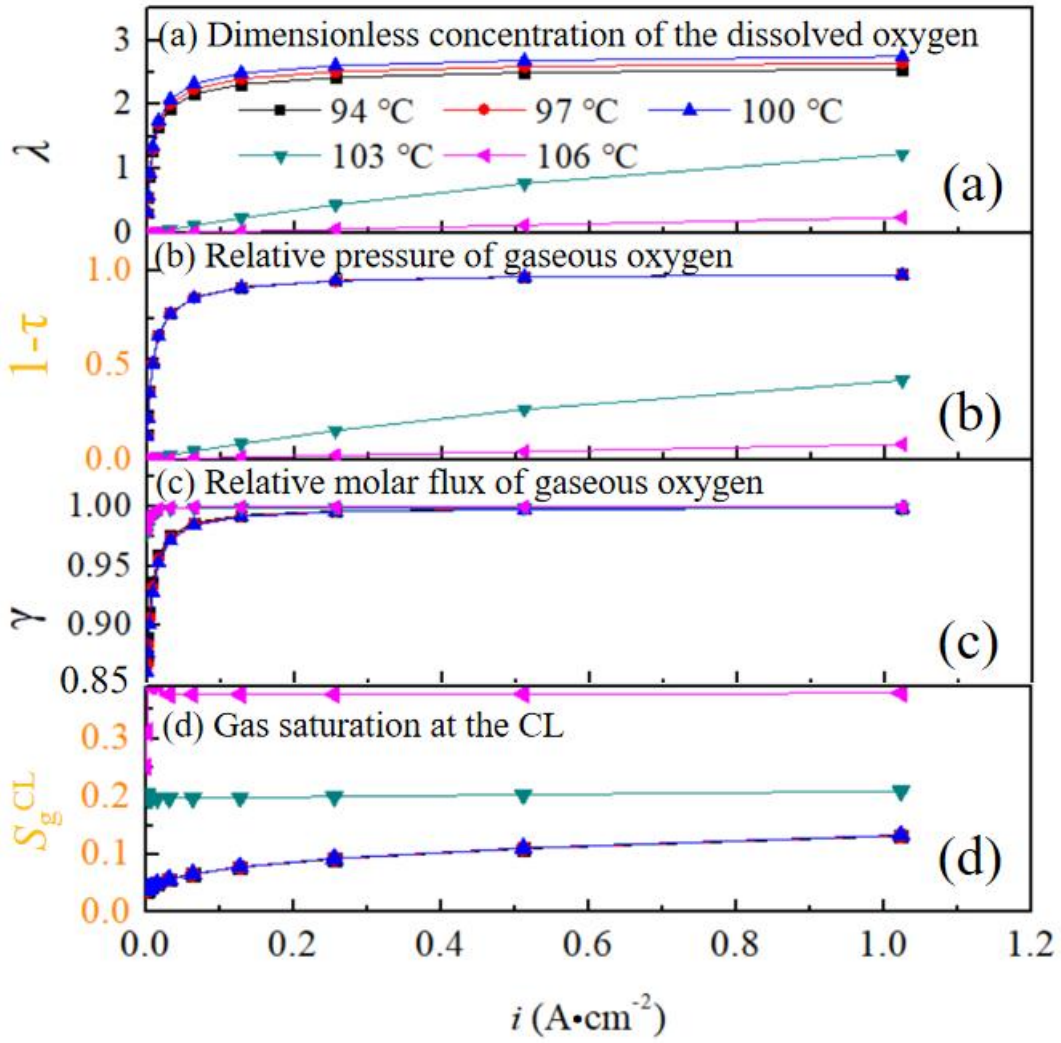

Fig. 3.7 Changes of basic mass transfer parameter. a. dimensionless concentration of the dissolved oxygen surrounding bubbles, λ; b. relative pressure of water vapor in bubbles, τ; and c. relative molar flux of gaseous oxygen, γ , d. gas saturation at the CL, S_g^{CL}

In Fig. 3.7a, below 100°C, the dimensionless concentration of dissolved oxygen at the CL surface increases with the current density and finally approaches 2.5, which is 2.5 times the standard dissolved oxygen concentration. The bubble pressure on the CL surface is about 0.1MPa. Because the partial pressure of gaseous oxygen at the CL cannot exceed the bubble pressure (0.1 MPa), the relative dissolved oxygen concentration approaches the limit of 2.5 according to Henry's Law when temperature approaches boiling point (100 °C). At each current density, the dimensionless concentration at 103 °C is significantly lower than that at

100 °C. Especially at 106°C, it is lower than 0.5 at 1.024 $A \cdot cm^{-2}$. Boiling is expected to reduce the OER overpotential by decreasing the oxygen concentration at the CL, according to Eq. (3.11). At 103°C and 106°C, the dimensionless concentration increases linearly with the current density. The higher current density increases the gaseous oxygen molar flux when the water vapor molar flux under boiling keeps constant at a specific overheating temperature. Therefore, more gaseous oxygen molar flux increases its partial pressure and the dimensionless concentration of dissolved oxygen.

The τ represents the relative pressure of water vapor in bubbles, while $1-\tau$ is the relative pressure of gaseous oxygen. The relative pressure of gaseous oxygen in Fig. 3.7b can determine the dimensionless concentration of dissolved oxygen in Fig. 3.7a. With increasing current density, more molar flux of gaseous oxygen makes its partial pressure higher in bubbles. Conversely, the increased water vapor molar flux by boiling increases the relative pressure of water vapor in the bubble, reducing the partial pressure of gaseous oxygen. At 106 °C, the relative pressure of gaseous oxygen is close to 0, resulting in the dimensionless concentration of dissolved oxygen surrounding bubbles close to 0, as shown in Fig.3.7a. Boiling can decrease the gaseous oxygen concentration in bubbles owing to the decrease in partial pressure of gaseous oxygen, which can reduce the OER overpotential in the bubbles.

Boiling increases the relative molar flux of gaseous oxygen. In Fig. 3.7c, the relative molar flux of gaseous oxygen increases more significantly at low current densities. At 0.001 $A \cdot cm^{-2}$, the relative molar flux of gaseous oxygen rises from 0.9 at unboiling to 0.99 at boiling. Because boiling causes low partial pressure of gaseous oxygen in the bubbles, more dissolved oxygen can be attracted into the bubbles, and the relative molar flux of gaseous oxygen increases. At large current densities, such as 1.024 $A \cdot cm^{-2}$, the relative molar flux of gaseous oxygen reaches 0.99 at unboiling. Over 100 °C, the relative molar flux of gaseous oxygen is approached 1. However, this increase of molar flux less than 0.01 is difficult to observe in Fig. 3.7c. The relative molar flux of gaseous oxygen is close to 1, which means that the relative molar flux of dissolved oxygen is close to 0. Boiling cannot reduce the concentration of dissolved oxygen directly discharged from the PTL. Therefore, only very little dissolved oxygen at the CL cannot be reduced concentration by boiling. In other words, boiling can reduce the concentration of most oxygen at the CL, thereby reducing the Nernst loss of the OER.

Boiling can significantly alter the gas saturation at the CL. Fig. 3.7d shows the gas

saturation at the CL as a temperature and current density function. Gas saturation increases with current density at 94-100 °C. Because the higher current density increases the molar flux of gaseous oxygen, the gas saturation at the CL rises. At 1.024 $A \cdot cm^{-2}$, the gas saturation is 0.13, implying that liquid water covers 87% of the CL area. The gas saturation of CL rises to 0.2 at 103 °C and 0.38 at 106 °C. In Fig. 3.7b, at 106 °C, boiling reduces the relative pressure of gaseous oxygen to 0.05. According to Eq. (3.32), the molar flux of water vapor during boiling is about ten times greater than that of gaseous oxygen, significantly increasing the gas saturation at the CL.

Next, how boiling changes the OER potential, relative current density, and current contribution ratio is presented in Fig. 3.8. Fig. 3.8 is the calculation result based on the model shown in chapter 3.2.1. Each diagram in Fig. 3.8 has 5 trends, which indicate different temperature cases with a 3 °C increment. The temperature legend is only shown in Fig. 3.8a.

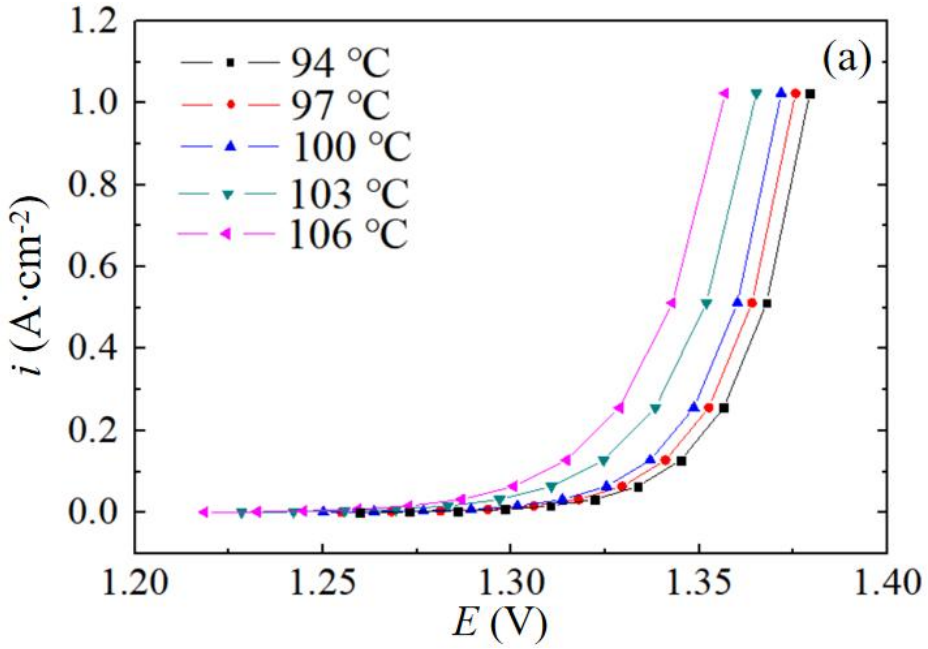

a. current density versus the OER potential

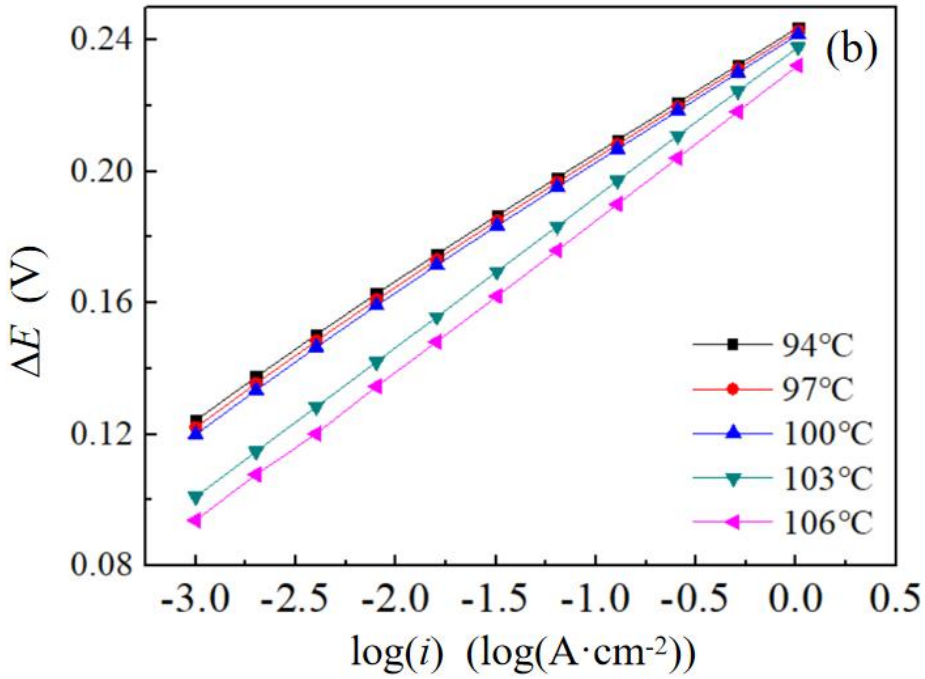

b. Tafel plot of OER

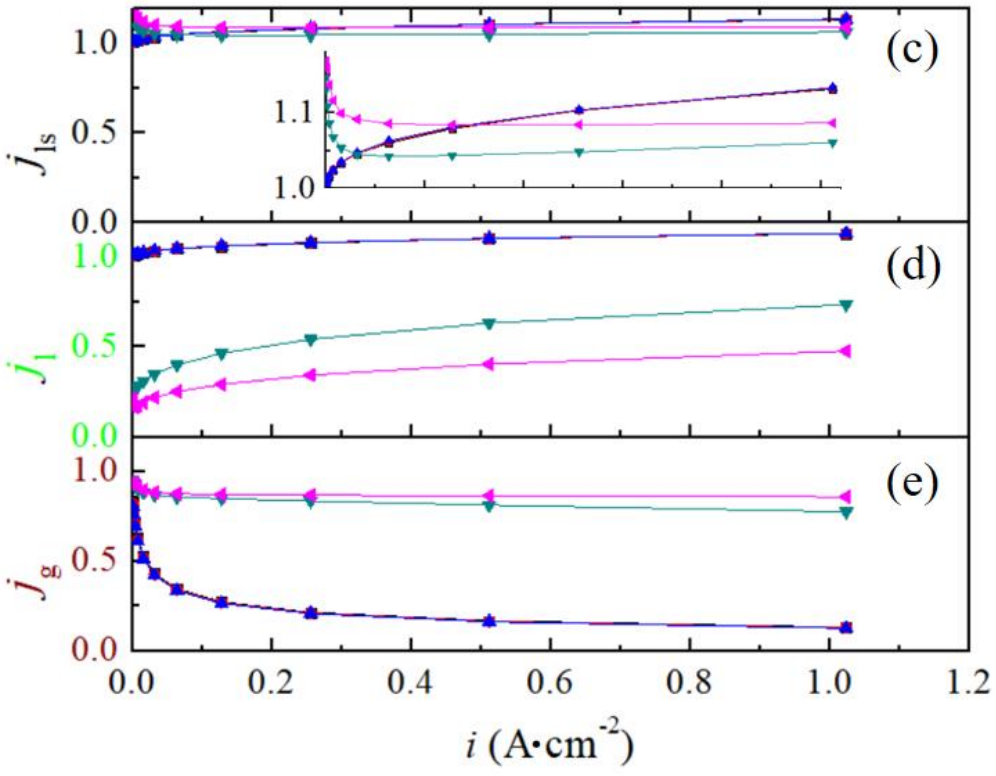

c-e. relative current density in liquid water surrounding, far from and in bubbles.

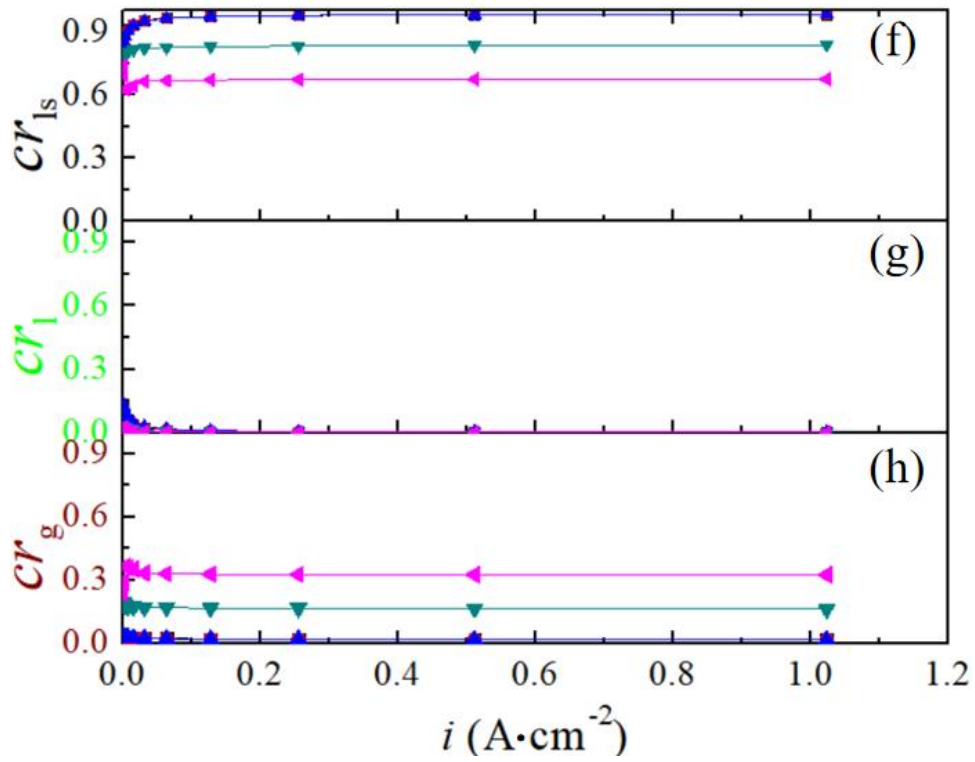

f-h. current contribution ratio of the CL in liquid water surrounding, far from and in bubbles.

Fig. 3.8 Boiling effect on the OER performance.

Fig. 3.8a is the voltammetry curve (OER potential and current density plot) with reference to the standard hydrogen electrode. Increasing temperature shifts towards lower potentials. The potential drop per increase of 3 °C is particularly enlarged when the temperature is over 100 °C, compared to that below 100 °C. This result surely implies that boiling can contribute to reducing OER potential.

Converting the voltammetry curve to a Tafel plot can predict how much boiling reduces the OER overpotential at high current densities. The OER overpotential has a Tafel relationship with the logarithmic current density, as shown in Fig. 3.8b. The overpotential trend significantly shifts when the temperature increases from 100 °C to 103 °C. The difference of overpotential between 100 °C and 103 °C decreases with increasing current density. Because the gaseous oxygen molar flux increases with current density, the partial pressure of gaseous oxygen and dissolved oxygen concentration at 103 °C is gradually close to that at 100 °C (Fig. 3.7a and 3.7b). Because of the increased oxygen concentration, the overpotential at 103 °C gradually approaches that at 100 °C. The advantage that boiling significantly reduces the OER potential gradually disappearing in the high current density region. To highlight the boilinng effect at high current density, the boiling temperature should

be higher, such as 106 °C or more. The significant reduction in the OER overpotential by boiling, as shown in Fig. 3.8a and 3.8b, attributes to the mechanism, where boiling reduces the oxygen partial pressure in bubbles and the dissolved oxygen concentration surrounding bubbles, as depicted in Fig. 3.7b and 3.7a. The partial pressure of gaseous oxygen and dissolved oxygen concentration at 106 °C is 1/10 lower than that at 100°C, resulting in a significant decrease in the OER overpotential, according to Eq. (3.11).

Boiling also largely influences the current density in bubbles and liquid water. As introduced in Fig. 3.2e, the current density component at the CL is three (i_{ls}, i_l and i_g). In addition, each current density component has its relative value (j_{ls}, j_l, and j_g). The j_{ls}, as defined in Eq. (3.3), is the relative current density in liquid water surrounding the bubbles. The j_l, as defined in Eq. (3.1), is the relative current density in liquid water far away from the bubbles. The j_g, as defined in Eq. (3.2), is the relative current density in the bubbles.

The j_{ls}, the relative current density in liquid water surrounding the bubbles, is plotted in Fig. 3.8c. The j_{ls} below 100 °C is always greater than 1 and continues to increase with the applied current density. This means that the current density in the liquid water surrounding the bubble is greater than the average current density applied. The reason is as follows. Below 100 °C and with increasing current density, the relative current density in the bubbles, j_g, is close to 0.2 (Fig. 3.8e), which means that the current density in the bubbles is 20% of the average current density, i. Therefore, the current density in liquid water needs to exceed the average current density to satisfy the applied current load. Then, the j_{ls} in liquid water surrounding bubbles is increased to take on more current load. Over boiling point, the j_{ls} hardly changes with the applied current density, such as 1.05 at 103 °C and 1.09 at 106 °C. The water vapor molar flux under boiling is about tenfold that of the gaseous oxygen molar flux even at high current densities. As shown in Fig. 3.7d, at 106 °C, the gas saturation keeps at 0.38. Therefore, an increase in the gaseous oxygen molar flux hardly changes the partial pressures of water vapor and gaseous oxygen. This is why the j_{ls} in Fig. 3.8c remains constant during boiling with increasing the applied current density.

Fig. 3.8d introduces the relative current density, j_l, in liquid water away from bubbles. The j_l decreases from 1.1 to 0.5 (below average current density), when the CL temperature changes from 100 to 103 °C. During boiling, the partial pressure of gaseous oxygen and the concentration of dissolved oxygen surrounding bubbles plummet (Fig. 3.7b and 3.7a). However, the dissolved oxygen concentration far from bubbles cannot be reduced by boiling,

as depicted in Fig. 3.2e. Therefore, j_{ls} and j_g are higher than j_l, resulting in j_l below 1 at boiling. Also, with higher boiling temperatures, the partial pressure of gaseous oxygen and the concentration of dissolved oxygen surrounding the bubbles are lower, while the concentration of dissolved oxygen far from the bubbles keeps unchanged. Therefore, j_l is also lower than j_{ls} and j_g.

Fig. 3.8e describes the relative current density, j_g, in the bubbles. The j_g exceeds 0.8 over 103 °C while it is less than 0.2 below 100 °C. As boiling increases the molar flux of water vapor, the partial pressure of the water vapor in the bubbles also rises while the partial pressure of gaseous oxygen decreases. The activities of water vapor and gaseous oxygen are positively related to their partial pressures. Thus, under boiling, the water vapor activity increases and the gaseous oxygen activity decreases, increasing the j_g in the bubbles. The CL in the bubbles is activated by boiling and contributes to higher current density, resulting in the reduction in the OER overpotential.

The current contribution ratio can highlight the importance of a certain current density (i_{ls}, i_l or i_g). Fig. 3.8f-h shows the current contribution ratios (cr_{ls}, cr_l and cr_g), which correspond to i_{ls}, i_l and i_g as introduced in Fig. 3.2e. The cr_{ls}, as defined in Eq. (3.6), is a current contribution ratio, which is the one in liquid water surrounding the bubbles and plotted in Fig. 3.8f. The cr_l, as defined in Eq. (3.7), is a current contribution ratio, which is the one in liquid water far away from the bubbles and plotted in Fig. 3.8g. The cr_g , as defined in Eq. (3.5), is a current contribution ratio, which is the one in the bubbles and plotted in Fig. 3.8h. The difference between the relative current density (Fig. 3.8c, d, and e) and the current contribution ratio (Fig. 3.8f, g, and h) is practical or not. The current contribution ratio considers the effect scope of the current density component (i_{ls}, i_l and i_g) at the CL, which is determined by gas saturation and the relative molar flux of gaseous oxygen. It can be utilized to judge how much the current component contributes under a given activity of water and oxygen, which is more practical than relative current density.

As shown in Fig. 3.8f, the cr_{ls} (current contribution ratio in the water surrounding bubbles) has a rather significant role in loading current. The cr_{ls} below 100°C almost bears more than 95% of the current load due to the water coverage fraction of 0.9 (Fig.3.7d) and relative current density of more than 1 (Fig. 3.8c). The cr_{ls} above 100°C decreases, because the CL in the bubbles improves the j_g and shares some current load from the cr_{ls}.

Compared with the cr_{ls}, the role of the cr_l is not significant. As shown in Fig. 3.8g, the

cr_l is less than 1% due to the low relative flux of dissolved oxygen in liquid water away from the bubbles. As Fig. 3.7c, the relative flux of gaseous oxygen is more than 0.99, and the relative flux of dissolved oxygen is less than 0.01.

The cr_g (current contribution ratio under bubbles) is the second significant. As shown in Fig. 3.8h, the cr_g is increased to 0.3 when the temperature is 106 °C, because boiling increases gas coverage fraction (Fig.3.7d) and relative current density (Fig. 3.8e). During boiling, the CL in the bubbles is activated, sharing more current load from the CL in the water. Then, the OER overpotential in liquid water can be reduced.

3.3.3 Mass transfer of the OER without boiling

Chapter 3.3.2 clarifies that the significant OER overpotential drop by boiling is attributed to the reduction of oxygen activity at the CL. This section further discusses how the dissolved oxygen with high concentration formats at the CL. The high transfer resistance of dissolved oxygen is one factor in forming its high concentration. The PTL thickness varies from 0.01 mm to 1 mm to create a wide range of oxygen transfer resistance. For purely discussing the concentration of dissolved oxygen at the CL without boiling, the OER temperature is set at 85 °C, the usual operating temperature below the boiling point. As shown in Fig. 3.9, the relative molar flux of gaseous oxygen and transfer resistance of the dissolved oxygen increase with the PTL thickness and current density. In Fig. 3.9a, the relative molar flux of gaseous oxygen, γ, is significantly increased by the PTL thickness below 0.02 $A \cdot cm^{-2}$. The relative molar flux of gaseous oxygen through the 1-mm PTL approaches 1 below 0.001 $A \cdot cm^{-2}$, meaning that nearly all dissolved oxygen flows into the bubbles. With increasing the current density, the relative molar flux of the gaseous oxygen also approaches 1 for all the PTL thicknesses. The reasons are introduced as follows.

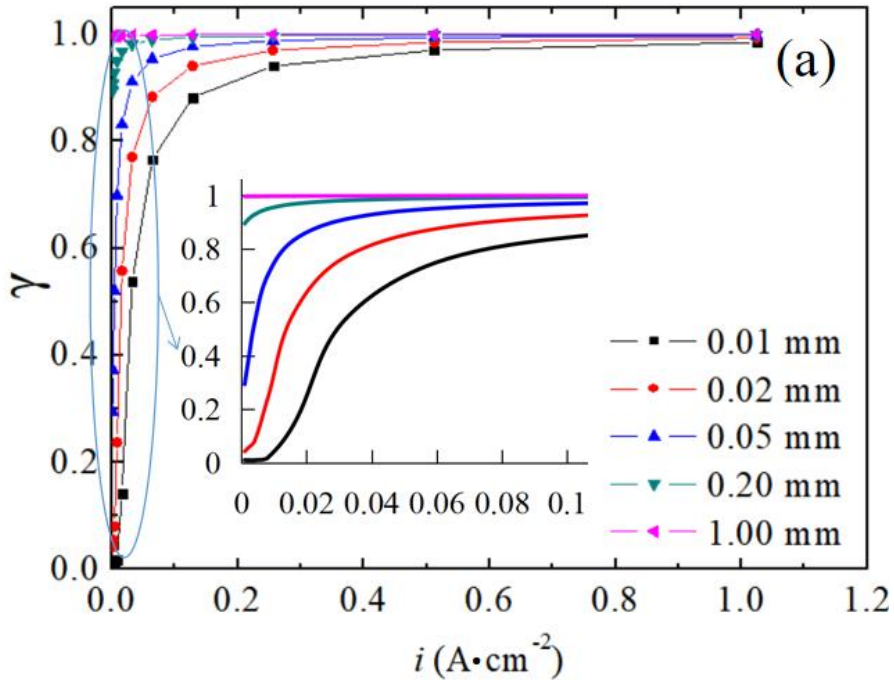

a. relative molar flux of the gaseous oxygen.

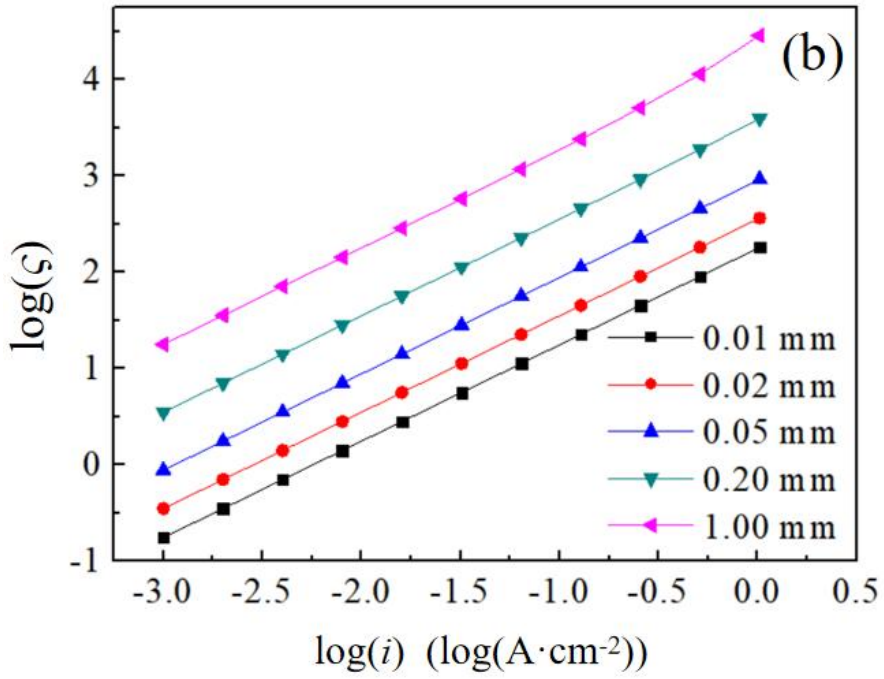

b. dimensionless transfer resistances of the dissolved oxygen.

Fig. 3.9 Transfer characteristics of oxygen gas at 85 °C.

The transfer resistance of the dissolved oxygen in Fig. 3.9b can explain the variation of the gaseous oxygen relative molar flux. The PTL thickness and current density increase the transfer resistance of dissolved oxygen, as presented in Fig. 3.9b. The transfer resistance increases with current density, especially at low current density (<0.1 A·cm^{-2}). For every

order-of-magnitude increase in current density or PTL thickness, oxygen transfer resistance also increases by one magnitude. The transfer resistance grows with current density, and PTL thickness is explained as follows. Increasing the PTL thickness prolongs the path of dissolved oxygen expulsion, thereby increasing its transfer resistance. Dissolved oxygen and liquid water transfer directions are opposite, as shown in Fig. 3.2b. The transfer direction of dissolved oxygen is opposite to the specified positive direction, and its flux is negative. According to Eq. (3.21), an increase in liquid water, whose velocity direction is positive, reduces the dissolved oxygen molar flux. Therefore, the increased liquid water molar flux inhibits the discharge of dissolved oxygen, improving the transfer resistance of dissolved oxygen.

The relative current densities in liquid water and bubbles seem to correlate with the gas saturation at the CL. Fig. 3.10 shows the gas saturation and relative current density in liquid water and bubbles. In Fig. 3.10a, the gas saturation at the CL increases with applied current density and PTL thickness, reducing the fractional coverage of liquid water at the CL. Increasing the current density increases the molar flux of gaseous oxygen, thereby increasing the gas saturation at the CL. In addition, the gas saturation continues to increase with the PTL thickness, and a higher gas saturation is formed at the CL.

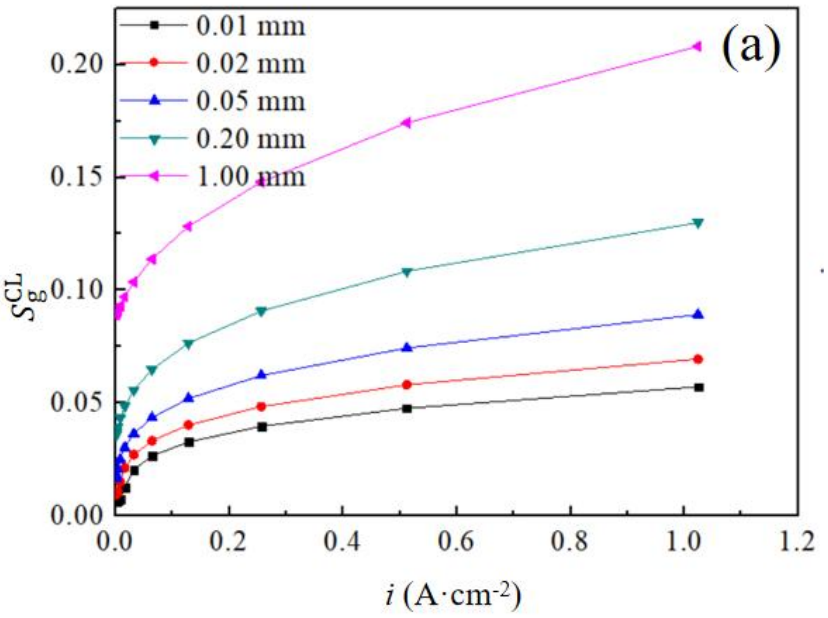

a. gas saturation at the CL

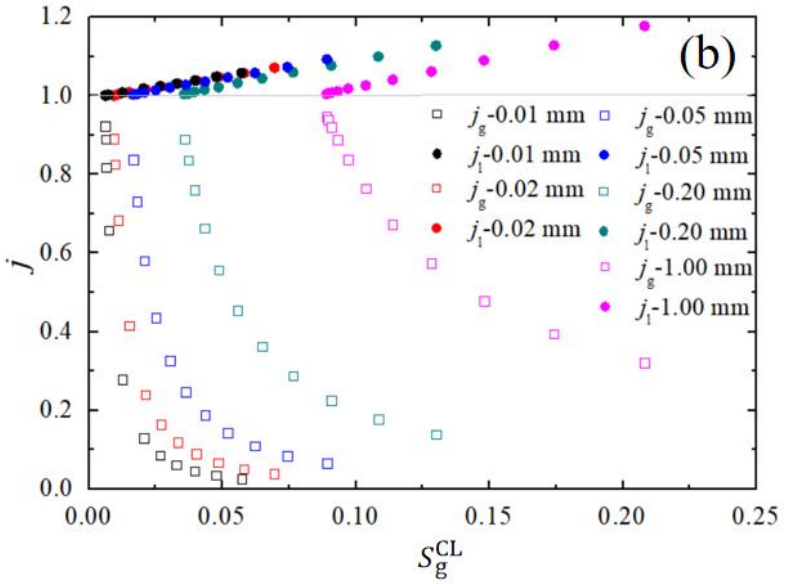

b. relative current density at the CL in the liquid water and bubbles

Fig. 3.10 Current density against the gas saturation at 85°C.

The relative current density in liquid water varies with the gas saturation at the CL. At unboiling (85 °C), the relative current densities around the bubbles and far from the bubbles, j_{ls} and j_l, are the same because the dissolved oxygen concentration is the same at the two locations. Thus, j_l also refers to the value of j_{ls}. In Fig. 3.10b, for all thicknesses of PTL, increasing gas saturation almost linearly increases the relative current density in liquid water. When the PTL thickness is constant, the relative current density in the bubbles decreases with increasing gas saturation. Increasing the applied current density increases the gaseous oxygen molar flux, leading to a higher gas saturation at the CL. The rising gaseous oxygen molar flux reduces the partial pressure and activity of water vapor in bubbles, reducing the current density in the bubbles. Therefore, the relative current density in the bubbles decreases as the applied current density increases. Correspondingly, the OER in liquid water generates a higher current density to fulfill the total current load. At a constant current density, increasing the PTL thickness increases the gas saturation at the CL. Therefore, the distribution of j_l and j_g shifts towards the higher gas saturation (the right direction of the x-axis) when increasing the PTL thickness, as Fig. 3.10b.

Fig. 3.11 shows the dimensionless concentration of dissolved oxygen and the relative pressure of water vapor in bubbles. In Fig. 3.11a, the dimensionless concentration monotonically increases with current density. Notably, the dimensionless concentration is maximally increased to about 2.1, meaning that the dissolved oxygen concentration is 2.1

times that at the standard conditions. This is because the partial pressure of gaseous oxygen, less than the bubble pressure (0.1MPa), restricts the dissolved oxygen dimensionless concentration below 2.1.

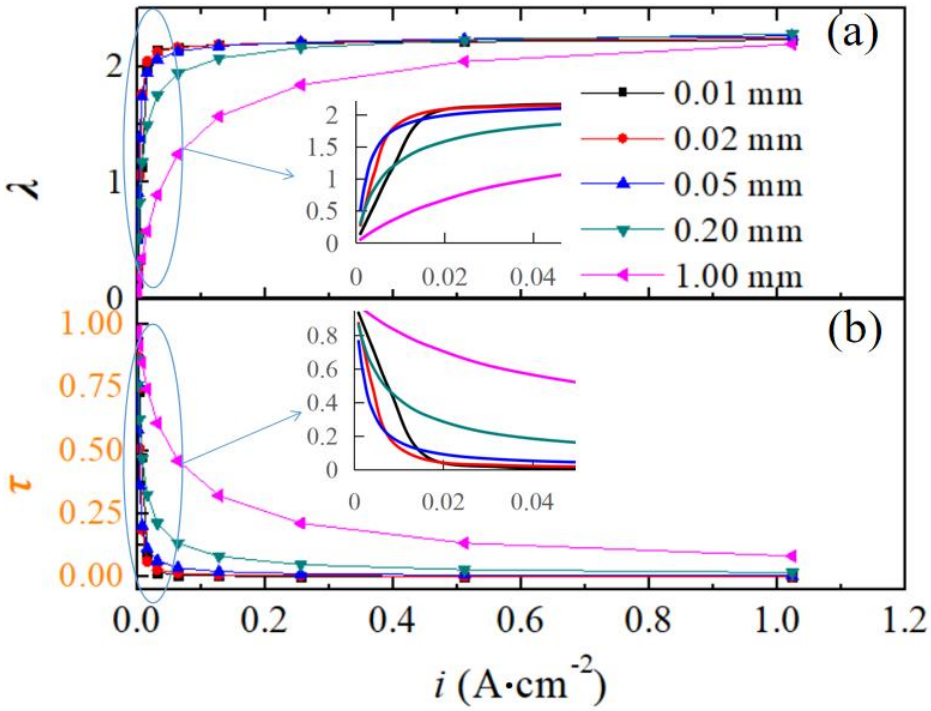

Fig. 3.11 The physical state of oxygen and water vapor at 85°C. a. dimensionless concentration of the dissolved oxygen and, b. relative pressure of water vapor at the CL.

The dimensionless concentration of dissolved oxygen changes conversely with the relative pressure of water vapor in bubbles. The relative pressure of water vapor decreases monotonically with current density but varies irregularly with PTL thickness, as shown in Fig. 3.11b.. Thickening the PTL increases the side-wall area of the bubbles (as depicted in Fig. 3.5b, which is also the evaporation area, increasing the water vapor molar flux as Eq. (3.51). The high partial pressure of water vapor restrains the vaporization rate, according to Eq. (3.52). Therefore, the partial pressure of water vapor in the bubbles does not monotonically increase with PTL thickness, as shown in Fig.3.11b. However, without boiling, the molar flux of gaseous oxygen is about 9 times that of water vapor by evaporation, according to Eq. (3.32), because the relative pressure of water vapor is below 0.1 in Fig. 3.11b. Therefore, the partial pressure of gaseous oxygen is 9 times larger than that of water vapor in the bubbles, which greatly affects the monotonic decrease in the relative pressure of water vapor.

This sub-sub chapter can be concluded from the oxygen transfer in the PTL at

unboiling. At unboiling, the dissolved oxygen at the CL has a high concentration because of the high partial pressure of gaseous oxygen in bubbles. This high partial pressure of gaseous oxygen and high dissolved oxygen concentration form disadvantageous factors to producing a low OER overpotential. Boiling will reduce the oxygen concentration at the CL to eliminate the disadvantageous factors.

3.4 Conclusions

In order to quantify the mechanism that boiling reduces the OER overpotential, a theoretical model is used to analyze the mass transfer and electrochemical performance of the OER by the dimensionless method. The theoretical model has a qualitative agreement with experimental results. Conclusions are summarized below.

(1) The theoretical model revealed that boiling reduces the OER overpotential. This phenomenon comes from the fact that considerable water vapor at boiling reduces the partial pressure of gaseous oxygen in bubbles. The decreasing partial pressure of gaseous oxygen in the bubbles attracts more dissolved oxygen to flow into the bubbles, reducing the dissolved oxygen concentration surrounding the bubbles. The decreasing dissolved oxygen concentration reduces the Nernst loss, which is the key to reducing the OER overpotential. The boiling effect, thus clarified, is enhanced when the oxygen transfer resistance of the dissolved oxygen through PTL is high.

(2) The transfer resistance of the dissolved oxygen is key to explaining the gas/liquid behavior in PTL and determining the boiling effect's worth. The dissolved oxygen transfer resistance increases greatly with the current density and PTL thickness so that the concentration of dissolved oxygen at the CL rises to a higher level. Compared to the high transfer resistance of dissolved oxygen expelling the PTL through the liquid water path, oxygen drained through bubbles has lower transfer resistance, resulting in more than 99% of the oxygen drained through the bubbles. The bubbles are almost filled with gaseous oxygen, forming a higher partial pressure of gaseous oxygen. The water vapor produced by boiling reduces the partial pressure of gaseous oxygen in the bubbles and the dissolved oxygen concentration surrounding the bubbles greatly, ultimately reducing the Nernst loss. In short, the high transfer resistance of dissolved oxygen through the PTL is the prerequisite for boiling to reduce the OER overpotential.

References

[1] Lickert T, Kiermaier ML, Bromberger K, Ghinaiya J, Metz S, Fallisch A, Smolinka T. On the influence of the anodic porous transport layer on PEM electrolysis performance at high current densities. International Journal of Hydrogen Energy. 2020;45(11):6047-58.

[2] Aubras F, Rhandi M, Deseure J, Kadjo AJ, Bessafi M, Majasan J, Grondin-Perez B, Druart F, Chabriat JP. Dimensionless approach of a polymer electrolyte membrane water electrolysis: Advanced analytical modelling. Journal of Power Sources. 2021;481:228858.

[3] Lee JK, Lee CH, Bazylak A. Pore network modelling to enhance liquid water transport through porous transport layers for polymer electrolyte membrane electrolyzers. Journal of Power Sources. 2019;437:226910.

[4] Sarker M, Rahman MA, Mojica F, Mehrazi S, Kort-Kamp WJ, Chuang PY. Experimental and computational study of the microporous layer and hydrophobic treatment in the gas diffusion layer of a proton exchange membrane fuel cell. Journal of Power Sources. 2021;509:230350.

[5] Lilavivat V, Shimpalee S, Van Zee JW, Xu H, Mittelsteadt CK. Current distribution mapping for PEMFCs. Electrochimica Acta. 2015;174:1253-60.

[6] Immerz C, Schweins M, Trinke P, Bensmann B, Paidar M, Bystroň T, Bouzek K, Hanke-Rauschenbach R. Experimental characterization of inhomogeneity in current density and temperature distribution along a single-channel PEM water electrolysis cell. Electrochimica acta. 2018;260:582-8.

[7] Milewski J, Guandalini G, Campanari S. Modeling an alkaline electrolysis cell through reduced-order and loss-estimate approaches. Journal of Power Sources. 2014;269:203-11.

[8] Ojong ET, Kwan JT, Nouri-Khorasani A, Bonakdarpour A, Wilkinson DP, Smolinka T. Development of an experimentally validated semi-empirical fully-coupled performance model of a PEM electrolysis cell with a 3-D structured porous transport layer. International journal of hydrogen energy. 2017;42(41):25831-47.

[9] Zhan S, Huang Y, Zhang W, Li B, Jiang M, Wang Z, Wang J. Experimental investigation on bubble growth and detachment characteristics on vertical microelectrode surface under electrode-normal magnetic field in water electrolysis. International Journal of Hydrogen Energy. 2021;46(74):36640-51.

[10] Cho KM, Deshmukh PR, Shin WG. Hydrodynamic behavior of bubbles at gas-evolving

electrode in ultrasonic field during water electrolysis. Ultrasonics Sonochemistry. 2021;80:105796.

[11] Lim A, Kim HJ, Henkensmeier D, Yoo SJ, Kim JY, Lee SY, Sung YE, Jang JH, Park HS. A study on electrode fabrication and operation variables affecting the performance of anion exchange membrane water electrolysis. Journal of Industrial and Engineering Chemistry. 2019;76:410-8.

[12] Todd D, Schwager M, Mérida W. Thermodynamics of high-temperature, high-pressure water electrolysis. Journal of Power Sources. 2014;269:424-9.

[13] Lu J H, Lei H Y, Dai C S. Analysis of Henry's law and a unified lattice Boltzmann equation for conjugate mass transfer problem. Chemical Engineering Science, 2019, 199: 319-331.

[14] Schnabel T, Vrabec J, Hasse H. Henry's law constants of methane, nitrogen, oxygen and carbon dioxide in ethanol from 273 to 498 K: Prediction from molecular simulation. Fluid Phase Equilibria, 2005, 233(2): 134-143.

[15] Ni M. An electrochemical model for syngas production by co-electrolysis of H2O and CO2. Journal of power sources, 2012, 202: 209-216.

[16] Lee CH, Lee JK, Zhao B, Fahy KF, LaManna JM, Baltic E, Hussey DS, Jacobson DL, Schulz VP, Bazylak A. Temperature-dependent gas accumulation in polymer electrolyte membrane electrolyzer porous transport layers. Journal of Power Sources. 2020;446:227312.

[17] Molina A, González J, Laborda E, Compton RG. On the meaning of the diffusion layer thickness for slow electrode reactions. Physical Chemistry Chemical Physics. 2013;15(7):2381-8.

[18] Rahim AA, Tijani AS, Kamarudin SK, Hanapi S. An overview of polymer electrolyte membrane electrolyzer for hydrogen production: Modeling and mass transport. Journal of Power Sources. 2016;309:56-65.

[19] Nakajima H, Kitahara T. In-situ Measurements of Current Distribution in the Solid Oxide Fuel Cell for Marine Power Applications. Journal of The Japan Institute of Marine Engineering, 2018, 53(2): 230-236.

[20] Schmidt G, Suermann M, Bensmann B, et al. Modeling overpotentials related to mass transport through porous transport layers of PEM water electrolysis cells. Journal of The Electrochemical Society, 2020, 167(11): 114511.

[21] Garcia-Navarro J C, Schulze M, Friedrich K A. Measuring and modeling mass transport

losses in proton exchange membrane water electrolyzers using electrochemical impedance spectroscopy. Journal of Power Sources, 2019, 431: 189-204.

[22] Torii K, Kodama M, Hirai S. Three-dimensional coupling numerical simulation of two-phase flow and electrochemical phenomena in alkaline water electrolysis. International Journal of Hydrogen Energy, 2021, 46(71): 35088-35101.

[23] Mann RF, Amphlett JC, Peppley BA, Thurgood CP. Henry's Law and the solubilities of reactant gases in the modelling of PEM fuel cells. Journal of power sources. 2006;161(2):768-74.

[24] Kalinnikov A A, Grigoriev S A, Bessarabov D G, et al. Two-phase mass transfer in porous transport layers of the electrolysis cell based on a polymer electrolyte membrane: Analysis of the limitations. Electrochimica Acta, 2021, 387: 138541.

[25] Zinser A, Papakonstantinou G, Sundmacher K. Analysis of mass transport processes in the anodic porous transport layer in PEM water electrolysers. International Journal of Hydrogen Energy, 2019, 44(52): 28077-28087.

[26] Kai J, Saito R, Terabaru K, Li H, Nakajima H, Ito K. Effect of temperature on the performance of polymer electrolyte membrane water electrolysis: numerical analysis of electrolysis voltage considering gas/liquid two-phase flow. Journal of The Electrochemical Society. 2019;166(4):F246.

[27] Bénet JC, Ouoba S, Ouedraogo F, Cherblanc F. Experimental study of water evaporation rate, at the surface of aqueous solution, under the effect of a discontinuity of chemical potential–Effect of water activity and air pressure. Experimental Thermal and Fluid Science. 2021;121:110233.

[28] Khan SA, Sezer N, Koç M. Design, fabrication and nucleate pool-boiling heat transfer performance of hybrid micro-nano scale 2-D modulated porous surfaces. Applied Thermal Engineering. 2019 May 5;153:168-80.

[29] Liso V, Savoia G, Araya SS, Cinti G, Kær SK. Modelling and experimental analysis of a polymer electrolyte membrane water electrolysis cell at different operating temperatures. Energies. 2018;11(12):3273.

[30] Lopata JS, Kang SG, Cho HS, Kim CH, Weidner JW, Shimpalee S. Investigating influence of geometry and operating conditions on local current, concentration, and crossover in alkaline water electrolysis using computational fluid dynamics. Electrochimica Acta. 2021;390:138802.

Chapter 4

Experimental and theoretical analysis of the boiling effect on the hydrogen evolution reaction

This chapter elucidates the mechanism by which boiling reduces the overpotential of hydrogen evolution reaction (HER) in experiments and theoretical models. The high water vapor molar flux at boiling is expected to reduce the HER overpotential. In experiment, the three-electrode cell (TEC) scans the galvanostatic potential of the working electrode (WE). A catalyst layer (CL) for HER is embedded on the top of the WE. An electric heater in the WE can control the CL temperature above the boiling point, coupling boiling into the HER. Three kinds of WEs, so-called WE1, WE2, and WE3, are prepared to clarify which voltage component is reduced by boiling. In the WE1, CL directly faces the flowing electrolyte, and concentration overvoltage can be ignored due to the low transfer resistance of hydrogen gas. Therefore, the WE1 can measure the boiling effect on the activation overvoltage of HER after IR correction. In WE2, CL surface is covered by a carbon paper, which generates Nernst loss (including concentration overvoltage) besides activation overvoltage. If boiling cannot change the HER activation overvoltage of the WE1, the WE2 could examine whether boiling reduces the Nernst loss. A simulation of the theoretical models considering the geometry of WE1 and WE2 quantitatively analyzed the boiling effect on HER overpotential. The model embeds the transfer process of gaseous hydrogen, dissolved hydrogen, liquid water, and water vapor in carbon paper. The model distinguishes hydrogen transfer through the gas bubbles and liquid water, and determines the hydrogen concentrations at the CL. This model clarifies the boiling role in reducing dissolved hydrogen concentration and HER overpotential. The results confirm that boiling accelerates gas transfer in carbon paper and reduces the dissolved hydrogen concentration at the CL, which is the reason for reducing the HER overpotential.

Although the theoretical model in this chapter is based on the structure of the WE in a TEC, rather than that of cathode CL in practical PEMWE, an additional concern is placed so that the theoretical model developed here is applicable when the simulation based on the model examines the boiling effect in case of the practical PEMWE. In the case of the WE in the TEC, the bubbles produced in and on CL cut the path for supplying proton into the WE.

Whereas, in the case of practical PEMWE cathode, the bubbles formed in CL do not disturb the proton supply to WE, because the protons can be supplied through PEM. Considering the difference between them, the theoretical model for the WE assumes an achievable proton supply in the case of the WE and is applicable in the HER process in a practical PEMWE cathode.

4.1 Introduction

In PEMWE, the porous transfer layer (PTL) in the cathode is an indispensable component for transferring hydrogen gas and water and conducting electrons [1]. However, the mass transfer resistance formed by this PTL may lead to excessive overpotential of hydrogen evolution reaction (HER) [2]. Especially, a thick PTL prevents hydrogen transfer and increases the HER concentration overvoltage [3], such as 50 mV. At high current densities, concentration overvoltage becomes significant in addition to activation overvoltage [4]. PTLs with graded pore size can induce hydrogen bubbles' splitting and expulsion, reducing HER's overvoltage [5]. Arshad and Ding believed that a PTL with large porosity could enhance hydrogen transfer [6,7]. Liu et al. expected to use a PTL with distributed concave pores to improve hydrogen gas permeability [8]. However, fabricating such complex pore structures increases the production cost of water electrolyzers.

Instead of embedding the sophisticated PTL, the boiling effect is suggested as for enhancing hydrogen gas transfer in a simple and effective way. Chapters 2 and 3 show the boiling effect on enhancing oxygen transfer and reducing OER overpotential. Considering the mechanism of the boiling effect on OER, the boiling effect can also hold in the HER case. Boiling may enhance hydrogen gas transfer and reduce HER overpotential. The boiling effect on HER overpotential is experimentally and theoretically studied in this chapter.

Two types of WE, so-called WE1 and WE2, are proposed to examine the boiling effect for HER. As shown in Fig. 4.1, CL is embedded on top of WE1, directly facing the electrolyte, and the hydrogen transfer resistance over the CL can be ignored. Therefore, the WE1 can be approximated only to have activation overvoltage after IR correction. As for WE2, a carbon paper covers the CL and hinders hydrogen gas transfer, highlighting the Nernst loss (including concentration overvoltage) in the HER process. Because WE2 is sufficient to judge whether

boiling reduces Nernst loss, WE structures with higher hydrogen transfer resistance, such as WE3 covering a PTL and ridges, were not additionally tested. A heater and thermocouple in the WE can control the CL temperature, switching the water at the CL surface between unboiling and boiling. Then, galvanostatic voltammetry (GV) measures the HER potential of WE1 and WE2 as a function of temperature. Because GV was sufficient to demonstrate whether boiling could reduce the overpotential of HER, additional tests, such as linear voltammetry (LSV), were not performed. If the HER overpotential of the WE1 decreases apparently at boiling, that boiling reduces the activation overvoltage can be confirmed, and vice versa. On the basis that boiling cannot reduce the activation overvoltage of WE1, if boiling can reduce the HER overpotential of WE2, then we can confirm that boiling reduces the Nernst loss of HER. The experimental plans above can qualitatively determine which HER overvoltage is reduced by boiling.

Although the experimental results can quantitatively reveal how much boiling reduces HER overpotential, it cannot clarify the mechanism of boiling effect on HER. Therefore, a theoretical model combining boiling and HER is established in chapter 4.4. The theoretical model refers to the experiment's WE1 (CL) and WE2 (CL + carbon paper). In models, no carbon paper covers the CL surface of WE1, but there is a thin liquid layer that the dissolved hydrogen concentration varies greatly. The thickness of the water layer is about 10 μm over the CL [9]. As for the WE2 model, it refers to the experimental WE2 structure covering a carbon paper of 0.11-mm thickness on the CL. The HER model follows charge conservation at the CL and momentum conservation for two-phase transfer within a carbon paper. The theoretical results finally elucidate why boiling reduces dissolved hydrogen concentration at the CL and then the HER overpotential.

4.2 Experiment

This sub-chapter describes the WE structure, experimental method and condition. The HER potential at each temperature, including boiling, was measured by GV. The temperature dependence of each electrode in the three-electrode cell (TEC) was also introduced to obtain accurate HER overpotential.

4.2.1 Experimental apparatus

The structures of TEC and WE are described in Fig. 4.1. In Fig. 4.1a, a 100-W electric heater and a 1 mm-diameter T-type thermocouple control the electrolyte temperature. In the WE, a 10-W electric heater and a 0.5 mm-diameter T-type thermocouple control the WE temperature, as shown in Fig. 4.1b. The WE, counter electrode (CE), and reference electrode (RE) were immersed in 0.1-M $HClO_4$ solution to form a closed-loop circuit. The CL is embedded on top of the WE, and the evolved hydrogen bubbles flow into the electrolyte. The CE is platinum wire. RE is an Ag/AgCl(sat.) electrode [10], providing a reference potential for the HER.

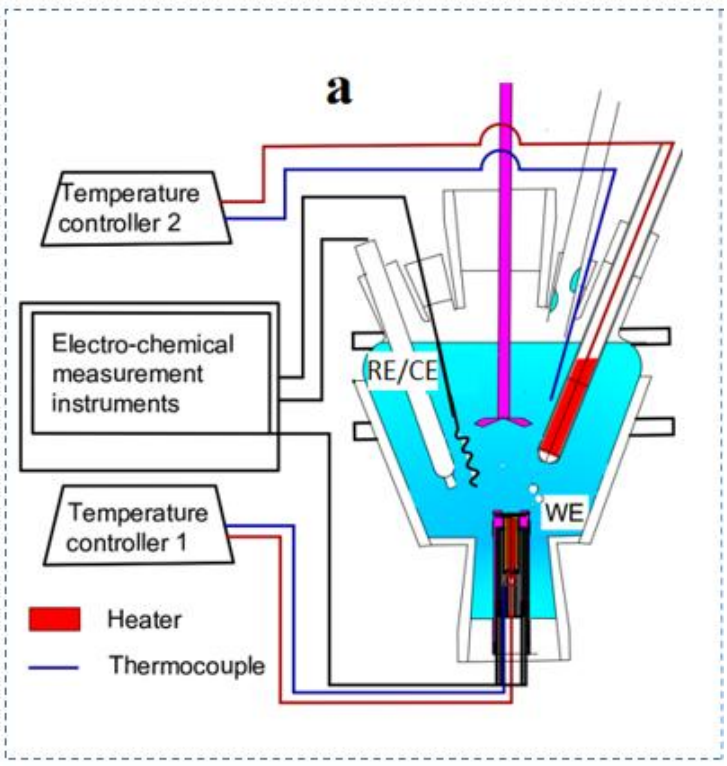

a. three-electrode cell

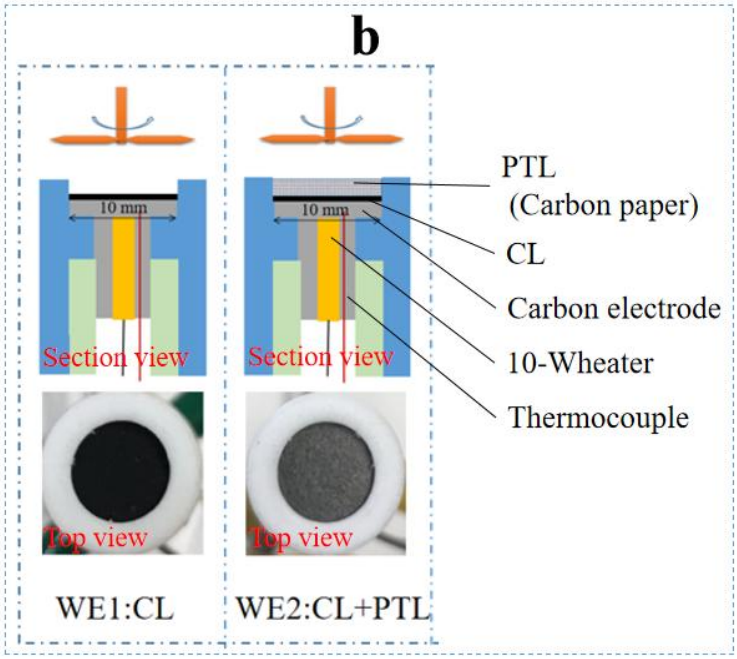

b. interior structures of WE1 and WE2.

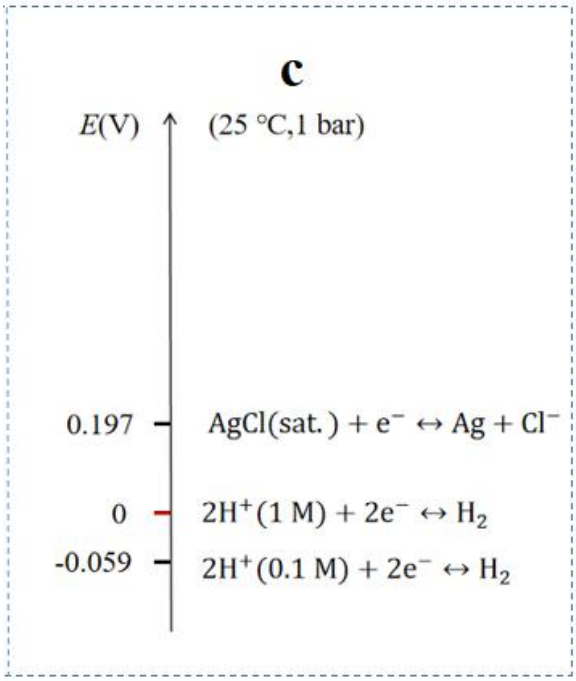

c. potential correction

Fig.4.1 Experimental apparatus introduction.

The WE1 and WE2 designed in this chapter are shown in Fig. 4.1b, while their structure parameters are introduced in Table 4.1. The only difference in the structures of WE1 and WE2 is whether the CL is covered by PTL (carbon paper). In these two WEs, the carbon component was used as the substrate electrode to carry CL because of the acid resistance of carbon materials. The location of the carbon components is shown in Fig. 4.1b, below the CL.

CL was attached to the top surface of the carbon component for HER. The CL was fabricated by spraying platinum particles of loading 0.5 $mg \cdot cm^{-2}$ and hot pressing on the carbon component. The CL is a circle with a diameter of 10 mm. The CL is also loaded with an Aquivion ionomer as a binder and proton conductor. A heater in the carbon component heated the CL and made boiling on it. The stirrer above the WEs was rotated at 2000 $r \cdot min^{-1}$ to agitate the electrolyte to remove hydrogen gas bubbles attached to the upper surface of the WEs. For the WE1, the flowing electrolyte directly removes the dissolved hydrogen and hydrogen gas bubbles at the CL surface, and the concentration overvoltage of the HER can be ignored. At boiling, if the WE1 overpotential decreases significantly, that the boiling reduces activation overvoltage will be determined, and vice versa. For the WE2, the hydrogen gas bubbles at the CL flow through the carbon paper. The WE2 has a higher hydrogen transfer resistance than WE1 because the capillary force in the carbon paper prevents the hydrogen gas bubbles' emission. Therefore, in addition to the activation overvoltage, the WE2 also has a significant Nernst loss (including concentration overvoltage). If the overpotential decreases above the boiling-point temperature in WE2 but not in WE1, we can conclude that boiling can decrease the hydrogen concentration at the CL to decrease the Nernst loss.

Table. 4.1 Parameters in the WEs

Components	Specification
CL	Thickness: 10 μm Diameter: 10 mm Catalyst and its load: Pt particles (TEC10E50E, TANAKA) and 0.5 $mg \cdot cm^{-2}$ Ionomer: Aquivion ionomer Material composition ratio: Pt/C=72 wt%, Ionomer=28 wt%
Carbon paper for the WE2	Thickness: 110 μm Material: Carbon paper (30-TGP-H-030) Porosity: 80% Substrate PTFE Treatment: 5wt%

4.2.2 Experimental method

The WEs ran in a wide temperature range to compare the overpotential changes of the HER without and with boiling. The temperature control strategy for the HER is described below. A 10-W heater adjusted the WE temperature, while a 100-W heater controlled the electrolyte temperature. The WE was increased from 25 to 110 °C. Because Aquivion ionomers can withstand higher temperatures than Nafion ionomers, the CL loaded Aquivion ionomers can run safely at 110 °C within a short period. When the WE temperature was lower than 90 °C, the electrolyte temperature increased with WE synchronously. The electrolyte temperature was heated up to 90 °C because of its boiling-point temperature limitation. If the WE temperature exceeds 90 °C, the WE temperature was individually increased from 90 to 110 °C while the electrolyte temperature was kept at 90 °C.

The RE used in this chapter is the standard silver chloride electrode (SSCE), which has the advantage of potential stabilization. The electrolyte is a 0.1-M $HClO_4$ solution with water as the solvent. As shown in Fig. 4.1c, at 25 °C, the 0.1-M acidic electrolyte changed the HER from the standard hydrogen electrode (SHE) potential, $E_0^{\mathrm{HER}} = 0\ \mathrm{V}$, to $E_{0,\mathrm{Shifted}}^{\mathrm{HER}} = -0.059\ \mathrm{V}$. Compared with SHE, the standard potential of SSCE is $E_0^{\mathrm{SSCE}} = 0.197\ \mathrm{V}$. Therefore, Eq. (4.1) gives the measured HER electrode potential with reference to SSCE,

$$E_{0,\mathrm{Measured}}^{\mathrm{HER}} = E_{0,\mathrm{Shifted}}^{\mathrm{HER}} - E_0^{\mathrm{SSCE}} = -0.059 - 0.197 = -0.256\ [\mathrm{V}]\ \mathrm{vs.\ SSCE} \quad (4.1)$$

Because the SSCE potential depends on temperature, clarifying the relationship between RE potential and temperature can help to determine accurate HER overpotentials. The equilibrium potential of the Ag/AgCl(sat.) electrode varies with temperature as Eq. (4.2) [11],

$$E_{\mathrm{eq}}^{\mathrm{SSCE}}(T) = E_0^{\mathrm{SSCE}} - \frac{1.01(T-25)}{1000} = 0.197 - \frac{1.01(T-25)}{1000}\ [\mathrm{V}]\ \mathrm{vs.\ SHE} \quad (4.2)$$

The HER overpotential can be used to evaluate whether boiling affects HER. In the experiment, the HER potentials tested by the TEC referenced the temperature-dependent SSCE. The equilibrium potential of HER, $E_{0,\mathrm{Measured}}^{\mathrm{HER}}(\mathrm{T})$, is also temperature-dependent. The potential of HER is lower than its equilibrium potential. The overpotential of the HER can be determined from Eq. (4.3), referring to the equilibrium potential. After IR correction, the HER overpotential of the WE1 is the activation overvoltage, while the HER overpotential of WE2 is composed of activation and Nernst loss. After substituting Eq. (4.1) into Eq. (4.3), the overpotential expression of HER is

$$\Delta E^{\mathrm{HER}} = E^{\mathrm{HER}}_{0,\mathrm{Measured}}(\mathrm{T}) - E^{\mathrm{HER}} - \eta^{\mathrm{HER}}_{\mathrm{ohm}} = (E^{\mathrm{HER}}_{0,\mathrm{Shifted}} - E^{\mathrm{SSCE}}_{\mathrm{eq}}(T)) - E^{\mathrm{HER}} - \eta^{\mathrm{HER}}_{\mathrm{ohm}}\ [\mathrm{V}]$$

(4.3)

Among them, ΔE^{HER} is the overpotential of HER, E^{HER} is the HER potential of the TEC test, $E^{\mathrm{HER}}_{0,\mathrm{Measured}}(\mathrm{T})$ is the equilibrium potential with a proton concentration of 1M, and $\eta^{\mathrm{HER}}_{\mathrm{ohm}}$ is the ohmic overvoltage.

The fundamental HER performance can be used to determine the experimental integrity of the TEC and WEs. Before studying the HER performance under boiling, the basic HER performance of the custom WE1 need to be inspected. Cyclic voltammetry (CV) can measure the electrochemical surface area (ECSA) of CL [12].

$$\mathrm{ECSA} = \frac{C^{\mathrm{E}}_{\mathrm{dl}}}{C_{\mathrm{dl}}} \quad (4.4)$$

where C_{dl} is the specific capacitance density of Pt material, 0.059 mF·cm^{-2} [12]. The $C_{\mathrm{dl}}^{\mathrm{E}}$ is the capacitance value of the Pt particles in the CL measured from the CV plot obtained at specific potential scan rates, such as Fig. 4.2a. In order to obtain accurate $C_{\mathrm{dl}}^{\mathrm{E}}$, the CV is measured 20 turns at 25 °C in the non-Faraday discharge range (0.55-0.75 V). Finally, the 20th cycle is selected to determine $C_{\mathrm{dl}}^{\mathrm{E}}$ because of its stability and accuracy. Table 4.2 gives the operating conditions of CV. By obtaining the ECSA, the electrochemical exchange membrane current density of the custom-made CL can be determined. The electrochemical current density was compared with a referred current density to verify the completeness of the CL and experimental apparatus.

After examining the basic electrochemical characteristics of the custom-made CL, the WE embedded the CL can test the effect of boiling on the HER overpotential. The WE temperature was swept from 85 to 110 °C (including unboiling and boiling) to measure the HER potential at a static current density. The potential at the current density was recorded for 300 s at a specific temperature to obtain sufficient potential data, as Table 4.2. Then, the mean of these potential values was selected as the experimental result, which determines the overpotential.

Table 4.2. Experiment conditions for each measurement

Measurement Method	Specification

IR correction	Potential	−0.1 V vs. SSCE
	Disturbance frequency	1000 Hz
	Testing time for a value	300 s
	AC amplitude	10 mV
Galvanostatic conditions	Testing time for a value	300 s
	HER current	−6.4 -−63.7 $mA \cdot cm^{-2}$
CV condition	Potential range	0.55–0.75 V vs. SSCE
	Sweeping speed	1-50 $mV \cdot s^{-1}$

4.3 Experimental results

Results introduce the integrity of the custom-made CL first. Then, the boiling effect on HER overpotential of WE1 and WE2 was analyzed. The HER galvanostatic overpotential measured over a wide temperature range confirms that the Nernst loss (including concentration overvoltage) is reduced by boiling.

4.3.1 Integrity verification of CL

The integrity validation of the experimental apparatus and custom-made CL is critical for the HER research. A CL with a circular area of 0.785 cm^2 (diameter: 1 cm) was manufactured by spraying Pt/C-Aquivion ionomer catalyst ink and hot pressing. At 25 °C, the potential was scanned to measure the potential-current plot for the estimation of the ECSA of CL with loading Pt of 0.5 $mg \cdot cm^{-2}$. Fig. 4.2 demonstrates the basic electrochemical performance of the custom-made CL. Fig. 4.2a shows the potential-current plot in a non-Faradaic potential region (0.55-0.75 V), which is the raw CV data. The charging currents increase with the potential scanning rate, which fits with the characteristics of capacitors.

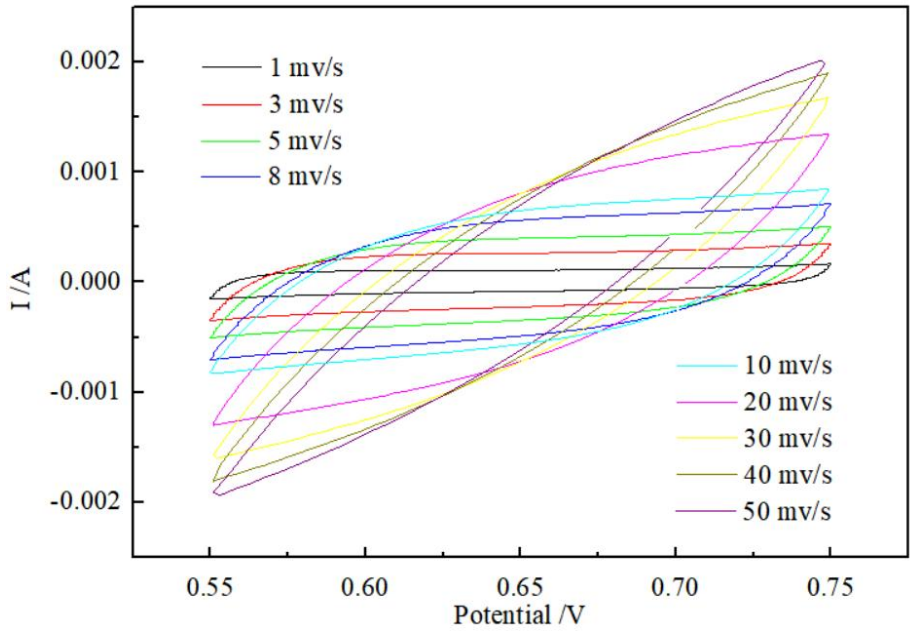

a. Potential-current plot by CV (potential vs. SSCE)

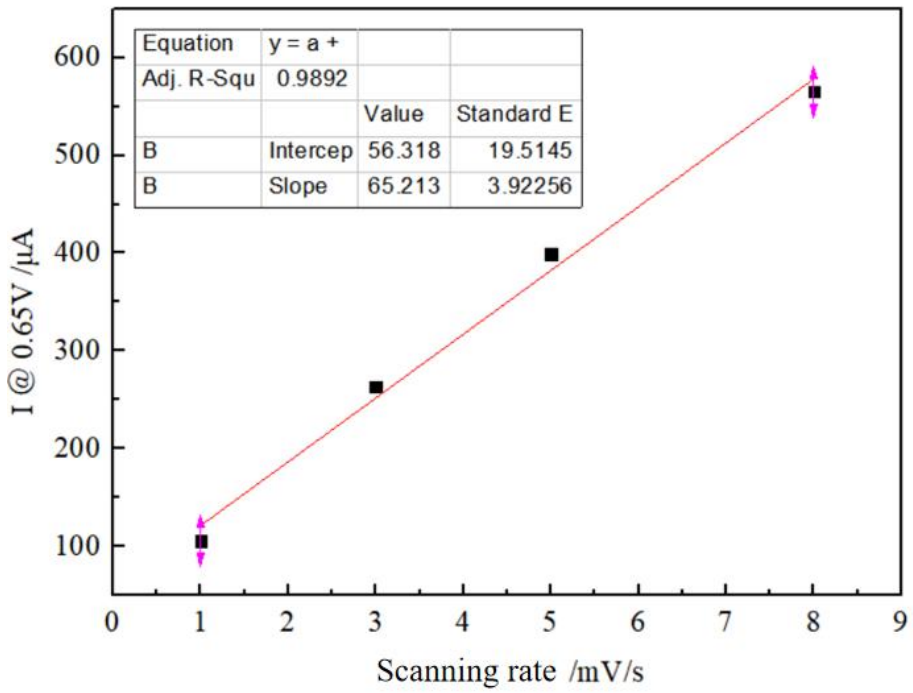

b. Non-faraday current and potential scanning rate

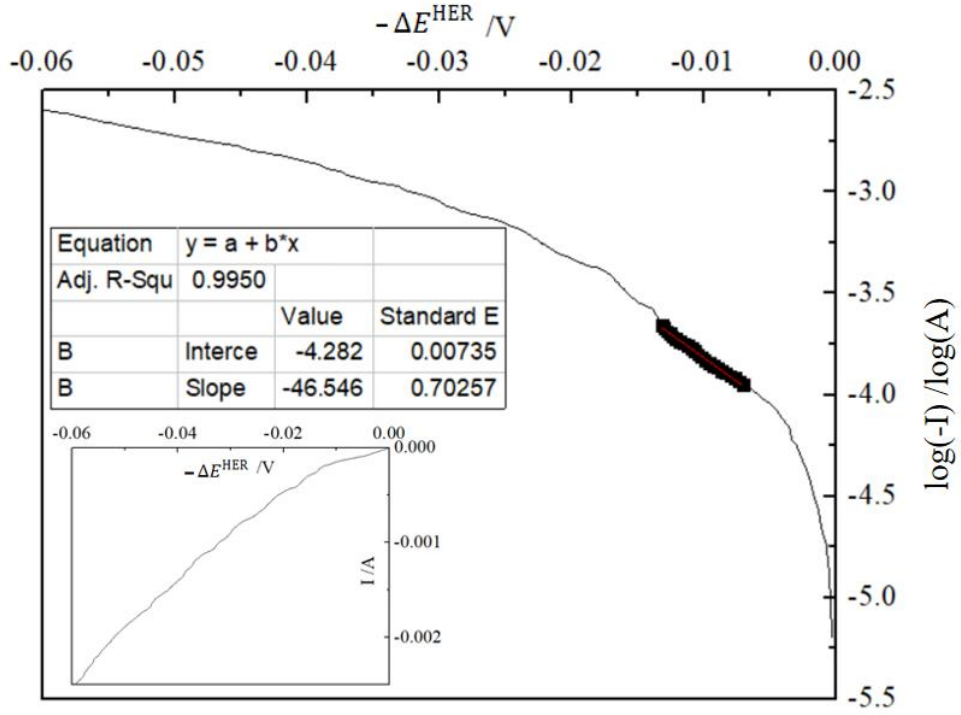

c. Tafel plot of HER (potential vs. SHE)

Fig. 4.2 Basic elctrochemical property of the custom-made CL at 25 °C and 0.1013 MPa.

The capacitance value of the CL can be obtained from the plot of the potential scanning rate and charging current. For each potential scanning rate in Fig. 4.2a, select the current at 0.65 V, which is approximately the average current in 0.55-0.75 V, as the charging current in Fig. 4.2b. The charging current was approximately linear with the potential scanning rate. The slope of the line in Fig. 4.2b is the capacitance, C_{dl}^{E}, of the CL sample, which is 65.21 mF. The Pt load in the CL is 0.5 mg·cm^{-2}, and the specific capacitance density is 0.059 mF·cm^{-2}. Therefore, the ECSA of the 10-mm diameter CL is (65.21 mF)/(0.059 mF·cm^{-2})=1105 cm^2. The ratio of the ECSA to the CL geometric area is 1105/0.785=1407, which is close to the reference value of 1500 in Ref. [13].

The Tafel plot can determine the exchange current density of the Pt catalyst in a hot-pressing CL. As shown in Fig. 4.2c, the voltammetric curve (small chart) at 25 °C was converted to a Tafel plot (big graph) after the logarithmic transformation of the current. The abscissa of Fig. 4.2c is the negative value of the HER overpotential, $-\Delta E^{HER}$. There is an approximately linear relationship between the $-\Delta E^{HER}$ and log(-*I*) around -0.01 V. The linear Tafel plot can predict the exchange current density because concentration overvoltage has not yet occurred in this low potential range (-0.01 V). In Fig. 4.2c, the intersection of the extended

line of the bold Tafel plot and the y-axis yields the exchange current, $10^{-4.28}$A. Therefore, the CL with a 10-mm diameter had a geometrical current density of $10^{-4.3}/0.785=6.4\times10^{-5}$ A·cm^{-2} and an electrochemical exchange current density of $6.4\times10^{-5}/1407=4.5\times10^{-8}$ A·cm^{-2}.

The exchange current density of this custom-made CL was much smaller than the electrochemical reference exchange current density, 10^{-3} A·cm^{-2} [4]. The reason of small exchange current density in the CL in this study attributes to its fabrication process. In the CL fabrication, the CL were hot-pressed so that the CL can withstand the mechanical damage caused by boiling bubbles. However, the compression with hot-press makes CL dense, resulting in an excessively high hydrogen transfer resistance in the CL, resulting in a smaller measurement value of the electrochemical exchange current density. On the other hand, in a generalHER evaluation in TEC, Pt-particles are just placed, with some weak attachment force, on the surface of WE and they are isolated each other. In addition, the general CL on WE is rotated. Thus, the general CL hardly has hydrogen transfer resistance. Although the CL itself does not exhibit excellent electrochemical performance, this CL can still evaluate the boiling effect on HER overpotential as follows.

4.3.2 Boiling effect on HER overpotential

Fig. 4.3 shows the HER overpotentials of the WE1 and WE2 as a function of temperature. For the WE1, the electrolyte driven by the stirrer removed the hydrogen transfer resistance over the CL. Therefore, the Nernst loss, including concentration overvoltage, can be ignored in the case of WE1, and only the activation overvoltage remains. Fig. 4.3a shows the result in the case of WE1 and indicates that the overpotential for any current density did not specially decrease over 100 °C. Thus, it can be concluded that boiling does not specially affect the activation overvoltage of the HER.

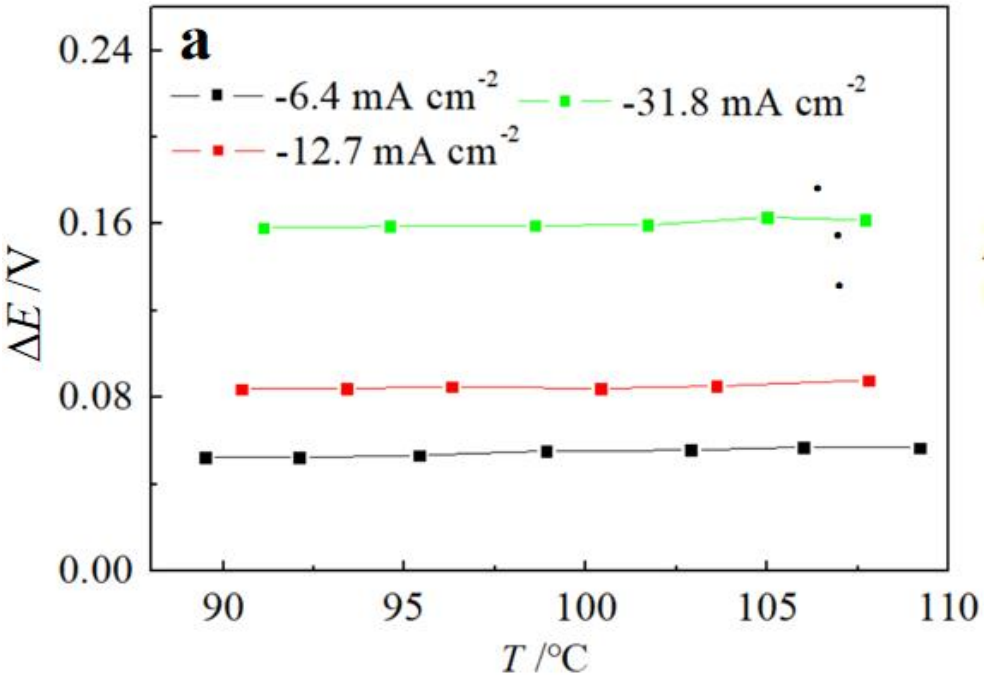

a. WE1 overpotential

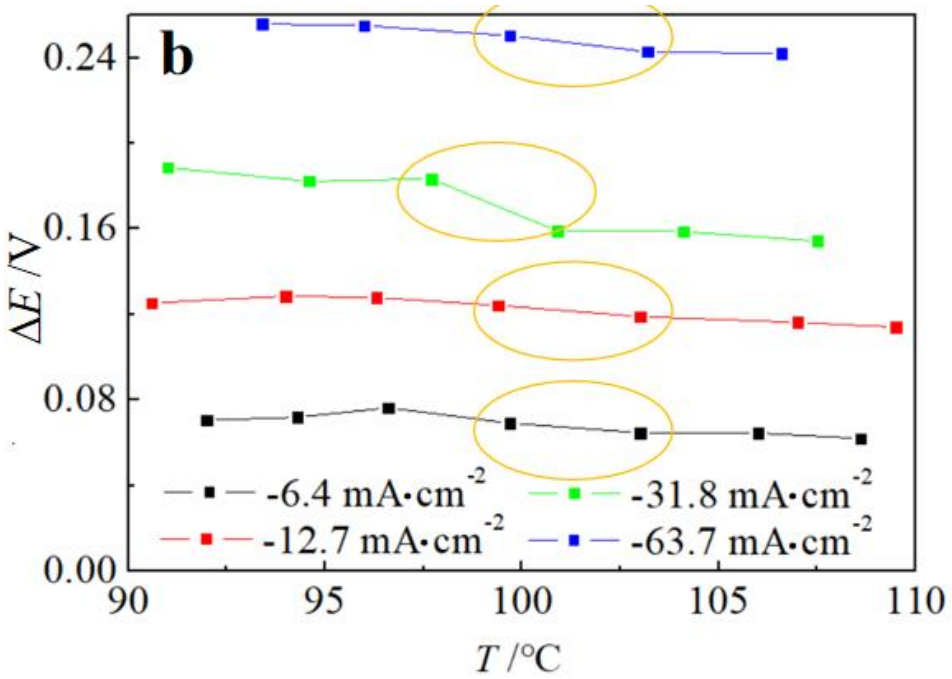

b. WE2 overpotential

Fig. 4.3 Boiling effect on HER overpotentials (IR correction).

For the WE2 covered with carbon paper, the overpotential below 100 °C (Fig. 4.3b) was slightly higher than that of WE1 (Fig. 4.3a) because of the additional Nernst loss in addition to the activation overvoltage. In Fig. 4b, the HER overpotentials for four current densities (-6.4, -12.7, -31.8, and -63.7 mA·cm^{-2}) exhibited a same tendency, they start to decrease slightly above 100 °C. Therefore, considering the case of WE1, the slight

overpotential drop of WE2 at boiling is suggested to come from the Nernst loss. How does the boiling decrease the Nernst loss. Following theoretical model and its numerical analysis shows that boiling reduce the hydrogen activity at the CL, resulting the Nernst loss reductionof HER.

4.4 Theoretical model of HER

The HER model describes the electrochemical equation and the mass transfer process, whose calculation logic is shown in Fig. 4.4. Mass transfer equations are used to solve the concentrations of dissolved hydrogen and gaseous hydrogen at the CL, $C_{H,dis}^{CL}$ and $C_{H,g}^{CL}$. The mass transfer equation includes the molar flux and momentum equations. In addition, the equations for capillary pressure, P_c, and dissolved hydrogen, water vapor fluxes, $Q_{H,dis}$ and $Q_{w,g}$, are supplemented to solve the molar flux and momentum equations. The boundary conditions at the upper surface of the carbon paper (CUS) are the liquid water pressure, $P_{w,l}$, gas saturation, S_g^0, and gas pressure P_g. The boundary conditions at the CL/carbon paper interface are hydrogen molar flux, Q_H, and water vapor molar flux by boiling, $Q_{w,g}^b$. Ultimately, the concentrations of dissolved hydrogen and gaseous hydrogen are substituted into the electrochemical equation of HER. Solving the HER model is cyclically calculated in Python with a convergence accuracy of 1%. Definitions of the remaining symbols in the flowchart are listed in Table 4.3. The cases in this chapter have conditions as listed in Table 4.4. The constants used in this model are listed in Table 4.5.

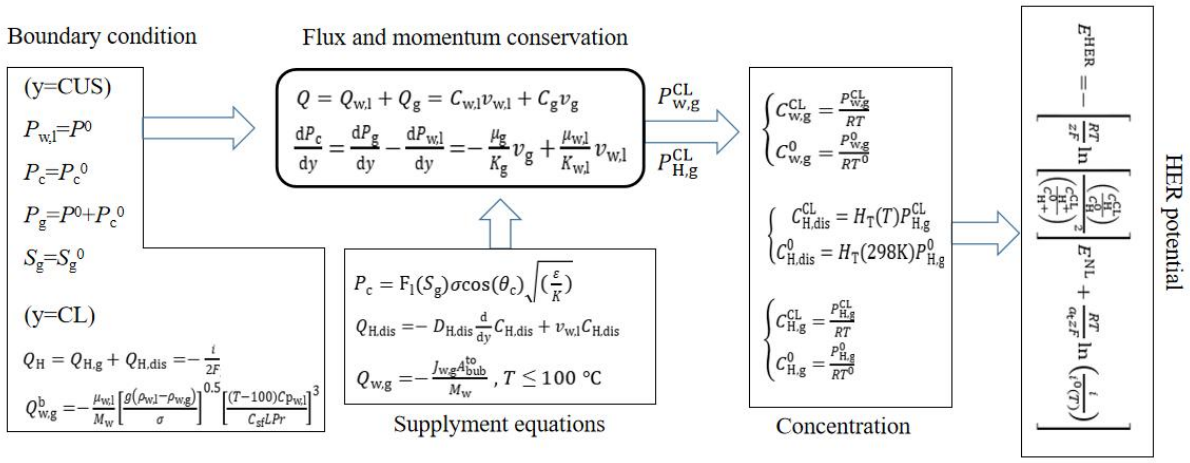

Fig. 4.4 Calculation flowchart of HER model.

Table 4.3 Nomenclature

Nomenclature

A	Bubble surface area for a unit geometric area, [-]	K	Permeability, [m^2]
C	Concentration, [$mol \cdot m^{-3}$]	L	Latent heat, [$J \cdot kg^{-1}$]
cr	Current contribution ratio, [-]	P	Pressure, [Pa]
D	Diffusion coefficient, [$m^2 \cdot s^{-1}$]	Pr	Prandtl number, [-]
E	Potential, [V]	Q	Molar flux, [$mol \cdot m^{-2} \cdot s^{-1}$]
H_T	Henry coefficient, [$mol \cdot m^{-3} \cdot Pa^{-1}$]	S	Saturation, [-]
i	Current density, [$A \cdot m^{-2}$]	T	Temperature, [K]
J	Evaporation rate, [$kg \cdot m^{-2} \cdot s^{-1}$]	v	Velocity, [$m \cdot s^{-1}$]

Greek symbols

α	Activity, [-]	μ	Dynamic viscosity, [Pa·s]
γ	Relative molar flux, [-]	ρ	Mass density, [$kg \cdot m^{-3}$]
δ	Thickness, [m]	σ	Water surface tension, [Pa·m]
ε	Porosity, [-]	τ	Relative pressure of water vapor, [-]
θc	Contact angel, [°]		

Superscripts and subscripts

b	Boiling	ls	Liquid water surrounding bubbles
bub	Bubble	H	Hydrogen
CL	Catalyst layer	CUS	Upper surface of carbon paper
dis	Dissolved	w	Water
det	Detachment	wv	Water vaporization
g	Gas	0	Standard
l	Liquid		

Table 4.4 Calculation condition.

Case	Current density ($mA \cdot cm^{-2}$)	Diffusion layer thickness (mm)	Temperature (°C)	Pressure (MPa)
1	−6.4-−31.8	0.01	88-109	0.1013
2	−1-−1024	0.11	88-109	0.1013

Table 4.5 Constants for the model.

C_{sf}	0.013	-	Surface fluid combination coefficient
$Cp_{w,l}$	4184	$J \cdot kg^{-1} \cdot K^{-1}$	Specific heat of liquid water
D	30	μm	Pore diameter of the carbon paper
d_{Pt}	3×10^{-5}	m	Diameter of Pt particle
En^{HER}	4300	$J \cdot mol^{-1}$	Anodic reference activation energy
F	96 485	$C \cdot mol^{-1}$	Faraday constant
g	9.81	$m \cdot s^{-2}$	Gravitational acceleration
H_{298K}	7.8×10^{-6}	$mol \cdot Pa^{-1} \cdot m^{-3}$	Henry coefficient of hydrogen
ΔH	4.4×10^{3}	$J \cdot mol^{-1}$	Dissolution enthalpy
i_{ref}^{0}	4.5×10^{-8}	$A \cdot cm^{-2}$	HER exchange current density
L	2.27	$MJ \cdot kg^{-1}$	Latent hear of water vaporization
L^{s}	6×10^{-9}	$kg \cdot K \cdot S \cdot m^{-4}$	Evaporation coefficient
M_{w}	18	$g \cdot mol^{-1}$	Molar mass of water
m_{Pt}	0.5	$mg \cdot cm^{-2}$	Pt load
P^{0}	101 325	Pa	Reference pressure
R	8.314	$J \cdot mol^{-1} \cdot k^{-1}$	Universal gas constant
T^{0}	298.15	K	Reference temperature
z	2	-	Number of electron transfer
a_{t}	0.5	-	Charge transfer coefficient
ε	0.6	-	Porosity of the carbon paper
θ_{c}	70	°	Contact angle of the carbon paper
μ_{s}	1.2×10^{-5}	Pa·s	Dynamic viscosity of water vapor

μ_{H}	2.47×10^{-5}	Pa·s	Dynamic viscosity of hydrogen
μ_{w}	2.822×10^{-4}	Pa·s	Dynamic viscosity of liquid water
ρ_{Pt}	11.2	$\mathrm{g\cdot cm^{-3}}$	Pt mass density
φ_{I}	0.75	-	Contact fraction of ionomer and catalyst

This section details the HER process and how boiling reduces hydrogen concentration. Boiling is expected to reduce the gaseous hydrogen partial pressure and dissolved hydrogen concentration at the CL, which is expected to reduce the HER overpotential. Therefore, to quantitatively study the effect of boiling on HER overpotential, the theoretical model includes

(1) HER process at the CL

(2) mass transfer in carbon paper

(3) water vaporization in carbon paper

These processes are introduced in the next sub-chapters.

The following sections detailedly describe the three sub-sections. The HER process includes hydrogen evolution and transfer of water and hydrogen, as shown in Fig. 4.5. In Fig. 4.5a, the WE1 model only consists of the CL, which corresponds to the experimental WE1 (Fig. 4.1b). In the case of the WE1, as shown in Fig. 4.5a, protons at the CL combine with electrons and become hydrogen molecules. Hydrogen molecules first dissolve into liquid water. Then, hydrogen gas bubbles form when the dissolved hydrogen concentration exceeds its saturation concentration [9]. For the CL under hydrogen gas bubbles, hydrogen molecules produced at the CL are directly released into the gas bubbles with a gas phase. Some water vapor is mixed into the hydrogen gas bubbles. In the following descriptions, the bubbles mixed with gaseous hydrogen and water vapor are simply named "bubbles". Different hydrogen activity in liquid water and bubbles yields different HER current densities, such as i_{l} and i_{g}. The transfer of protons under the bubble is assumed to be accessible to the catalyst layer (CL) in the model. It is noted that, even in a practical situation, protons are accessible to CL when the bubbles cover CL. This is because protons can be delivered through ionomers (proton transport media) embedded in the porous CL. Therefore, the electrolyte solution, which has a role in delivering proton to CL (Fig. 4.1a), is simplified to just behave as liquid water in the model as shown in Fig. 4.5a and Fig. 4.5b. In Fig. 4.5a, no carbon paper covers the CL of WE1, so the dissolved hydrogen and hydrogen bubbles at the CL directly drain into the flowing water, corresponding to the flowing electrolyte in the experiment. Even so, a

dissolved hydrogen diffusion layer with a thickness of about 10 μm exists on the CL surface of WE1 [9]. The diffusion layer is a thin water layer with a sharply varying dissolved hydrogen concentration. The boiling at the CL consumes liquid water, so the net flow direction of liquid water is from the bulk region toward the CL. The flowing water removed the bubbles attached to the CL, and the water velocity refers to the average velocity formed by the experimental rotor on the WE surface (1.05 $m \cdot s^{-1}$).

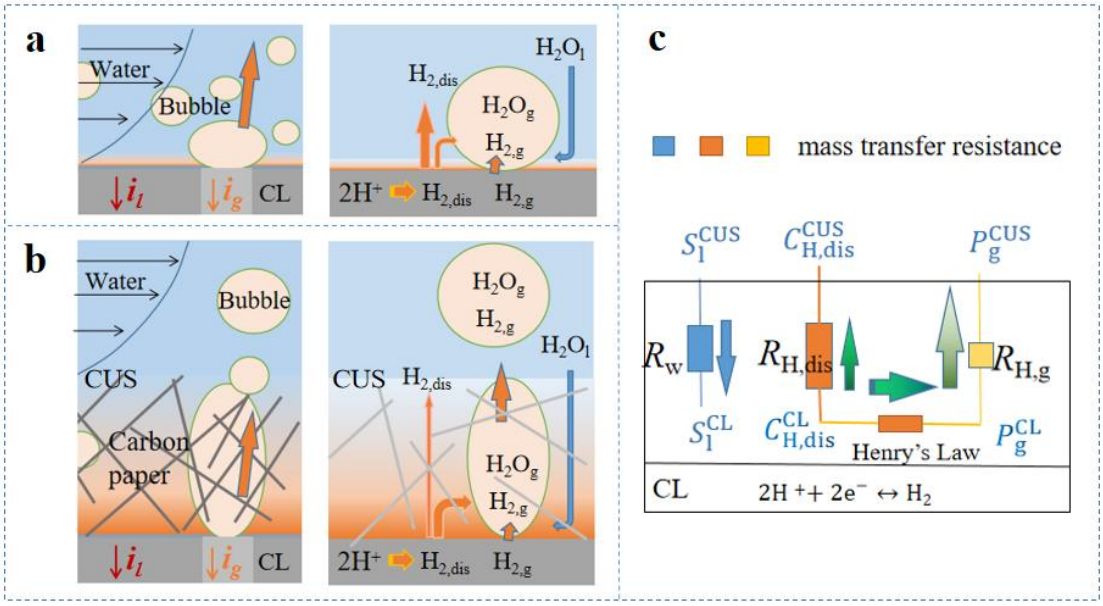

Fig. 4.5 Theoretical model. of a.WE1, b.WE2, c. transfer resistance of hydrogen gas and water

Fig. 4.5b describes the HER process of WE2, whose CL is covered with a carbon paper, corresponding to the experimental WE2 in Fig. 4.1b. The hydrogen gas bubbles at the CL flow through the carbon paper, and are drained into the bulk water. In the carbon paper, the gas saturation and capillary pressure of bubbles gradually decrease from the CL to the CUS, driving the hydrogen bubbles out of the carbon paper. Because of the high transfer resistance of dissolved hydrogen through the thick carbon paper (0.11 mm), the dissolved hydrogen has a low molar flux. Most dissolved hydrogen flows into the bubbles and is drained out of the carbon paper in gaseous hydrogen under a gradient pressure.

Fig. 4.5c especially presents the transfer resistance of liquid water, dissolved hydrogen, and bubbles during HER. This description of transfer resistance applies to WE1 and WE2. The bubbles pressure, P_g, consists of the partial pressures of gaseous hydrogen and water vapor, $P_{H,g}$ and $P_{W,g}$, then $P_g = P_{H,g} + P_{W,g}$. The bubbles' pressure at the CL, P_g^{CL}, is higher than

at the CUS, P_g^{CUS}. The pressure difference drives the bubbles to move from the CL to CUS. Dissolved hydrogen in liquid water transfers from the CL to the CUS by diffusion and convection. The transfer resistance of dissolved hydrogen, $R_{H,dis}$, depends on its transfer layer thickness. For WE1, the CL faces the flowing bulk water, and the transfer thickness of dissolved hydrogen is about 10 μm [9]. For WE2, the transfer layer thickness of dissolved hydrogen equals the carbon paper thickness, 110 μm. Therefore, dissolved hydrogen in WE2 has higher transfer resistance than in WE1.

4.4.1 Overpotential and current density

In an acidic condition, HER consumes hydrogen ions. Eq. (4.5) introduces the expression of HER in the acidic condition.

$$2H^+ + 2e^- \rightarrow H_2 \quad (4.5)$$

Eq. (4.6) introduces the HER potential, which is derived from the cathodic voltage component of the PEMWE [13].

$$E^{HER} = -\left[\frac{RT}{zF}\ln\left[\frac{\left(\frac{C_H^{CL}}{C_H^0}\right)}{\left(\frac{C_{H^+}^{CL}}{C_{H^+}^0}\right)^2}\right] + \frac{RT}{a_t zF}\ln\left(\frac{i}{i^0(T)}\right)\right] \text{ vs. SHE} \quad (4.6)$$

The first term on the right-hand side (RHS) of Eq. (4.6) is the Nernst loss of the HER, which includes the concentration overvoltage, where H and H^+ represent hydrogen gas and proton, and the second term is the activation overvoltage of the HER. In the experimental results of chapter 4.3, the ohmic overvoltage of the HER was removed by IR correction. Therefore, Eq. (4.6) omits ohmic overvoltage. In addition, boiling cannot change the proton transfer in the ionomer and the electrons conduction in the electrode. In Eq. (4.6), the exchange current density of HER, i_0(T), is defined at which the hydrogen gas and proton concentrations are standard values. At 25 °C and 0.1013 MPa, the C_H^0 represents the standard hydrogen gas concentration, and $C_{H^+}^0$ represents the standard proton concentration, which is 1 M. The z is the number of electron transfers, which is 2 in HER, and a_t is the charge transfer coefficient of HER, which is 0.5.

Derived from Eq. (4.6), the HER overpotential is defined with reference to the SHE potential as Eq. (4.7), which is related to the HER current density and the concentrations of

hydrogen gas and proton at the CL. Under SHE, the proton concentration is 1-M, then $C_{H^+}^{CL}/C_{H^+}^{0}$=1. If the hydrogen activity, C_{H}^{CL}/C_{H}^{0}, is rather less than 1, the Nernst loss can be negative, contributing to a lower HER potential.

$$\Delta E = E^{SHE} - E^{HER} = 0 - E^{HER} = \frac{RT}{a_t zF} ln\left(\frac{i}{i^0(T)}\right) + \frac{RT}{zF}\ln\left[\frac{\left(\frac{C_H^{CL}}{C_H^0}\right)}{\left(\frac{C_{H^+}^{CL}}{C_{H^+}^0}\right)^2}\right]$$

$$= \frac{RT}{a_t zF} ln\left(\frac{i}{i^0(T)}\right) + \frac{RT}{zF}\ln\left(\frac{C_H^{CL}}{C_H^0}\right) \quad (4.7)$$

Eq. (4.8) shows the HER current density, obtained from a simple mathematical transformation of Eq. (4.7).

$$i = i^0(T)\left(\frac{C_H^0}{C_H^{CL}}\right)^{a_t} \exp\left(\frac{za_tF\Delta E}{RT}\right) \quad (4.8)$$

The value of $\frac{C_H^0}{C_H^{CL}}$ in this equation is just the inverse of hydrogen gas activity. Precisely speaking, it suggests both dissolved hydrogen in liquid water and gaseous hydrogen in bubbles, and the two have different activities.Therefore, HER can generate different current densities in liquid water and bubbles (marked by a thick dashed line), as shown in Fig. 4.6.

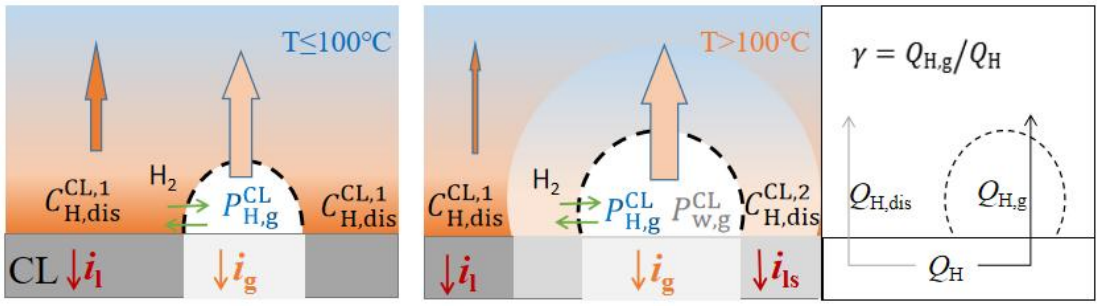

Fig. 4.6 Current density in liquid water and bubbles.

The relation between the gaseous hydrogen pressure and the dissolved hydrogen concentration obeys Henry's law [14]. Below 100 °C, the bubbles are dominated by gaseous hydrogen followed by water vapor. There are three HER current components at the CL. One is i_g, with gaseous hydrogen as the product. The other is i_l, with dissolved hydrogen as a product. The third i_{ls} only appears at boiling. Above 100 °C, boiling vaporizes a large amount of water vapor to reduce the partial pressure of gaseous hydrogen. Then, the concentration of dissolved hydrogen surrounding the bubbles also decreases with the lower partial pressure of gaseous hydrogen. The i_{ls} with low hydrogen activity is higher than i_l. The bubbles with low hydrogen

partial pressure can attract more dissolved hydrogen to flow into the bubbles. Then, the molar flux of gaseous hydrogen through the bubbles will increase, which can be evaluated with a relative value of gaseous hydrogen molar flux, $\gamma = Q_{\mathrm{H,g}}/Q_{\mathrm{H}}$, as Fig. 4.6. $Q_{\mathrm{H,g}}$ is the molar flux of gaseous hydrogen, while Q_{H} is the total molar flux of hydrogen gas. Replacing $\frac{C_{\mathrm{H}}^{0}}{C_{\mathrm{H}}^{CL}}$ with $\frac{C_{\mathrm{H,g}}^{0}}{C_{\mathrm{H,g}}^{CL}}$ in Eq. (4.8) provides the expression of HER current density in the bubbles:

$$i_{\mathrm{g}} = i^{0}(T)\left(\frac{C_{\mathrm{H,g}}^{0}}{C_{\mathrm{H,g}}^{\mathrm{CL}}}\right)^{a_t}\exp\left(\frac{za_tF\Delta E}{RT}\right) \quad (4.9)$$

The gaseous hydrogen in the bubbles is regarded as an ideal gas, and the concentration of gaseous hydrogen is obtained in Eq. (4.10). Superscript "0" means under standard conditions of 25 °C and 0.1013 MPa.

$$\begin{cases} C_{\mathrm{H,g}}^{\mathrm{CL}} = \frac{P_{\mathrm{H,g}}^{\mathrm{CL}}}{RT} \\ C_{\mathrm{H,g}}^{0} = \frac{P_{\mathrm{H,g}}^{0}}{RT^{0}} \end{cases} \quad (4.10)$$

Similar to Eq. (4.9), the current density in liquid water far from bubbles is

$$i_l = i^{0}(T)\left(\frac{C_{\mathrm{H,dis}}^{0}}{C_{\mathrm{H,dis}}^{\mathrm{CL,1}}}\right)^{a_t}\exp\left(\frac{za_tF\Delta E}{RT}\right) \quad (4.11)$$

The dissolved hydrogen concentration, $C_{\mathrm{H,dis}}^{\mathrm{CL,1}}$, is the key parameter to solve Eq. (4.11). As shown in Fig. 4.6, $C_{\mathrm{H,dis}}^{\mathrm{CL,1}}$ represents the concentration of dissolved hydrogen far from bubbles, which is not affected by boiling. Henry's law [15] shows the relationship between the dissolved hydrogen concentration and the gaseous hydrogen pressure in Eq. (4.12).

$$\begin{cases} C_{\mathrm{H,dis}}^{\mathrm{CL,1}} = H_{\mathrm{T}}(T)P_{\mathrm{H,g}}^{\mathrm{CL}} \\ C_{\mathrm{H,dis}}^{0} = H_{\mathrm{T}}(T^{0})P_{\mathrm{H,g}}^{0} \end{cases} \quad (4.12)$$

Henry's coefficient of dissolved hydrogen is temperature-dependent as Eq. (4.13). In Eq. (4.13), ΔH is the dissolution enthalpy of hydrogen.

$$H_{\mathrm{T}} = H_{298\mathrm{K}}\exp\left[\frac{-\Delta H}{\mathrm{R}}\left(\frac{1}{T}-\frac{1}{T^{0}}\right)\right] \quad (4.13)$$

The current density in liquid water surrounding bubbles is,

$$i_{\mathrm{ls}} = i^{0}(T)\left(\frac{C_{\mathrm{H,dis}}^{0}}{C_{\mathrm{H,dis}}^{\mathrm{CL,2}}}\right)^{a_t}\exp\left(\frac{za_tF\Delta E}{RT}\right) \quad (4.14)$$

where $C_{\mathrm{H,dis}}^{\mathrm{CL,2}}$ represents the concentration of dissolved hydrogen surrounding bubbles as shown in Fig. 4.6. The $C_{\mathrm{H,dis}}^{\mathrm{CL,2}}$ is one influenced by boiling, and is lower than $C_{\mathrm{H,dis}}^{\mathrm{CL,1}}$. This is because, as mentioned above, boiling produces water vapor, and reduces the water vapor pressure and increases hydrogen gas pressure in the bobble, resulting in a smaller

concentration of dissolved hydrogen. Both $C_{\mathrm{H,dis}}^{\mathrm{CL},1}$ and $C_{\mathrm{H,dis}}^{\mathrm{CL},2}$ refer to the dissolved hydrogen concentration in liquid water. Still, the $C_{\mathrm{H,dis}}^{\mathrm{CL},1}$ refers specifically to the high dissolved hydrogen concentration not affected by boiling, and the $C_{\mathrm{H,dis}}^{\mathrm{CL},2}$ refers to the low dissolved hydrogen concentration which can be changed by boiling. During boiling, the concentration of dissolved hydrogen surrounding the bubbles plummeted from $C_{\mathrm{H,dis}}^{\mathrm{CL},1}$ to $C_{\mathrm{H,dis}}^{\mathrm{CL},2}$, as shown in Fig. 4.6.

The HER in liquid water and bubbles produces different current densities. The following equation shows the relationship between partial current density and the applied average current density, where the gas saturation at the CL, $S_{\mathrm{g}}^{\mathrm{CL}}$, approximates the bubbles' coverage fraction at the CL [16].

$$i = S_{\mathrm{g}}^{\mathrm{CL}} i_{\mathrm{g}} + (1 - S_{\mathrm{g}}^{\mathrm{CL}})\gamma i_{\mathrm{ls}} + \left(1 - S_{\mathrm{g}}^{\mathrm{CL}}\right)(1 - \gamma) i_{\mathrm{l}} \quad (4.15)$$

As shown in Fig. 4.6, the hydrogen produced by the CL is expelled in dissolved and gaseous states, forming respective molar fluxes. Among them, boiling cannot decrease the concentration of dissolved hydrogen discharged through the liquid water, such as $C_{\mathrm{H,dis}}^{\mathrm{CL},1}$. The γ in Eq. (4.15) is the ratio of gaseous hydrogen molar flux, $Q_{\mathrm{H,g}}$, to the sum of Q_{H}, as plotted in Fig. 4.6. The dissolved hydrogen molar flux, $Q_{\mathrm{H,dis}}$, is also shown in this figure. The relative molar flux of dissolved hydrogen discharged through liquid water, 1-γ, is the fraction of dissolved hydrogen whose concentration is not changed by boiling. Accordingly, the relative molar flux of dissolved hydrogen flowing into the bubbles and expelling through bubbles approaches the relative molar flux of gaseous hydrogen, γ, which is the fraction of dissolved hydrogen whose concentration is lowered by boiling.

Knowing which current density component is the highest can inspire how to optimize the HER performance. The current contribution ratio, cr_{x}, can evaluate how much the respective HER current component is. Eq.s. (4.16-4.18) lists the contribution ratio of the three HER current components. Each current contribution ratio is less than 1, and the sum of the three components equals 1.

For the CL in the bubbles:

$$cr_{\mathrm{g}} = \frac{i_{\mathrm{g}} S_{\mathrm{g}}^{\mathrm{CL}}}{i} \quad (4.16)$$

For the CL in liquid water far from bubbles:

$$cr_{\mathrm{l}} = \frac{(1-S_{\mathrm{g}}^{\mathrm{CL}})(1-\gamma)i_{\mathrm{l}}}{i} \quad (4.17)$$

For the CL in liquid water surrounding bubbles:

$$cr_{\mathrm{ls}} = \frac{(1-S_{\mathrm{g}}^{\mathrm{CL}})\gamma i_{\mathrm{ls}}}{i} \quad (4.18)$$

γ can be used to approximate the fractional coverage of the boiling effect on the dissolved hydrogen since the dissolved hydrogen near the bubbles eventually flows into the bubbles.

4.4.2 Dissolved hydrogen transfer

The concentration of dissolved hydrogen in CL is related to its transfer process. The dissolved hydrogen concentration at the CL determines i_{ls} and i_{l}, as shown in Fig. 4.6. Dissolved hydrogen in liquid water transfers by diffusion and convection. The transfer equation for dissolved hydrogen is simplified to a one-dimensional model along the vertical direction, y, of facing the CL.

$$Q_{\mathrm{H,dis}} = -D_{\mathrm{H,dis}}\frac{\mathrm{d}}{\mathrm{d}y}C_{\mathrm{H,dis}} + v_{\mathrm{w,l}}C_{\mathrm{H,dis}} \quad (4.19)$$

where $Q_{\mathrm{H,dis,}}$ $D_{\mathrm{H,dis}}$ and $C_{\mathrm{H,dis}}$ represent the molar flux, diffusion coefficient, and concentration of dissolved hydrogen in liquid water, respectively. The $v_{\mathrm{w,l}}$ is the liquid water velocity. Integrating Eq. (4.19) can determine the concentration of dissolved hydrogen at the CL with the boundary condition, $C_{\mathrm{H,dis}}{}^{\mathrm{CUS}}$ (dissolved hydrogen at the CH/carbon paper interface).

$$C_{\mathrm{H,dis}}^{\mathrm{CL}} = C_{\mathrm{H,dis}}^{\mathrm{CUS}}\exp\left(\frac{\delta v_{\mathrm{w,l}}}{D_{\mathrm{H,dis}}}\right) + \frac{Q_{\mathrm{H,dis}}}{v_{\mathrm{w,l}}}\left[1-\exp\left(\frac{\delta v_{\mathrm{w,l}}}{D_{\mathrm{H,dis}}}\right)\right] \quad (4.20)$$

Eq. (4.20) can determine the dissolved hydrogen concentration at the CL, $C_{\mathrm{H,dis}}^{\mathrm{CL}}$, which can represent $C_{\mathrm{H,dis}}^{\mathrm{CL,1}}$ or $C_{\mathrm{H,dis}}^{\mathrm{CL,2}}$. Flowing water with a velocity, $v_{\mathrm{w,l}}$, dilutes the dissolved hydrogen concentration at the CUS close to 0. If the dissolved hydrogen concentration at CUS is 0, the dissolved hydrogen concentration at the CL is

$$C_{\mathrm{H,dis}}^{\mathrm{CL}} = \frac{Q_{\mathrm{H,dis}}}{v_{\mathrm{w,l}}}\left[1-\exp\left(\frac{\delta v_{\mathrm{w,l}}}{D_{\mathrm{H,dis}}}\right)\right] \quad (4.21)$$

4.4.3 Liquid-gas transfer in the carbon paper

The liquid-gas transfer equation in the transfer layer can determine the unknown molar

flux of dissolved hydrogen, $Q_{\mathrm{H,dis}}$, in Eq. (4.21). The dissolved hydrogen transfers by convection and diffusion, while gaseous hydrogen and water vapor are expelled through bubbles, as shown in Fig. 4.5. The bubbles' pressure consists of the partial pressures of gaseous hydrogen and water vapor. The molar flux equation and momentum conservation for the liquid-gas flow are introduced to determine the partial pressure of gaseous hydrogen and the concentration of dissolved hydrogen. In addition, boundary conditions for solving the transfer equations are also introduced. The liquid-gas transfer equation applies to WE1 and WE2. To facilitate the interpretation of the transfer equation, the CUS (upper surface of carbon paper) position of WE2 also refers to the upper boundary of the thin transfer layer (10 μm thickness) of WE1.

Molar flux

This section introduces the molar fluxes of water and hydrogen gas. The flow direction from the CUS to the CL is defined as the positive direction. Because no water is required in HER process, the net water molar flux, including liquid water and water vapor through the carbon paper, Q_{w}, is 0. Liquid water with a positive molar flux flows from the CUS to CL. The molar flux of water vapor is negative because water vapor produced by evaporation or boiling flows from the CL to the CUS.

$$Q_{\mathrm{w}} = Q_{\mathrm{w,l}} + Q_{\mathrm{w,g}} = 0 \quad (4.22)$$

According to Faraday's law, Eq. (4.23) gives the hydrogen molar flux, Q_{H}, as the sum of the molar fluxes of gaseous hydrogen, $Q_{\mathrm{H,g}}$, and dissolved hydrogen, $Q_{\mathrm{H,dis}}$.

$$Q_{\mathrm{H}} = Q_{\mathrm{H,g}} + Q_{\mathrm{H,dis}} = -\frac{i}{2F} \quad (4.23)$$

The hydrogen generated at the CL flows towards the CUS, whose molar flux is negative. The hydrogen molar flux at the CL/carbon paper interface is a boundary condition for the transfer equation.

In the bubbles, the molar fluxes of gaseous hydrogen and water vapor determine the partial pressure of water vapor. Because the water vapor is continuously carried out of the carbon paper by the gaseous hydrogen, the partial pressure of the water vapor is in a non-equilibrium state. Therefore, the partial pressure of water vapor is related to its molar flux rather than the saturation vapor pressure. As Eq. (4.24), in bubbles, τ is the ratio of the water vapor molar flux, $Q_{\mathrm{w,g}}$, to the molar flux sum of gaseous hydrogen and water vapor. The τ is

also the relative pressure of water vapor, which is the ratio of water vapor's partial pressure to the bubbles' pressure [17].

$$\tau = \frac{Q_{\mathrm{w,g}}}{Q_{\mathrm{w,g}}+Q_{\mathrm{H,g}}} = \frac{P_{\mathrm{w,g}}}{P_{\mathrm{g}}} \quad (4.24)$$

From the mathematical transformation of Eq. (4.24), the molar flux of the water vapor in bubbles is

$$Q_{\mathrm{w,g}} = \frac{\tau Q_{\mathrm{H,g}}}{1-\tau} \quad (4.25)$$

And the molar flux of liquid water, $Q_{\mathrm{w,l}}$, according to Eq. (4.22) is determined as follows.

$$Q_{\mathrm{w,l}} = 0 - \frac{\tau Q_{\mathrm{H,g}}}{1-\tau} = -\frac{\tau Q_{\mathrm{H,g}}}{1-\tau} \quad (4.26)$$

The water vapor molar flux can change the partial pressure of gaseous hydrogen in the bubbles, usually depending on the temperature of water vaporization. Below the boiling temperature, liquid water is rather slowly evaporated to water vapor. The evaporation flux with a unit of $\mathrm{mol \cdot m^{-2} \cdot s^{-1}}$ is expressed in Eq. (4.27),

$$Q_{\mathrm{w,g}} = -\frac{J_{\mathrm{w,g}} A_{\mathrm{bub}}^{\mathrm{to}}}{M_{\mathrm{w}}}, T \leq 100\ ^{\circ}\mathrm{C} \quad (4.27)$$

where $J_{\mathrm{w,g}}$ is the water evaporation rate [18], which has been introduced as Eq. (3.52), and $A_{\mathrm{bub}}^{\mathrm{to}}$ is the relative evaporation area in a unit geometric area, which is a crucial parameter of determining the molar flux of water vapor at evaporation. M_{w} is the molar mass of water, which is 0.018 $\mathrm{kg \cdot mol^{-1}}$. The relative evaporation area, $A_{\mathrm{bub}}^{\mathrm{to}}$, is the ratio of the total side-wall surface area for all bubbles in the carbon paper to a unit geometric area. It is a non-dimensional value, and it has been derived in chapter 3.2.3. When the water temperature exceeds the boiling point, the water vapor molar flux is increased by boiling based on evaporation, as shown in Eq. (4.28).

$$Q_{\mathrm{w,g}} = -\frac{J_{\mathrm{w,g}} A_{\mathrm{bub}}^{\mathrm{to}}}{M_{\mathrm{w}}} + Q_{\mathrm{w,g}}^{\mathrm{b}}, T > 100\ ^{\circ}\mathrm{C} \quad (4.28)$$

where the water vapor molar flux at boiling, $Q_{\mathrm{w,g}}^{\mathrm{b}}$, is a boundary condition at the CL/carbon paper interface for transfer equation.

$$Q_{\mathrm{w,g}}^{\mathrm{b}} = -\frac{\mu_{\mathrm{w,l}}}{M_{\mathrm{w}}}\left[\frac{g(\rho_{\mathrm{w,l}}-\rho_{\mathrm{w,g}})}{\sigma}\right]^{0.5}\left[\frac{(T-100)C_{\mathrm{pw,l}}}{C_{\mathrm{sf}} L Pr}\right]^{3} \quad (4.29)$$

where L is the latent heat of water vaporization, g is the gravitational acceleration, $Cp_{\mathrm{H2O,l}}$ is the specific heat capacity of liquid water, C_{sf} is the surface fluid coupling coefficient, and Pr is the Prandtl number.

Ultimately, the fluid in the carbon paper, which consists of liquid water, water vapor,

and gaseous hydrogen, obeys the total molar flux as Eq. (4.30) [19]. The total molar flux, Q, is a crucial parameter when solving the molar flux and momentum equations.

$$Q = Q_{w,l} + Q_g = C_{w,l}v_{w,l} + C_g v_g \quad (4.30)$$

Momentum conservation

To determine the molar fluxes above (liquid water, water vapor, and gaseous hydrogen), momentum equations are required. The pressure gradient of liquid water forms its velocity, $v_{w,l}$, as Eq. (4.31) [19], where $K_{w,l}$ and $\mu_{w,l}$ are the permeability and dynamic viscosity of liquid water.

$$\frac{dP_{w,l}}{dy} = -\frac{\mu_{w,l}}{K_{w,l}} v_{w,l} \quad (4.31)$$

The permeability of liquid water can be obtained from Eq. (4.32), where K is the fluid permeability coefficient in carbon paper, $S_{w,l}$ is the saturation of liquid water, and S_g is the gas saturation [19].

$$K_{w,l} = K{S_{w,l}}^3 = K(1 - S_g)^3 \quad (4.32)$$

Eq. (4.33) gives the fluid permeability coefficient in the carbon paper, where D is the average pore diameter of the carbon paper, and ε is the porosity of the carbon paper [19].

$$K = \frac{D^2\varepsilon^3}{180(1-\varepsilon)^2} \quad (4.33)$$

The momentum equation for gas transfer is introduced as follows. Similarly, the gas pressure gradient forms the gas velocity, v_g, where K_g is the gas permeability, and μ_g is the gas dynamic viscosity.

$$\frac{dP_g}{dy} = -\frac{\mu_g}{K_g} v_g \quad (4.34)$$

The relationship between gas permeability and saturation is shown in Eq. (4.35).

$$K_g = K{S_g}^3 \quad (4.35)$$

The pressure difference between bubbles and liquid water is the capillary pressure, P_c. Eq. (4.36) provides the gradient of capillary pressure after Eq. (4.34) subtracting Eq. (4.31).

$$\frac{dP_c}{dy} = \frac{dP_g}{dy} - \frac{dP_{w,l}}{dy} = -\frac{\mu_g}{K_g} v_g + \frac{\mu_{w,l}}{K_{w,l}} v_{w,l} \quad (4.36)$$

The additional equations of capillary pressure is supplemented to solve Eq. (4.36) [20].

$$P_c = \sigma\cos(\theta_c)\sqrt{\left(\frac{\varepsilon}{K}\right)}\ \mathrm{F_l}(S_g) \quad (4.37)$$

where the Leverett function, $\mathrm{F_l}(S_g)$, is expressed in Eq. (4.38).

$$F_l(S_g) = 1.417S_g - 2.12{S_g}^2 + 1.263{S_g}^3 \quad (4.38)$$

Combining the above molar flux and momentum equations (Eq. (4.30) and Eq. (4.36)) can determine the gas saturation at the CL. Specifically, the molar flux and capillary pressure equations are substituted into the momentum conservation equation. The boundary conditions of the transfer equation, such as gas saturation (S_g^0), gas pressure (P_g), and the pressure of liquid water ($P_{w,l}$) at the CUS, are determined by bulk water velocity and operating pressure, which is the same as the boundary conditions of the OER model described in chapter 3.2.3. The velocity of the liquid water at the CUS is 1.05 $m \cdot s^{-1}$, corresponding to the rotor rotating speed of 2000 $r \cdot min^{-1}$. The gas pressure at the CUS is the average pressure of the bubbles in one growth cycle. The capillary pressure at CUS is obtained by subtracting the pressure of liquid water from the bubble pressure. Then, the gas saturation at the CUS can be determined from the capillary pressure. The pressure of liquid water is equal to the operating pressure P^0 (0.1013 MPa).

4.5 Theoretical results and discussions

Chapter 4.5 introduces the results in the following two parts. The first section compares the theoretical and experimental results of WE1 and WE2, and verifies the model's accuracy. In the second section, we theoretically analyze how boiling changes the hydrogen transfer and HER overpotential for WE2 which approximates the PEMWE cathode structure. The results confirm that boiling enhances liquid-gas transfer and reduces the partial pressure of gaseous hydrogen and dissolved hydrogen concentration, reducing the HER overpotential.

4.5.1 HER model verification

Validating the model's correctness is crucial for accurately revealing the boiling effect on HER. The Pt load in the HER model is 0.5 $mg \cdot cm^{-2}$, as shown in Table 4.5. The electrochemical exchange current density in the model is 4.5×10^{-8} $A \cdot cm^{-2}$, taken from the experimental results in chapter 4.3.1. This section shows the overpotentials of WE1 and WE2 as a function of temperature. For the WE1, no carbon paper covers the CL surface, and only a 10-μm-thickness transfer layer of dissolved hydrogen exists on the CL [9]. For the WE2, a

110-μm-thickness carbon paper covers the CL surface. Fig. 4.7 compares the experimental and theoretical HER overpotentials for the two WEs. The overpotential, ΔE, is the potential difference between the HER potential, E, and the standard hydrogen electrode potential, E^{SHE}.

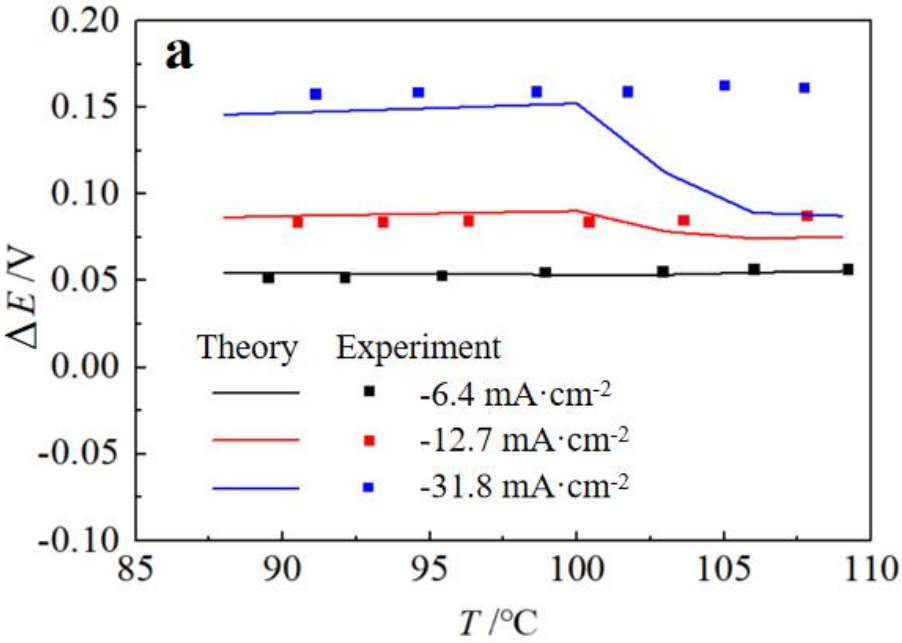

a.WE1 overpotential

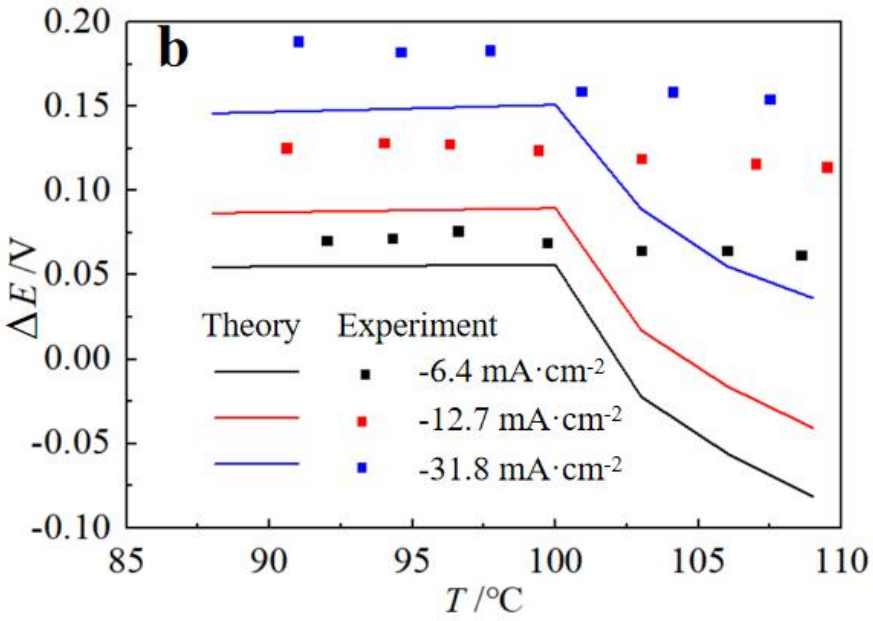

b. WE2 overpotential

Fig. 4.7 Comparison of HER overpotential in experiment and theory.

Fig. 4.7a compares the theoretical and experimental overpotentials for the WE1, where the CL is not covered by the carbon paper. The theoretical and experimental overpotentials

below 100 °C agree well. At -6.4 mA·cm^{-2}, the theoretical and experimental overpotentials above 100 °C do not significantly decrease. Because most of the dissolved hydrogen is expelled through the liquid water, boiling cannot effectively reduce the concentration of the dissolved hydrogen. Then, the Nernst loss cannot be reduced according to Eq. (4.7). At -12.7 and -31.8 mA·cm^{-2}, the theoretical overpotential starts to decrease when the temperature exceeds 100 °C, while the experimental overpotential did not decrease significantly. At higher current densities, the theoretical model fails to accurately reproduce the constant trend of the experimental overpotentials at boiling. A possible explanation is presented as follows. At higher current densities (-12.7 and -31.8 mA·cm^{-2}), the proportion of gaseous hydrogen passing through the bubbles to the total hydrogen gas increases. Boiling can effectively reduce the hydrogen concentration in CL, as depicted in Figure 4.6. Then, the Nernst loss will be reduced by boiling. In the experiments, the CL under the bubble could not conduct HER, and the reduced reaction area increased the activation overvoltage. The increase in activation overpotential and the decrease in Nernst loss may keep the HER overpotential unchanged in the experiment. In the model, the CL under the bubble is set to perform HER. Since bubbles do not reduce the theoretical activation overpotential, the theoretical HER overpotential decreases only with Nernst loss during boiling. However, the model has not yet been able to precisely clarify the specific reasons for the experimental and theoretical difference, which can be a topic for future research.

Fig. 4.7b compares the theoretical and experimental overpotentials for the WE2. In Fig. 4.7b, at -6.4 mA·cm^{-2}, both theoretical and experimental overpotentials decrease above 100 °C. Since the 0.11-mm-thickness carbon paper covers the CL of WE2, the large transfer resistance of the dissolved hydrogen through liquid water derives more dissolved hydrogen surrounding bubbles to flow into the bubbles. Boiling can only reduce the gaseous hydrogen partial pressure in the bubbles and the dissolved hydrogen concentration surrounding the bubbles. Therefore, for the WE2, most of the dissolved hydrogen in the CL can be boiled to reduce the concentration, effectively decreasing the Nernst loss. At -12.7 and -31.8 mA·cm^{-2}, the theoretical and experimental overpotentials also decrease above 100 °C. The reason for this is also that boiling reduces most of the hydrogen concentration in the CL, at -6.4 mA·cm^{-2}. At the three current densities (-6.4, -12.7 and -31.8 mA·cm^{-2}) over 100 °C, the decrease in theoretical WE2 overpotential is more significant than the experimental one. The effect of boiling to reduce the overpotential is weakened in the experiment, which may be related to the reduction of the reaction area by bubbles. The HER models have the same structure as experimental working electrode 2. Both the theoretical model and experiment have a porous

transfer layer (PTL) on the catalyst layer (CL). Therefore, the model structure is not the reason to cause the huge difference between the theoretical and experimental HER overpotentials. However, the theoretical model assumes that the proton as a reactant for HER is supplied from CL. This is a point to consider the difference. In the HER experiment, the bubbles, mixing hydrogen and water vapor, prevented the electrolyte from flowing into the CL. The protons in the electrolyte cannot be supplied to the CL under the bubble. Therefore, the CL under the bubbles cannot conduct HER, and then the bubbles reduce the reaction area of HER and increase the activation overvoltage. On the other hand, the Nernst loss of HER can be reduced by boiling. Moreover, the decreased value of Nernst loss is thought to be slightly larger than the increased value of activation overvoltage. Therefore, the overpotential of the experimental HER only decreases slightly at temperatures above the boiling point (100 °C). When the author utilizes a practical PEMWE and examines the HER overpotential, the bubbles will not change the activation overvoltage for HER, because protons are supplied from CL side through the polymer electrolyte membrane. Namely, HER can be performed even when the bubble covers the CL. This situation of experimental PEMWE is reproduced in the theoretical model for HER. Therefore, the theoretical overpotential of HER drops more than the experimental one at boiling, when we utilize the three electrodes cell in Chapter 4.

To sum up, for WE1 and WE2, the theoretical model has a qualitative agreement with the experiment. HER models employing similar transfer equations did not match theoretical and experimental results well for the WE1 compared to OER. The exploration of its reasons can be a research topic in the future.

4.5.2 Boiling effect on HER overpotential of the WE2

Because the WE2 model structure is closer to the cathode of the practical PEMWE, this sub-sub chapter specifically investigates the mechanism that boiling decreases the HER overpotential of the WE2. Elucidating the effect of boiling on mass transfer is critical to clarifying how boiling reduces HER overpotentials. Here, to elucidate it, a further theoretical analysis is conducted. The HER temperature gradually increases from 88 to 109 °C, covering the unboiled and boiled temperature range. The current density increases from 0.001 to 1.024 $A \cdot cm^{-2}$ to analyze whether boiling reduces the HER overpotential at any current density. Additionally, the broad current density range predicts the tendency of how much boiling decreases the HER overpotential with current density. Fig. 4.8 shows the effect of temperature and current density on essential values at the CL:

- partial pressure of gaseous hydrogen, $P_{H,g}$;

- dissolved hydrogen concentration at the CL, $C_{H,dis}^{CL}$;

- the relative flux of gaseous hydrogen, γ ;

-gas saturation at the CL, S_g^{CL}.

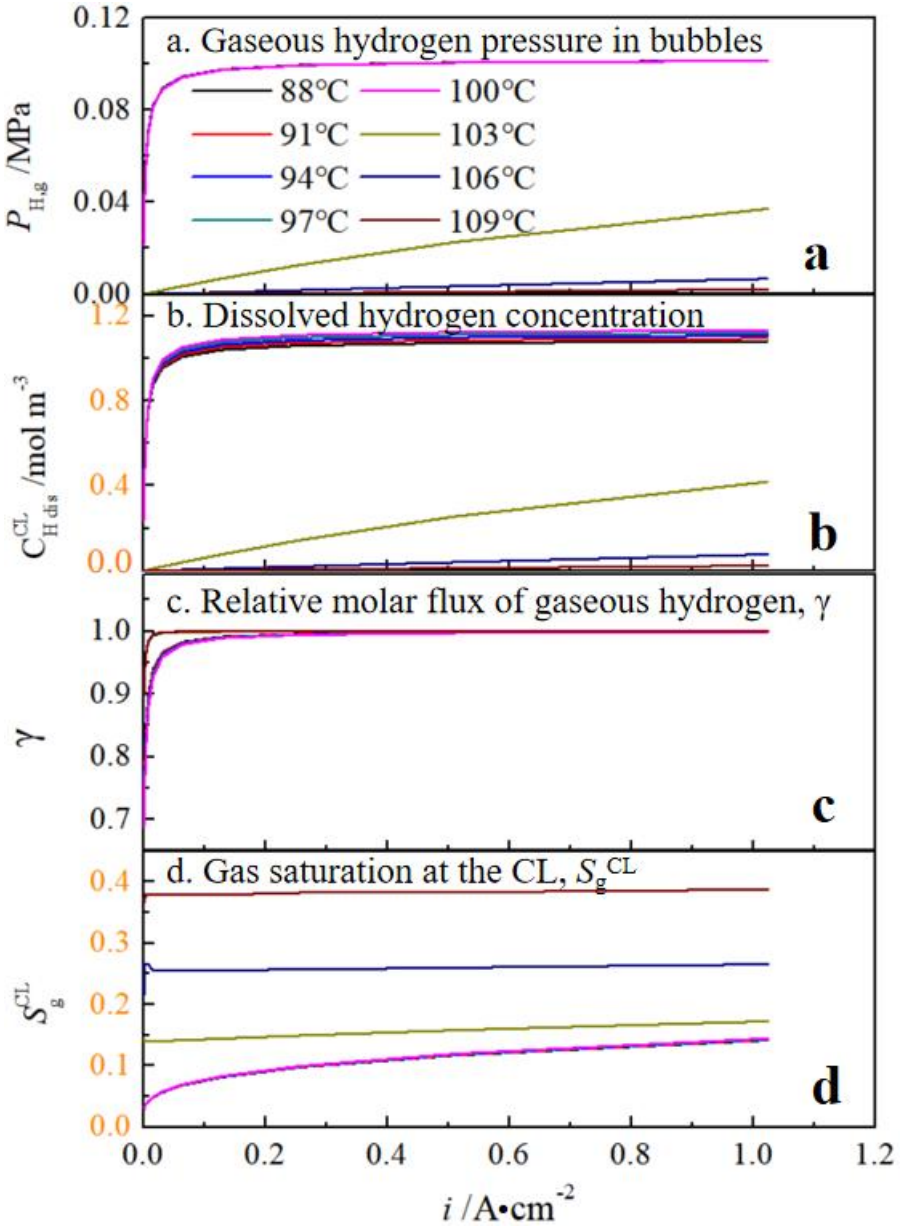

Fig. 4.8 Essential values of mass transfer at the CL. a. gaseous hydrogen partial pressure in bubbles, $P_{H,g}$; b. dissolved hydrogen concentration, $C_{H,dis}^{CL}$; c. relative molar flux of gaseous hydrogen, γ; d. gas saturation at the CL, S_g^{CL}.

Fig. 4.8a shows the partial pressure of gaseous hydrogen at the CL. Below 100 °C, the partial pressure of gaseous hydrogen increases with current density to a maximum of about 0.1 MPa. This is because the molar flux of gaseous hydrogen increases with current density,

forming a higher partial pressure in the bubbles. At boiling, the water vapor molar flux in the bubbles surges, drastically reducing the partial pressure of gaseous hydrogen. Above the boiling point, the boiling rate increases with the temperature. At 109 °C, the water vapor generated by boiling makes the partial pressure of gaseous hydrogen approach 0 MPa, which will significantly reduce the Nernst loss of HER in the bubbles.

Fig. 4.8b shows the dissolved hydrogen concentration surrounding the bubbles. According to Henry's law, the dissolved hydrogen concentration is limited by the partial pressure of the gaseous hydrogen,, which shows consistent variation trends with the partial pressure of the gaseous hydrogen (Fig. 4.8a). Below 100 °C, limited by the maximum pressure of gaseous hydrogen in the bubble (0.1 MPa), the maximum concentration of dissolved hydrogen reaches 1.15 $mol \cdot m^{-3}$. When the temperature exceeds 100 °C, the dissolved hydrogen concentration decreases as the boiling temperature increases. At 109 °C, the concentration of dissolved hydrogen is close to 0 $mol \cdot m^{-3}$, because the partial pressure of gaseous hydrogen is close to 0 MPa (Fig. 4.8a). Boiling is expected to reduce the dissolved hydrogen concentration and decrease the HER overpotential in liquid water.

Fig. 4.8c shows the relative molar flux of gaseous hydrogen through the bubbles. At 0.001 $A \cdot cm^{-2}$ and below 100 °C, the relative molar flux of gaseous hydrogen is less than 0.9. Above 100 °C, the relative molar flux is increased to 0.99. During boiling, the low partial pressure of gaseous hydrogen attracts more dissolved hydrogen into the bubbles, increasing the relative molar flux of gaseous hydrogen. At 1.024 $A \cdot cm^{-2}$, boiling can substantially reduce the partial pressure of gaseous hydrogen (Fig. 4.8a) in bubbles. Then, the dissolved hydrogen concentration surrounding the bubble also decreases. The concentration difference of dissolved hydrogen far from the bubbles and around the bubbles increases, thereby increasing the molar flux of dissolved hydrogen into the bubbles. The relative molar flux of gaseous hydrogen expelled through bubbles exceeds 0.99, meaning that the relative molar flux of the dissolved hydrogen expelled through liquid water is below 0.01. Boiling cannot reduce the concentration of this dissolved hydrogen far from bubbles but can reduce the concentration of the dissolved hydrogen surrounding the bubbles. The concentration of dissolved hydrogen, which is far from bubbles and whose relative molar flux is below 1%, cannot be reduced by boiling. Accordingly, the concentration of more than 99% of the dissolved hydrogen can be reduced by boiling. Since boiling can reduce most of the hydrogen concentration, boiling can effectively reduce the HER overpotential.

Boiling can change the gas coverage fraction at the CL. The fractional coverage of the CL by the gas is approximately equal to the gas saturation at the CL. Fig. 4.8d shows the gas saturation at the CL as a function of current density and temperature. Below 100 °C, gas saturation increases monotonically with current density due to an increase in the molar flux of gaseous hydrogen. Below 100 °C, the molar flux of water vapor under evaporation is low. At 88-100 °C, the bubbles mainly consist of gaseous hydrogen, and the gas saturation at 88-100 °C is close at each current density. In Fig. 4.8d, the saturation vs. current density curves at 88-100 °C are overlapped. Above 100 °C, the molar flux of water vapor is dramatically increased at boiling. The gas saturation at the CL is 0.15 at 103 °C, 0.25 at 106 °C, and 0.38 at 109 °C. Boiling increases the bubbles' coverage fraction on the CL, which will increase the current contribution ratio of the HER occurring in the bubbles.

Another effect of boiling on HER is accelerating water and gas transfer in the carbon paper. Fig. 4.9 shows the liquid water and gas velocities through the carbon paper, along the thickness direction of the carbon paper. Below 100 °C, the molar flux of water vapor produced by evaporation is much lower than that of gaseous hydrogen, resulting in the bubbles being mainly filled with gaseous hydrogen. The molar flux of gaseous hydrogen increases with the current density, linearly increasing the gas velocity, as shown in Fig. 4.9a (small chart). Boiling soars the molar flux of water vapor, causing the bubbles in the carbon paper to be filled primarily with water vapor, as depicted by the low partial pressure of gaseous hydrogen in Fig. 4.8a. As shown in Fig. 4.9a, at 1.024 $A \cdot cm^{-2}$, the gas velocity is 1.6 $mm \cdot s^{-1}$ at 100 °C, reaching 4.4 $mm \cdot s^{-1}$ at 103 °C, 24.5 $mm \cdot s^{-1}$ at 106 °C, and 80 $mm \cdot s^{-1}$ at 109 °C. The boiling greatly enhanced the gas velocity in the carbon paper. In Fig. 4.9b, below 100 °C, the velocity of liquid water increases with the current density because the increased gas saturation (Fig. 4.8d) increases the evaporation area at the liquid/gas phase, and the water vapor molar flux by evaporation increases. So more liquid water flows into the carbon paper for evaporation, increasing the velocity of the liquid water. Correspondingly, above 100 °C, the velocity of liquid water in the carbon paper increases due to being consumed by boiling. At 1 $A \cdot cm^{-2}$, it grows from 0.008 $\mu m \cdot s^{-1}$ at 100 °C to 57 $\mu m \cdot s^{-1}$ at 109 °C.

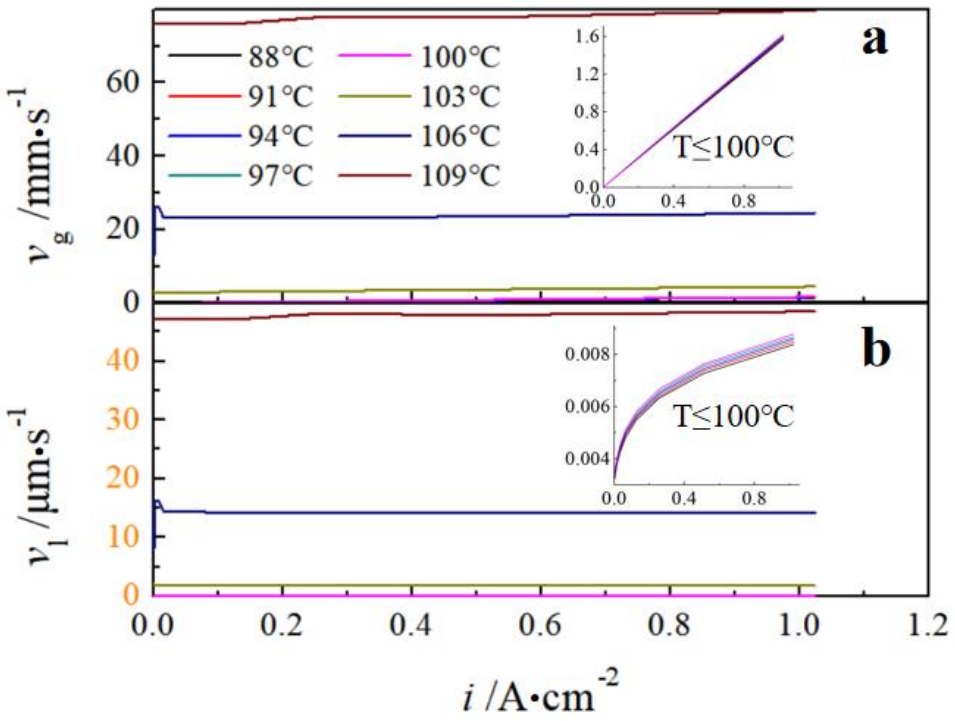

Fig. 4.9 Gas and liquid velocity in the carbon paper of 0.11-mm thickness. a. gas velocity and b. water velocity.

This section will discuss how boiling changes the HER overpotential. Fig. 4.10 shows the voltammetry curve (HER potential and current density plot) and Tafel plot of WE2, which are the theoretical results based on the model in chapter 4.4.1. Each diagram of Fig. 4.10 has 8 trends, which indicate different temperature cases with 3 °C increments. Below 100 °C, the voltammetry curve shifts towards lower potentials (to the left of Fig. 4.10a) with increasing temperature. Above 100 °C, the voltammetry curve moves to the right with increasing temperature. This result surely implies that boiling can contribute to reducing HER overpotential. The Tafel plot is the relationship between the HER overpotential and the logarithmic current density, which is transformed from the voltammetry curve. The Tafel plot can predict how much boiling reduces the HER overpotential at higher current densities. The overpotential trend significantly shifts when the temperature increases from 100 °C to 103 °C. With increasing current density, the HER overpotential at 103 °C gradually approaches that at 100 °C. The water vapor molar flux by boiling at 103 °C remains constant. The molar flux of gaseous hydrogen increases with current density, increasing the partial pressure of gaseous hydrogen and the dissolved hydrogen concentration. Therefore, as the current density increases, the HER overpotential at 103 °C approaches that at 100 °C. At a higher current density, the molar flux of water vapor needs to be further improved by the higher boiling

temperature, such as 106 °C and 109 °C, to lower the hydrogen concentration. The high molar flux of water vapor reduces the partial pressure of gaseous hydrogen (Fig. 4.8a) and dissolved hydrogen concentration (Fig. 4.8b), so as reduce the Nernst loss.

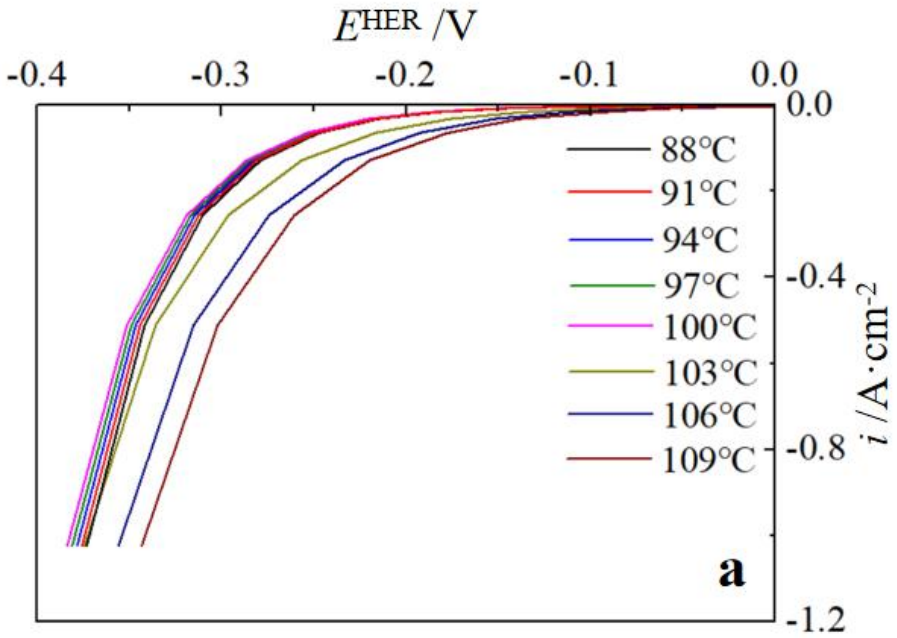

a. voltammetry plot (vs. SHE)

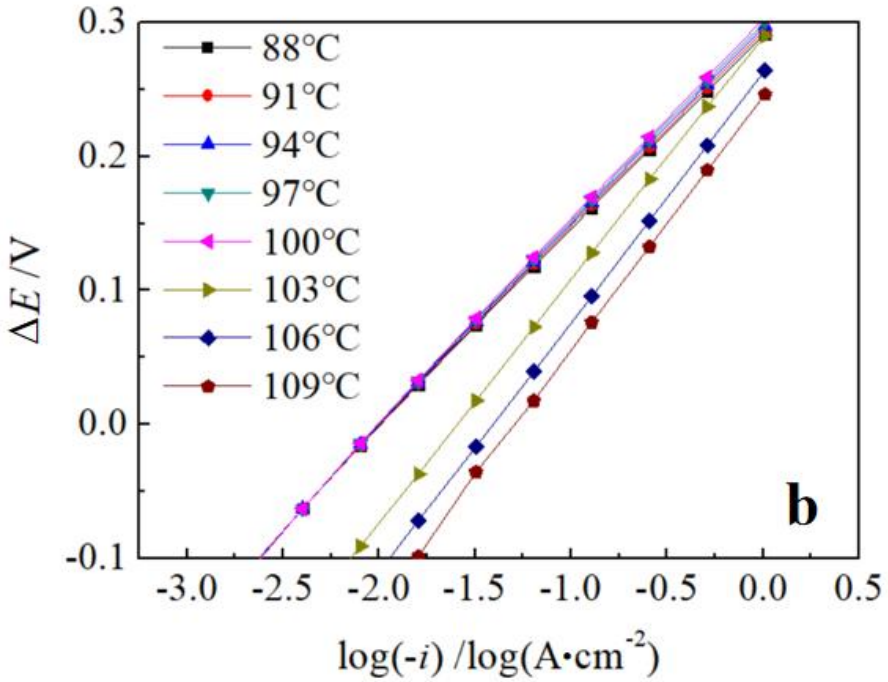

b. Tafel plot

Fig. 4.10 Electrochemical performance of the WE2.

The current contribution ratio can distinguish which current density component is the

most important. Fig. 4.11 shows the HER current contribution ratio (cr_g, cr_{ls}, and cr_l), which corresponds to i_{ls}, i_l and i_g, as introduced in Fig. 4.6. The cr_g , as defined in Eq. (4.16), is a current contribution ratio, which is the one in bubbles and plotted in Fig. 4.11a. The cr_{ls}, as defined in Eq. (4.18), is a current contribution ratio, which is the one in liquid water surrounding bubbles and plotted in Fig. 4.11b. The cr_l, as defined in Eq. (4.17), is a current contribution ratio, which is the one in liquid water far from bubbles and plotted in Fig. 4.11c. The current contribution ratio considers the effect scope of the current density component (i_{ls}, i_l and i_g) at the CL, which is determined by gas saturation and the relative molar flux of gaseous hydrogen. It can be utilized to judge how much the current component contributes.

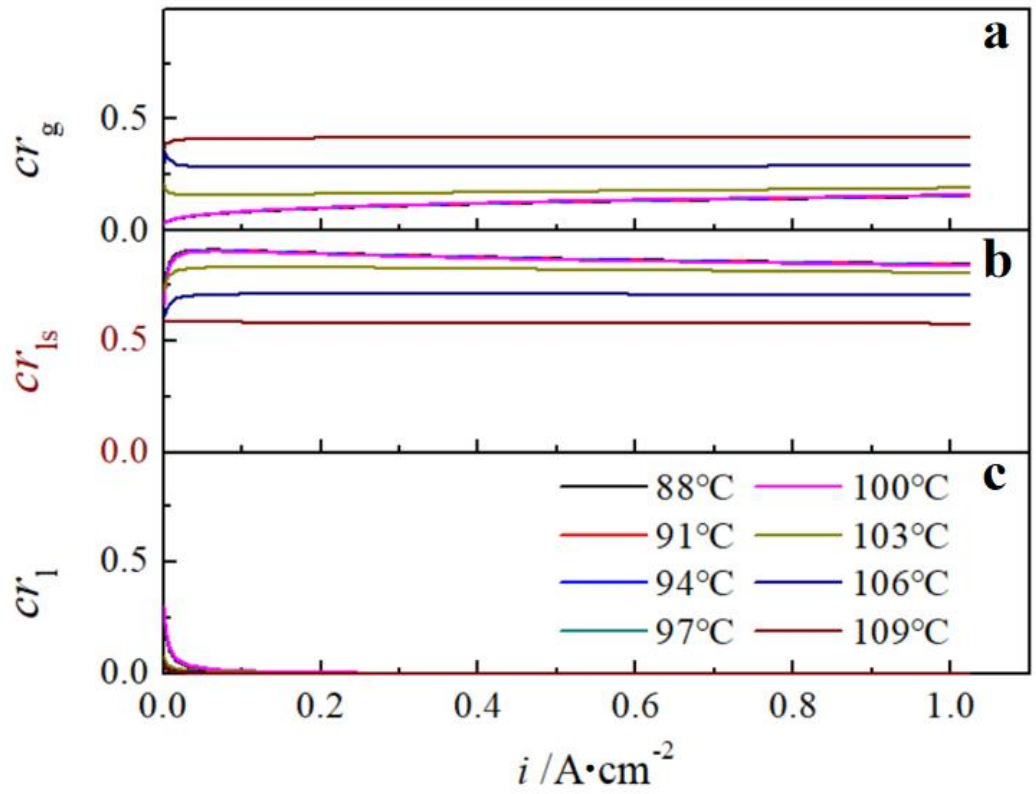

Fig. 4.11 HER current contribution ratio at the CL. a. in the bubbles, b. in the water surrounding bubbles c. in the water far from bubbles.

The three current contribution ratios as a function of temperature and current density are introduced as follows. In Fig. 4.11a, below 100 °C, the cr_g increases with current density because the high current density forms the high gas saturation at the CL (Fig. 4.8d). Over 100 °C, the current contribution ratio in the bubbles increases with temperature. At 109 °C, the CL in the bubbles contributed about 40% of the current load. The first reason is that the water vapor generated by boiling increases the gas saturation at the CL, increasing the

reaction area where HER occurs in the bubbles. The second reason is that the high molar flux of water vapor reduces the partial pressure of gaseous hydrogen in the bubbles (Fig. 4.8a), increasing the HER current density in the bubbles. At boiling, the current contribution ratio in the liquid water surrounding the bubbles decreases, as Fig. 4.11b, because the CL in the bubbles shares some current load from the CL in liquid water. The current load, cr_{ls}, decreases from 0.8 of 100 °C to 0.6 of 109 °C. Compared with the cr_{ls}, the role of the cr_{l} is not significant. As shown in Fig. 4.8c, the relative molar flux of gaseous hydrogen is more than 0.99, and the relative molar flux of dissolved hydrogen is less than 0.01. The cr_{l} is less than 1% due to the low relative molar flux of dissolved hydrogen far from the bubbles, as shown in Fig. 4.11c. In summary, at boiling, the CL in the bubbles bears some current load from that in liquid water, thereby reducing the overall HER overpotential.

4.6. Conclusions

To examine how boiling affects the HER overpotentials, two WEs with different hydrogen transfer resistances are investigated by experiment and theoretical model. The WE1 only contains a CL facing the electrolyte directly, while a carbon paper covers the CL of WE2. The HER in WE2 has higher hydrogen transfer resistance than that in WE1. In the experiments, galvanostatic voltammetry was used to investigate which overvoltage component is reduced by boiling. Then, the HER model is established based on the two experimental WEs to study how boiling reduces the HER overpotential. The results are summarized as follows:

(1) The HER overpotential of WE1 containing only the activation overvoltage did not drop significantly above the boiling temperature. Therefore, the experimental HER activation overvoltage cannot be specially decreased by boiling.

(2) Boiling decreases the Nernst loss of HER. Specifically, boiling reduces the partial pressure of gaseous hydrogen in bubbles and the dissolved hydrogen concentration surrounding the bubbles by vaporizing more water vapor. Therefore, the hydrogen activity at the CL decreases, reducing the Nernst loss of HER.

(3) The basic function of boiling in reducing the Nernst loss is that boiling soars the molar flux of water vapor, increasing the gas transfer velocity in carbon paper by several

orders of magnitude. Therefore, the hydrogen gas at the CL can be expelled more quickly at boiling, forming a low hydrogen concentration at the CL.

(4) The boiling mechanism to reduce HER overpotential is similar to that of OER. Boiling also reduces the Nernst loss of HER by increasing the molar flux of water vapor in the bubbles, reducing the partial pressure of gaseous hydrogen and the concentration of dissolved hydrogen surrounding the bubbles. The decreased partial pressure of water vapor by boiling itself reduces the Nernstian loss for OER because water acts as a reactant for OER. However, water vapor itself does not affect the Nernst loss of HER because the reactants of HER are protons.

References

[1] Ito H, Maeda T, Nakano A, Hwang CM, Ishida M, Kato A, Yoshida T. Experimental study on porous current collectors of PEM electrolyzers. International journal of hydrogen energy. 2012;37(9):7418-28.

[2] Li Z, Wu A, Xie Y, Gu Y, Yan H, Wang D, Wang S, Jin C, Wang L, Tian C. Integration of heterointerface and porosity engineering to achieve efficient hydrogen evolution of 2D porous NiMoN nanobelts coupled with Ni particles. Electrochimica Acta. 2022 Jan 20;403:139702.

[3] Zhang Y, Cui W, Li L, Zhan C, Xiao F, Quan X, Li W. Effect of the thickness of nickel electrode with aligned porous structure on hydrogen evolution reaction. International Journal of Hydrogen Energy. 2022 Apr 1;47(28):13552-60.

[4] Correa G, Marocco P, Muñoz P, Falagüerra T, Ferrero D, Santarelli M. Pressurized PEM water electrolysis: Dynamic modelling focusing on the cathode side. International Journal of Hydrogen Energy. 2022 Jan 22;47(7):4315-27..

[5] Yang Y, Li J, Yang Y, Lan L, Liu R, Fu Q, Zhang L, Liao Q, Zhu X. Gradient porous electrode-inducing bubble splitting for highly efficient hydrogen evolution. Applied Energy. 2022 Feb 1;307:118278.

[6] Arshad F, ul Haq T, Khan A, Haik Y, Hussain I, Sher F. Multifunctional porous NiCo bimetallic foams toward water splitting and methanol oxidation-assisted hydrogen production. Energy Conversion and Management. 2022 Feb 15;254:115262.

[7] Ding X, Chen S, Xiao P, Wang L, Zhang P. SO2-depolarized electrolysis using porous graphite felt as diffusion layer in proton exchange membrane electrolyzer. International Journal of Hydrogen Energy. 2022 Jan 12;47(4):2200-7.

[8] Liu J, Kim MH, Um S. Microscopic investigation of multi-transfer characteristics in digitally replicated porous gas transport media with locally variable through-plane porosities of Eulerian formulae for electrochemical applications. Journal of Power Sources. 2022 May 15;530:231280.

[9] Molina A, González J, Laborda E, et al. On the meaning of the diffusion layer thickness for slow electrode reactions[J]. Physical Chemistry Chemical Physics, 2013, 15(7): 2381-2388.

[10] G. Yang, H. Xiang, M. Rauf, H. Mi, X. Ren, P. Zhang, Y. Li, Plasma enhanced

atomic-layer-deposited nickel oxide on Co3O4 arrays as highly active electrocatalyst for oxygen evolution reaction, J. Power Sources 481 (2021) 228925.

[11] E. Afshari, S. Khodabakhsh, N. Jahantigh, S. Toghyani, Performance assessment of gas crossover phenomenon and water transport mechanism in high pressure PEM electrolyzer, Int. J. Hydrogen Energ. 46(19) (2021) 11029–11040.

[12] Vos JG, Liu Z, Speck FD, Perini N, Fu W, Cherevko S, Koper MT. Selectivity trends between oxygen evolution and chlorine evolution on iridium-based double perovskites in acidic media. ACS catalysis. 2019 ;9(9):8561-74.

[13] Sartory M, Wallnöfer-Ogris E, Salman P, Fellinger T, Justl M, Trattner A, Klell M. Theoretical and experimental analysis of an asymmetric high pressure PEM water electrolyser up to 155 bar. International Journal of Hydrogen Energy. 2017;42(52):30493-508.

[14] Schnabel T, Vrabec J, Hasse H. Henry's law constants of methane, nitrogen, oxygen and carbon dioxide in ethanol from 273 to 498 K: Prediction from molecular simulation[J]. Fluid Phase Equilibria, 2005, 233(2): 134-143.

[15] Garcia-Navarro J C, Schulze M, Friedrich K A. Measuring and modeling mass transport losses in proton exchange membrane water electrolyzers using electrochemical impedance spectroscopy[J]. Journal of Power Sources, 2019, 431: 189-204.

[16] Nakajima H, Kitahara T. In-situ Measurements of Current Distribution in the Solid Oxide Fuel Cell for Marine Power Applications[J]. Journal of The Japan Institute of Marine Engineering, 2018, 53(2): 230-236.

[17] Schmidt G, Suermann M, Bensmann B, et al. Modeling overpotentials related to mass transport through porous transport layers of PEM water electrolysis cells[J]. Journal of The Electrochemical Society, 2020, 167(11): 114511.

[18] Bénet J C, Ouoba S, Ouedraogo F, et al. Experimental study of water evaporation rate, at the surface of aqueous solution, under the effect of a discontinuity of chemical potential–Effect of water activity and air pressure[J]. Experimental Thermal and Fluid Science, 2021, 121: 110233.

[19] Kalinnikov A A, Grigoriev S A, Bessarabov D G, et al. Two-phase mass transfer in porous transport layers of the electrolysis cell based on a polymer electrolyte membrane: Analysis of the limitations[J]. Electrochimica Acta, 2021, 387: 138541.

[20] Zinser A, Papakonstantinou G, Sundmacher K. Analysis of mass transport processes in the anodic porous transport layer in PEM water electrolysers[J]. International Journal of

Hydrogen Energy, 2019, 44(52): 28077-28087.

Chapter 5

Theoretical analysis of boiling effect on electrolysis voltage of polymer electrolyte membrane water electrolyzer (PEMWE)

Although this study has examined the boiling effect on water electrolysis in a fundamental system (three-electrode cell), the boiling effect in the case of a practical polymer electrolyte membrane water electrolyzer (PEMWE) was also experimentally verified. This challenge concluded that the boiling effect, which reduces electrolysis voltage, also holds in a practical cell. This chapter intensively studied the mechanism of how boiling reduces the electrolysis voltage, even in the case of a practical cell. This chapter proposes a theoretical model considering the geometry and structure of a PEMWE. In the model, the gas saturation at the interface between the flow channel and porous transfer layer (PTL) is important, and it is assigned as a boundary condition for solving the liquid/gas transfer equation of the PTL. Theoretical analysis based on the model clarifies the gas transfer in a detailed manner and confirms that boiling can accelerate bubble detachment in the channel (CH). Then, the partial pressures of oxygen and hydrogen at the catalyst layer (CL) decrease, which is obtained from the gas transfer equation, lowering the Nernst loss of the PEMWE.

The activation overvoltage and Nernst loss of the models in this chapter are derived from the electrochemical models in chapters 3 and 4. According to the theoretical results in chapters 3 and 4, for the CL covered by the PTL, almost all the oxygen and hydrogen are expelled through the gas bubbles. The model in this chapter is based on the actual PEMWE, with both the anode and cathode covered with a PTL. The fluxes of dissolved oxygen and hydrogen through the PTL are close to 0. To simplify the model in this chapter, the transfer equations for dissolved hydrogen and dissolved oxygen in the PTL are not included in the model. The dissolved oxygen and dissolved hydrogen concentrations surrounding the bubbles are only decided by the partial pressures of the gaseous oxygen and hydrogen in the bubbles. The effects of dissolved oxygen and dissolved hydrogen on overvoltages are included in one variable, $\bar{\theta}$, of the activation overvoltages in this chapter. The $\bar{\theta}$ is called the activation fraction and is evaluated on how much the CL area is activated. In addition, the model in this chapter includes liquid/gas flow in the CH and PTL, and water transfer through the polymer electrolyte membrane (PEM) according to a practical PEMWE.

5.1 Introduction

Ito et al. [1] found that coupling boiling decreases the electrolysis voltage of the PEMWE. As this study so far discussed, oxygen bubbles in a porous transfer layer (PTL) prevent water from flowing to the anodic catalyst layer (CL) [2], causing water starvation, especially at high current density [3]. Water starvation can form a high concentration overvoltage at the PEMWE anode. In addition, the oxygen bubbles also cover the CL, reducing the active area of the anodic CL and increasing the activation overvoltage [4]. The high oversaturation of dissolved oxygen prompts the nuclear production of an oxygen bubble [5]. Boiling may enhance the transfer of dissolved oxygen [6], restricting the formation of oxygen bubbles. Although the possible mechanism for how boiling reduces electrolysis voltage in a practical PEMWE is thus listed, quantitative theoretical prediction for the voltage reduction by boiling in the case of the practical one still remains. How much boiling affects Nernst losses, activation, and ohmic overvoltages of the PEMWE attracts our concern.

The structure of the PEMWE unit used in the experiment is shown in Fig. 5.1. A serpentine flow channel was processed in the anodic and cathodic plates of the PEMWE, respectively. The PTL in the anode was Ti mesh, and the cathode one was carbon paper. The Ti mesh and carbon paper wrapped a membrane electrode assembly which includes anodic and cathodic CLs and an Aquivion ionomer electrolyte membrane. IrO_2 (loading 1.5 $mg \cdot cm^{-2}$)/Aquivion ionomer was sprayed and hot-pressed to one side of the electrolyte membrane to form the anodic CL, while Pt (loaded 0.5 $mg \cdot cm^{-2}$)/C/Aquivion ionomer was sprayed and hot-pressed to another side of the electrolyte membrane form cathodic CL.

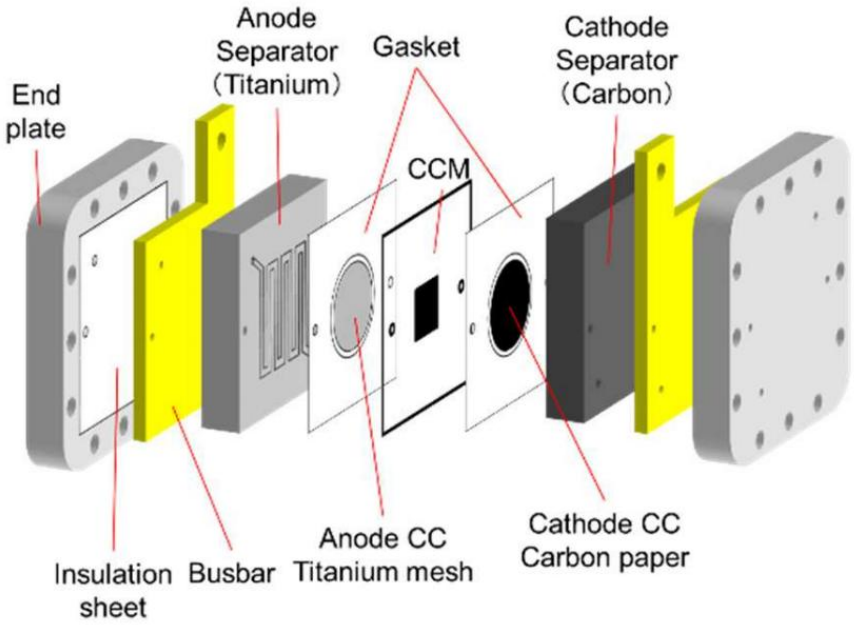

Fig. 5.1 Structure of a practical PEMWE

Considering the structure of experimental PEMWE, this chapter builds up a model to theoretically predict the boiling effect in the case of a PEMWE unit. The meanings of the parameters in the model are listed in the nomenclature in Table 5.1. The theoretical and experimental voltage at 0.002 and 1 $A \cdot cm^{-2}$ are compared in a wide temperature range to verify the accuracy of the PEMWE model. As a result, we clarify that boiling accelerates the transfer of the bubbles mixed with gaseous oxygen and water vapor. The model reveals significant changes in oxygen and hydrogen activities under boiling, which is critical for decreasing the electrolysis voltage.

Table 5.1 Nomenclature

Nomenclature			
A	Area, [cm^2]	$\overline{n}$	Molar flux, [$mol \cdot m^{-2} \cdot s^{-1}$]
C	Concentration, [$mol \cdot m^{-3}$]	P	Pressure, [Pa]
D	Diffusion coefficient, [$m^2 \cdot s^{-1}$]	q	Heat flux, [$W \cdot m^{-2}$]
E	Voltage, [V]	r	Radius, [cm]
G	Gibbs energy, [$J \cdot mol^{-1}$]	RH	Relative humidity, [-]
H	Height, [mm]	S	Saturation, [-]
h	Enthalpy, [$J \cdot mol^{-1}$]	s	Entropy, [$J \cdot mol^{-1} \cdot K^{-1}$]
i	Current density, [$A \cdot cm^{-2}$]	T	Temperature, [K]

J	Evaporation rate, [kg·m^{-2}·s^{-1}]	t	Time, [s]
K	Permeability coefficient, [m^2]	V	Volume, [m^3]
m	Molar number, [mol]	$\overline{V}$	Volume flow rate, [m^3·s^{-1}]
N	Bubble number, [-]	v	Velocity, [m·s^{-1}]
n	Molar flow rate, [mol·s^{-1}]	y	Thickness, [m]
Greek symbols			
α	Activity, [-]	μ	Dynamic viscosity, [Pa·s]
η	Overvoltage, [V]	ρ	Density, [kg·m^{-3}]
ε	Porosity, [-]	$\overline{\rho}$	Resistivity, [Ω·m^2]
θc	Contact angel of PTL, [°]	σ	Water surface tension, [Pa·m]
$\overline{\theta}$	Activation fraction, [-]	$\overline{\sigma}$	Conductivity, [S·m^{-1}]
λ	Water content in PEM, [-]		
Superscripts and subscripts			
an	Anode	g	Gas
act	Activation	gl	Gas-liquid interface
b	Boiling	in	Inlet
bp	Boiling point	l	Liquid
bub	Bubble	NL	Nernst loss
C	Critical	out	Outlet
CL	Catalyst layer	ohm	Ohmic
CH	Channel	PTL	Porous transfer layer
c	Capillary	PEM	Polymer electrolyte membrane
ca	Cathode	pre	Pressure gradient
cons	Consumption	ref	Reference
det	Detachment	sat	Saturation
diff	Diffusion	t	Time
e	Evaporation	to	Total
eod	Electro-osmotic drag	0	Standard
eff	Effective		

5.2 PEMWE structure and experimental conditions

This section presents the PEMWE structure and experimental test conditions, whose parameters are applied to the theoretical model. In Fig. 5.1, the thickness of the PEM (Aquivion E87-12S) is 0.178 mm. The anodic and cathodic CL has a geometric area of 2×2 cm^2 and a thickness of 10 μm. The anodic porous electrode is a Ti mesh with a thickness of 0.2 mm, a porosity of 0.72, and an average pore diameter of 40 μm. The cathodic carbon paper (SGL34AA) has a thickness of 0.2 mm, an average pore diameter of 50 μm, and a porosity of 0.8. The anodic and cathodic flow field is designed as a single serpentine channel (CH), and its width and depth are 1 mm. The width of the rib adjacent to CH is 1 mm. The thickness of the anodic and cathodic electrode plates embedded CHs is 10 mm. The resistivity of the anodic Ti plate is 43.1×10^{-6} Ω·cm^{-1}, while the resistivity of the cathodic carbon plate is 16×10^{-3} Ω·cm^{-1} [7]. The two resistivities are used to calculate the ohmic resistance of the collector. Other parameters related to PEMWE are shown in Table 5.2.

Table 5.2 PEMWE parameters

PEM	Thickness: 0.178 mm
CL	Areas: 2×2 cm^2
Anodic PTL	Thickness: 0.2 mm
	Porosity: 0.72
	Average pore radius: 40 μm
	Contact angle: 70°
Cathodic PTL	Thickness: 0.2 mm
	Porosity: 0.8
	Average pore radius: 50 μm
	Contact angle: 80°
CH	Cross-sectional area: 1×1 mm^2

Then, the experimental conditions for the PEMWE unit running at boiling are introduced. In the experimental conditions, the anodic and cathodic pressure of the PEMWE

was set at 0.1013 MPa. Then the boiling point temperature of the anode and cathode side is 100 °C. Because the water is electrolyzed at the anodic CL, the water is continuously supplied at the anode inlet, while the cathode inlet does not have a water supply. According to Faraday's law, the current density is positively correlated with the molar flux of water by electrolysis. The water flow rate of the anode inlet was 0.5 ml·min^{-1} at 0.002 A·cm^{-2}, while the water flow rate was increased to 1 ml·min^{-1} at 1 A·cm^{-2}. When PEMWE runs at 0.002 or 1 A·cm^{-2}, the temperature of PEMWE was scanned from 80 to 110 °C. Within 80-110 °C, the PEMWE condition changes from non-boiling and boiling to drying up.

The model uses the same conditions as the experiment to verify the model's correctness, as shown in Table 5.3. With reference to the structure of a practical PEMWE unit, the model parameters are correspondingly given in Table 5.4.

Table 5.3 Calculation conditions

Case	Current density [A·cm^{-2}]	Water flow [cm^3·min^{-1}]	Temperature [°C]	Anode pressure [MPa]	Cathode pressure [MPa]
1	0.002	0.5	80-120	0.1013	0.1013
2	1	1	80-120	0.1013	0.1013

Table 5.4 Model parameters

Parameter	Value	Unit	Description
$D_{H_2O}^{PEM}$	1.28×10^{-10}	m^2·s^{-1}	Water diffusion coefficient in PEM
d_{IrO_2}	8.35×10^{-7}	m	Particle size of IrO_2
d_{Pt}	3×10^{-5}	m	Particle size of Pt
En^{an}	76 000	J·mol^{-1}	Anode reference activation energy
En^{ca}	4300	J·mol^{-1}	Cathode reference activation energy
F	96 485	C·mol^{-1}	Faraday constant
$H_{T,O_2}(T^0)$	1.2×10^{-5}	mol·Pa^{-1}·m^{-3}	Henry coefficient of dissolved oxygen
$H_{T,H_2}(T^0)$	7.8×10^{-6}	mol·Pa^{-1}·m^{-3}	Henry coefficient of dissolved hydrogen
ΔH_{O_2}	1.4×10^4	J·mol^{-1}	Dissolution enthalpy of oxygen

ΔH_{H_2}	4.4×10^{3}	$J\cdot mol^{-1}$	Dissolution enthalpy of hydrogen
$i_{0,ref}^{an}$	5×10^{-12}	$A\cdot cm^{-2}$	Anode exchange current density
$i_{0,ref}^{ca}$	10^{-3}	$A\cdot cm^{-2}$	Cathode exchange current density
Kp	1×10^{-11}	m^2	Permeability of the PTL
L^s	6×10^{-9}	$kg\cdot K\cdot s\cdot m^{-4}$	Evaporation coefficient [14]
M_{H_2O}	18	$g\cdot mol^{-1}$	Molar mass of water
m_{IrO_2}	1.5	$mg\cdot cm^{-2}$	IrO_2 load
m_{Pt}	0.5	$mg\cdot cm^{-2}$	Pt load
P^0	101 325	Pa	Pressure at standard condition
R	8.314	$J\cdot mol^{-1}\cdot k^{-1}$	Universal gas constant
T^0	298.15	K	Reference temperature
z^{an}	4	-	Number of electron transferred in OER
z^{ca}	2	-	Number of electron transferred in HER
α_t^{an}	0.5	-	Anode charge transfer coefficient
α_t^{ca}	0.5	-	Cathode charge transfer coefficient
$\mu_{H_2O,l}$	2.822×10^{-4}	Pa·s	Dynamic viscosity of liquid water
$\mu_{H_2O,g}$	1.2×10^{-5}	Pa·s	Dynamic viscosity of water vapor
μ_{H_2}	2.47×10^{-5}	Pa·s	Dynamic viscosity of gaseous hydrogen
μ_{O_2}	1.04×10^{-5}	Pa·s	Dynamic viscosity of gaseous oxygen
ρ_{IrO_2}	11.66	$g\cdot cm^{-3}$	IrO_2 mass density
ρ_{Pt}	11.2	$g\cdot cm^{-3}$	Pt mass density
φ_I	0.75	-	Contact fraction of ionomer and catalyst

5.3 Mass transfer in the PEMWE

This section shows the transfer equations of water, oxygen, and hydrogen. Notably, the PEMWE model assumes temperature uniformity. In this model, liquid water is continuously supplied with a flow rate only at the anode inlet. The mass transfer process within the PEMWE is crucial for determining the electrolysis voltage. The molar fluxes of water, oxygen, and hydrogen are first introduced. These molar fluxes affect the velocity of the fluid in the CH. The detachment frequency of gas bubbles attached at the PTL/CH interface is positively

related to the fluid (liquid water and gas bubbles) velocity in the CH, which can be accelerated by boiling. Then, the gas transfer equation in the PTL, which determines the gas saturation and gas pressure at the CL, is introduced. The transfer equations emphasize the anode side of the PEMWE model because the cathode side uses the same transfer equations as the anode side.

5.3.1 Molar fluxes of oxygen, hydrogen and water

Fig. 5.2 meticulously describes the cross-section of the PEMWE, which includes the electrolysis process and mass transfer progress.. It is noted that Fig. 5.2 supports the boiling superimposed. In the left picture of Fig. 5.2, the anode and cathode have symmetrical designs. Both sides consist of the CL, PTL, CH, and electrode collector. Water is electrolyzed to oxygen and protons at the anode CL. The protons through the PEM are reduced to hydrogen at the cathodic CL. Water supplied from the anode inlet also penetrates through the PEM and reaches the cathode by a pressure gradient, electro-osmotic drag, and concentration diffusion. More water distributes in the anode than in the cathode because of supplying water only to the anode side. Thus, less water in the cathode is wholly vaporized at a high temperature above boiling point first while the anode is still under boiling. Oxygen gas bubbles generated by the anodic CL are mixed with water vapor. The gas bubbles mixed with gaseous oxygen and water vapor can be called “bubbles” in the subsequent description. The bubbles pass through the anodic PTL and flow out with the water in the CH. At this condition, the gaseous hydrogen and water vapor diffuse through the cathodic PTL.

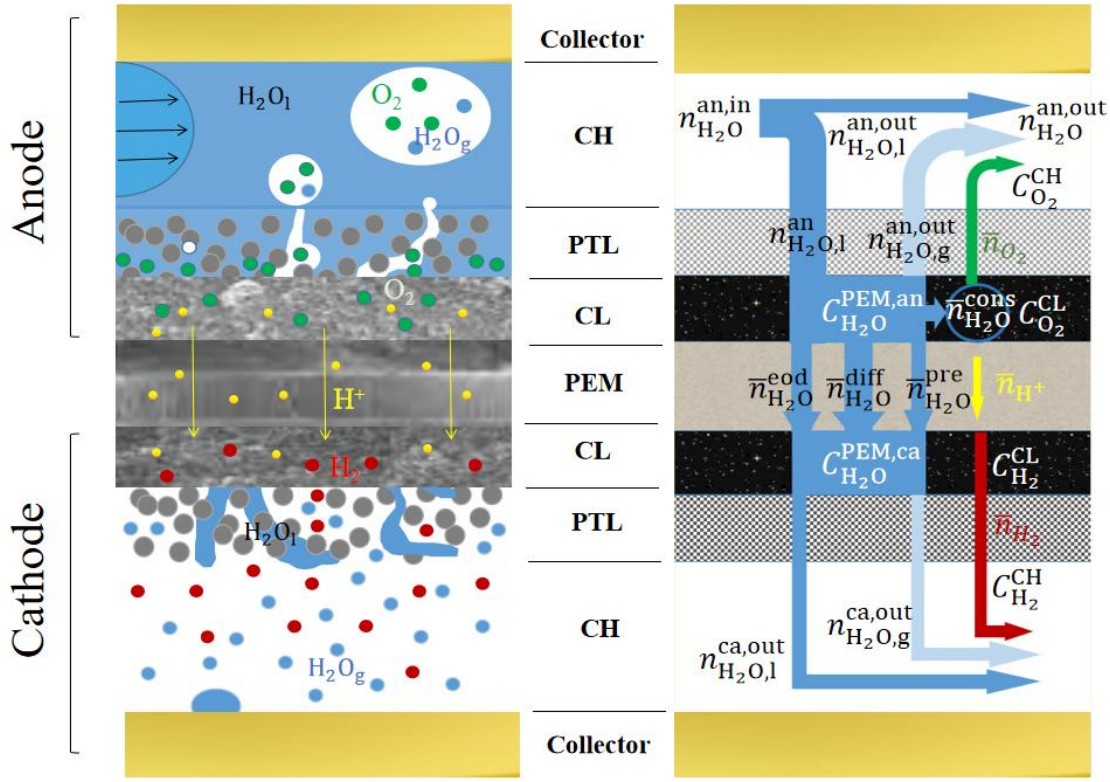

Fig. 5.2 Structure (left) and mass flow rate (right) in a PEMWE

Eq. (5.1) expresses the net molar flow rate of water through the anodic PTL [7], where A^{PEM} is the PEM area.

$$n_{\mathrm{H_2O}}^{\mathrm{PTL,an}} = A^{\mathrm{PEM}}(\overline{n}_{\mathrm{H_2O}}^{\mathrm{eod}} + \overline{n}_{\mathrm{H_2O}}^{\mathrm{pre}} + \overline{n}_{\mathrm{H_2O}}^{\mathrm{diff}} + \overline{n}_{\mathrm{H_2O}}^{\mathrm{cons}}) \quad (5.1)$$

The RHS consists of molar flow rate components, which are also shown in Fig. 5.2. In Eq. (5.1), water molar fluxes by electro-osmotic drag, $\overline{n}_{\mathrm{H_2O}}^{\mathrm{eod}}$, pressure gradient, $\overline{n}_{\mathrm{H_2O}}^{\mathrm{pre}}$, concentration diffusion, $\overline{n}_{\mathrm{H_2O}}^{\mathrm{diff}}$, and electrolysis consumption, $\overline{n}_{\mathrm{H_2O}}^{\mathrm{cons}}$, are introduced below. The water molar flux by electrolysis consumption is expressed in Eq. (5.2) [8].

$$\overline{n}_{\mathrm{H_2O}}^{\mathrm{cons}} = \frac{i}{2\mathrm{F}} \quad (5.2)$$

A proton at the anodic CL, which carries several water molecules, diffuses through the PEM. The water molar flux by the electro-osmotic drag is as Eq. (5.3), where n_{d} is the electro-osmotic drag coefficient, which is n_{d}=0.0134T+0.03 molH$_2$O/molH$^+$ with a Kelvin temperature, T [9].

$$\overline{n}_{\mathrm{H_2O}}^{\mathrm{eod}} = \frac{n_{\mathrm{d}} i}{\mathrm{F}} \quad (5.3)$$

The water molar flux under the water pressure gradient and water concentration gradient is presented as follows. This paper neglects the water molar flux by pressure

difference because the anode and cathode are set up at the same atmospheric pressure. The water concentration difference on both sides of the PEM drives the water to diffuse from the high-concentration side to the low-concentration side, as shown in Fig. 5.2. Eq (5.4) gives the water molar flux through the PEM by water concentration diffusion, where $D_{H_2O}^{PEM}$ is the water diffusion coefficient in the PEM. δ^{PEM} is the PEM thickness, while $C_{H_2O}^{PEM,an}$ and $C_{H_2O}^{PEM,ca}$ represent the water concentration at the anode and cathode side of the PEM, respectively.

$$\overline{n}_{H_2O}^{diff} = \frac{D_{H_2O}^{PEM}}{\delta^{PEM}}\left[C_{H_2O}^{PEM,an} - C_{H_2O}^{PEM,ca}\right] \quad (5.4)$$

The water phase state on both sides of the PEM can be either liquid water or water vapor. Eq. (5.5) gives the concentration expressions for liquid water and water vapor, $C_{H_2O,l}^{PEM}$ and $C_{H_2O,g}^{PEM}$, which apply to the water on PEM's anode and cathode sides. In Eq. (5.5), $\rho_{H_2O,l}^{PEM}$ is the density of liquid water on the PEM surface, and $P_{H_2O,g}^{PEM}$ is the partial pressure of water vapor on the PEM surface.

$$\begin{cases} C_{H_2O,l}^{PEM} = \frac{\rho_{H_2O,l}^{PEM}}{M_{H_2O}} & \text{, for liquid water} \\ C_{H_2O,g}^{PEM} = \frac{P_{H_2O,g}^{PEM}}{RT} & \text{, for water vapor} \end{cases} \quad (5.5)$$

If the anode boils while the cathode dries up, the concentration of liquid water in the anode is much higher than the concentration of water vapor in the cathode. Then, the water molar flux from the anode to the cathode under the concentration gradient will become significant. If both the anode and the cathode are dry, both sides of the PEM are water vapor. Water vapor concentrations in the anode and cathode are almost identical, making $\overline{n}_{H_2O}^{diff}$ close to 0.

Water permeates through the PEM from the anode to the cathode and finally flows out of the cathodic PTL. Eq. (5.6) gives the net molar flow rate of water through the cathodic PTL [7] in the manner of liquid water and water vapor.

$$n_{H_2O}^{PTL,ca} = A^{PEM}\left(\overline{n}_{H_2O}^{eod} + \overline{n}_{H_2O}^{pre} + \overline{n}_{H_2O}^{diff}\right) \quad (5.6)$$

Partial water from the anodic inlet flows into the anodic PTL, and the rest water flows out along the CH. Water flows out of the CH in the forms of liquid water and water vapor, and has molar flow rate as

$$n_{H_2O}^{out,an} = n_{H_2O}^{in,an} - n_{H_2O}^{PTL,an} = n_{H_2O,g}^{,out,an} + n_{H_2O,l}^{out,an} \quad (5.7)$$

The molar fluxes of oxygen and hydrogen depend on the Farady current density,

which is a crucial parameter addressing gas transfer in the PTL and fluid velocity in the CH. Then, the oxygen molar flux at the anodic CL is

$$\overline{n}_{O_2} = \frac{i}{4F} \quad (5.8)$$

while the hydrogen molar flux at the cathodic CL is

$$\overline{n}_{H_2} = \frac{i}{2F} \quad (5.9)$$

In the model, both oxygen and hydrogen gas are considered to transfer only through gas channels in the PTL. Since both the anodic and cathodic CLs are covered with PTLs, dissolved oxygen and hydrogen has high transfer resistance. The molar fluxes of dissolved oxygen and hydrogen transferred through PTL are close to 0 $mol \cdot m^{-2} \cdot s^{-1}$, as the results in chapters 3 and 4.

5.3.2 Bubble detachment in the CH

Chapter 5.3.1 introduces the molar fluxes of oxygen gas and water, which can determine the fluid velocity in the CH. This section discusses the bubble detachment in the CH. When the temperature exceeds the boiling point, the flow rate of water vapor by boiling increases sharply, which will accelerate the liquid-gas fluid flow in the CH. Then, the bubbles at the PTL/CH interface are accelerated to detach, decreasing the gas saturation at the PTL/CH interface. The gas saturation at the PTL/CH interface provides the boundary condition for solving the gas transfer equation in the PTL. The gas saturation can be determined by the average pressure of the bubbles at the PTL/CH interface. As plotted in Fig. 5.3, the flowing water in CH removes bubbles (mixing gaseous oxygen and water vapor) growing at the PTL/CH interface, and drains these bubbles out of the anodic CH. When the adhesion force, F_σ, to the bubble at the PTL/CH interface is larger than the drag force, F_u, caused by flowing water, the bubble attaches there.

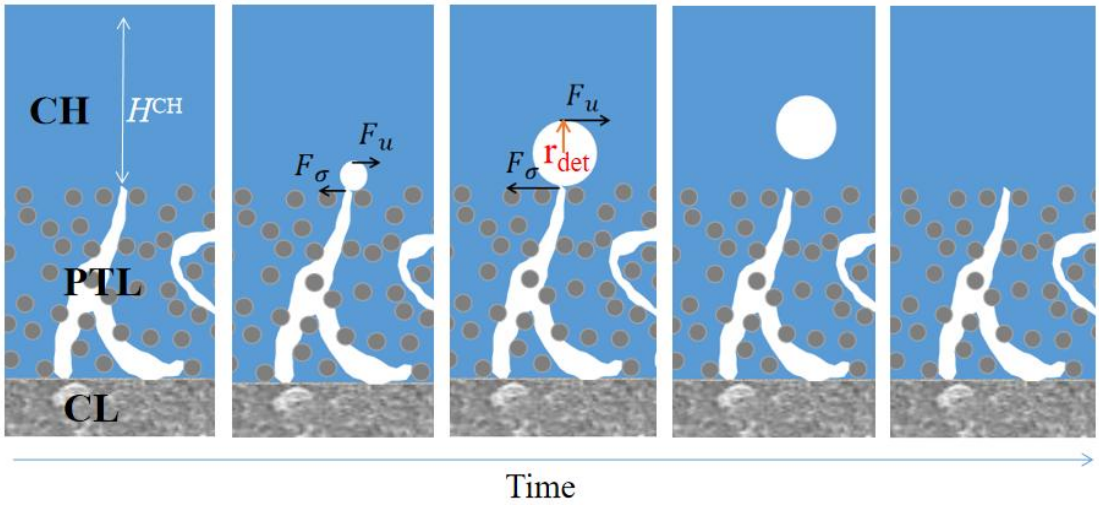

Fig. 5.3 Growth and detachment for the gas bubbles on the PTL with time.

The drag force increases with the bubble volume. When the drag force equals the adhesion force, the bubble is ready to detach with a detachment radius, r_{det}, in Eq. (5.10) [10].

$$r_{det} = \sqrt{\frac{H^{CH}\sigma r^{PTL}\sin\theta_c}{18\mu_l v_0}} \quad (5.10)$$

where H^{CH} is the CH depth, r^{PTL} is the average pore radius of PTL, σ is the surface tension of liquid water, the μ_l is the dynamic viscosity of liquid water, and v_0 is the velocity of the liquid-gas fluid in the CH.

Apparently, in Eq. (5.10), the bubble detachment radius is inverse proportion to the fluid velocity in the CH. The average velocity of the liquid-gas fluid in the CH can be derived with the volumetric flow rate of each fluid ($\overline{V}_{O_2}$, $\overline{V}_{H_2O,l}$, $\overline{V}_{H_2O,g}$).

$$v_0 = \frac{\overline{V}_{O_2}+\overline{V}_{H_2O,l}+\overline{V}_{H_2O,g}}{A^{CH}} \quad (5.11)$$

where A^{CH} is the sectional area of the CH, which is 1×1 mm^2. Volumetric flow rates of the gaseous oxygen, water vapor, and liquid water are shown in Eq.s (5.12-5.14), respectively. M_i and ρ_i represent the molar mass and mass density of the species i, where the subscript i represents the gaseous oxygen, or the liquid water or the water vapor.

$$\overline{V}_{O_2} = \frac{\overline{n}_{O_2}A^{CL}M_{O_2}}{\rho_{O_2}} \quad (5.12)$$

$$\overline{V}_{H_2O,g} = \frac{n^{an,out}_{H_2O,g}M_{H_2O}}{\rho_{H_2O,g}} \quad (5.13)$$

$$\overline{V}_{H_2O,l} = \frac{n^{an,out}_{H_2O,l}M_{H_2O}}{\rho_{H_2O,l}} \quad (5.14)$$

Boiling possibly shortens the growth period of the bubbles at the PTL/CH interface. The detachment time for one bubble is derived below. The one bubble attached to the PTL is approximated as a sphere with a volume, V_{bub}, in Eq. (5.15).

$$V_{\text{bub}} = \frac{4\pi r_{\text{bub}}^3}{3} \quad (5.15)$$

where r_{bub} refers to the bubble radius at any volume, and r_{det} in Eq. (5.10) refers to the bubble detachment radius that will detach. The mixed gas, including gaseous oxygen and water vapor in the bubble, meets the thermodynamic relation as Eq. (5. 16).

$$P_{\text{bub}} V_{\text{bub}} = m_{\text{bub}} RT \quad (5.16)$$

where m_{bub} is the molar number of the mixed gas in one bubble [10]. The surface tension of water surrounding the bubble forms the pressure difference between the bubble and liquid water [10].

$$\frac{2\sigma}{r_{\text{bub}}} = P_{\text{bub}} - P_{\text{H}_2\text{O,l}} \quad (5.17)$$

Finally, after substituting Eq.s (5.15) and (5.16) into (5.17), the bubble radius has a relation with the molar number of mixed gas in the bubble, as Eq. (5.18).

$$P_{\text{H}_2\text{O,l}} {r_{\text{bub}}}^3 + 2\sigma {r_{\text{bub}}}^2 = \frac{3 m_{\text{bub}} RT}{4\pi} \quad (5.18)$$

The molar number of mixed gas has a relation with the molar number of gaseous oxygen, m_{O2}, as

$$m_{\text{bub}} = m_{\text{O}_2} \frac{P_{\text{bub}}}{P_{\text{O}_2}} \quad (5.19)$$

where the m_{O2} can determine the molar number of the mixed gas when the partial pressure of gaseous oxygen, P_{O2}, is known. The P_{O2} in Eq. (5.19) is specifically indicated as the oxygen partial pressure in the bubble. Eq. (5.20) gives the expression of the molar number of gaseous oxygen, m_{O_2}, in one bubble.

$$m_{\text{O}_2} = \frac{A_0 \bar{n}_{\text{O}_2} t}{N_{\text{bub}}} \quad (5.20)$$

where the t is the arbitrary time within one detachment period for a bubble, and the N_{bub} is the number of bubbles for a unit area, A_0, as Fig. 5.4.

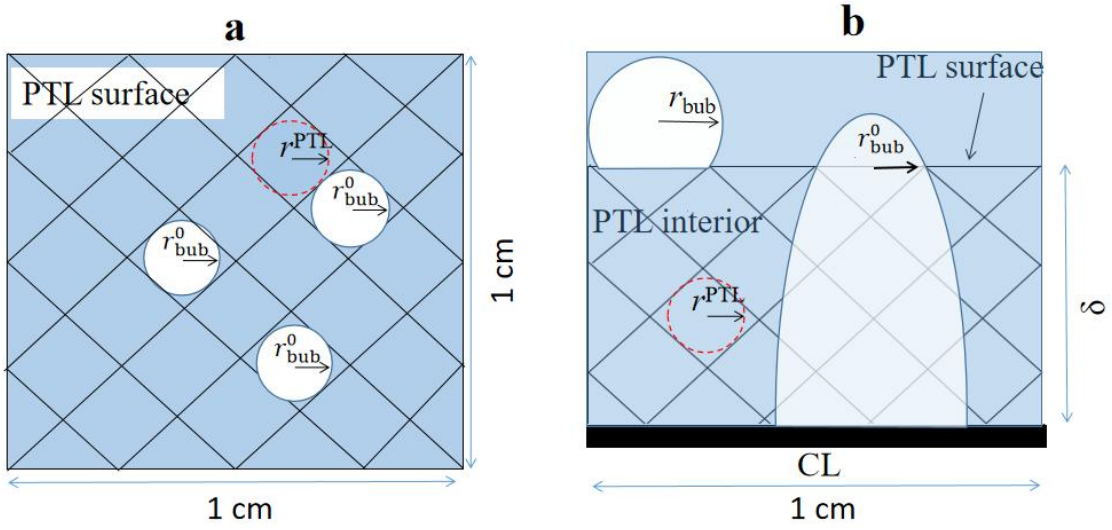

Fig. 5.4 Determining the relative evaporation area. a. the bubble number on the PTL surface for a unit area (top view), and b. the bubble radius at the PTL/CH interface (sectional view)

Fig. 5.4a demonstrates the bubble number for a unit area (1×1 cm^2) of the PTL surface. The bubble radiusat the PTL/CH interface, r_{bub}^0, is assumed to be equal to the average radius of the PTL pore, r^{PTL}. The radius of the bubble attached to the PTL/CH interface at any time, r_{bub}, is shown in Fig. 5.4b. Eq. (5.21) determines the N_{bub} where the A_0 represents the unit area of 1 cm^2. The S_g^0 is the gas saturation at the PTL/CH interface. In Fig. 5.4a, for the PTL/CH interface of a unit area, the area covered by the bubbles is $A_0 S_g^0$. Then, the number of bubbles per unit of geometric area is

$$N_{bub} = \frac{A_0 S_g^0}{\pi {r_{bub}^0}^2} \quad (5.21)$$

Boiling can accelerate the liquid-gas fluid flow in the CH, which can reduce the detachment radius of the bubbles and shorten the time that bubbles attach to the PTL/CH interface. Eq. (5.22) provides the relationship between bubble radius and time. Combining Eq.s (5.15-5.20) and (5.8), the relationship between time and the radius of the attached bubble is

$$t = \frac{16\pi F N_{bub} P_{O_2} \left(P_{H_2O,l} {r_{bub}}^3 + 2\sigma {r_{bub}}^2\right)}{3RTiP_{bub}A_0} \quad (5.22)$$

If substituting the detachment radius, r_{det}, into Eq. (5.22) to replace r_{bub}, the detachment period, t_{det}, of one bubble attached to the PTL/CH interface can be determined.

Another effect of obtaining the bubble detachment time is to determine the gas saturation at the PTL/CH interface, S_g^0, as the boundary condition of the gas transfer equation in the PTL. The capillary pressure, P_c, is related to the gas saturation, S_g, as shown in Eq.

(5.23), [11]. If the capillary pressure at the PTL/CH interface, P_c^0, is known, then S_g^0 can be determined by Eq. (5.23). In Eq. (5.23), ε is the PTL porosity, and K_p is the fluid permeability in the PTL.

$$P_c = \sigma \cos\theta_c \sqrt{\frac{\varepsilon}{K_p}} \left[1.472 S_g - 2.120 (S_g)^2 + 1.263 (S_g)^3\right] \quad (5.23)$$

Next, how to determine P_c^0 is introduced. The bubble capillary pressure P_c^0 is the pressure difference between the bubble at the PTL/CH interface, P_{bub}^0, and the liquid water, $P_{H_2O,l}$. It is $P_c^0 = P_{bub}^0 - P_{H_2O,l}$, where $P_{H_2O,l}$ is 0.1013 MPa. Eq. (5.24) gives the expression for P_{bub}^0, which is the average pressure for the bubble in one detachment period.

$$P_{bub}^0 = \frac{\sum_{k=1}^{k=100} P_{bub}\left(\frac{k t_{det}}{100}\right)}{100} \quad (5.24)$$

In order to obtain the average gas pressure, P_{bub}^0, of the bubbles attached to the PTL/CH interface during the growth process, the lifetime, t_{det}, of the bubble is divided into 100 equal parts. If r_{det} is known, t_{det} can be determined by Eq. (5.22). The k increases from 1 to 100 in turn and $\frac{k t_{det}}{100}$ represents the incremental moments in turn. Substitute time, $\frac{k t_{det}}{100}$, into Eq. (5.22), then the bubble radius, r_{bub}, at this moment will be determined. Then, substituting r_{bub} into Eq. (5.17), the bubble pressure, $P_{bub}(\frac{k t_{det}}{100})$, at $\frac{k t_{det}}{100}$ will be obtained. The P_{bub}^0 can be obtained by averaging the bubble pressures at these 100 moments.

5.3.3 Gas transfer in the PTL

This sub-sub chapter introduces the gas transfer in the PTL. In CH, the mixed gas, including gaseous oxygen and water vapor, is periodically detached in the form of bubbles. In PTL, the mixed gas is transferred continuously and is specially named "gas". "Bubble" and "gas" all refer to the mixed gaseous oxygen and water vapor. P_{bub}^0 is equal to P_g^0. The gas saturation at the PTL/CH interface is obtained from the capillary pressure of the bubbles at the interface, which functions as the boundary condition of the gas transfer in the PTL. Liquid-gas flow appears under unboiling and boiling but does not appear in the dry PTL. The only gas phase transfer in the dry PTL will be introduced in the next sub-sub chapter. To precisely obtain the distribution of gas pressure in the PTL, the PTL is discretized, as depicted in Fig. 5.5.

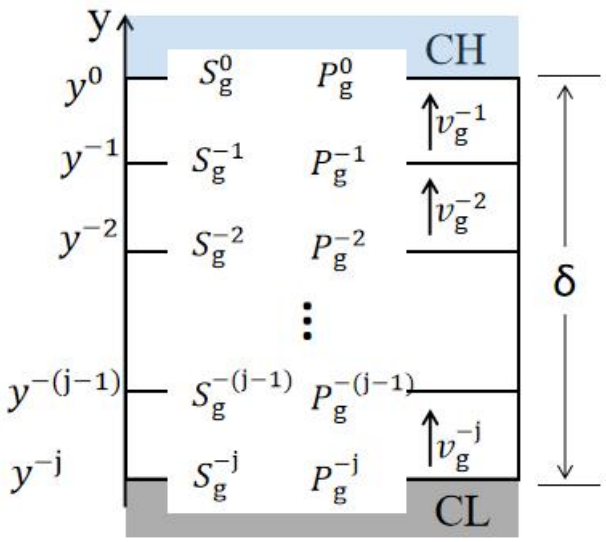

Fig. 5.5 Discretized PTL model

During the gas transfer, the gas pressure gradient drives the gas mixed gaseous oxygen and water vapor to flow from the CL to the CH, as Eq. (5.25).

$$\frac{\mathrm{d}P_\mathrm{g}}{\mathrm{d}y} = -\frac{\mu_\mathrm{g}\overline{n}_\mathrm{g}}{K_\mathrm{g}C_\mathrm{g}} \quad (5.25)$$

where the gas molar flux of the mixed gas, $\overline{n}_\mathrm{g}$, can be determined by Eq. (5.26). The $\overline{n}_{\mathrm{O}_2}$ is the molar flux of the gaseous oxygen.

$$\overline{n}_\mathrm{g} = \overline{n}_{\mathrm{O}_2}\frac{P_\mathrm{g}}{P_{\mathrm{O}_2}} \quad (5.26)$$

, and the gas concentration is listed below.

$$C_\mathrm{g} = \frac{P_\mathrm{g}}{RT} \quad (5.27)$$

The gas permeability in the PTL is

$$K_\mathrm{g} = K_\mathrm{p}\left(S_\mathrm{g}\right)^3 \quad (5.28)$$

where K_p is the liquid permeability coefficient in the PTL, and Eq. (5.29) gives the average dynamic viscosity of the mixed gas. The μ_{O_2} and $\mu_{\mathrm{H_2O,g}}$ are the dynamic viscosity coefficients of the gaseous oxygen and water vapor, respectively.

$$\mu_\mathrm{g} = \mu_{\mathrm{O}_2}\frac{\overline{n}_{\mathrm{O}_2}}{\overline{n}_{\mathrm{O}_2}+\overline{n}_{\mathrm{H_2O,g}}} + \mu_{\mathrm{H_2O,g}}\frac{\overline{n}_{\mathrm{H_2O,g}}}{\overline{n}_{\mathrm{O}_2}+\overline{n}_{\mathrm{H_2O,g}}} \quad (5.29)$$

The gas saturation at the CL can determine the gas pressure at the CL. Finally, from Eq.s (5.25-5.28), we get

$$\left[1.472\left(S_\mathrm{g}\right)^3\text{-}4.24\left(S_\mathrm{g}\right)^4 + 3.789\left(S_\mathrm{g}\right)^5\right]\left(\sigma\cos\theta_\mathrm{c}\sqrt{\frac{\varepsilon}{K_\mathrm{p}}}\right)\mathrm{d}S_\mathrm{g} = -\frac{iRT\mu_\mathrm{g}}{4FK_\mathrm{p}P_{\mathrm{O}_2}}\mathrm{d}y \quad (5.30)$$

After integrating Eq. (5.30) with the gas saturation at PTL/CH interface, S_g^0, as the boundary

condition, the gas saturation, S_g, at any position, y, of the PTL can be determined.

$$\left(\sigma\cos\theta_c\sqrt{\frac{\varepsilon}{K_p}}\right)\left[0.368\left(S_g\right)^4\text{-}0.848\left(S_g\right)^5+0.632\left(S_g\right)^6\right]\Big|_{S_g^0}^{S_g}=-\frac{iRT\mu_g y}{4FK_pP_{O_2}}\Big|_0^y \quad (5.31)$$

In Eq. (5.31), P_{O2} is considered to be approximately constant along the PTL thickness direction, which applies to both evaporation and boiling conditions. Chapter 3.3.2 shows that the water vapor flux under evaporation is much lower than the gaseous oxygen flux. The slight change of the water vapor molar flux along the thickness direction of the PTL hardly changes P_{O2}. When the temperature exceeds the boiling temperature, the boiling that occurs only at the CL does not change the water vapor molar flux along the thickness direction of the PTL, and therefore does not change the partial pressure of gaseous oxygen. The surface tension, σ, of liquid water functions with temperature, as shown in Eq. (5.32). The T_c in Eq. (5.32) is 647.3 K, which is the temperature at the water critical point.

$$\sigma = 235.8\times10^{-3}\left(1\text{-}\frac{T}{T_C}\right)^{1.256}\left[1-0.625\left(1-\frac{T}{T_C}\right)\right] \quad (5.32)$$

The gas velocity through the PTL can reflect how much the gas transfer is accelerated by boiling. The gas velocity is related to its molar flux, as shown in Eq. (5.33) [12]. When substituting Eq. (5.27) and Eq. (5.25) into Eq. (5.33), the gas velocity at any PTL location can be determined by the pressure gradient.

$$v_g=\frac{\overline{n}_gRT}{P_g}=\frac{\overline{n}_g}{C_g}=-\frac{K_g\mathrm{d}P_g}{\mu_g\mathrm{d}y} \quad (5.33)$$

By discretizing the PTL, as in Fig.5.5, the gas velocity, $v_g^j=\frac{K_g\left(P_g^j-P_g^{j-1}\right)}{\mu_g\Delta y}$, in the discrete layer can be obtained by the pressure difference between the discrete layer and its adjacent discrete layer. Therefore, the variation of the gas velocity along the thickness direction of the PTL will be determined, which can reflect the characteristics of the gas transfer in the PTL.

5.3.4 Gas transfer in the dry PTL

The gas transfer equation described in chapter 5.3.3 cannot apply to the dry PTL without liquid water. Because the flow rate of liquid water supplied at the anode inlet is limited, boiling will thoroughly vaporize all the liquid water from a specific temperature. Then, only water vapor and gaseous oxygen exist in the PTL, as shown in Fig. 5.6.

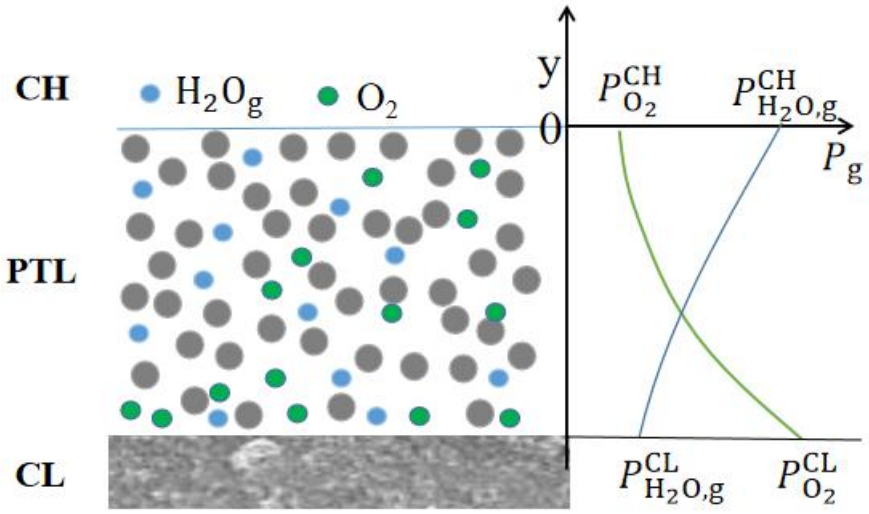

Fig. 5.6 Transfer of gaseous oxygen and water vapor in the PTL

The capillary pressure in the PTL will disappear over the specific temperature. The specific temperature can be defined as the "drying temperature". The drying temperature is determined by the water molar flow rate at the anode outlet, $n_{H_2O}^{out,an}$, which is the maximum molar flow rate of water vapor. At the drying temperature, T_{dry}, the water flow rate at the anode outlet is equal to the product of the water vapor molar flux and the vaporization area, $n_{H_2O}^{out,an} = \overline{n}_{H_2O,g}^{PTL}(T_{dry}) \times A^{CL}$. The water vapor flux will be described in chapter 5.3.5. The gaseous oxygen and water vapor follow the transfer equation (5.34) [13], where the subscript, x, represents gaseous oxygen or water vapor.

$$\frac{dP_x}{dy} = -\frac{RT}{\left(D_x^{eff} + \frac{P_x K_p}{\mu_x}\right)} \overline{n}_x \quad (5.34)$$

For gaseous oxygen or water vapor in the PTL, D_x^{eff} is the effective diffusion coefficient, μ_x is the dynamic viscosity, and $\overline{n}_x$ is the molar flux. The integration expression of Eq. (5.34) is

$$D_x^{eff} P_x + \frac{K_p (P_x)^2}{2\mu_x}\Big|_{P_x^{CH}}^{P_x^{CL}} = -RT\overline{n}_x|_0^{\delta} \quad (5.35)$$

When the partial pressures and molar fluxes of gaseous oxygen and water vapor in the CH are substituted into Eq. (5.35), the partial pressures of gaseous oxygen and water vapor at the CL will be determined. The partial pressures of gaseous oxygen and water vapor can determine the oxygen and water activities.

5.3.5 Water vaporization

The molar flux of water vapor can affect the partial pressure of gaseous oxygen. The gas pressure in the PTL is the sum of the partial pressures of gaseous oxygen and water vapor. The partial pressure of water vapor in the bubble is not equal to the saturated vapor pressure because the water vaporization in bubbles is in a non-equilibrium state when water vapor continuously flows out of the PTL with gaseous oxygen. Then, the partial pressure of gaseous oxygen is determined by the molar flux of water vapor and gaseous oxygen, as shown in Eq. (5.36). Boiling vaporizes water faster than evaporation, which can significantly increase the water vapor molar flux and decrease the partial pressure of gaseous oxygen.

$$P_{O_2} = P_g \frac{\overline{n}_{O_2}}{\overline{n}^{PTL}_{H_2O,g} + \overline{n}_{O_2}} \quad (5.36)$$

The water vapor molar flux varies greatly from evaporation to boiling. Because the operating pressure in the PEMWE is set at one atmospheric pressure, the boiling point in the anode and cathode sides is 100 °C. Below 100 °C, the molar flux of water vapor by evaporation is

$$\overline{n}^{PTL}_{H_2O,g} = \frac{J_{H_2O,g}\overline{A}^{to}_{gl}}{M_{H_2O}} \quad (5.37)$$

where the evaporation rate, $J_{H_2O,g}$, [14] has a unit of kg·m^{-2}·s^{-1}, and $\overline{A}^{to}_{gl}$ is the relative area of the liquid-gas phase interface in the PTL to a unit geometric area (A_0), which is dimensionless. The evaporation rate of water vapor is

$$J_{H_2O,g} = -L^s \frac{R}{M_{H_2O}} \ln\left(\frac{P_{H_2O,g}}{P_{sat}}\right) \quad (5.38)$$

L^s in Eq. (5.38) is the evaporation coefficient with a unit of kg·K·s·m^{-4}. Eq. (5.39) introduces the saturated vapor pressure with a unit of Pa as a function of temperature [15]. The temperature, T, in Eq. (5.39), has a unit of K.

$$P^{sat}_{H_2O} = 10^{10.08354 - 1.663.125/(T - 45.622)} \quad (5.39)$$

The relative evaporation area is a key parameter affecting the water vapor molar flux. Next, we describe how to calculate the relative evaporation area. The interface of the liquid/gas phase in the PTL is considered the evaporation surface. As shown in Fig. 5.7a, on the unit geometric area A_0 (1×1 cm^2), the number of gas channels in the PTL is N_{bub}. The sidewall area of these gas channels on A_0 is the relative evaporation area.

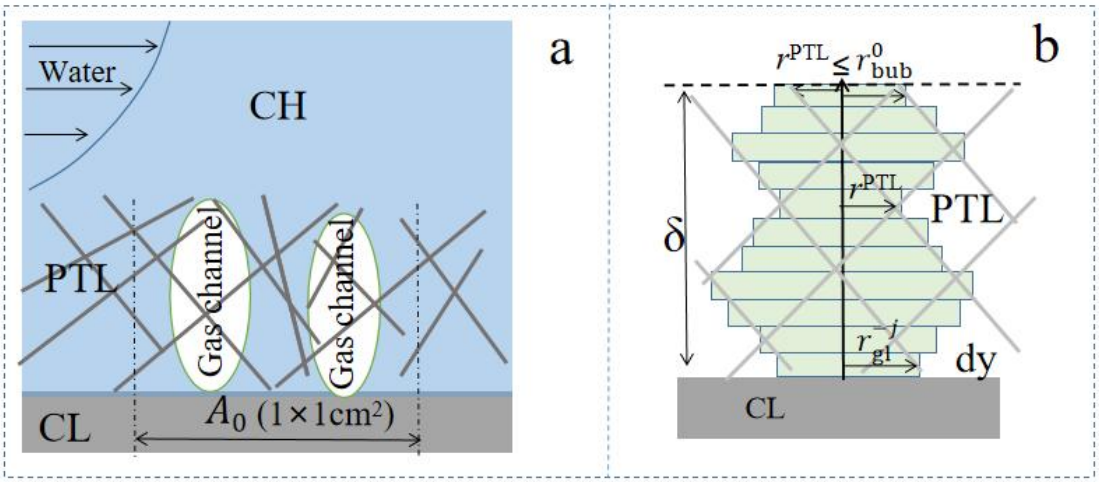

Fig. 5.7 Calculating the relative evaporation area in the PTL. a. number of gas channel over a unit area, and b. the sidewall area of a gas channel

The sidewall area of the one gas channel is A_{gl}, then the relative evaporation area, $\overline{A}^{to}_{gl}$, on the unit area A_0 is

$$\overline{A}^{to}_{gl} = \frac{N_{bub} A_{gl}}{A_0} \quad (5.40)$$

The N_{bub} is also the bubbles' number per unit area, A_0, which has been introduced in chapter 5.3.2. The area of a channel sidewall, A_{gl}, is calculated discretely, as shown in Fig. 5.7b. Integrating the sidewall area of each discrete layer yields the sidewall area of the gas channel, which is

$$A_{gl} = \int_0^{\delta} 2\pi r_{gl}(y)\mathrm{d}y \quad (5.41)$$

Substituting Eq.s (5.21) and (5.41) into Eq. (5.40), the total evaporation area for a unit geometric area is

$$\overline{A}^{to}_{gl} = \frac{2\sqrt{S^0_g}}{r^0_{bub}} \int_0^{\delta} \sqrt{S_g(y)}\mathrm{d}y \quad (5.42)$$

As shown in Fig. 5.7b, because the bubble radius at the PTL/CH interface, r^0_{bub}, in Eq. (5.42) is considered larger than the average pore radius of the PTL, r^{PTL},[16] the inequality, $\overline{A}^{to}_{gl} \leq \frac{2\sqrt{S^0_g}}{r^{PTL}} \int_0^{\delta} \sqrt{S_g(y)}\mathrm{d}y$, is established.

Above the boiling-point temperature, the water vapor molar flux increases sharply. When the water temperature approaches the boiling point, the evaporation rate reaches the maximum. Above the boiling point, the remaining liquid water starts to be vaporized by

boiling and produces water vapor with a molar flux as

$$\overline{n}_{\mathrm{H_2O,g}}^{\mathrm{PTL}} = \left[\frac{J_{\mathrm{H_2O,g}}\overline{A}_{\mathrm{gl}}^{\mathrm{to}}}{M_{\mathrm{H_2O}}}\right]_{100°\mathrm{C}} + \frac{q(T)}{1000LM_{\mathrm{H_2O}}} \quad (5.43)$$

The first term of RHS in Eq. (5.43) is the maximum molar flux of water evaporation at the boiling-point temperature. Because the anodic and cathodic pressure in this chapter is set to 0.1013 MPa, the boiling temperature of the water is 100 °C. The second term of RHS is the water molar vapor flux produced by boiling, where L is the latent heat of water vaporization. Eq. (5.44) introduces the heat flux, $q(T)$, of nucleate boiling [17].

$$q(T) = \mu_{\mathrm{H_2O,l}} L\left[\frac{g\left(\rho_{\mathrm{H_2O,l}} - \rho_{\mathrm{H_2O,g}}\right)}{\sigma}\right]^{0.5}\left[\frac{(T - T_{\mathrm{bp}})Cp_{\mathrm{H_2O,l}}}{C_{\mathrm{sf}}LPr}\right]^{3} \quad (5.44)$$

where g is the gravitational acceleration, $Cp_{\mathrm{H2O,l}}$ is the specific heat capacity of liquid water, C_{sf} is the surface fluid coupling coefficient which is 0.013, Pr is the Prandtl number. In Eq. (5.44), increasing the temperature, T, increases the heat flux, $q(T)$. Therefore, the water vapor molar flux also increases with the boiling temperature, as Eq. (5.43).

5.4 Electrolysis overvoltage

The electrolysis voltage of the PEMWE consists of the standard redox potential, E^0, the Nernst loss, E^{NL}, and the activation and ohmic overvoltages [18], as shown in Eq. (5.45).

$$E_{\mathrm{cell}} = E^0 + E^{\mathrm{NL}} + \eta^{\mathrm{act}} + \eta^{\mathrm{ohm}} \quad (5.45)$$

where the standard redox potential is

$$E^0 = -\frac{\Delta G_{\mathrm{f}}^0(T)}{2F} \quad (5.46)$$

where the difference of Gibbs free energy, $\Delta G_{\mathrm{f}}^0(T)$, among the water, oxygen, and hydrogen is described in Eq. (5.47) [9]. In Eq (5.47), $h_{\mathrm{x}}{}^0$ is enthalpy, and $s_{\mathrm{x}}{}^0$ is entropy, where the subscript x represents oxygen, hydrogen or water.

$$\Delta G_{\mathrm{f}}^0(T) = \left[h_{\mathrm{H_2}}^0(T) + \frac{1}{2}h_{\mathrm{O_2}}^0(T) - h_{\mathrm{H_2O}}^0(T)\right] - T\left[s_{\mathrm{H_2}}^0(T,P) + \frac{1}{2}s_{\mathrm{O_2}}^0(T,P) - s_{\mathrm{H_2O}}^0(T,P)\right]$$

(5.47)

Below the drying temperature, the anodiv CL is mainly covered with liquid water as the reactant, and its enthalpy and entropy values are substituted into Eq. (5.47). If the PEMWE temperature exceeds the drying temperature in the anode, the anodic CL is covered with water vapor. Then, as the reactant, the entropy and enthalpy of water vapor are substituted into Eq.

(5.47).

Additionally, the Nernst loss, activation, and ohmic overvoltages are also related to the state of oxygen, hydrogen, and water. The activities of oxygen, hydrogen, and water at the CL determine the Nernst loss, which is a hypothetical equilibrium potential. The activation fraction, related to the gas saturation and the dissolved-state oxygen and hydrogen, influences the activation overvoltage. If the PEMWE is dry, the high resistivity of the PEM can form a large ohmic overvoltage. The Nernst loss, activation and ohmic overvoltages are introduced in the following subsections.

5.4.1 Nernst loss

The Nernst loss is mainly determined by the physical state of water, oxygen and hydrogen. Eq. (5.48) defines the comprehensive Nernst loss, which consists of Nernst losses of water, oxygen and hydrogen.

$$E^{\mathrm{NL}} = E^{\mathrm{NL}}_{\mathrm{H_2O}} + E^{\mathrm{NL}}_{\mathrm{O_2}} + E^{\mathrm{NL}}_{\mathrm{H_2}} = \frac{\mathrm{RT}}{\mathrm{2F}} \ln \left[\frac{\alpha^{\mathrm{CL}}_{\mathrm{H_2}} \left(\alpha^{\mathrm{CL}}_{\mathrm{O_2}} \right)^{0.5}}{\alpha^{\mathrm{CL}}_{\mathrm{H_2O}}} \right] \quad (5.48)$$

Usually, the activities of oxygen and hydrogen at the CL depend on their concentration. Water is in a liquid-gas phase below the drying temperature and in a gas phase above the drying temperature. The activity of liquid water partially determines the water Nernst loss. The activity difference between water vapor and liquid water can slightly change the anodic activation overvoltage, whose effect is attributed to the anodic activation fraction. To independently analyze the boiling effect on Nernst losses of oxygen, hydrogen and water, Eq. (5.48) is divided into three components according to the oxygen, hydrogen and water activity. The Nernst loss related to oxygen activity is

$$E^{\mathrm{NL}}_{\mathrm{O_2}} = \frac{RT}{4F} \ln \left(\alpha^{\mathrm{CL}}_{\mathrm{O_2}} \right) = \frac{RT}{4F} \ln \left(\frac{C^{\mathrm{CL}}_{\mathrm{O_2}}}{C^{0}_{\mathrm{O_2}}} \right) \quad (5.49)$$

where the $C^{\mathrm{CL}}_{\mathrm{O_2}}$ and $C^{0}_{\mathrm{O_2}}$ are the concentration of gaseous oxygen at the CL and under the standard condition (0.1013 MPa and 25 °C). The concentration expression of gaseous oxygen at the CL is $C^{\mathrm{CL}}_{\mathrm{O_2}} = \frac{P^{\mathrm{CL}}_{\mathrm{O_2}}}{RT}$, while the concentration under the standard condition is $C^{0}_{\mathrm{O_2}} = \frac{P^{0}_{\mathrm{O_2}}}{RT}$. In this chapter, the effect of dissolved oxygen on anodic overvoltage is attributed to the activation fraction, a parameter including gas saturation and Henry's coefficient of dissolved oxygen. Similarly, the effect of dissolved hydrogen on cathodic overvoltage is attributed to

the activation fraction of the cathodic activation overvoltage, which is a parameter related to Henry's coefficient of dissolved hydrogen. The Nernst loss related to gaseous hydrogen activity is as

$$E_{\mathrm{H_2}}^{\mathrm{NL}} = \frac{RT}{2F}\ln\left(\alpha_{\mathrm{H_2}}^{\mathrm{CL}}\right) = \frac{RT}{2F}\ln\left(\frac{C_{\mathrm{H_2}}^{\mathrm{CL}}}{C_{\mathrm{H_2}}^{0}}\right) \quad (5.50)$$

where the $C_{\mathrm{H_2}}^{\mathrm{CL}}$ and $C_{\mathrm{H_2}}^{0}$ are the concentration of gaseous hydrogen at the CL and under the standard condition. The concentration expression of gaseous hydrogen at the CL is $C_{\mathrm{H_2}}^{\mathrm{CL}} = \frac{P_{\mathrm{H_2}}^{\mathrm{CL}}}{RT}$, while it at the standard condition is $C_{\mathrm{H_2}}^{0} = \frac{P_{\mathrm{H_2}}^{0}}{RT}$. The Nernst loss is related to water activity.

$$E_{\mathrm{H_2O}}^{\mathrm{NL}} = -\frac{RT}{2F}\ln\left(\alpha_{\mathrm{H_2O}}^{\mathrm{CL}}\right) = -\frac{RT}{2F}\ln\left(\frac{C_{\mathrm{H_2O,l}}^{\mathrm{CL}}}{C_{\mathrm{H_2O,l}}^{0}}\right) \quad (5.51)$$

The water activity in Eq. (5.51) depends on the concentration of liquid water at the CL, $C_{\mathrm{H_2O,l}}^{\mathrm{CL}}$, which is expressed as $C_{\mathrm{H_2O,l}}^{\mathrm{CL}} = \frac{\rho_{\mathrm{H_2O,l}}^{\mathrm{CL}}}{M_{\mathrm{H_2O}}}$. In addition, $C_{\mathrm{H_2O,l}}^{0}$ is the concentration of liquid water under the standard condition, which is expressed as $C_{\mathrm{H_2O,l}}^{0} = \frac{\rho_{\mathrm{H_2O,l}}^{0}}{M_{\mathrm{H_2O}}}$.

Fig. 5.8 compares the oxygen and water activities under non-boiling (90 °C), boiling (105 °C), and dry conditions (120 °C), where the three temperatures are just examples. Because water vapor molar flux at 90 °C is rather low than gaseous oxygen molar flux, the gas bubbles are almost filled with gaseous oxygen, yielding an oxygen activity approaching 1. However, boiling at 105 °C vaporizes considerable water vapor, largely reducing gaseous oxygen's partial pressure and activity. At 120 °C, liquid water is wholly vaporized to water vapor. The water activity is still approximately 1 at 120 °C because the water vapor molar flux is much higher than the gaseous oxygen molar flux.

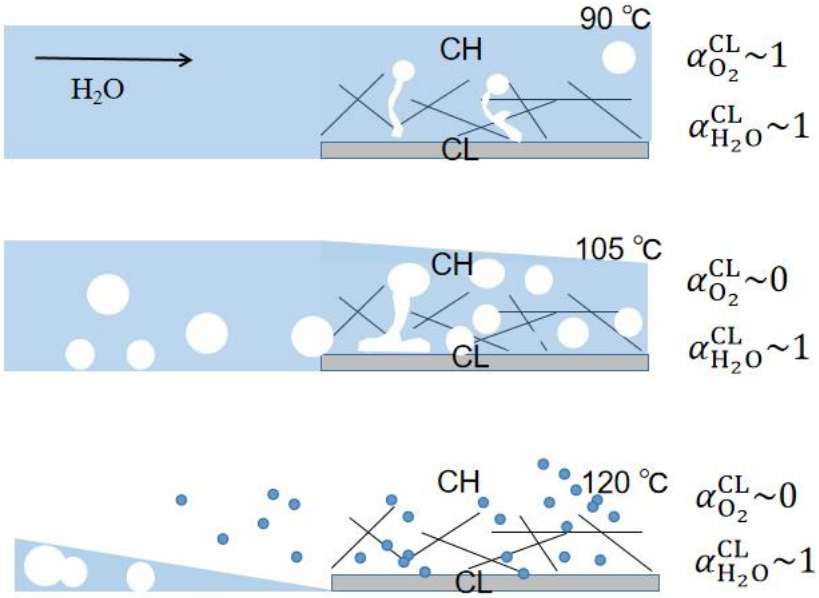

Fig. 5.8 Schematic diagram of the water and oxygen activity at non-boiling (90 °C), boiling (105 °C), and dry condition (120 °C)

5.4.2 Activation overvoltage

Gaseous oxygen covering the anodic CL can reduce the active area in the anode. At boiling, the gas saturation at the anodic CL increases sharply, which significantly reduces the coverage fraction of liquid water to the CL. In addition, the activity between dissolved oxygen and gaseous oxygen is slightly different, as are liquid water and water vapor. The gas coverage fraction and the dissolved oxygen can affect the active degree of the oxygen evolution reaction (OER) in the anode. Therefore, the activation fraction, $\bar{\theta}^{\mathrm{an}}$, can be used to evaluate the effect of the gas coverage fraction and the dissolved oxygen on the anodic activation overvoltage. The activation overvoltage in this chapter is affected by the activation fraction besides the current density, which is different from the activation overvoltage in chapters 3 and 4. To distinguish the activation overvoltage within chapters 3 and 4, the activation overvoltage including the activation fraction in this chapter is defined as "comprehensive activation overvoltage". Eq. (5.52) gives the anodic comprehensive activation overvoltage of water electrolysis [10].

$$\eta^{\mathrm{act,an}} = \frac{RT}{\alpha_{\mathrm{t}}^{\mathrm{an}} z^{an} F} \ln\left(\frac{i}{\bar{\theta}^{an} i_0^{\mathrm{an}}(T)}\right) \quad (5.52)$$

where $\alpha_{\mathrm{t}}^{\mathrm{an}}$ is the anodic charge transfer coefficient, and z^{an} is the number of electron transferred in the anodic OER. The anodic activation fraction, $\bar{\theta}^{an}$, as shown in Eq. (5.53), is

a parameter to evaluate how much the OER is activated. Eq. (5.53) is derived from the OER average current density expressed in chapter 3. The derivation process of the activation fraction is listed in the appendix at the end of the thesis. The expression for the activation fraction is directly given here.

$$\bar{\theta}^{an} = S_{\mathrm{g}}^{\mathrm{CL,an}} \left(\frac{\frac{p_{\mathrm{H_2O,g}}^{\mathrm{CL}} T^0}{p_{\mathrm{H_2O,g}}^{0} T}}{\frac{\rho_{\mathrm{H_2O,l}}^{\mathrm{CL}}}{\rho_{\mathrm{H_2O,l}}^{0}}} \right)^{\alpha_{\mathrm{t}}^{\mathrm{an}}} + \left(1 - S_{\mathrm{g}}^{\mathrm{CL,an}}\right) \left(\frac{H_{\mathrm{T,O_2}}(T_0) T^0}{H_{\mathrm{T,O_2}}(T) T} \right)^{0.5\alpha_{\mathrm{t}}^{\mathrm{an}}} \quad (5.53)$$

In Eq. (5.53), the first term on the RHS is related to the gas saturation and water activity in the gas and liquid phase. The second term is associated with the liquid water saturation, $1 - S_{\mathrm{g}}^{\mathrm{CL,an}}$, and Henry's coefficient of dissolved oxygen in liquid water. The Henry coefficient is as in Eq. (5.54), where $\Delta H_{\mathrm{O_2}}$ is the dissolution enthalpy of dissolved oxygen.

$$H_{\mathrm{T,O_2}}(T) = H_{\mathrm{T,O_2}}(T^0) \exp\left[\frac{-\Delta H_{\mathrm{O_2}}}{\mathrm{R}} \left(\frac{1}{T} - \frac{1}{T^0}\right)\right] \quad (5.54)$$

In Eq. (5.52), the exchange current density, $i_0^{\mathrm{an}}(T)$, for the geometric active area is expressed in Eq. (5.55), where the $i_{0,\mathrm{ref}}^{\mathrm{an}}$ is the electrochemical exchange current density [19].

$$i_0^{\mathrm{an}}(T) = \gamma^{\mathrm{an}} i_{0,\mathrm{ref}}^{\mathrm{an}} \exp\left[-\frac{E^{\mathrm{an}}}{R}\left(\frac{1}{T} - \frac{1}{T^0}\right)\right] \quad (5.55)$$

where E^{an} is the anodic activation energy. The roughness [19], γ^{an}, of the anodic CL is

$$\gamma^{\mathrm{an}} = \varphi_{\mathrm{I}} m_{\mathrm{IrO_2}} \frac{6}{\rho_{\mathrm{IrO_2}} d_{\mathrm{IrO_2}}} \quad (5.56)$$

where φ_{I} is the contact fraction of ionomer and catalyst. The $m_{\mathrm{IrO_2}}$, $\rho_{\mathrm{IrO_2}}$ and $d_{\mathrm{IrO_2}}$ are the load, mass density and average particle diameter of IrO_2, respectively.

In the cathodic hydrogen evolution reaction (HER), protons are transferred through the PEM. The gas coverage does not reduce the active area of the cathodic CL. Because the cathodic reactants are the protons transferred through the ionomer, CL has the same proton activity under gas and liquid water. However, the activity of dissolved hydrogen is different from that of gaseous hydrogen, and its effect on the cathodic comprehensive activation overvoltage is attributed to the cathodic activation fraction, $\bar{\theta}^{ca}$. Eq. (5.57) expresses the cathodic comprehensive activation overvoltage, where the $i_0^{\mathrm{ca}}(T)$ is the cathodic exchange current density,[20].

$$\eta^{\mathrm{act,ca}} = \frac{RT}{z^{\mathrm{ca}} \alpha_{\mathrm{t}}^{\mathrm{ca}} \mathrm{F}} \ln\left(\frac{i}{\bar{\theta}^{ca} i_0^{\mathrm{ca}}(T)}\right) \quad (5.57)$$

where $\alpha_{\mathrm{t}}^{\mathrm{ca}}$ is the cathodic charge transfer coefficient, and z^{ca} is the number of electron transferred in the cathodic HER. The cathodic activation fraction, $\bar{\theta}^{ca}$, is

$$\bar{\theta}^{ca} = S_{\mathrm{g}}^{\mathrm{CL,ca}} + \left(1 - S_{\mathrm{g}}^{\mathrm{CL,ca}}\right)\left(\frac{H_{\mathrm{T,H_2}}(T_0)T^0}{H_{\mathrm{T,H_2}}(T)T}\right)^{0.5\alpha_{\mathrm{t}}^{\mathrm{ca}}} \quad (5.58)$$

The cathodic activation fraction is derived from the average current density of the HER. The derivation process of the cathodic activation fraction is also listed in the appendix. The effect of dissolved hydrogen on the cathodic comprehensive activation overvoltage is realized by the second term of RHS, where $H_{\mathrm{T,H_2}}(T)$ is the Henry coefficient of dissolved hydrogen.

5.4.3 Ohmic overvoltage

The electrode and the PEM generate the ohmic overvoltage of water electrolysis. Among them, the proton transfer in the PEM forms the main ohmic overvoltage. The ohmic overvoltage of the PEM is expressed in Eq. (5.59).

$$\eta_{\mathrm{ohm}}^{\mathrm{PEM}} = \frac{i\delta^{\mathrm{PEM}}}{\overline{\sigma}^{\mathrm{PEM}}(T)} \quad (5.59)$$

where δ^{PEM} is the PEM thickness. The PEM conductivity, $\overline{\sigma}^{\mathrm{PEM}}(T)$, is related to the water content, λ, in the PEM [9], as shown in Eq. (5.60). Then, the PEM resistivity is $\bar{\rho}^{\mathrm{PEM}} = \frac{\delta^{\mathrm{PEM}}}{\overline{\sigma}^{\mathrm{PEM}}(T)}$.

$$\overline{\sigma}^{\mathrm{PEM}}(T) = (1.4642\lambda\text{-}2.8753)\exp\left(1268\left(\frac{1}{303} - \frac{1}{T}\right)\right) \quad (5.60)$$

The PEM water content is determined by relative humidity (RH) in the PEMWE.

$$\lambda = 0.043\text{+}17.81\mathrm{RH}\text{-}39.85\mathrm{RH}^2 + 36\mathrm{RH}^3 \quad (5.61)$$

The RH is 1 when PEM is immersed in liquid water. If the PEMWE is dry, the RH depends on the water vapor pressure, and saturation pressure decided by temperature.

$$\mathrm{RH} = \begin{cases} 1 & ,T < T_{\mathrm{dry}} \\ \frac{P_{\mathrm{H_2O,g}}}{P_{\mathrm{H_2O}}^{\mathrm{sat}}(T)} & ,T \geq T_{\mathrm{dry}} \end{cases} \quad (5.62)$$

As the definition of the drying temperature in chapter 5.3.4, T_{dry} is the temperature at which all liquid water starts to become water vapor. The saturated pressure of water vapor, $P_{\mathrm{H_2O}}^{\mathrm{sat}}(T)$, has been introduced in Eq. (5.39).

5.4.4 Efficiency

Water electrolysis is an endothermic reaction that requires both electrical and thermal energy. PEMWEs convert the input electrical and thermal energy into the hydrogen and

oxygen chemical energy, and the energy conversion efficiencies are presented as follows. The hydrogen outlet flow rate is lower than the theoretical hydrogen production rate due to the crossover of hydrogen and oxygen through the PEM [21]. The Faradaic efficiency is defined in Eq. (5.63) as the ratio of the actual hydrogen molar flux at the cathode outlet ($\overline{n}_{\mathrm{H_2}}^{\mathrm{out}}$) to the theoretical hydrogen molar flux ($\frac{i}{2F}$) [22]. Eq. (5.63), $\overline{n}_{\mathrm{H_2}}^{\mathrm{per}}$ is the molar flux of hydrogen permeating to the anode, and $\overline{n}_{\mathrm{O_2}}^{\mathrm{per}}$ is the molar flux of oxygen permeating to the cathode. In chapter 5, due to the low pressure of hydrogen gas (0.1MPa) on the cathode side, the hydrogen molar flux through the PEM is close to 0 mol·m^{-2}·s^{-1}. Therefore, the Faradaic efficiency in Eq. (5.63) is close to 1.

$$\varepsilon_{\mathrm{F}} = \frac{2F\overline{n}_{\mathrm{H_2}}^{\mathrm{out}}}{i} = 1 - \frac{2F\overline{n}_{\mathrm{H_2}}^{\mathrm{per}}}{i} - \frac{4F\overline{n}_{\mathrm{O_2}}^{\mathrm{per}}}{i} \approx 1 \quad (5.63)$$

where the molar flux of hydrogen permeating to the anode is listed in Eq. (5.64) [23]. The molar flux of oxygen permeating to the cathode is considered two times lower than the hydrogen [24]. In Eq. (5.64), $K_{\mathrm{H_2},T^0}$ is the permeability coefficient of hydrogen at T^0, En^{PEM} is the activation energy of wet nafion.

$$\overline{n}_{\mathrm{H_2}}^{\mathrm{per}} = K_{\mathrm{H_2},T^0} \exp\left[\frac{En^{\mathrm{PEM}}}{R}\left(\frac{1}{T^0} - \frac{1}{T}\right)\right] \frac{P^{\mathrm{ca}}}{\delta^{\mathrm{PEM}}} \quad (5.64)$$

The PEMWE efficiency ($\varepsilon_{\mathrm{PEMWE}}$) is shown in Eq. (5.65) [25], where Δq_{rev} is the supplemental reversible heat of the water electrolysis, and Δh_{rev} is the high combustion heat of hydrogen gas. Different from the classical electrolysis efficiency, $\varepsilon_{\mathrm{PEMWE}} = \frac{\Delta h_{\mathrm{rev}} \varepsilon_{\mathrm{F}}}{nFE}$, the PEMWE efficiency shown in Eq. (5.65) considers the supplement of thermal energy, which is more practical in the application.

$$\varepsilon_{\mathrm{PEMWE}} = \frac{\Delta h_{\mathrm{rev}} \varepsilon_{\mathrm{F}}}{nFE + \Delta q_{\mathrm{rev}}} \quad (5.65)$$

Eq. (5.66) shows the expression for reversible heat (Δq_{rev}), where ΔE is the electrolysis overpotential. If the heat energy released by the electrolysis reaction ($2F\Delta E$) is larger than the reversible heat, $T\Delta s$, the electrolysis reaction does not require additional heat energy, and vice versa. The electrolysis overpotential is the sum of the Nernst loss, activation and ohmic overvoltage.

$$\begin{cases} \Delta q_{\mathrm{rev}} = 0, \ T\Delta s < 2F\Delta E \\ \Delta q_{\mathrm{rev}} = T\Delta s - 2F\Delta E, \ T\Delta s \geq 2F\Delta E \end{cases} \quad (5.66)$$

5.5 Result and discussions

The model accuracy is validated first by comparing the experimental and theoretical voltage in a wide temperature range. Then, the theoretical model reveals the boiling effect on gas transfer. Finally, how boiling influences the Nernst loss, the activation, and the ohmic overvoltage is introduced, respectively.

5.5.1 Model accuracy verification

Validating the model's accuracy is crucial to illustrate how boiling reduces the electrolysis voltage quantitatively. Fig. 5.9 compares the theoretical and experimental electrolysis voltages at 1 and 0.002 A·cm^{-2}. The 1 A·cm^{-2} is usually the current density for practical PEMWE. And 0.002 A·cm^{-2} can generate negligible ohmic overvoltage, which is convenient to show whether boiling acts on Nernst loss or comprehensive activation overvoltage.

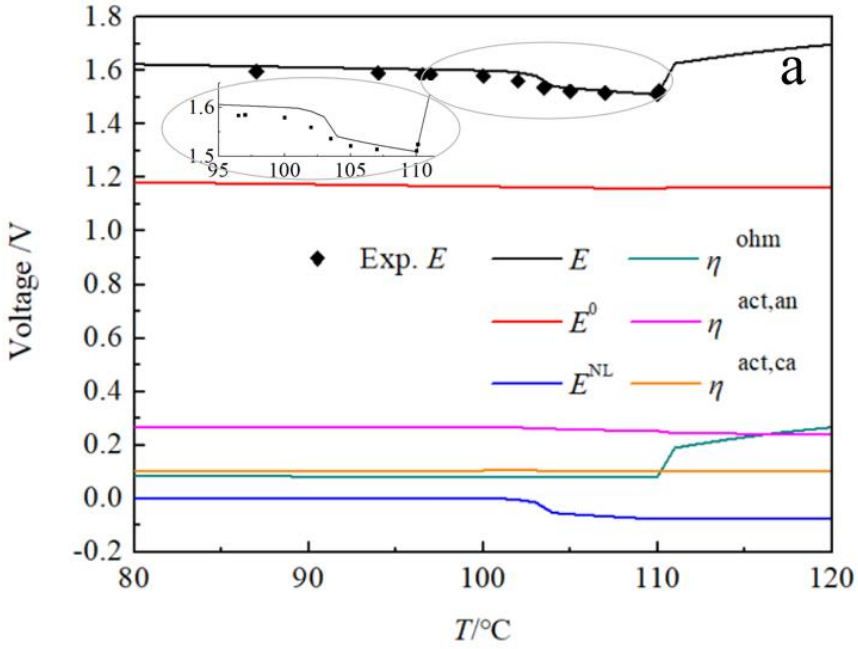

a. voltage at 1 A·cm^{-2}.

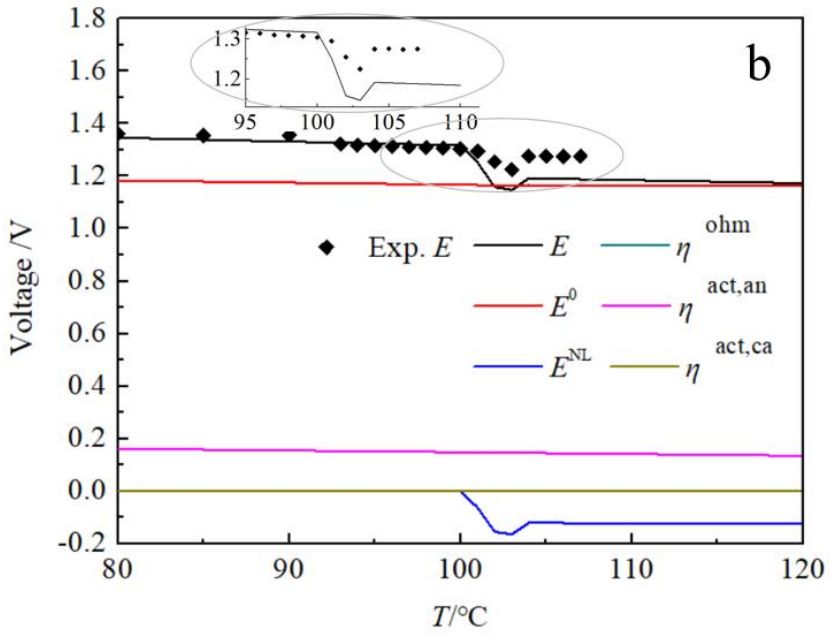

b. voltage at 0.002 A·cm^{-2}.

Fig. 5.9 Comparison between the theoretical and experimental voltages.

Fig. 5.9a shows the comparison of theoretical and experimental electrolysis voltage at 1 A·cm^{-2}. In Fig. 5.9a, at 1 A·cm^{-2}, the electrolysis voltage, *E*, decreased significantly above 100 °C. Because boiling greatly reduces the partial pressure of oxygen and hydrogen at the CL, the Nernst loss is reduced by 70 mV during boiling (100-110 °C). Boiling also slightly reduces the anodic comprehensive activation overvoltage. Since boiling increases the partial pressure of water vapor at the anode, the anodic activation fraction in Eq. (5.53) is increased. Therefore, the anodic comprehensive activation overvoltage is slightly reduced. Because the cathodic activation fraction is not affected by the partial pressure of water vapor, the cathodic activation fraction and comprehensive activation overvoltage are not altered by boiling. The *E* rises largely at 111 °C because the liquid water with a flow rate of 1 cm^3·min^{-1} is completely vaporized. At 111 °C, the ohmic overvoltage increases by 0.12 V. Because of the water-vapor circumstance in the PEMWE, the low water content of the PEM greatly increases its resistivity, resulting in a significant ohmic overvoltage. In Fig. 5.9a, the average difference between the theoretical and experimental voltages is 0.9%. The small difference between the theoretical and experimental results can ensure the correct model.

Fig. 5.9b compares the theoretical and experimental electrolysis voltage at 0.002 A·cm^{-2}. In Fig. 5.9b, the average difference between the theoretical and experimental electrolysis voltage at 0.002 A·cm^{-2} is 2.1%. This small difference again verifies the model's

correctness. In Fig. 5.9b, at 0.002 $A \cdot cm^{-2}$, the boiling reduces the electrolysis voltage significantly because the Nernst loss decreases by 0.15 V. However, the Nernst loss slightly rises at 104 °C. At 104 °C, the liquid water in the anode is wholly vaporized, greatly decrease the water concentration. Then, the water molar flux permeates from the anode to the cathode plummets, which is based on the concentration gradient, reducing the water vapor molar flux in the cathode. Therefore, the partial pressure of gaseous hydrogen rises at 104 °C, increasing the Nernst loss. Because 0.002 $A \cdot cm^{-2}$ is a low current density, the ohmic overvoltage at this current density is close to 0 V, according to ohm's law.

In the following sections, the case of 1 $A \cdot cm^{-2}$ is only analyzed because the current density is rather practical and because boiling has the same effect on electrolysis voltage at high and low current densities.

5.5.2 Mass transfer in anodic PTL and CH

Boiling can accelerate the gas transfer through the PTL. Fig. 5.10 shows distributions of gas velocity, gas saturation, and capillary pressure in the anodic PTL when the current density is 1 $A \cdot cm^{-2}$. The abscissa represents the position in the PTL interior to the PTL/CH interface, such as 0.2 mm representing the position at the PTL/CL interface. The gas velocities are almost the same at 96, 98, and 100 °C, which overlap, as shown in Fig. 10a.. However, boiling greatly improves the gas velocity. In particular, at 106 °C, the gas velocity in the PTL increases five times larger than that at 100 °C. Notably, the gas velocity near 0 mm is highlighted. The gas saturation near 0 mm approaches 0, as shown in Fig. 5.10b, resulting in a narrow cross-section of gas flow through the PTL/CH interface. Thus, the gas through the PTL is accelerated near 0 mm. In Fig. 5.10b, the gas saturation rises with the position approaching the CL because the gas pressure gradient increases towards the CL direction. Below 100 °C, the gas saturation at the CL is 0.1. At 106 °C, the gas saturation at the CL becomes 0.2 because boiling increases the water vapor molar flux and forms a larger cross-section of gas flow. The capillary pressure is positively related to gas saturation, as Eq. (5.23). Thus, the capillary pressure also increases with approaching the CL.

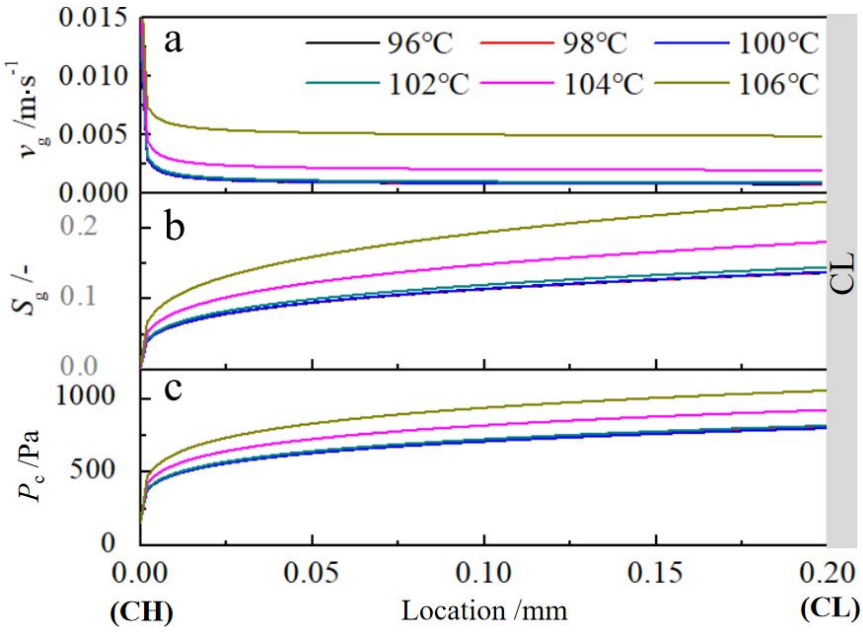

Fig. 5.10 Distribution of gas velocity, gas saturation, and capillary pressure in the anodic PTL a. gas velocity, b. gas saturation, and c. capillary pressure(The abscissa represents the distance from the PTL/CH interface to somewhere in the PTL).

Boiling also accelerates the detachment of the gas bubbles in the CH. Fig. 5.11 shows the life cycle of the bubble from its inception to detachment from the anodic PTL/CH interface. At 96-100 °C, the bubble takes about 1.35 s from growing to suddenly detaching. However, when boiling is superimposed, the cycle time is shortened to 0.85 s at 102 °C, 0.15 s at 104 °C, and 0.04 s at 106 °C. This is because water vapor produced by boiling increases the velocity of the liquid-gas fluid in the CH, enlarging the drag force to the bubble and shrinking the detachment radius. Therefore, the time for bubbles to adhere to the PTL/CH interface is shortened. The accelerated bubble detachment in the CH means that the gaseous oxygen transfer is improved by boiling.

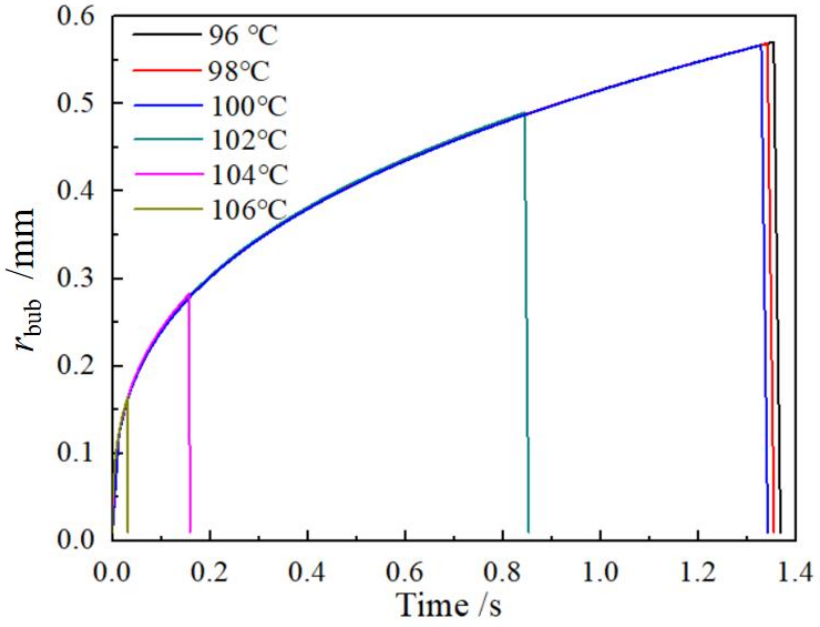

Fig. 5.11 Life cycle of bubbles from inception to detachment at the anode CH/PTL interface.

5.5.3 Boiling effect on overvoltage

This subsection discusses the boiling effect on each component of the overvoltage: Nernst loss (including concentration overvoltage), activation overvoltage, and ohmic overvoltage.

Nernst loss

Fig. 5.12 presents the Nernst loss and the water, oxygen, and hydrogen activities. Fig. 5.12a shows the Nernst loss and its component (E_{O2}^{NL}, E_{H2}^{NL}, E_{H2O}^{NL}) at 1 A·cm^{-2}. Below 100 °C, the Nernst loss, E^{NL}, nearly does not change with temperature. However, during boiling (100-110 °C), the Nernst loss decreases by 0.07V. The decrease in E^{NL} comes from the reduction in E_{O2}^{NL} and E_{H2}^{NL}, as shown in Fig. 5.12a. The Nernst loss of anodic water, E_{H2O}^{NL}, is hardly changed by boiling because water activity keeps constant in 80-120 °C.

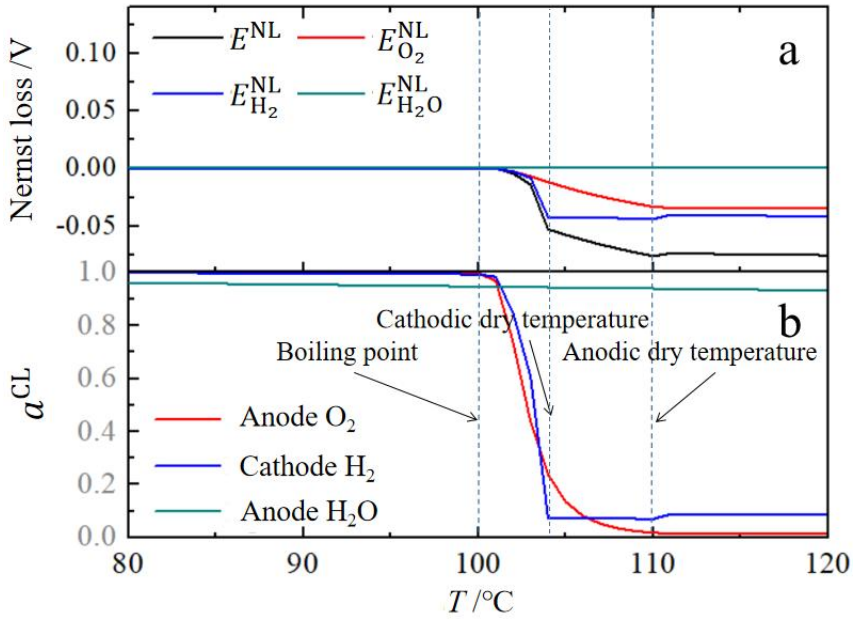

Fig. 5.12 Changes on the Nernst losses and activities of water, oxygen, and hydrogen with temperature. a. Nernst losses, and b. activities of water, oxygen, and hydrogen.

Fig. 5.12b introduces the activities of oxygen and water in the anode, and hydrogen activity in the cathode. Below 100 °C, the activities of oxygen and hydrogen are close to 1, and water activity is about 0.95. At 104 °C, the activities of oxygen and hydrogen decrease to 0.25 and 0.2, respectively. Water vapor produced by boiling lowers the partial pressures of oxygen and hydrogen, so as their activities. Above 104 °C, the hydrogen activity cannot be further reduced since the liquid water in the cathode is completely vaporized. Above 104 °C, the oxygen activity decreases less. This is because the oxygen activity is reduced to 0.25 at 104 °C, and there is less space for reducing oxygen activity by boiling. In summary, the Nernst loss decreases faster in the temperature range slightly above the boiling point and decreases more slowly at the high boiling temperature. A slight-high boiling temperature is conducive to inputting less heat energy to reduce the Nernst loss.

Activation overvoltage

Fig. 5.13 shows the anodic and cathodic comprehensive activation overvoltage and activation fraction. In Fig. 5.13a, due to the high activation energy of the OER (76 000 $J \cdot mol^{-1}$), the first derivative of the anodic comprehensive activation overvoltage with respect to the temperature of Eq. (5.52) is negative. Below 100 °C, the anodic comprehensive activation overvoltage decreases linearly with temperature. In 100-110 °C, the anodic comprehensive activation overvoltage is significantly reduced by 25 mV due to the active

fraction rising from 0.3 to 1. Boiling increases the partial pressure of water vapor at the CL, activating the CL covered by bubbles. In addition, boiling increases the gas saturation at the anodic CL, expanding the gas coverage fraction at the CL. Both two effects can increase the anodic activation fraction and reduce the anodic comprehensive activation overvoltage.

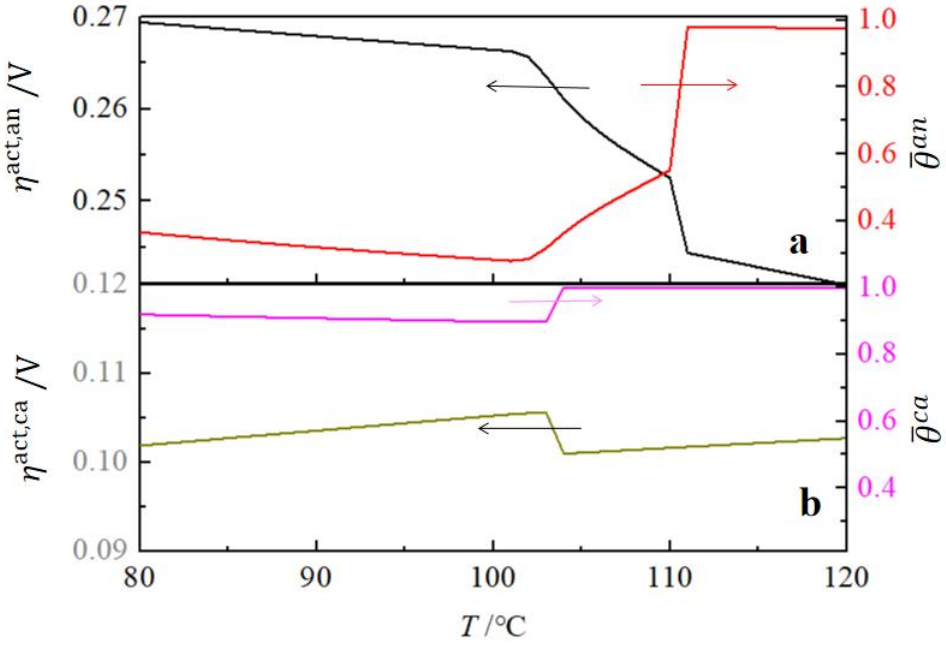

Fig. 5.13 Changes on the comprehensive activation overvoltage and activation fraction with temperature. a. comprehensive activation overvoltage, b. activation fraction.

In Fig. 5.13b, below 100 °C, the cathodic comprehensive activation overvoltage increases with temperature. Due to the low activation energy of the HER (4300 $J \cdot mol^{-1}$), the first derivative of the cathodic comprehensive activation overvoltage with respect to the temperature of Eq. (5.57) is positive. During boiling (100-104 °C), the cathodic comprehensive activation overvoltage is not notably reduced since the cathodic activation fraction is not affected by the partial pressure of water vapor. At 104 °C, the cathodic comprehensive activation overvoltage decreases by 5 mV because the cathodic activation fraction increases by 0.1. Because the gas saturation at the cathodic CL becomes 1 from 0.1, the coverage fraction of gas hydrogen is expanded, increaing the cathodic activation fraction of 0.1.

Ohmic overvoltage

The ohmic overvoltage is mainly affected by the PEM resistivity. Fig. 5.14 shows the

ohmic overvoltage, the PEM resistivity, the water content in the PEM, and the RH in the PEMWE. In Fig. 5.14a, the ohmic overvoltage produced from the PEM and current collectors is maintained at 0.08 V below 111 °C but drastically increased to 0.2 V at 111 °C. Because liquid water totally becomes water vapor at 111 °C, the RH in the PEMWE suddenly decreases, as shown in Fig. 5.14d. Then, as shown in Fig. 5.14c, the water content in the PEM decreases with the decreasing RH. Therefore, the theoretical PEM resistivity at 111 °C, as Fig. 5.14b, starts to jump from 62 to 180 $\Omega \cdot cm^2$ due to dehydration, which increases the ohmic overvoltage. The experimental PEM resistivity also showed the same increasing trend at the drying temperature (111 °C).

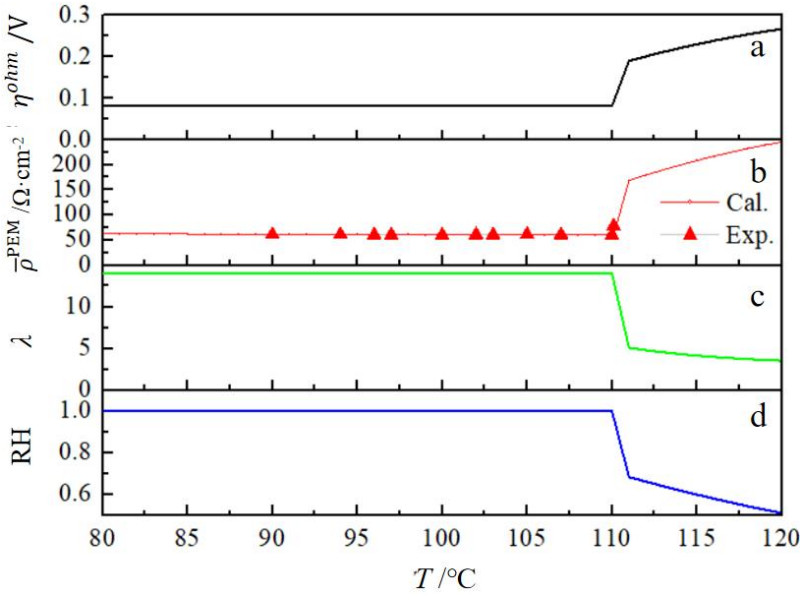

Fig.5.14 Changes on the ohmic overvoltage, PEM resistivity, PEM water content, and RH in the anode with temperature. a. ohmic overvoltage, b. PEM resistivity, c. PEM water content, and d. RH in the anode.

In summary, boiling can greatly reduce the Nernst losses on the anode and cathode sides and slightly reduce the anodic comprehensive activation overvoltage, without changing the cathodic comprehensive activation overvoltage and ohmic overvoltage. The above results determine the optimal temperature to achieve the lowest electrolysis voltage. Under unboiling, boiling, and dry conditions, PEMWE has the lowest voltage at the boiling temperature.

5.5.4 Boiling effect at each current density and efficiency

This subsection presents the electrolysis voltages and electrolysis efficiencies under boiling over wide current densities. Fig. 5.15 mainly introduces the comparison of voltage components without and with boiling. Fig. 5.16 shows the electrolysis voltage and PEMWE efficiency as a function of current density and temperature.

Fig. 5.15 compares the variation of voltage components below and above the boiling point in the range of 0.01-2 A·cm^{-2}. In Fig. 5.15a, the electrolysis temperature is 95 °C. As the current density increases, the standard redox potential remains essentially unchanged. The ohmic overvoltage and the comprehensive activation overvoltage in the anode and cathode increase continuously with the current density. In Fig. 5.15a, the three voltage curves ($E^0 + \eta^{\mathrm{ohm}} + \eta^{\mathrm{act,an}} + \eta^{\mathrm{act,an}}$, $E^0 + \eta^{\mathrm{ohm}} + \eta^{\mathrm{act,an}} + \eta^{\mathrm{act,an}} + E^{\mathrm{NL,an}}$, E) almost overlap. This is because the Nernst losses at the anode and cathode at 95 °C are close to 0.

Fig. 5.15b shows the voltage components at boiling (105 °C). Compared with Fig. 5.15a, boiling does not change the standard redox potential and ohmic overvoltage, while boiling only slightly reduces the anode activation overvoltage in Fig. 5.15b. At boiling, the Nernst losses in the anode and cathode are both negative. The voltage Including the anode Nernst loss ($\eta^{\mathrm{ohm}} + \eta^{\mathrm{act,an}} + \eta^{\mathrm{act,an}} + E^{\mathrm{NL,an}}$) is lower than that not including the Nernst loss ($E^0 + \eta^{\mathrm{ohm}} + \eta^{\mathrm{act,an}} + \eta^{\mathrm{act,an}}$). After adding the cathodic Nernst loss to the electrolysis voltage, the electrolysis voltage (E) becomes lower.

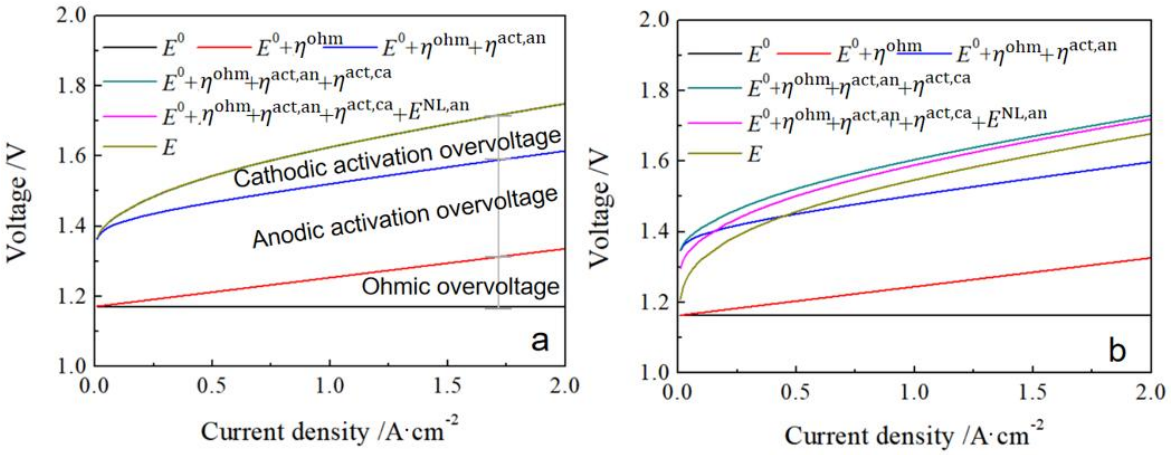

Fig. 5.15 Voltage components. a. at non-boiling (95 °C) and, b. boiling (105 °C)

Fig. 5.16 shows the electrolysis voltage and efficiency of the PEMWE superimposed boiling effect under the adequate water supply (10 cm^3·min^{-1}). From 100-120 °C, the inside of PEMWE is at boiling. The electrolysis voltage is plotted in Fig. 5.16a with changing current

density and temperature. When the temperature exceeds 100 °C, the voltage drops significantly at each current density. When the current density increases from 0.1 to 5 A·cm^{-2}, the voltage reduction value by boiling decreases from 70 to 50 mV. Increasing current density reduces voltage drop by boiling. Increasing the current density increases the molar flux of oxygen and hydrogen. At a specific boiling temperature, the molar flux of water vapor produced by boiling is constant. Therefore, increasing oxygen and hydrogen molar fluxes increase their partial pressure and activity in the bubbles, increasing Nernst losses. Ultimately, the increased current density reduces the voltage drop under boiling.

Fig. 5.16b plots the PEMWE efficiency with the current density and temperature. The PEMWE efficiency approaches 1 at low current densities (<0.5 A·cm^{-2}) and decreases with current density. At 1 A·cm^{-2}, boiling increases the PEMWE efficiency by 5%. However, at 0.2 A·cm^{-2}, the PEMWE efficiency nearly does not change under boiling. The maximum electrolytic efficiency of PEMWE is lower than 1. At 0.2 A·cm^{-2} , because the efficiency of PEMWE below the boiling temperature is close to 1, there is little room for boiling to improve the PEMWE efficiency. Therefore, boiling cannot greatly improve PEMWE efficiency at low current density.

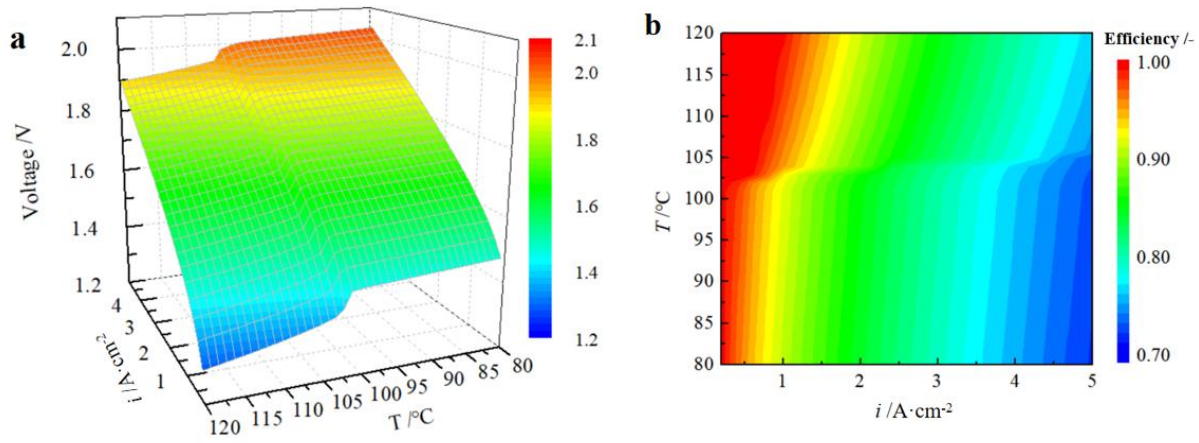

Fig. 5.16 Variation of electrolysis voltage and PEMWE efficiency with temperature and current density. a. electrolysis voltage, b. PEMWE efficiency

5.6 Conclusion

A PEMWE model is built to study the boiling mechanism decreasing the electrolysis voltage of PEMWE. The consistent voltage tendency between the theory and experiment

validates the model's correctness. Boiling mainly improves mass transfer to reduce the electrolysis voltage. More specific conclusions are summarized below:

1) Boiling accelerates mass transfer in the CH and PTL. The water vapor molar flux increases sharply during boiling, accelerating the gas flow in the PTL and reducing the detachment radius and lifetime of the bubbles attached to the PTL. Then, this high water vapor molar flux by boiling reduces oxygen and hydrogen's activity at the CL.

2) Boiling can reduce some components of the electrolysis voltage. Because the water vapor significantly reduces the activities of oxygen and hydrogen under boiling, boiling reduces the Nernst loss most, which exceeds 70 mV at 1 $A \cdot cm^{-2}$, which consists of Nernst loss components formed by the oxygen and the hydrogen activity.

3) Boiling also increases the water vapor activity at the CL covered by bubbles because the high water vapor molar flux at boiling improves the partial pressure of water vapor. Thus, boiling activates the anodic reaction at the CL under the bubbles. As boiling increases the gas fractional coverage (the gas saturation), the activated CL under boiling bubbles slightly decreases the anodic comprehensive activation overvoltage of 25 mV at 1 $A \cdot cm^{-2}$. However, boiling cannot reduce the cathodic comprehensive activation overvoltage because the cathodic reaction is not affected by water vapor activity.

4) Boiling does not change the PEM resistivity and the ohmic overvoltage. However, the PEMWE runs at a drying temperature, such as a high temperature above the boiling point, which can cause its interior to dry out, reducing the water content in the PEM. Drying out greatly increases the PEM resistivity, resulting in an ohmic overvoltage increase of 0.12 V at 1 $A \cdot cm^{-2}$.

5) To sum up, the PEMWE at boiling has the lowest electrolysis voltage among non-boiling, boiling, and dry conditions. To balance the Nernst loss reduction by boiling and ohmic overvoltage increase by high temperature (the drying temperature), the PEMWE should be controlled at a boiling temperature slightly above the boiling point. Besides, boiling can only significantly increase the electrolysis efficiency by about 5% above 0.5 $A \cdot cm^{-2}$.

References

[1] Ito K, Terabaru K, Li H, Inada A, Nakajima H. Challenging of Reducing Electrolysis Voltage by Superimposing Boiling on PEMWE–A Thermodynamic Coupling–. ECS Transactions. 2017 Aug 24;80(8):1117.

[2] Arbabi F. Oxygen Bubble Propagation in Polymer Electrolyte Membrane Electrolyzer Porous Transport Layers (Doctoral dissertation, University of Toronto (Canada)).

[3] Nouri-Khorasani A, Ojong ET, Smolinka T, Wilkinson DP. Model of oxygen bubbles and performance impact in the porous transport layer of PEM water electrolysis cells. International journal of hydrogen energy. 2017;42(48):28665-80.

[4] Leonard E, Shum AD, Normile S, Sabarirajan DC, Yared DG, Xiao X, Zenyuk IV. Operando X-ray tomography and sub-second radiography for characterizing transport in polymer electrolyte membrane electrolyzer. Electrochimica Acta. 2018;276:424-33.

[5] Kadyk T, Bruce D, Eikerling M. How to enhance gas removal from porous electrodes?. Scientific reports, 2016, 6(1): 1-14.

[6] Shen, Chen, Artin Afacan, Jingli Luo, and Stan J. Klimas.. Mass transfer of dissolved oxygen using rotating cylinder electrode under bulk boiling conditions. International Journal of Heat and Mass Transfer, 2014, 70: 162-168.

[7] Marangio F, Santarelli M, Cali M. Theoretical model and experimental analysis of a high pressure PEM water electrolyzer for hydrogen production. International Journal of Hydrogen Energy, 2009, 34(3): 1143-1158.

[8] Yigit T, Selamet O F. Mathematical modeling and dynamic Simulink simulation of high-pressure PEM electrolyzer system. International Journal of Hydrogen Energy, 2016, 41(32): 13901-13914.

[9] Liso V, Savoia G, Araya SS, Cinti G, Kær SK. Modelling and experimental analysis of a polymer electrolyte membrane water electrolysis cell at different operating temperatures. Energies. 2018 ;11(12):3273.

[10] Abdin Z, Webb C J, Gray E M A. Modelling and simulation of a proton exchange membrane (PEM) electrolyzer cell. International Journal of Hydrogen Energy, 2015, 40(39): 13243-13257.

[11] Kai J, Saito R, Terabaru K, Li H, Nakajima H, Ito K. Effect of temperature on the performance of polymer electrolyte membrane water electrolysis: numerical analysis of

electrolysis voltage considering gas/liquid two-phase flow. Journal of The Electrochemical Society. 2019;166(4):F246.

[12] Kalinnikov A A, Grigoriev S A, Bessarabov D G, et al. Two-phase mass transfer in porous transport layers of the electrolysis cell based on a polymer electrolyte membrane: Analysis of the limitations. Electrochimica Acta, 2021, 387: 138541.

[13] Leonard E, Shum AD, Normile S, Sabarirajan DC, Yared DG, Xiao X, Zenyuk IV. Operando X-ray tomography and sub-second radiography for characterizing transport in polymer electrolyte membrane electrolyzer. Electrochimica Acta. 2018;276:424-33.

[14] Bénet J C, Ouoba S, Ouedraogo F, et al. Experimental study of water evaporation rate, at the surface of aqueous solution, under the effect of a discontinuity of chemical potential–Effect of water activity and air pressure[J]. Experimental Thermal and Fluid Science, 2021, 121: 110233.

[15] Pant L M, Mitra S K, Secanell M. Absolute permeability and Knudsen diffusivity measurements in PEMFC gas diffusion layers and micro porous layers. Journal of Power Sources, 2012, 206: 153-160.

[16] Arbabi F. Oxygen Bubble Propagation in Polymer Electrolyte Membrane Electrolyzer Porous Transport Layers (Doctoral dissertation, University of Toronto (Canada)).

[17] Khan S A, Sezer N, Koç M. Design, fabrication and nucleate pool-boiling heat transfer performance of hybrid micro-nano scale 2-D modulated porous surfaces. Applied Thermal Engineering, 2019, 153: 168-180.

[18] Carmo M, Fritz DL, Mergel J, Stolten D. A comprehensive review on PEM water electrolysis. International journal of hydrogen energy, 2013, 38(12): 4901-4934.

[19] Nakajima H, Kitahara T. In-situ Measurements of Current Distribution in the Solid Oxide Fuel Cell for Marine Power Applications. Journal of The Japan Institute of Marine Engineering, 2018, 53(2): 230-236.

[20] Aubras, Farid, J. Deseure, J-JA Kadjo, I. Dedigama, J. Majasan, Brigitte Grondin-Perez, J-P. Chabriat, and D. J. L. Brett. Two-dimensional model of low-pressure PEM electrolyzer: Two-phase flow regime, electrochemical modelling and experimental validation. International journal of hydrogen energy, 2017, 42(42): 26203-26216.

[21] Fragiacomo P, Genovese M. Modeling and energy demand analysis of a scalable green hydrogen production system. International Journal of Hydrogen Energy, 2019, 44(57): 30237-30255.

[22] Kianfard H, Khalilarya S, Jafarmadar S. Exergy and exergoeconomic evaluation of hydrogen and distilled water production via combination of PEM electrolyzer, RO desalination unit and geothermal driven dual fluid ORC. Energy conversion and management, 2018, 177: 339-349.

[23] Scheepers F, Stähler M, Stähler A, Rauls E, Müller M, Carmo M, Lehnert W. Temperature optimization for improving polymer electrolyte membrane-water electrolysis system efficiency. Applied Energy. 2021;283:116270.

[24] Garbe S, Futter J, Schmidt TJ, Gubler L. Insight into elevated temperature and thin membrane application for high efficiency in polymer electrolyte water electrolysis. Electrochimica Acta. 2021;377:138046.

[25] Hernández-Gómez Á, Ramirez V, Guilbert D. Investigation of PEM electrolyzer modeling: Electrical domain, efficiency, and specific energy consumption. International Journal of Hydrogen Energy, 2020.

Chapter 6

Summary and prospect

The final chapter summarizes the research findings of all the above chapters and provides a prospect for future research. In the summary section, the effect of boiling and its mechanism on the components of PEMWE electrolysis voltage is introduced one by one. In the prospect section, a proposal, that boiling is superimposed in an industrial-scale PEMWE stack, is proposed to reduce the investment cost of the PEMWE stack.

6. 1 Summary

Solving the high initial cost of polymer electrolyte membrane water electrolyzer (PEMWE) can help to realize commercial hydrogen production. Increasing the current density of the PEMWE can reduce areas of the catalyst layer (CL), porous transfer layer (PTL), and polar plate, leading to decreasing the initial cost of PEMWE. Boiling is expected to decrease the electrolysis voltage of water electrolysis. The decreased electrolysis voltage by boiling can be converted to increasing current density. Thus, the boiling effect can contribute to reducing the initial cost of PEMWE.

The reaction of water electrolysis consists of the oxygen evolution reaction (OER) and hydrogen evolution reaction (HER). Thus, the thesis first studies the effect of boiling on OER and then examines the boiling effect on HER. To conduct this step-by-step verification, a three-electrodes cell (TEC) was introduced. The TEC could qualitatively distinguish whether boiling reduces Nernst loss or activation overvoltage of OER. In addition, the OER model established quantitatively illustrated the effect of boiling on mass transport and overpotential. Then, similar to the OER case, the boiling effect on HER was examined in an experimental and theoretical manner. Finally, the knowledge thus obtained was applied to a practical PEMWE, and it was clarified that the boiling effect holds in practical PEMWE with a detailed analysis of how boiling affects Nernst loss, activation overvoltage, and ohmic overvoltage there. The main achievements of the thesis are listed as follows.

(1) First, the effect of boiling on the OER overpotential was qualitatively studied by a

three-electrode cell in the experiment and quantitatively analyzed by a theoretical OER model. The results show that boiling cannot change the activation overvoltage but can reduce the Nernst loss of OER. When OER occurs at a CL covered with PTL, the dissolved oxygen concentration at CL during boiling is much lower than without boiling. Boiling produces a lot of bubbles filled with water vapor. The water vapor reduces the partial pressure of gaseous oxygen in the bubbles. The decreasing partial pressure of gaseous oxygen in the bubbles attracts more dissolved oxygen to flow into the bubbles, reducing the dissolved oxygen concentration surrounding the bubbles. The decreasing dissolved oxygen concentration reduces the Nernst loss, which is the key to reducing the OER overpotential. The dissolved oxygen transfer resistance increases greatly with the current density and PTL thickness so that the concentration of dissolved oxygen at the CL rises to a higher level. The water vapor produced by boiling reduces the dissolved oxygen concentration surrounding the bubbles greatly, ultimately reducing the Nernst loss. In short, the high transfer resistance of dissolved oxygen through the PTL is the prerequisite for boiling to reduce the OER overpotential.

(2) Secondly, the three-electrode cell and the HER model jointly investigate the mechanism by which boiling affects the HER overpotential. Boiling cannot reduce the activation overvoltage of HER. Boiling reduces the Nernst loss of HER when large hydrogen transfer resistance exists over the CL. Specifically, boiling reduces the partial pressure of gaseous hydrogen in bubbles and the dissolved hydrogen concentration surrounding the bubbles by vaporizing more water vapor. Therefore, the hydrogen activity at the CL decreases, reducing the Nernst loss of HER. The basic function of boiling in reducing the Nernst loss is that boiling soars the molar flux of water vapor, increasing the gas transfer velocity in carbon paper by several orders of magnitude. Therefore, the hydrogen gas at the CL can be expelled more quickly at boiling, forming a low hydrogen concentration at the CL.

(3) Finally, a PEMWE model is built to study the boiling mechanism decreasing the electrolysis voltage of PEMWE. Boiling mainly improves mass transfer to reduce the electrolysis voltage. The water vapor molar flux increases sharply during boiling, accelerating the gas flow in the PTL and reducing the detachment radius and lifetime of the bubbles attached to the PTL. Then, this high water vapor molar flux by boiling reduces oxygen and hydrogen's activity at the CL, reducing the Nernst loss most, which exceeds 70 mV at 1 $A \cdot cm^{-2}$. Boiling also increases the water vapor activity at the CL covered by bubbles. Thus, boiling activates the anodic reaction at the CL under the bubbles. However, boiling cannot

reduce the cathodic activation overvoltage because the cathodic reaction is not affected by water vapor activity. However, the PEMWE runs at a drying temperature, such as a high temperature above the boiling point, which can cause its interior to dry out, reducing the water content in the PEM. Drying out greatly increases the PEM resistivity, resulting in an ohmic overvoltage increase of 0.12 V at 1 $A \cdot cm^{-2}$. To balance the Nernst loss reduction by boiling and ohmic overvoltage increase by high temperature, the PEMWE should be controlled at a boiling temperature slightly above the boiling point. Besides, boiling can only significantly increase the electrolysis efficiency by about 5% above 0.5 $A \cdot cm^{-2}$.

6.2 Prospect

The above results give the advantage that boiling reduces the PEMWE voltage. Hydrogen production also needs consideration of the production cost, including investment, maintenance, and operating cost of the system [1]. Some researchers propose multi-system hydrogen gas co-production to reduce its operating cost [2-5]. However, blindly superimposing PEMWE and additional devices, such as the equipment that provides heat sources for boiling, may increase the investment cost of hydrogen production.

In future research, the PEMWE investment cost issue is discussed when boiling is introduced to a practical PEMWE stack. A theoretical model, including PEMWEs and exergoeconomic analysis, is built to study the boiling effect on the investment cost of the PEMWE stack. Boiling can be achieved in a PEMWE, as presented in Fig. 6.1. Waste vapor, as a heat source, is discharged from thermal power plants and flows into the bipolar plates (BPs) of a PEMWE. Because the waste vapor can discharge enormous latent heat during condensation, the latent heat is used to boil the liquid water in a PEMWE. Pressure in the BP is higher than that inside the PEMWE to ensure that the condensation temperature of the heat-source vapor is always higher than the boiling temperature of the water in the PEMWE. If water is only supplied at the anode inlet, part of the anode water can permeate to the cathode through the PEM. Boiling in the anode and cathode decreases the partial pressure of oxygen and hydrogen. If water is also supplied at the cathodic inlet, the cathode can further boil at a higher boiling temperature because of the increased flow rate of liquid water, resulting in a lower gaseous hydrogen partial pressure.

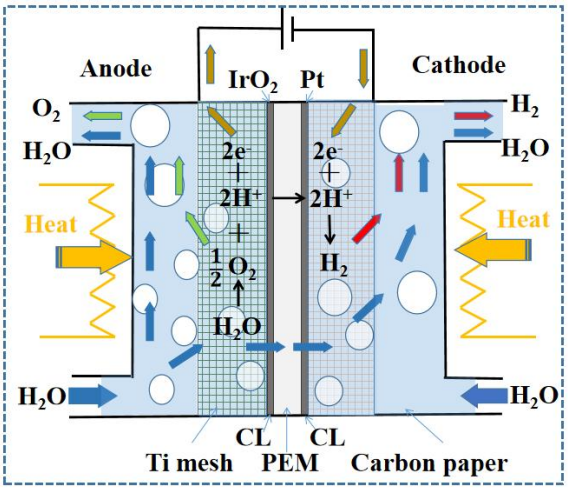

Fig. 6.1 Structure of a PEMWE unit with boiling.

Fig. 6.2 presents the system designs and temperature-entropy plots for hydrogen production systems using waste vapor from a thermal power plant as a heat source. The waste vapor is used to only heat the PEMWE stack in the system, as depicted in Fig. 6.2. An expansion valve isentropically expands the high-pressure vapor of state 14, and the low-pressure vapor of state 15 is isobarically condensed to release latent heat to boil water in the PEMWE stack. The saturated liquid water at state 16 is finally drained from the system outside. The thermodynamic states of the water circulating inside the PEMWE stack are marked at positions 1 – 11. Water from the surrounding (state 1: 25 ℃, 0.1 MPa) is supplied to the PEMWE stack for electrolysis consumption. The supplemental water (state 1) is mixed with the water at the anode outlet (state 8). Then, the liquid water at the outlet of the gas-liquid separator (state 10) is transported to the anode inlet (state 2) of the PEMWE stack by pump 1. Similarly, water (state 9) at the hydrogen separator outlet is pumped to the cathode inlet (state 3) by pump 2. The liquid water at the anode and cathode inlets (states 2 and 3) boils in the PEMWE stack and is drained from the anode and cathode outlets (states 4 and 5). The operating pressures in the anode and cathode of the PEMWE stack are independently controlled, and the pressure of the gas-liquid separator is equal to the atmospheric pressure. The temperature-entropy plot demonstrates the change in entropy of the water in the anode and cathode at boiling (anode: state 2-state 4, cathode: state 3-state 5), when the anode pressure is higher than the cathode pressure. In the temperature-entropy plot, it can be determined that the heat energy released by the condensation of waste water vapor is huge. Adjusting a specific flow rate of waste water vapor can meet the thermal energy required for the water boiling in the anode and cathode of the PEMWE stack. This is the case

that waste water vapor heats the PEMWE stack to achieve boiling in the PEMWE.

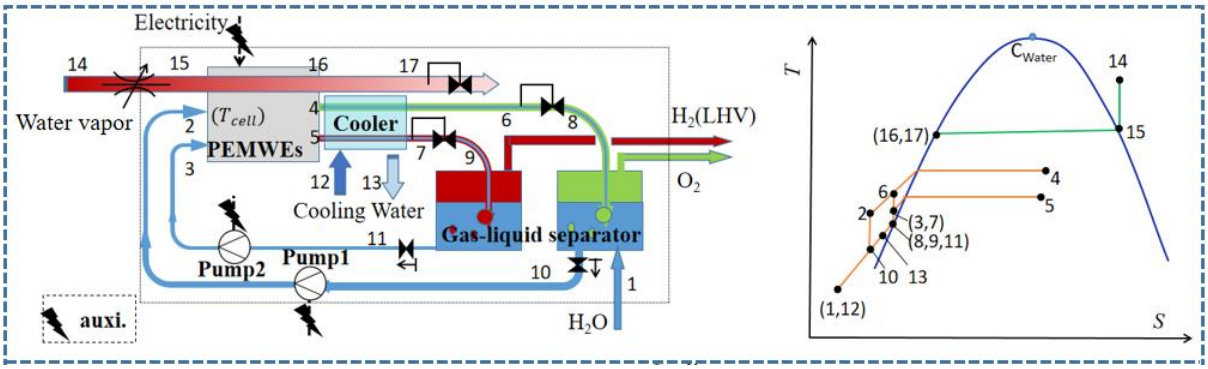

Fig. 6.2 Hydrogen production system.

The above gives the strategy of applying waste water vapor from thermal power plants to a practical PWMWE stack for hydrogen production. Fig. 6.3 shows the hydrogen gas production process by water electrolysis superimposed boiling in the future hydrogen energy society. The thermal energy required for boiling in the PEMWE can be extended to more heat sources, such as solar and geothermal. In addition, electricity for the PEMWE stack can also be considered to be obtained through solar and wind power. These clean and renewable energy sources can truly be used to produce "green hydrogen" with "zero carbon emissions".

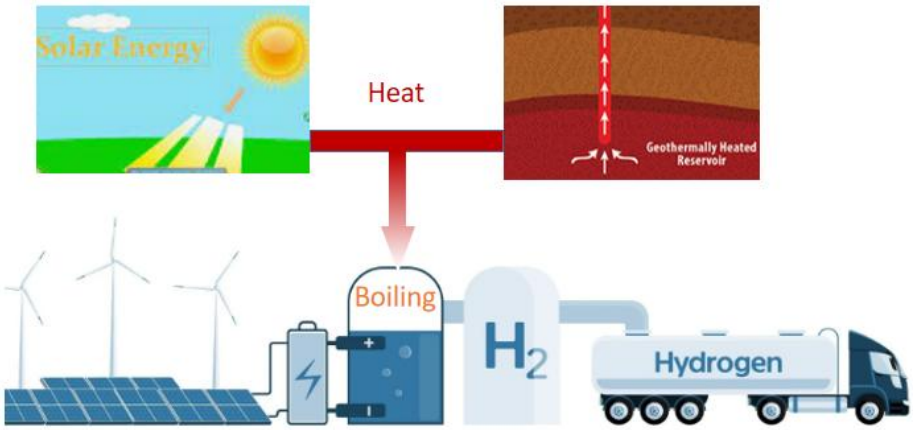

Fig. 6.3 Future energy society when the boiling effect is embedded in a water electrolyzer.

References

[1] Nami H, Mohammadkhani F, Ranjbar F. Utilization of waste heat from GTMHR for hydrogen generation via combination of organic Rankine cycles and PEM electrolysis. Energy Conversion and Management, 2016, 127: 589-598.

[2] Lümmen N, Karouach A, Tveitan S. Thermo-economic study of waste heat recovery from condensing steam for hydrogen production by PEM electrolysis. Energy Conversion and Management, 2019, 185: 21-34.

[3] Akrami E, Nemati A, Nami H, Ranjbar F. Exergy and exergoeconomic assessment of hydrogen and cooling production from concentrated PVT equipped with PEM electrolyzer and LiBr-H2O absorption chiller. International Journal of Hydrogen Energy. 2018;43(2):622-33.

[4] Espinoza-Quinones FR, Romani M, Borba CE, Modenes AN, Utzig CF, Dall'Oglio IC. A mathematical approach based on the Nernst-Planck equation for the total electric voltage demanded by the electrocoagulation process: Effects of a time-dependent electrical conductivity. Chemical Engineering Science. 2020;220:115626.

[5] Koponen J, Kosonen A, Huoman K, Ahola J, Ahonen T, Ruuskanen V. Specific energy consumption of PEM water electrolysers in atmospheric and pressurised conditions. In2016 18th European Conference on Power Electronics and Applications (EPE'16 ECCE Europe) 2016 (pp. 1-10). IEEE.

Appendix A. Anodic and cathodic activation fraction

Oxygen and hydrogen bubbles are ubiquitous in polymer electrolyte membrane water electrolyzers (PEMWE) and greatly influence electrolysis overvoltage [1-3]. Some researchers considered that oxygen bubbles would reduce the water coverage fraction of the anodic CL, thereby reducing the active area for the PEMWE anode [4, 5]. Therefore, they considered the water coverage fraction a parameter to determine the anodic activation overvoltage [2,6]. However, only considering the effect of water coverage fraction on the anodic activation overvoltage is still not comprehensive enough. Usually, the oxygen bubbles are mixed with water vapor. OER in the gas bubbles produces a weak current density. Because the activities of dissolved oxygen and gaseous oxygen are slightly different, the activation degree of oxygen evolution reaction (OER) in liquid water and water vapor is different. The low activity of water vapor in bubbles results in a lower OER current density, as the results in chapter 3. This will increase the current loading of the OER in liquid water, thereby increasing the activation overvoltage.

Similarly, the activity difference between dissolved hydrogen and gaseous hydrogen will also affect the activation overvoltage of the hydrogen evolution reaction (HER). Therefore, in addition to the water coverage fraction, this chapter additionally considers the effects of dissolved oxygen and dissolved hydrogen on the activation overvoltage. The expressions of the anodic and cathodic activation overvoltages in this chapter are derived based on the current density expressions of OER in chapter 3 and HER in chapter 4, respectively. More accurate expressions for anodic and cathodic activation overvoltages of the PEMWE are derived. The parameters such as the gas saturation, dissolved oxygen, and water vapor activity at the anodic CL are attributed to the anodic activation fraction, while the dissolved hydrogen activity is attributed to the cathodic activation fraction.

Derivation of anodic activation overvoltage

The anodic activation overvoltage of the PEMWE model is derived from the current density formula of the OER. As described in chapter 3, OER occurs in gas bubbles, in the water surrounding bubbles, and away from bubbles, yielding an average current density as

shown in Eq. (A.1). The i_g, i_{ls}, and i_l are the current densities of the CL in the bubbles, in the water surrounding the bubbles, and far from the bubbles, respectively. The $S_g^{CL,an}$ is the gas saturation at the anode CL, and r is the relative molar flux of gaseous oxygen through the PTL.

$$i = S_g^{CL,an} i_g + \gamma(1 - S_g^{CL,an}) i_{ls} + (1-\gamma)(1 - S_g^{CL,an}) i_l \quad \text{(A.1)}$$

In the results of chapter 3, the relative molar flux, γ, of gaseous oxygen through the 0.2-mm PTL is close to 1. Set γ = 1, Eq. (A.1) is simplified to Eq. (A.2). Then, the average current density is only related to the current density in the bubbles and in the water surrounding the bubbles.

$$i = S_g^{CL,an} i_g + (1 - S_g^{CL,an}) i_{ls} \quad \text{(A.2)}$$

The OER current density expressions between in bubbles and in liquid water are different because of the different mass phase state. The current density of the OER in the bubbles, i_g, is expressed in Eq. (A.3). The $i^0(T)$ is the exchange current density defined at standard pressure (0.1013 MPa) [6]. The α_t^{an} is the anode charge transfer coefficient, and z^{an} is the number of electron transferred in OER. The ΔE_g is the overpotential of OER in gas bubbles, the R is the universal gas constant, T is the Kelvin temperature, and F is the Faraday constant. $C_{w,g}^{CL}$ and $C_{O,g}^{CL}$ represent the concentrations of water vapor and gaseous oxygen at the CL, and $C_{w,g}^{0}$ and $C_{O,g}^{0}$ represent the concentrations of water vapor and gaseous oxygen at standard conditions (0.1013 MPa, 25 °C).

$$i_g = i^0(T) \frac{\left(\frac{C_{w,g}^{CL}}{C_{w,g}^{0}}\right)^{\alpha_t^{an}}}{\left(\frac{C_{O,g}^{CL}}{C_{O,g}^{0}}\right)^{0.5\alpha_t^{an}}} \exp\left(\frac{z^{an}\alpha_t^{an} F \Delta E_g}{RT}\right) \quad \text{(A.3)}$$

To substitute i_g into Eq. (A.2), Eq. (A.3) is mathematically transformed into Eq. (A.4).

$$i_g = i^0(T) \frac{\left(\frac{C_{w,g}^{CL}}{C_{w,g}^{0}}\right)^{\alpha_t^{an}}}{\left(\frac{C_{O,g}^{CL}}{C_{O,g}^{0}}\right)^{0.5\alpha_t^{an}}} \exp\left[\frac{z^{an}\alpha_t^{an} F\left(\Delta E_g - \Delta E_l + \Delta E_l\right)}{RT}\right]$$

$$= i^0(T) \left(\frac{\frac{C_{w,g}^{CL}}{C_{w,g}^{0}}}{\frac{C_{w,l}^{CL}}{C_{w,l}^{0}}}\right)^{\alpha_t^{an}} \frac{\left(\frac{C_{w,l}^{CL}}{C_{w,l}^{0}}\right)^{\alpha_t^{an}}}{\left(\frac{C_{O,g}^{CL}}{C_{O,g}^{0}}\right)^{0.5\alpha_t^{an}}} \exp\left[\frac{z^{an}\alpha_t^{an} F\left(\Delta E_g - \Delta E_l\right)}{RT}\right] \exp\left(\frac{z^{an}\alpha_t^{an} F \Delta E_l}{RT}\right)$$

$$= \left(\frac{\frac{c_{\mathrm{w,g}}^{\mathrm{CL}}}{c_{\mathrm{w,g}}^{0}}}{\frac{c_{\mathrm{w,l}}^{\mathrm{CL}}}{c_{\mathrm{w,l}}^{0}}} \right)^{\alpha_{\mathrm{t}}^{\mathrm{an}}} \exp\left[\frac{z^{\mathrm{an}}\alpha_{\mathrm{t}}^{\mathrm{an}}F(\Delta E_g - \Delta E_l)}{RT}\right] i^0(T) \frac{\left(\frac{c_{\mathrm{w,l}}^{\mathrm{CL}}}{c_{\mathrm{w,l}}^{0}}\right)^{\alpha_{\mathrm{t}}^{\mathrm{an}}}}{\left(\frac{c_{\mathrm{O,g}}^{\mathrm{CL}}}{c_{\mathrm{O,g}}^{0}}\right)^{0.5\alpha_{\mathrm{t}}^{\mathrm{an}}}} \exp\left(\frac{z^{\mathrm{an}}\alpha_{\mathrm{t}}^{\mathrm{an}}F\Delta E_l}{RT}\right) \quad \text{(A.4)}$$

Then, the expression for the current density of the OER in water, i_{ls}, makes similar mathematical transformations. Eq. (A.5) gives the current density of OER in the liquid water surrounding the bubbles, where ΔE_l is the overpotential of OER in liquid water. $C_{\mathrm{w,l}}^{\mathrm{CL}}$ and $C_{\mathrm{O,dis}}^{\mathrm{CL}}$ are the concentrations of liquid water and dissolved oxygen at the CL, while $C_{\mathrm{w,l}}^{0}$ and $C_{\mathrm{O,dis}}^{0}$ are the concentrations of liquid water and dissolved oxygen at standard conditions.

$$i_{ls} = i^0(T) \frac{\left(\frac{c_{\mathrm{w,l}}^{\mathrm{CL}}}{c_{\mathrm{w,l}}^{0}}\right)^{\alpha_{\mathrm{t}}^{\mathrm{an}}}}{\left(\frac{c_{\mathrm{O,dis}}^{\mathrm{CL}}}{c_{\mathrm{O,dis}}^{0}}\right)^{0.5\alpha_{\mathrm{t}}^{\mathrm{an}}}} \exp\left(\frac{z^{\mathrm{an}}\alpha_{\mathrm{t}}^{\mathrm{an}}F\Delta E_l}{RT}\right) \quad \text{(A.5)}$$

In order to substitute i_{ls} into Eq. (A.2), Eq. (A.5) is mathematically transformed into Eq. (A.6).

$$i_{ls} = i^0(T) \frac{\left(\frac{c_{\mathrm{O,g}}^{\mathrm{CL}}}{c_{\mathrm{O,g}}^{0}}\right)^{0.5\alpha_{\mathrm{t}}^{\mathrm{an}}}}{\left(\frac{c_{\mathrm{O,dis}}^{\mathrm{CL}}}{c_{\mathrm{O,dis}}^{0}}\right)^{0.5\alpha_{\mathrm{t}}^{\mathrm{an}}}} \frac{\left(\frac{c_{\mathrm{w,l}}^{\mathrm{CL}}}{c_{\mathrm{w,l}}^{0}}\right)^{\alpha_{\mathrm{t}}^{\mathrm{an}}}}{\left(\frac{c_{\mathrm{O,g}}^{\mathrm{CL}}}{c_{\mathrm{O,g}}^{0}}\right)^{0.5\alpha_{\mathrm{t}}^{\mathrm{an}}}} \exp\left(\frac{z^{\mathrm{an}}\alpha_{\mathrm{t}}^{\mathrm{an}}F\Delta E_l}{RT}\right)$$

$$= \left(\frac{\frac{c_{\mathrm{O,g}}^{\mathrm{CL}}}{c_{\mathrm{O,g}}^{0}}}{\frac{c_{\mathrm{O,dis}}^{\mathrm{CL}}}{c_{\mathrm{O,dis}}^{0}}} \right)^{0.5\alpha_{\mathrm{t}}^{\mathrm{an}}} i^0(T) \frac{\left(\frac{c_{\mathrm{w,l}}^{\mathrm{CL}}}{c_{\mathrm{w,l}}^{0}}\right)^{\alpha_{\mathrm{t}}^{\mathrm{an}}}}{\left(\frac{c_{\mathrm{O,g}}^{\mathrm{CL}}}{c_{\mathrm{O,g}}^{0}}\right)^{0.5\alpha_{\mathrm{t}}^{\mathrm{an}}}} \exp\left(\frac{z^{\mathrm{an}}\alpha_{\mathrm{t}}^{\mathrm{an}}F\Delta E_l}{RT}\right) \quad \text{(A.6)}$$

Finally, in order to unify the expression of the average current density, substitute Eq.s (A.4) and (A.6) into Eq. (A.2) to get the average current density, as Eq. (A.7).

$$i = S_{\mathrm{g}}^{\mathrm{CL,an}} \left(\frac{\frac{c_{\mathrm{w,g}}^{\mathrm{CL}}}{c_{\mathrm{w,g}}^{0}}}{\frac{c_{\mathrm{w,l}}^{\mathrm{CL}}}{c_{\mathrm{w,l}}^{0}}} \right)^{\alpha_{\mathrm{t}}^{\mathrm{an}}} \exp\left[\frac{z^{\mathrm{an}}\alpha_{\mathrm{t}}^{\mathrm{an}}F(\Delta E_g - \Delta E_l)}{RT}\right] i^0(T) \frac{\left(\frac{c_{\mathrm{w,l}}^{\mathrm{CL}}}{c_{\mathrm{w,l}}^{0}}\right)^{\alpha_{\mathrm{t}}^{\mathrm{an}}}}{\left(\frac{c_{\mathrm{O,g}}^{\mathrm{CL}}}{c_{\mathrm{O,g}}^{0}}\right)^{0.5\alpha_{\mathrm{t}}^{\mathrm{an}}}} \exp\left(\frac{z^{\mathrm{an}}\alpha_{\mathrm{t}}^{\mathrm{an}}F\Delta E_l}{RT}\right) + (1 -$$

$$S_{\mathrm{g}}^{\mathrm{CL,an}}) \left(\frac{\frac{c_{\mathrm{O,g}}^{\mathrm{CL}}}{c_{\mathrm{O,g}}^{0}}}{\frac{c_{\mathrm{O,dis}}^{\mathrm{CL}}}{c_{\mathrm{O,dis}}^{0}}} \right)^{0.5\alpha_{\mathrm{t}}^{\mathrm{an}}} i^0(T) \frac{\left(\frac{c_{\mathrm{w,l}}^{\mathrm{CL}}}{c_{\mathrm{w,l}}^{0}}\right)^{\alpha_{\mathrm{t}}^{\mathrm{an}}}}{\left(\frac{c_{\mathrm{O,g}}^{\mathrm{CL}}}{c_{\mathrm{O,g}}^{0}}\right)^{0.5\alpha_{\mathrm{t}}^{\mathrm{an}}}} \exp\left(\frac{z^{\mathrm{an}}\alpha_{\mathrm{t}}^{\mathrm{an}}F\Delta E_l}{RT}\right)$$

$$= \left\{ S_{\mathrm{g}}^{\mathrm{CL,an}} \left(\frac{\frac{c_{\mathrm{w,g}}^{\mathrm{CL}}}{c_{\mathrm{w,g}}^{0}}}{\frac{c_{\mathrm{w,l}}^{\mathrm{CL}}}{c_{\mathrm{w,l}}^{0}}} \right)^{\alpha_{\mathrm{t}}^{\mathrm{an}}} \exp\left[\frac{z^{\mathrm{an}}\alpha_{\mathrm{t}}^{\mathrm{an}}F(\Delta E_g - \Delta E_l)}{RT}\right] + (1 -$$

$$S_{\mathrm{g}}^{\mathrm{CL,an}}\left(\frac{\frac{C_{\mathrm{O,g}}^{\mathrm{CL}}}{C_{\mathrm{O,g}}^{0}}}{\frac{C_{\mathrm{O,dis}}^{\mathrm{CL}}}{C_{\mathrm{O,dis}}^{0}}}\right)^{0.5\alpha_{\mathrm{t}}^{\mathrm{an}}}\Bigg\} i^{0}(T)\frac{\left(\frac{C_{\mathrm{w,l}}^{\mathrm{CL}}}{C_{\mathrm{w,l}}^{0}}\right)^{\alpha_{\mathrm{t}}^{\mathrm{an}}}}{\left(\frac{C_{\mathrm{O,g}}^{\mathrm{CL}}}{C_{\mathrm{O,g}}^{0}}\right)^{0.5\alpha_{\mathrm{t}}^{\mathrm{an}}}}\exp\left(\frac{z^{\mathrm{an}}\alpha_{\mathrm{t}}^{\mathrm{an}}F\Delta E_{l}}{RT}\right) \quad \text{(A.7)}$$

In order to simplify Eq. (A.7), replace the expression in the big brackets in Eq. (A.7) with a parameter, $\bar{\theta}^{an}$, such as Eq. (A.8).

$$\bar{\theta}^{an}=S_{\mathrm{g}}^{\mathrm{CL,an}}\left(\frac{\frac{C_{\mathrm{w,g}}^{\mathrm{CL}}}{C_{\mathrm{w,g}}^{0}}}{\frac{C_{\mathrm{w,l}}^{\mathrm{CL}}}{C_{\mathrm{w,l}}^{0}}}\right)^{\alpha_{\mathrm{t}}^{\mathrm{an}}}\exp\left[\frac{z^{\mathrm{an}}\alpha_{\mathrm{t}}^{\mathrm{an}}F\left(\Delta E_{g}-\Delta E_{l}\right)}{RT}\right]+\left(1-S_{\mathrm{g}}^{\mathrm{CL,an}}\right)\left(\frac{\frac{C_{\mathrm{O,g}}^{\mathrm{CL}}}{C_{\mathrm{O,g}}^{0}}}{\frac{C_{\mathrm{O,dis}}^{\mathrm{CL}}}{C_{\mathrm{O,dis}}^{0}}}\right)^{0.5\alpha_{\mathrm{t}}^{\mathrm{an}}} \quad \text{(A.8)}$$

The equation, $\Delta E_g-\Delta E_l=\left[E-E_{\mathrm{g}}^{0}(T)\right]-\left[E-E_{\mathrm{l}}^{0}(T)\right]=E_{\mathrm{l}}^{0}(T)-E_{\mathrm{g}}^{0}(T)$, can be determined from the definition of overpotential, where $E_{\mathrm{g}}^{0}(T)$ and $E_{\mathrm{l}}^{0}(T)$ are the redox poterntial in gas bubbles and liquid water. As the result of chapter 3, $E_{\mathrm{l}}^{0}(T)$ approaches $E_{\mathrm{g}}^{0}(T)$, so Eq. (A.8) can be simplified to Eq. (A.9). The parameters in Eq. (A.9), such as gas saturation at the CL, the activities of water vapor, liquid water, gaseous oxygen and dissolved oxygen, affect the reactivity of OER. Hence, $\bar{\theta}^{an}$ is named the anodic activation fraction.

$$\bar{\theta}^{an}=S_{\mathrm{g}}^{\mathrm{CL,an}}\left(\frac{\frac{C_{\mathrm{w,g}}^{\mathrm{CL}}}{C_{\mathrm{w,g}}^{0}}}{\frac{C_{\mathrm{w,l}}^{\mathrm{CL}}}{C_{\mathrm{w,l}}^{0}}}\right)^{\alpha_{\mathrm{t}}^{\mathrm{an}}}+\left(1-S_{\mathrm{g}}^{\mathrm{CL,an}}\right)\left(\frac{\frac{C_{\mathrm{O,g}}^{\mathrm{CL}}}{C_{\mathrm{O,g}}^{0}}}{\frac{C_{\mathrm{O,dis}}^{\mathrm{CL}}}{C_{\mathrm{O,dis}}^{0}}}\right)^{0.5\alpha_{\mathrm{t}}^{\mathrm{an}}} \quad \text{(A.9)}$$

The concentrations of water vapor, liquid water, gaseous oxygen, and dissolved oxygen all affect the anodic activation fraction. The expressions for the water and oxygen concentrations are introduced as follows. The concentration of water vapor at the CL and the standard conditions are $C_{\mathrm{w,g}}^{\mathrm{CL}}$ and $C_{\mathrm{w,g}}^{0}$, as Eq. (A.10). $P_{\mathrm{w,g}}^{\mathrm{CL}}$ and $P_{\mathrm{w,g}}^{0}$ are the water vapor pressure at the CL and at the standard conditions, respectively. T^0 is 298 K.

$$\begin{cases}C_{\mathrm{w,g}}^{\mathrm{CL}}=\dfrac{P_{\mathrm{w,g}}^{\mathrm{CL}}}{RT}\\ C_{\mathrm{w,g}}^{0}=\dfrac{P_{\mathrm{w,g}}^{0}}{RT^{0}}\end{cases} \quad \text{(A.10)}$$

The concentrations of liquid water at the CL, $C_{\mathrm{w,l}}^{\mathrm{CL}}$, and the standard condition, $C_{\mathrm{w,l}}^{0}$, are listed in Eq. (A.11), where $\rho_{\mathrm{w,l}}^{\mathrm{CL}}$ and $\rho_{\mathrm{w,l}}^{0}$ are the mass density of liquid water at the CL and standard conditions, and M_{w} is the molar mass of water.

$$\begin{cases}C_{\mathrm{w,l}}^{\mathrm{CL}}=\dfrac{\rho_{\mathrm{w,l}}^{\mathrm{CL}}}{M_{\mathrm{w}}}\\ C_{\mathrm{w,l}}^{0}=\dfrac{\rho_{\mathrm{w,l}}^{0}}{M_{\mathrm{w}}}\end{cases} \quad \text{(A.11)}$$

Eq. (A.12) describes the concentration of gaseous oxygen at the CL, $C_{\mathrm{O,g}}^{\mathrm{CL}}$, and the standard conditions, $C_{\mathrm{O,g}}^{0}$, and $P_{\mathrm{O,g}}^{\mathrm{CL}}$ and $P_{\mathrm{O,g}}^{0}$ are the pressures of gaseous oxygen at the CL and standard conditions, respectively.

$$\begin{cases} C_{\mathrm{O,g}}^{\mathrm{CL}} = \frac{P_{\mathrm{O,g}}^{\mathrm{CL}}}{RT} \\ C_{\mathrm{O,g}}^{0} = \frac{P_{\mathrm{O,g}}^{0}}{RT^{0}} \end{cases} \quad \text{(A.12)}$$

Eq. (A.13) describes the concentration, $C_{\mathrm{O,dis}}^{\mathrm{CL}}$ and $C_{\mathrm{O,dis}}^{0}$, of dissolved oxygen at the CL and the standard conditions, respectively. $H_{\mathrm{T,O_2}}(T)$ and $H_{\mathrm{T,O_2}}(T^0)$ are Henry's coefficients of dissolved oxygen at T and T_0.

$$\begin{cases} C_{\mathrm{O,dis}}^{\mathrm{CL}} = H_{\mathrm{T,O_2}}(T) P_{\mathrm{O,g}}^{\mathrm{CL}} \\ C_{\mathrm{O,dis}}^{0} = H_{\mathrm{T,O_2}}(T^0) P_{\mathrm{O,g}}^{0} \end{cases} \quad \text{(A.13)}$$

Substitute Eq.s (A.10-A.13) into Eq. (A.9) to obtain Eq. (A.14).

$$\bar{\theta}^{an} = S_{\mathrm{g}}^{\mathrm{CL,an}} \left(\frac{\frac{P_{\mathrm{H_2O,g}}^{\mathrm{CL}} T^0}{P_{\mathrm{H_2O,g}}^{0} T}}{\frac{\rho_{\mathrm{H_2O,l}}^{\mathrm{CL}}}{\rho_{\mathrm{H_2O,l}}^{0}}} \right)^{\alpha_{\mathrm{t}}^{\mathrm{an}}} + (1 - S_{\mathrm{g}}^{\mathrm{CL,an}}) \left(\frac{H_{\mathrm{T,O_2}}(T_0) T^0}{H_{\mathrm{T,O_2}}(T) T} \right)^{0.5\alpha_{\mathrm{t}}^{\mathrm{an}}} \quad \text{(A.14)}$$

Simplifying the expression of the average current density can easily deduce the overpotential expression of OER. Using the intermediate parameter, $\bar{\theta}^{an}$, to simply the Eq. (A.7), the simplified expression of the average current density is

$$i = \bar{\theta}^{an} i^0(T) \frac{\left(\frac{c_{\mathrm{w,l}}^{\mathrm{CL}}}{c_{\mathrm{w,l}}^{0}} \right)^{\alpha_{\mathrm{t}}^{\mathrm{an}}}}{\left(\frac{c_{\mathrm{O,g}}^{\mathrm{CL}}}{c_{\mathrm{O,g}}^{0}} \right)^{0.5\alpha_{\mathrm{t}}^{\mathrm{an}}}} \exp\left(\frac{z^{\mathrm{an}} \alpha_{\mathrm{t}}^{\mathrm{an}} F \Delta E_l}{RT} \right) \quad \text{(A.15)}$$

In order to obtain the expression of OER overpotential, Eq. (A.15) is mathematically transformed to Eq. (A.16).

$$\Delta E_l = \frac{RT}{zF} \ln \left[\frac{\left(\frac{c_{\mathrm{O,g}}^{\mathrm{CL}}}{c_{\mathrm{O,g}}^{0}} \right)^{0.5}}{\left(\frac{c_{\mathrm{w,l}}^{\mathrm{CL}}}{c_{\mathrm{w,l}}^{0}} \right)} \right] + \frac{RT}{z^{\mathrm{an}} \alpha_{\mathrm{t}}^{\mathrm{an}} F} ln \left(\frac{i}{\bar{\theta}^{an} i^0(T)} \right) \quad \text{(A.16)}$$

The first term on RHS of Eq. (A.16) is the Nernst loss of OER, and the second term is the expression of activation overvoltage. The anodic activation fraction becomes an intermediate parameter that affects the anodic activation overvoltage. Therefore, the anodic activation overvoltage is

$$\eta^{\mathrm{act,an}} = \frac{RT}{z^{\mathrm{an}} \alpha_{\mathrm{t}}^{\mathrm{an}} F} \ln \left(\frac{i}{\bar{\theta}^{an} i_0^{\mathrm{an}}(T)} \right) \quad \text{(A.17)}$$

Derivation of cathodic activation fraction

The cathodic activation overvoltage of the PEMWE model can be derived from the expression for the average current density of the HER. The bubbles covering the cathode CL consist of gaseous hydrogen and water vapor. HER at the CL can occur in bubbles, in liquid water surrounding bubbles, and away from bubbles, with an average current density as shown in Eq. (A.18). The i_g, i_{ls}, and i_l are the current densities of HER in the bubbles, in liquid water surrounding the bubbles and away from the bubbles, respectively. $S_g^{CL,ca}$ is the gas saturation at the cathodic CL, and $1 - S_g^{CL,ca}$ represents the coverage fraction of liquid water at the CL. The *r* is the relative molar flux of gaseous hydrogen through the PTL.

$$i = S_g^{CL,ca} i_g + (1 - S_g^{CL,ca})\gamma i_{ls} + \left(1 - S_g^{CL,ca}\right)(1 - \gamma) i_l \quad \text{(A.18)}$$

As the results in chapter 4, hydrogen gas passes through the PTL almost as gas hydrogen, with *r* approximately equal to 1. Therefore Eq. (A.18) is simplified to Eq. (A.19).

$$i = S_g^{CL,ca} i_g + (1 - S_g^{CL,ca}) i_{ls} \quad \text{(A.19)}$$

The average current density of HER is related to the current density in gas bubbles and in liquid water. Because protons are sufficiently transferred through the PEM, the proton activity in the ionomer is considered to be 1. Eq. (A.20) shows the HER current density in gas bubbles, [7]. ΔE is the overpotential of HER, $C_{H,g}^{CL}$ and $C_{H,g}^{0}$ are the concentration of gaseous hydrogen at the CL and standard conditions. The α_t^{ca} is the cathode charge transfer coefficient, and z^{ca} is the number of electron transferred in HER.

$$i_g = i^0(T)\left(\frac{C_{H,g}^{0}}{C_{H,g}^{CL}}\right)^{\alpha_t^{ca}} \exp\left(\frac{z^{ca}\alpha_t^{ca} F \Delta E}{RT}\right) \quad \text{(A.20)}$$

The current density of HER in liquid water is shown in Eq. (A.21), where $C_{H,dis}^{CL}$ and $C_{H,dis}^{0}$ are the concentrations of dissolved hydrogen at the CL and standard conditions. Because the proton exists in the ionomer, and its physical state is the same in gas bubbles and liquid water. The HER overpotential in liquid water is also ΔE.

$$i_{ls} = i^0(T)\left(\frac{C_{H,dis}^{0}}{C_{H,dis}^{CL}}\right)^{\alpha_t^{ca}} \exp\left(\frac{z^{ca}\alpha_t^{ca} F \Delta E}{RT}\right) \quad \text{(A.21)}$$

In order to substitute i_{ls} into Eq. (A.19), Eq. (A.21) is mathematically transformed into Eq.

(A.22).

$$i_{\mathrm{ls}} = \left(\frac{\frac{C^{0}_{\mathrm{H,dis}}}{C^{\mathrm{CL}}_{\mathrm{H,dis}}}}{\frac{C^{0}_{\mathrm{H,g}}}{C^{\mathrm{CL}}_{\mathrm{H,g}}}} \right)^{\alpha_{\mathrm{t}}^{\mathrm{ca}}} i^{0}(T) \left(\frac{C^{0}_{\mathrm{H,g}}}{C^{\mathrm{CL}}_{\mathrm{H,g}}} \right)^{\alpha_{\mathrm{t}}^{\mathrm{ca}}} \exp\left(\frac{z^{\mathrm{ca}} \alpha_{\mathrm{t}}^{\mathrm{ca}} F \Delta E}{RT} \right) \quad \text{(A.22)}$$

Finally, Eq.s (A.20) and (A.22) are substituted into Eq. (A.19) to obtain the expression of HER average current density.

$$i = S_{\mathrm{g}}^{\mathrm{CL,ca}} i^{0}(T) \left(\frac{C^{0}_{\mathrm{H,g}}}{C^{\mathrm{CL}}_{\mathrm{H,g}}} \right)^{\alpha_{\mathrm{t}}^{\mathrm{ca}}} \exp\left(\frac{z^{\mathrm{ca}} \alpha_{\mathrm{t}}^{\mathrm{ca}} F \Delta E}{RT} \right) + (1 -$$

$$S_{\mathrm{g}}^{\mathrm{CL,ca}}) \left(\frac{\frac{C^{0}_{\mathrm{H,dis}}}{C^{\mathrm{CL}}_{\mathrm{H,dis}}}}{\frac{C^{0}_{\mathrm{H,g}}}{C^{\mathrm{CL}}_{\mathrm{H,g}}}} \right)^{\alpha_{\mathrm{t}}^{\mathrm{ca}}} i^{0}(T) \left(\frac{C^{0}_{\mathrm{H,g}}}{C^{\mathrm{CL}}_{\mathrm{H,g}}} \right)^{\alpha_{\mathrm{t}}^{\mathrm{ca}}} \exp\left(\frac{z^{\mathrm{ca}} \alpha_{\mathrm{t}}^{\mathrm{ca}} F \Delta E}{RT} \right)$$

$$= \left[S_{\mathrm{g}}^{\mathrm{CL,ca}} + (1 - S_{\mathrm{g}}^{\mathrm{CL,ca}}) \left(\frac{\frac{C^{0}_{\mathrm{H,dis}}}{C^{\mathrm{CL}}_{\mathrm{H,dis}}}}{\frac{C^{0}_{\mathrm{H,g}}}{C^{\mathrm{CL}}_{\mathrm{H,g}}}} \right)^{\alpha_{\mathrm{t}}^{\mathrm{ca}}} \right] i^{0}(T) \left(\frac{C^{0}_{\mathrm{H,g}}}{C^{\mathrm{CL}}_{\mathrm{H,g}}} \right)^{\alpha_{\mathrm{t}}^{\mathrm{ca}}} \exp\left(\frac{z^{\mathrm{ca}} \alpha_{\mathrm{t}}^{\mathrm{ca}} F \Delta E}{RT} \right) \quad \text{(A.23)}$$

In order to further simplify Eq. (A.23), the hydrogen concentration needs to be substituted into Eq. (A.23). The concentration expressions of gaseous hydrogen and dissolved hydrogen are introduced as follows. The concentrations of gaseous hydrogen at the CL and standard conditions are as in Eq. (A.24), where the $P^{\mathrm{CL}}_{\mathrm{H,g}}$ and $P^{0}_{\mathrm{H,g}}$ are the pressure of gaseous hydrogen at the CL and standard conditions.

$$\begin{cases} C^{\mathrm{CL}}_{\mathrm{H,g}} = \frac{P^{\mathrm{CL}}_{\mathrm{H,g}}}{RT} \\ C^{0}_{\mathrm{H,g}} = \frac{P^{0}_{\mathrm{H,g}}}{RT^{0}} \end{cases} \quad \text{(A.24)}$$

The concentration of dissolved hydrogen at the CL and standard conditions, $C^{\mathrm{CL}}_{\mathrm{H,dis}}$ and $C^{0}_{\mathrm{H,dis}}$, are shown in Eq. (A.25), where $P^{\mathrm{CL}}_{\mathrm{H,g}}$ and $P^{0}_{\mathrm{H,g}}$ are the pressures of gaseous hydrogen at the CL and standard conditions, respectively.

$$\begin{cases} C^{\mathrm{CL}}_{\mathrm{H,dis}} = H_{\mathrm{T,H_2}}(T) P^{\mathrm{CL}}_{\mathrm{H,g}} \\ C^{0}_{\mathrm{H,dis}} = H_{\mathrm{T,H_2}}(T_0) P^{0}_{\mathrm{H,g}} \end{cases} \quad \text{(A.25)}$$

Finally, combining the current densities in the gas bubbles and in liquid water yields the average HER current density. Substituting Eq.s (A.24) and (A.25) into Eq. (A.23), the average current density of HER is

$$i = \left[S_{\mathrm{g}}^{\mathrm{CL,ca}} + (1 - S_{\mathrm{g}}^{\mathrm{CL,ca}}) \left(\frac{H_{\mathrm{T,H_2}}(T_0) T^{0}}{H_{\mathrm{T,H_2}}(T) T} \right)^{\alpha_{\mathrm{t}}^{\mathrm{ca}}} \right] i^{0}(T) \left(\frac{C^{0}_{\mathrm{H,g}}}{C^{\mathrm{CL}}_{\mathrm{H,g}}} \right)^{\alpha_{\mathrm{t}}^{\mathrm{ca}}} \exp\left(\frac{z^{\mathrm{ca}} \alpha_{\mathrm{t}}^{\mathrm{ca}} F \Delta E}{RT} \right) \text{(A.26)}$$

The expression in the square bracket of Eq. (A.26) can be represented by the cathodic activation fraction.

$$\bar{\theta}^{ca} = S_{\mathrm{g}}^{\mathrm{CL,ca}} + (1 - S_{\mathrm{g}}^{\mathrm{CL,ca}})\left(\frac{H_{\mathrm{T,H_2}}(T_0)T^0}{H_{\mathrm{T,H_2}}(T)T}\right)^{\alpha_{\mathrm{t}}^{\mathrm{ca}}} \quad \text{(A.27)}$$

Next, Eq. (A.27) is substituted into Eq. (A.26) to simplify the expression of HER current density.

$$i = \bar{\theta}^{ca} i^0(T)\left(\frac{C_{\mathrm{H,g}}^0}{C_{\mathrm{H,g}}^{\mathrm{CL}}}\right)^{\alpha_{\mathrm{t}}^{\mathrm{ca}}} \exp\left(\frac{z^{\mathrm{ca}}\alpha_{\mathrm{t}}^{\mathrm{ca}}F\Delta E}{RT}\right) \text{(A.28)}$$

The expression of HER overvoltage can be obtained by mathematical transformation of Eq. (A.28).

$$\Delta E = \frac{RT}{z^{\mathrm{ca}}F}\ln\left(\frac{C_{\mathrm{H,g}}^{\mathrm{CL}}}{C_{\mathrm{H,g}}^0}\right) + \frac{RT}{z^{\mathrm{ca}}\alpha_{\mathrm{t}}^{\mathrm{ca}}F} ln\left(\frac{i}{\bar{\theta}^{ca} i^0(T)}\right) \quad \text{(A.29)}$$

The first term of Eq. (A.29) RHS is the Nernst loss of HER, and the second term is the expression of HER activation overvoltage, as Eq. (A.30). Among them, the cathodic activation fraction becomes the intermediate parameter of cathodic activation overvoltage.

$$\eta^{\mathrm{act,ca}} = \frac{RT}{z^{\mathrm{ca}}\alpha_{\mathrm{t}}^{\mathrm{ca}}\mathrm{F}}\ln\left(\frac{i}{\bar{\theta}^{ca} i_0^{\mathrm{ca}}(T)}\right) \quad \text{(A.30)}$$

So far, the OER current density model in chapter 3 and the HER current density model in chapter 4 are linked with the PEMWE overpotential model in chapter 5.

References

[1] Kadyk T, Bruce D, Eikerling M. How to enhance gas removal from porous electrodes?. Scientific reports. 2016 Dec 23;6(1):1-4.

[2] Nouri-Khorasani A, Ojong ET, Smolinka T, Wilkinson DP. Model of oxygen bubbles and performance impact in the porous transport layer of PEM water electrolysis cells. International journal of hydrogen energy. 2017 Nov 30;42(48):28665-80.

[3] Leonard E, Shum AD, Normile S, Sabarirajan DC, Yared DG, Xiao X, Zenyuk IV. Operando X-ray tomography and sub-second radiography for characterizing transport in polymer electrolyte membrane electrolyzer. Electrochimica Acta. 2018 Jun 20;276:424-33.

[4] Zhang D, Zeng K. Evaluating the behavior of electrolytic gas bubbles and their effect on the cell voltage in alkaline water electrolysis. Industrial & Engineering Chemistry Research. 2012 Oct 24;51(42):13825-32.

[5] Mo J. Fundamental studies of electrochemical reactions and microfluidics in proton exchange membrane electrolyzer cells.

[6] Schmidt G, Suermann M, Bensmann B, et al. Modeling overpotentials related to mass transport through porous transport layers of PEM water electrolysis cells. Journal of The Electrochemical Society, 2020, 167(11): 114511.

[7] Angulo A, van der Linde P, Gardeniers H, Modestino M, Rivas DF. Influence of bubbles on the energy conversion efficiency of electrochemical reactors. Joule. 2020;4(3):555-79.